NASA CR-135312
TRW 29999-6013-RU-00

ION ENGINE AUXILIARY PROPULSION APPLICATIONS AND INTEGRATION STUDY

(NASA-CR-135312) ION ENGINE AUXILIARY PROPULSION APPLICATIONS AND INTEGRATION STUDY (TRW Defense and Space Systems Group) 280 p HC A13/MF A01 CSCL 21C
N78-15168
Unclas
G3/20 55558

TRW DEFENSE AND SPACE SYSTEMS GROUP

prepared for

NATIONAL AERONAUTICS AND SPACE ADMINISTRATION

NASA Lewis Research Center
Contract NAS 3-20113

JAN 1978
RECEIVED
NASA STI FACILITY

1. Report No.	2. Government Accession No.	3. Recipient's Catalog No
NASA CR-135312		

4. Title and Subtitle	5. Report Date
Ion Engine Auxiliary Propulsion Applications and Integration Study	July 7, 1977
	6. Performing Organization Code
7. Author(s)	8. Performing Organization Report No
S. Zafran, Editor	29999-6013-RU-00
9. Performing Organization Name and Address	10. Work Unit No
TRW Defense and Space Systems Group One Space Park Redondo Beach, California 90278	YOS 7264
	11. Contract or Grant No
	NAS 3-20113
12. Sponsoring Agency Name and Address	13. Type of Report and Period Covered
National Aeronautics and Space Administration Washington, D. C. 20578	Contractor Report
	14. Sponsoring Agency Code

15. Supplementary Notes

Project Manager, Shigeo Nakanishi, Space Propulsion and Power Division, NASA-Lewis Research Center, Cleveland, Ohio 44135

16. Abstract

This study was conducted to assess the benefits to be derived from application of the NASA-LeRC 8-cm mercury electron-bombardment ion thruster. Two specific spacecraft missions were studied. Also, a thruster was tested to provide additional needed information on its efflux characteristics and interactive effects. A Users Manual was then prepared describing how to integrate the thruster for auxiliary propulsion on geosynchronous satellites.

By incorporating ion engines on an advanced communications mission, the weight available for added payload increases by about 82 kg (181 lb) for a 1000 kg (2200 lb) satellite which otherwise uses electrothermal hydrazine.

Ion engines can be integrated into a High Performance Propulsion Module that is compatible with the standard NASA Multimission Modular Spacecraft (MMS) and can be used for both geosynchronous and low earth orbit applications. The low disturbance torques introduced by the ion engines permit accurate spacecraft pointing with the payload in operation during thrusting periods. Pointing transients of less than 4×10^{-4} degree are predicted from computer simulation results for the MMS.

The feasibility of using the thruster's neutralizer assembly for neutralization of differentially charged spacecraft surfaces at geosynchronous altitude was demonstrated during the testing program.

17. Key Words (Suggested by Author(s))	18. Distribution Statement
Spacecraft design Spacecraft propulsion Attitude and velocity control Thruster interactions	

19. Security Classif. (of this report)	20. Security Classif. (of this page)	21. No. of Pages	22. Price*
Unclassified	Unclassified		

* For sale by the National Technical Information Service, Springfield, Virginia 22161

NASA-C-168 (Rev 10-75)

FOREWORD

The Ion Engine Auxiliary Propulsion Applications and Integration Study was performed by TRW Defense and Space Systems Group under the technical direction of S. Nakanishi, NASA Lewis Research Center. S. Zafran served as the TRW program manager, and performed the propulsion subsystem investigation. D.H. Mitchell directed the spacecraft design activities, J.M. Sellen conducted the thruster interfaces investigation, and M.H. Gran studied the attitude control subsystems. Other contributors to the technical effort included J.J. Biess, G.K. Komatsu, H. Nakano, L.G. Robertson, D.W. Rusta, and D.D. Sherwood. Special deposition plate analysis was performed by D.F. Hall of Aerospace Corporation.

PRECEDING PAGE BLANK NOT FILMED

PRECEDING PAGE BLANK NOT FILMED

CONTENTS

		Page
1.	SUMMARY	1
2.	INTRODUCTION	3
3.	MISSION APPLICATIONS	5
3.1	Selection of Candidate Missions	5
3.1.1	Potential Uses for Ion Engine Auxiliary Propulsion	5
3.1.2	Comparison with Mission Models	6
3.1.3	Selection of Two Candidate Missions	8
3.1.3.1	Mission 1 Summary	11
3.1.3.2	Mission 2 Summary	11
3.2	Mission 1: Advanced Communications Satellite	14
3.2.1	Ion Engine Auxiliary Propulsion Functions	15
3.2.1.1	Transfer Orbit Attitude Control and Apogee Boost	17
3.2.1.2	Acquisition and Initial Station Positioning	18
3.2.1.3	North-South Stationkeeping	19
3.2.1.4	East-West Stationkeeping	23
3.2.1.5	Attitude Control and Momentum Dump (Normal Mode)	24
3.2.1.6	Change of Station	24
3.2.2	Ion Propulsion Subsystem	25
3.2.3	Interactions with Attitude and Velocity Control Subsystem	29
3.2.3.1	Baseline AVCS and Propulsion Subsystem Designs	31
3.2.3.2	Momentum Bias	35
3.2.3.3	Pointing Accuracy	41
3.2.3.4	Control System Stability	52
3.2.4	Electrical Power Sources	54
3.2.4.1	Electric Power Subsystem Configuration	55
3.2.4.2	Integration of Power Processor with Spacecraft Power Sources	57
3.2.4.3	Analysis of Power Source Requirements	61
3.2.5	Thermal Control	66
3.2.6	Net Mass Savings with Ion Propulsion for Mission 1	67
3.2.7	Reliability Analyses	68

CONTENTS (Continued)

Page

3.2.7.1 Summary and Block Diagrams 68
3.2.7.2 Markov Models for Reliability Calculations 76
3.2.7.3 Failure Rate Data 81

3.3 Mission 2: High-Performance Propulsion Module for the Multimission Modular Spacecraft 84

3.3.1 High-Performance Propulsion Module Description 84
3.3.2 Ion Propulsion Module Functions 90

3.3.2.1 Geosynchronous Orbit MMS Mission . 90
3.3.2.2 Low Earth Orbit MMS Mission 91

3.3.3 Interactions with MMS Attitude Control Subsystem Module 93

3.3.3.1 Mission Requirements 95
3.3.3.2 Baseline Mission 2 Attitude Control Subsystem 95
3.3.3.3 MMS Pointing Accuracies with Ion Propulsion 99
3.3.3.4 Other ACS – Ion Propulsion Interactions 103

3.3.4 Interactions with MMS Power Module 104

3.3.4.1 Synchronous Orbit MMS 108
3.3.4.2 Low Earth Orbit MMS 110
3.3.4.3 Summary of Impacts 113

3.3.5 Other Design Considerations 115

3.3.5.1 Net Mass Property Impact 115
3.3.5.2 Thermal Control 117
3.3.5.3 Reliability 117

4. THRUSTER INTERFACES 119

4.1 Thruster Test Chamber 119

4.2 Unshielded Charged Particle Efflux 122

4.2.1 Charged Particle Measurements 122
4.2.2 Normalized Efflux Determinations 136

4.2.2.1 Thrust Ions 136
4.2.2.2 Group II Ions 140
4.2.2.3 Group IV Ions 144
4.2.2.4 Piggy-Back J_+ Probe Measurements 147

4.3 Thruster Sputter Shield 148

CONTENTS (Continued)

		Page
4.4	Shielded Charged Particle Efflux	148
4.4.1	Shielded J_+ Faraday Cup Measurements	148
4.4.2	Swinging J_+ Faraday Cup Measurements	154
4.4.3	4-Inch J_+ Probe Measurements	155
4.5	Sputter Shield Material Transport	160
4.5.1	Sputtering Plate Sample Measurements	160
4.5.1.1	Sputtering Plate Layer Fabrication	163
4.5.1.2	Sputtering Plate Configuration and Mounting	165
4.5.1.3	Sputtering Plate Sample Properties After Exposure	165
4.5.1.4	Calculated Thrust Ion Erosion Rates	171
4.5.2	Deposition Plate Measurements	173
4.5.2.1	Experimental Array	174
4.5.2.2	ESCA Analyses of Deposition Plates	174
4.6	Neutral Mercury Efflux	176
4.7	Optical Emission	182
4.7.1	Optical Power Density Measurements	182
4.7.2	Spectral Measurements	184
4.7.3	Ratio of Photon Generation to Ion Generation in the Electron Bombardment Discharge	196
4.8	Magnetic Fields	197
4.8.1	Experimental Apparatus for Magnetic Measurements	198
4.8.2	Thruster Permanent Magnetic Moment Measurements	200
4.8.3	Magnetic Moment Levels for an Operating Ion Thruster Compared to the Inactive (Nonoperating) Thruster	203
4.9	Neutralization of Differentially Charged Surfaces	205
4.9.1	Experiment Setup	206
4.9.2	Drainage Current Measurements	208
4.9.3	Implications of the Observed Ion Current Drainage Behavior	213

CONTENTS (Continued)

Page

5. USERS MANUAL 216

6. DISCUSSION OF RESULTS 219

7. CONCLUSIONS 222

REFERENCES 224

APPENDICES

A SYMBOLS 226

B DESIGN OF BOOST REGULATOR BETWEEN SPACECRAFT BUS AND ION ENGINE POWER PROCESSOR 229

C REACTION WHEEL ATTITUDE CONTROL SUBSYSTEM 233

D FACTORS IN THE DESIGN OF A SPUTTER SHIELD FOR AN 8 CM MERCURY ION THRUSTER 239

ILLUSTRATIONS

		Page
1.	Search for Candidate Paylods that can Benefit from Ion Engines	8
2.	Advanced Communications Satellite with Ion Auxiliary Propulsion	13
3.	Location of Ion Thrusters on Advanced Communications Satellite	14
4.	Multimission Modular Spacecraft Bus (Exploded View)	15
5.	Geometry of Orbit Corrections	20
6.	Orbital Efficiency and Thrusting Time for North-South Stationkeeping	22
7.	Annual East-West Stationkeeping Velocity Requirement	23
8.	Ion Propulsion Subsystem Schematic	25
9.	Integration of Ion Propulsion Subsystem with Intelsat V Design	28
10.	Schematic Representation of Various Biased Momentum Wheel/Gimbal Configurations	37
11.	Precession Due to Inertially Constant Torque	44
12.	Precession Management - Sample Case	45
13.	Optimum Precession Management with Two Control Pulses per Day	47
14.	Optimum Precession Management with Four Control Pulses per Day	48
15.	Performance Characteristics with Two Daily Control Pulses	50
16.	Performance Characteristics with Four Daily Control Pulses	51
17.	Advanced Communications Satellite Electric Power Subsystem	56
18.	Typical Battery Controls	56

ILLUSTRATIONS (Continued)

		Page
19.	Option 1 - Dedicated 70 Vdc Solar Array for Electric Propulsion	58
20.	Option 2 - Add Boost Regulators to Standard 28-Volt Spacecraft Bus	59
21.	Option 3 - Modify Power Processor to Operate from Standard 28-Volt Power Subsystem	60
22.	Reliability Block Diagram for Nonredundant Propulsion Configuration	70
23.	Reliability Block Diagram for Propulsion Configuration with Cross-Strapped Controllers	71
24.	Reliability Block Diagram for Propulsion Configuration with Redundant Thrusters	71
25.	Reliability Block Diagram for Propulsion Configuration with Redundant Thrusters and Cross-Strapped Controllers	72
26.	Propulsion Subsystem with Redundant Thrusters and Cross-Strapped Controllers	75
27.	Markov State Transition Diagram for Nonredundant Propulsion Subsystem	78
28.	Interpretation of Markov States	78
29.	Markov Transition Rate Matrix for Nonredundant Configuration	80
30.	Ion Propulsion Subsystem Schematic for MMS Missions	85
31.	High-Performance Propulsion Module for Multimission Modular Spacecraft (MMS)	85
32.	Layout of High Performance Propulsion Module with LandSat Configuration	86
33.	MMS StormSat Configuration with Ion Auxiliary Propulsion	88
34.	Possible Low Earth Orbit MMS Mission with Ion Propulsion	92
35.	Effects of Momentum Unloading Loop Gain	101
36.	MMS Attitude Control Transients Due to Wheel Unloading During Stationkeeping	102

ILLUSTRATIONS (Continued)

		Page
37.	Allowable Illumination at Star Tracker (within 0.35 to 0.75μ spectral band)	106
38.	MMS Power Regulator Unit Power Module	106
39.	5- by 10-foot Test Chamber Dimensions	120
40.	Diagnostic Instrument Array	121
41.	Engine J_+ Probe Dimensions	121
42.	1-1/2 inch J_+ Probe Dimensions	122
43.	Swinging J_+ Probe Dimensions	123
44.	4-inch J_+ and Piggy-Back Probe Dimensions	124
45.	Probe Motion and Mounting Rod Locations	126
46.	Engine J_+ Probe Data 5 cm Downstream	126
47.	Engine J_+ Probe Data 10 cm Downstream	127
48.	Engine J_+ Probe Data 15 cm Downstream	127
49.	Engine J_+ Probe Data 20 cm Downstream	128
50.	Engine J_+ Probe Data 30 cm Downstream	128
51.	Ion Current Versus Polar Angle	131
52.	Swinging J_+ RPA Probe Data	133
53.	Swinging J_+ RPA Probe Data on Other Side of Beam	133
54.	4-inch J_+ Probe Data	135
55.	Piggy-Back J_+ Probe Data	135
56.	Normalized Thrust Ion Efflux at R = 1 Meter	138
57.	Normalized Group II Ion Efflux at R = 1 Meter from Swinging J_+ Probe Measurements	141
58.	Normalized Group II Ion Efflux at R = 1 Meter from 4-inch J_+ Probe Measurements	141
59.	Comparison of Normalized Group II Ion Efflux from Swinging J_+ Probe and 4-inch J_+ Probe Data	142

ILLUSTRATIONS (Continued)

		Page
60.	Normalized Group IV Ion Efflux at R = 1 Meter from Swinging J_+ Probe Measurements	146
61.	Normalized Group IV Ion Efflux at R = 1 Meter from 4-inch J_+ Probe Measurements	146
62.	Normalized Hard Ion Efflux at the Piggy-Back J_+ Probe	149
63.	Normalized Soft Ion Efflux at the Piggy-Back J_+ Probe	149
64.	Thruster Sputter Shield	150
65.	Sputter Shield Mounted on Thruster	151
66.	Engine J_+ Probe Data, 20 cm Downstream	152
67.	Engine J_+ Probe Data, 25 cm Downstream	152
68.	Engine J_+ Probe Data, 30 cm Downstream	153
69.	Engine J_+ Probe Data, 35 cm Downstream	153
70.	Ion Current Density Versus Polar Angle	156
71.	Normalized Total Ion Efflux at R = 1 Meter	157
72.	4-Inch J_+ RPA Probe Data	159
73.	Normalized Group IV Ion Efflux at R = 1 Meter	161
74.	4-Inch J_+ Current Measurements	162
75.	4-Inch J_+ RPA Data, E < 50 eV	162
76.	4-Inch J_+ RPA Data, E >100 eV	163
77.	Sputtering Plate Sample	164
78.	Thruster, Sputtering Sample Plates and Deposition Sample Plates; Test Configuration	166
79.	Sputtering Samples SS-1, SS-2, and SS-3 After Exposure	167
80.	SS-1 Microphotographs	169
81.	Rear Face Deposit	171
82.	SS-2 Photographs	172

ILLUSTRATIONS (Continued)

		Page
83.	ECSA Data	177
84.	Movable Ion Gauge	178
85.	Movable Ion Gauge Measurement of Discharge Chamber (Cathode) Hg^o Release	180
86.	Movable Ion Gauge Measurement of Neturalizer Hg^o Release	181
87.	Movable Ion Gauge Measurement of Discharge Chamber (Cathode) and Neutralizer Hg^o Release	181
88.	Photodiode Mounting Arrangement	183
89.	Electron Bombardment Discharge Emission as a Function of Probe Rotation Angle, Θ	185
90.	Plasma Discharge Neutralizer Emission as a Function of Probe Rotation Angle, Θ	186
91.	Spectral Measurements Apparatus	187
92.	Monochrometer Output as a Function of Wavelength for the Electron Bombardment Discharge, [J(CK) = 0.55 A, V(CK) = 9.2 V, J(E) = 1.01 A, ΔV = 30 V, Dynode Chain Voltage = 700 V]	189
93.	Monochrometer Output as a Function of Wavelength for the Neutralizer Discharge. [J(NK) = 0.5 A, V(NK) = 15.7 V, Dynode Chain Voltage = 900 V]	190
94.	Monochrometer Output as a Function of Wavelength for Mercury Calibration Lamp	191
95.	Permanent Magnetic Moments Test Apparatus	199
96.	Magnetometer Signal (B_r) as a Function of Rotation Table Angle (Θ) for a Series of Magnetometer-Thruster Separation Distances (r)	201
97.	Maximum B_r as a Function of Magnetometer-Thruster Separation Distance, r	201
98.	Overall Test Configuration for the Neutralization of Differentially Charged Surfaces Tests	207
99.	Ion Drainage Current to the Cylinder	209

ILLUSTRATIONS (Continued)

		Page
100.	Ion Drainage Current to the Cylinder, Logarithmic Presentation	211
101.	Ion Drainage Current to Upper Shroud	212
102.	Ion Drainage Current to Sputter Shield	214
103.	Electron Drainage Current to Sputter Shield	214
B-1.	Block Regulator, Power Section	230
B-2.	Boost Regulator, Power Section	230
B-3.	Timing Diagram	232
C-1.	Transient Response During Wheel Speed Reversal (System A)	238
C-2.	Transient Response During Wheel Speed Reversal (System B)	238
D-1.	Spherical Polar, Cylindrical, and Cartesian Coordinate Systems to be Used in the Sputter Shield Design Calculations	241
D-2.	Dimensions and Configuration of the Three Shield Designs	243
D-3.	Intersection of the Umbra Region of a Point Source with the Plane z_p = 100 cm as a Function of Source Position for Shield Design 1	245
D-4.	Intersection of the Umbra Region of a Point Source with the Plane z_p = 100 cm as a Function of Source Position for Shield Design 2	246
D-5.	Intersection of the Umbra Region of a Point Source with the Plane z_p = 100 cm as a Function of Source Position for Shield Design 2	246
D-6.	Intersection of the Umbra Region of a Point Source with the Plane z_p = 100 cm as a Function of Source Position for Shield Design 3	248
D-7.	Normalized Thrust Ion Efflux, $\varepsilon_{+,t}$, as a function of y_p in the Plane z_p = 100 cm	250
D-8.	Normalized Thrust Ion Efflux Contours as $f(y_p)$ for z_p = 100, 200, and 400 cm for Shield Absent and Shield Present Conditions	252

TABLES

		Page
1.	Possible Auxiliary Propulsion Application for Ion Engines	7
2.	Upcoming Synchronous Orbit Payloads (from Summarized NASA Payload Descriptions - 1975)	9
3.	Upcoming Payloads Requiring Orbit Sustenance and Maneuvering (from Summarized NASA Payload Descriptions, 1975)	10
4.	Possible Payloads for Ion Engines	10
5.	Mission 1: Advanced Communications Satellite	12
6.	Mission 2: High Performance Propulsion Module for Multimission Modular Spacecraft (MMS)	16
7.	Propulsion Functions for Advanced Communications Satellite	17
8.	Ion Propulsion Subsystem Weight (Advanced Communications Satellite)	26
9.	Ion Propulsion Subsystem Electrical Interface	27
10.	Ion Propulsion Subsystem Power Requirements	27
11.	Advanced Communications Satellite Ion Thruster Requirements	30
12.	Attitude and Velocity Control Requirements for Advanced Communications Satellite	32
13.	AVCS and Propulsion Subsystem Configurations for Advanced Communications Satellite	33
14.	Biased Momentum Versus Zero Momentum Attitude Control Comparisons	36
15.	Comparison of Various Biased Momentum Attitude Control Configurations	39
16.	Antenna Pointing Error Sources (degrees)	41
17.	Characteristics of Boost Regulator	60
18.	Comparison of Proposed Options for Electrical Interface Between Ion Propulsion Subsystem and Spacecraft	62

TABLES (Continued)

		Page
19.	Mission 1 Solar Array Power Capability (watts)	63
20.	Mission 1 Battery Depth of Discharge as a Function of Mission Year	65
21.	Additional Payload Mass Available with Ion Propulsion on Advanced Communications Satellite (1000 kg)	68
22.	Summary of Ion Propulsion Subsystem Reliability Assessments for Advanced Communications Satellite	69
23.	Reliability Tradeoff Comparison (10,000 Bit Thruster Failure Rate, 7-year Mission)	74
24.	Propulsion Subsystem Weight with Redundant Thrusters and Cross-Strapped Controllers	75
25.	Daily Hours of Thruster Operation for Advanced Communications Satellite with Ion Propulsion	79
26.	Controller Parts List and Failure Rate Calculation	83
27.	Ion Propulsion Subsystem Weight, Geosynchronous MMS Mission	89
28.	Ion Propulsion Subsystem Weight, Low Earth Orbit MMS Mission	89
29.	Ion Thruster Performance Requirements for MMS Missions	94
30.	ACS Module Pointing Requirements for MMS	96
31.	Mission 2 Attitude and Velocity Control Propulsion Requirements	97
32.	Description of ACS Module for MMS	98
33.	Star Tracker Shade Design Factors	105
34.	StormSat Solar Array Power Capability: Baseline Subsystem (Watts)	109
35.	StormSat Battery Depth-of-Discharge as a Function of Mission Year	109
36.	StormSat Solar Array Power Capability after 3 Years: PRU Subsystem (watts)	110

TABLES (Continued)

		Page
37.	LandSat Power Source Capability after 2 Years: Baseline Subsystem	112
38.	LandSat Power Source Capability after 2 Years: PRU Subsystem	112
39.	Power Source Area and Mass Increment Summary for MMS Missions	114
40.	Net Mass Impact of High Performance Propulsion Module on MMS	116
41.	Predicted Geosynchronous MMS Ion Propulsion Subsystem Reliability	117
42.	Electron Bombardment Discharge Radiation Power Density	185
43.	Plasma Discharge Neutralizer Radiation Power Density	186
44.	Electron Bombardment Discharge Spectral Measurements	192
45.	Neutralizer Discharge Spectral Measurements	192
46.	Mercury Calibration Lamp Spectral Measurements	193
47.	Normalized Spectral Comparison	193
48.	8-cm Thruster Magnetic Moment Data	202
49.	Users Manual Outline	216
D-1.	Values of Minimum and Maximum Divergence Angle, θ_{min} and θ_{max} From Source Points on Ion Thruster Surface to Surface Elements at Upper Edge of Sputter Shield for Designs 1, 2, 3	256
D-2.	Total Sputter Shield Area Exposed to Thrust Ion Sputtering in Height Element, dz, at Height, z, for Designs 1, 2, and 3	257

I. SUMMARY

The purpose of the ion engine auxiliary propulsion study was to realistically assess the benefits to be derived from application of the NASA-LeRC 8-cm mercury electron-bombardment ion thruster. Ion engines offer significant advantages when used for certain spacecraft auxiliary propulsion applications because of two inherent characteristics. The first is high specific impulse, over 2500 seconds, which is an order of magnitude higher than current standards. The second is low thrust level, in the millipound range. This is a great advantage in minimizing spacecraft attitude disturbance torques, but may be a handicap if maneuvers have to be performed rapidly.

Two specific spacecraft missions were studied. In addition, a thruster was tested to provide additional information on its efflux characteristics and interactive effects. A Users Manual was then prepared describing how to integrate the thruster for auxiliary propulsion on geosynchronous satellites.

Ion engines afford a large payload increase when compared with hydrazine propulsion for missions requiring large added velocity (Δv). This usually means that some form of orbit correction is needed. Propulsive functions to achieve large Δv include north-south stationkeeping, low earth orbit drag makeup, and orbit maneuvers. Once ion thrusters have been selected for these functions, they may then be available for other applications, such as east-west stationkeeping, attitude control, momentum dumping, and station changing. In this manner, ion propulsion can complement, or even completely replace hydrazine propulsion subsystems, for certain missions.

The low disturbance torques introduced by ion engines permit accurate spacecraft pointing with the payload in operation during thrusting periods. Constraints on spacecraft design to minimize solar disturbance torques are alleviated by the engine's high specific impulse. The weight penalty to overcome torques from offset reflectors or positioning solar arrays all on one side of the spacecraft is greatly reduced.

With these advantages in mind, the first mission selected for detailed study was an advanced communications satellite that has the same housekeeping

requirements as Intelsat V but is slightly larger. By incorporating ion engines, the weight available for added payload increases by about 82 kg (181 lb) for this 1000 kg (2200 lb) satellite which otherwise uses electro-thermal hydrazine.

The second mission was a high performance propulsion module that is compatible with the standard NASA Multimission Modular Spacecraft (MMS) and can be used for both geosynchronous and low earth orbit applications. The above mentioned advantages for ion propulsion are incorporated into the module design.

The study shows that the 8-cm ion thruster can be integrated on all types of geosynchronous spacecraft: spin stabilized; three-axis stabilized, symmetrical spacecraft (deploying symmetrical solar arrays about the spacecraft central body) with body mounted or solar array mounted thrusters; and three-axis stabilized, asymmetric spacecraft. The most difficult case, the three-axis stabilized symmetrical spacecraft with body mounted thrusters, is typified by the advanced communictions satellite studied. Thruster integration requires lateral separation of the thrusters from the solar array axis, canting with respect to this axis, and the addition of a sputter shield on the thruster. The shield is not required for the high performance propulsion module on MMS.

Thruster efflux measurements were taken with and without the shield installed. Charged particle and neutral particle determinations were made. Thruster optical radiation measurements showed very low power densities, thereby demonstrating compatibility with current sun sensor attitude control systems. Sensitive star tracker systems are also probably compatible with the thruster. Thruster magnetic field measurements showed that the thruster can be characterized as a magnetic dipole, and is compatible with all but very sensitive scientific spacecraft.

A final program task investigated the neutralization of differentially charged spacecraft surfaces by using the thruster's neutralizer assembly as a source of low energy ions. The feasibility of this concept was verified in the laboratory experiment performed.

2. INTRODUCTION

The Lewis Research Center has a strong program in both in-house research and development and contractual activities to produce an 8-cm mercurcy ion thruster specifically designed for auxiliary propulsion (ref. 1). This thruster is a second generation device taking advantage of the design improvements incorporated as a result of extensive 5-cm thruster testing (ref. 2). The laboratory model 8-cm thruster has completed over 15,000 hours of endurance testing (ref. 3), thereby demonstrating that previously identified wearout mechanisms are now under control.

As the thruster was proceeding into engineering model development, together with its associated gimbal assembly, propellant reservoir, and power processor (ref. 4), it was appropriate to identify near-term applications for this equipment and to examine its integration on typical spacecraft in more detail. Thus, the ion engine auxiliary propulsion applications and integration study was organized into four major tasks:

Task I	Mission Applications
Task II	Thruster Interfaces
Task III	Users Application Manual
Task IV	Reporting

The objective of Task I was to study application of the NASA-LeRC mercury ion thruster subsystem to two specific geosynchronous spacecraft. The study assessed thruster subsystem applicability, advantages, and interface requirements imposed on the subsystem for each spacecraft mission. The study developed spacecraft layout drawings, subsystem descriptions and design analyses, and comparisons with other subsystems for performing the same auxiliary propulsion functions.

The Task II objective was to review the Government-furnished Interface Specifications Document for the thruster subsystem, and to document additional interface data necessary for Tasks I and III. The effort involved testing of an 8-cm electron bombardment mercury ion thruster to verify performance, measure efflux characteristics with and without a sputter shield, and measure electric and magnetic fields and optical radiation. Tests were

also conducted to evaluate the ability of the thruster to neutralize differentially charged surfaces.

Task III utilized the data contained in the Government-furnished Interface Specifications Document, and the results from the Task I applications study and Task II interfaces investigation, to comprise the essentials of a Users Application Manual to be published at the completion of the technical effort. The manual expands on the two specific spacecraft studied in Task I to treat the more general case of mercury ion thruster integration for auxiliary propulsion on geosynchronous spacecraft.

Task IV reports included monthly technical progress narratives, financial management reports, this final technical report, and the Users Application Manual.

Prior work on ion propulsion for geosynchronous applications (ref. 5) examined north-south stationkeeping of communications satellites. The present study narrowed the investigation to the 8-cm thruster subsystem, but expanded it to include other propulsive functions as well. The 8-cm thruster subsystem is currently scheduled to be space flight tested on a joint NASA/Air Force experiment.

Thruster testing during the program was conducted in a 5 x 10 foot (1.5 x 3 meter) vacuum test facility that had previously been employed for 30-cm thruster testing (ref 6). Much of the instrumentation from the prior effort was retained and used again with the 8-cm thruster.

3. MISSION APPLICATIONS

In order to identify near-term missions that could benefit from ion auxiliary propulsion, and to select two representative missions for further study, all of the available unclassified NASA, commercial, foreign, and DOD data sources have been examined. The two specific missions selected for detailed study are:

- Mission 1 – Advanced Communications Satellite. A geosynchronous mission that has the same housekeeping requirements as Intelsat V, but is slightly larger and has a much larger payload.
- Mission 2 – High Performance Propulsion Module. A module that is compatible with the standard NASA Multimission Modular Spacecraft and can be used for both geosynchronous and low earth orbit applications.

Detailed examination of these missions shows that the 8-cm ion engine affords large improvements for selected auxiliary propulsion functions.

The key spacecraft integration issues for ion propulsion are (1) the source of electric power, (2) the electrical interface between the propulsion subsystem and the spacecraft power bus, and (3) the impact on the spacecraft attitude and velocity control subsystem. Each of these issues is examined in some detail. Other important considerations that are discussed include efflux compatibility, thermal control, structural requirements and reliability.

3.1 SELECTION OF CANDIDATE MISSIONS

In order to demonstrate the advantages and disadvantages of ion auxiliary propulsion, it was necessary to select two satellite missions for detailed study. These candidate missions were to not only be ones where there is a payoff with ion propulsion, but ones which were likely new starts. This section describes the method by which the two candidate missions have been selected.

3.1.1 Potential Uses for Ion Engine Auxiliary Propulsion

The two fundamentally unique characteristics of ion propulsion are (1) very high specific impulse, and (2) very low thrust levels. There are two general cases for which these characteristics are ideally suited. These are: (1) missions where there are requirements for a very large total

impulse to provide a significant amount of added velocity (Δv) or torque; and (2) missions where there is a requirement for minimum disturbance torques during propulsion maneuvers. Some auxiliary propulsion applications which fit these cases are shown in Table 1.

3.1.2 Comparison with Mission Models

The search for candidate payloads that can use ion engines is shown graphically in Figure 1. The latest editions of the NASA, foreign and commerical automated payload mission models were obtained from references 7 and 8 and various military documents.

In an initial search of at least 82 candidate payloads, 35 were identified that fit one or both of the cases discussed in the last section. These candidates could be divided into two groups: 15 geosynchronous orbit missions and 20 other missions with large propellent requirements.

The geosynchronous payload candidates, shown in Table 2, were further screened for technical and practical considerations. These considerations included the need for north-south stationkeeping, no need for rapid station changes (this eliminated most of the military missions), and the likelihood of being a new start. Six candidate payloads passed this screening, five body-stabilized and one spin-stabilized spacecraft.

The other missions were screened for such technical considerations as tolerating very low thrust levels and the likelihood of being a new start. Nine candidates passed this screening and are shown in Table 3.

The most likely mission candidates for ion propulsion from this screening process are:

- International Telecommunications Satellite (Intelsat)
- Tracking and Data Relay Satellites (TDRS)
- Advanced Domestic Satellite (U.S. Domsats)
- Storm Satellite (Stormsat)
- Landsat

The program status and fundamental requirements for these missions are summarized in Table 4.

Table 1. Possible Auxiliary Propulsion Applications for Ion Engines

A. Provide Added Velocity (Δv) for:			
Requirement	Possible Mass Savings	Other Advantages	Potential Problems
North-south stationkeeping	Very large (100 kg or more)	Low disturbances permit tight pointing during operation	Contamination must be minimized
Orbit sustenance (low earth orbit)	Large	Permits tight pointing during operation	Array for additional electric power increases drag
Initial station positioning	Large, if apogee motor errors are significant	Can completely replace hydrazine	Requires many hours
Change of station	Moderate	Can completely replace hydrazine	Time to perform station change may be excessive
East-west stationkeeping	Slight	Permits tight pointing. Can completely replace hydrazine	
B. Provide Attitude Control Torques for:			
Attitude control during Δv maneuvers	Moderate	Can completely replace hydrazine	Two thrusters must operate together
Acquisition	Moderate	Can completely replace hydrazine	Acquisition maneuver may require change
Momentum dump	Moderate	Eliminates need of separate momentum dump mechanism (i.e., magnetic). Small gimballed engines permit tight pointing during payload operation	May require changes in attitude control subsystem design

ORIGINAL PAGE IS OF POOR QUALITY

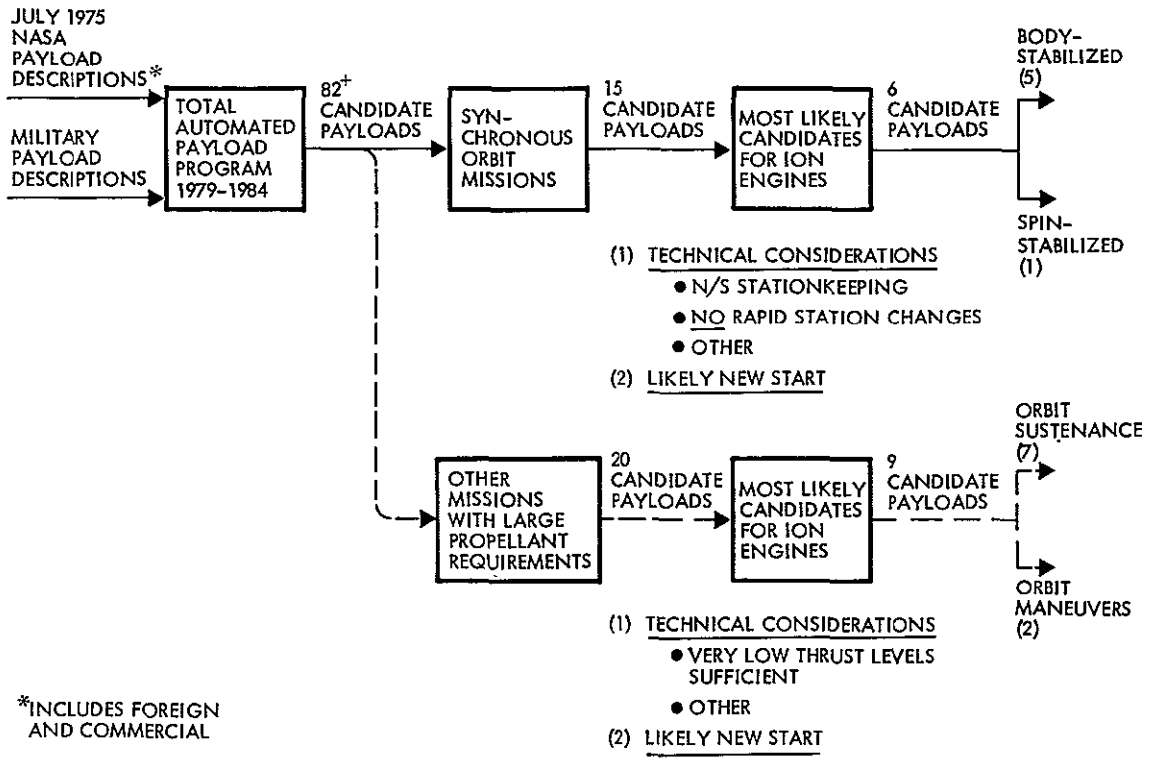

Figure 1. Search for Candidate Payloads that can Benefit from Ion Engines

3.1.3 Selection of Two Candidate Missions

Two candidate missions have been selected to represent the payloads shown in Table 4. Mission 1 is a geosynchronous communications satellite, called the Advanced Communications Satellite for this study. Mission 1 is representative of the class of satellite planned to provide active repeaters which relay data between fixed earth-based stations. The mission is typified by the need to provide a fixed satellite location with respect to the earth to eliminate the need for gimballed earth-based transponders (hence the need for geosynchronous orbit with both north-south and east-west stationkeeping). The satellite pointing requirements are moderate and are sized by the beamwidths of the antenna subsystem. Cost considerations dictate long orbital lives (7-10 years). There are military (DSCS-III), international commercial (Intelsat V and Aerosat) and purely national* (Advanced AT&T, Western

*Called U.S. DOMSAT in Table 2.

ORIGINAL PAGE IS
OF POOR QUALITY

Table 2. Upcoming Synchronous Orbit Payloads (from Summarized NASA Payload Descriptions - 1975)

PAYLOAD NUMBER	NAME	DEVELOPMENT AGENCY	APPROX. INITIAL LAUNCH DATE	APPROX. LAUNCH MASS (KG)	STABILIZATION MODE	SPECIAL REQUIREMENTS
AS-05-A	Advanced Radio Astronomy Explorer	NASA	1983	596	3-axis	• Long (225m) booms
EO-09-A	Synchronous Earth Observatory Satellite (SEOS)	NASA	1983	3300	3-axis	• Large (1.5m) telescope
*EO-15-A	Storm Satellite	NASA	1982	910	3-axis	• Uses multimission spacecraft
EO-57-A	Foreign Synchronous Meteorological Satellite (FSMS)	Foreign	1982	286	Spin (100 rpm)	• Return & refurbish • similar to GOES
EO-58-A	Geosynchronous Operational Environmental Satellite (GOES)	NOAA	1982	286	Spin (100 rpm)	• Operational version of SMS
*CN-51-A	International Telecommunications Satellite	COMSAT Corp.	1983	1472	3-axis	• Study had ion thrusters
*CN-52-A	U.S. DOMSAT-A	NASA/FCC	1979	559	Spin (10 rpm)	• Despun antenna • Modified ANIK
*CN-53-A	U.S. DOMSAT-B	FCC	1982	1472	3-axis	• Study had ion thrusters
*CN-54-A	Disaster Warning Satellite	NASA/NOAA	1982	583	3-axis	• Study had ion thrusters
CN-55-A	Traffic Management Satellite	MARAD/FAA	1982	298	3-axis	
CN-56-A	Foreign Communications Satellite-A	Foreign	1982	308	3-axis	
*CN-58-A	U.S. Tracking and Data Relay Satellite-C	NASA	1983	2100	3-axis	• Shared mission will require north-south stationkeeping
CN-59-A	Communication R&D/ Prototype Satellite	?(U.S.)	1983	1438	3-axis	
Military	Defense Satellite Communications System (DSCS-III)	USAF	1982	1600	3-axis	
Military	Others	USAF	1982	1200 to 3200	3-axis	

* Candidate payloads for ion engine auxiliary propulsion

Union or RCA satellites) applications. Although each application tends to have its unique requirements which dictate design variations, the requirements are sufficiently similar to provide a representative example. The sample selected for this study is a generalized, advanced Intelsat V.

Two of the missions shown in Table 4 will use the Multimission Modular Spacecraft (MMS), NASA's standardized modular spacecraft that will be adapted to various types of missions ranging from near-earth orbit to geosynchronous. The standard propulsion module for this spacecraft uses

ORIGINAL PAGE IS
OF POOR QUALITY

Table 3. Upcoming Payloads Requiring Orbit Sustenance and Maneuvering (from Summarized NASA Payload Descriptions, 1975)

PAYLOAD NUMBER	PAYLOAD NAME	ORBITAL ALTITUDE (km)	APPROX. LAUNCH MASS (kg)	ADDED VELOCITY REQUIREMENT (ms)	APPROX. INITIAL LAUNCH DATE	COMMENTS
HE-01-A	LARGE X-RAY TELESCOPE FACILITY	463x463	11869	93	1982+	
HE-03-A	EXTENDED X-RAY SURVEY	370x370	8011	93	1982+	
HE-07-A	SMALL HIGH ENERGY SATELLITE	371x371	595	101	1982+	
HE-08-A	LARGE HIGH ENERGY OBSERVATORY A (GAMMA RAY)	371x371	8700	93	1982	MAY BE HEAO-C REFLIGHT
HE-09-A	LARGE HIGH ENERGY OBSERVATORY B (MAGNETIC SPECTROMETER)	371x371	6591	93	1982+	
HE-11-A	LARGE HIGH ENERGY OBSERVATORY D (1.2m X-RAY TELESCOPE	463x463	6771	93	1982+	
EO-08-A	LANDSAT-D (EOS-D)	700x700	1787	150 kg*	1979	ORBIT ADJUST, ORBIT TRANSFER AND ACS MANEUVERS
EO-12-A	TIROS 0	833x833	1636	178 kg*	1983	ORBIT ADJUST, ORBIT TRANSFER AND ACS MANEUVERS
OP-04-A	GRAVITY FIELD SATELLITE	300x300	1000	300 kg*	1981	"SURFACE FORCE COMPENSATION"

* EXPENDABLE MASS

Table 4. Possible Payloads for Ion Engines

PAYLOAD NAME	CURRENT DEVELOPMENT STATUS	NORTH-SOUTH STATIONKEEPING	EAST-WEST STATIONKEEPING	CHANGE OF STATION	INITIAL STATION POSITIONING	ACQUISITION	ATTITUDE CONTROL DURING Δv	POINTING REQUIREMENT	MOMENTUM DUMP	ORBIT SUSTENANCE
INTELSAT V	UNDER DEVELOPMENT BY AERONUTRONIC FORD	YES	YES	YES	YES	YES	YES	0.2°	YES	NO
TRACKING & DATA RELAY SATELLITE (TDRS)	UNDER DEVELOPMENT BY TRW	YES	YES	YES	YES - BEFORE SHUTTLE	YES	YES	0.15°	YES	NO
ADVANCED DOMESTIC SATELLITE	PRELIMINARY DESIGN	YES	YES	YES	NO - IF SHUTTLE-LAUNCHED	YES	YES	0.05°	YES	NO
SYNCHRONOUS MULTIMISSION MODULAR SPACECRAFT (e.g., STORMSAT)	PRELIMINARY DESIGN	YES	YES	MAYBE	NO	YES	YES	$<0.01^{\circ}$	YES	NO
SUBSYNCHRONOUS MULTIMISSION MODULAR SPACECRAFT (e.g., LANDSAT)	HARDWARE RFP IMMINENT	NO	NO	NO	NO	YES	YES	$<0.01^{\circ}$	YES - POSSIBLY FOR TWO-AXES ONLY	YES

hydrazine, using as much as 1000 lb (454 kg) of propellant in some applications.

Mission 2 for this study is a high performance propulsion module for the MMS. Two payloads are examined that represent two quite different uses for this module. A geosynchronous mission (e.g., Stormsat) with north-south stationkeeping is quite similar to Mission 1 but uses the MMS hardware. A low earth orbit mission (e.g., standard Landsat) uses the ion engines for orbit maneuvers and drag make-up.

3.1.3.1 Mission 1 Summary

The Mission 1 satellite is based on an advanced version of the Intelsat V communications satellite. The mission and ground rules used to design the ion engine auxiliary propulsion subsystem are shown in Table 5.

The spacecraft mass of 1000 kg represents the Atlas-Centaur launch vehicle capability within a few years or the Space Shuttle with a spinning solid upper stage. The rest of the parameters are directly from Intelsat V.

A sketch of the Intelsat V spacecraft with ion thrusters is shown in Figure 2 and details are shown in Figure 3. This represents the simplest form of the Advanced Communications Satellite mission. The spacecraft in geosynchronous orbit has its solar arrays deployed along the north-south axis. The central body rotates once an orbit to continuously point at the earth while the solar arrays maintain a sun-pointing attitude.

The ion engines are shown on the east-west faces of the central spacecraft body. They are pointed in the north and south directions and tilted outward to minimize potential contamination of the solar arrays.

3.1.3.2 Mission 2 Summary

Mission 2 is a high-performance propulsion module for the MMS which is the standardized spacecraft bus intended for a range of missions in the Space Shuttle era. It is described in detail in reference 9. New projects can be adapted to the capabilities of the MMS without going through a costly spacecraft design and development effort. NASA Goddard Space Flight Center (GSFC) is the technical manager for the MMS.

Table 5. Mission 1: Advanced Communications Satellite

Payoff with ion propulsion	20% more payload mass than Intelsat V
Orbit	Geosynchronous
Spacecraft mass (beginning of life)	1000 kg
Mission life	7 yr
Total north-south stationkeeping Δv requirement	350 m/s
North-south stationkeeping	±0.1 deg
Attitude control mode	Body-stabilized momentum wheels
Required pointing accuracy	Roll 0.2 deg Pitch 0.2 deg Yaw 0.4 deg
Spacecraft power load (end of life)	1160 watts
Bus voltage	27 to 42.5 volts
Spacecraft power sources	(1) Hybrid solar cells (2) Lightweight nickel-cadmium batteries

The MMS bus, shown in Figure 4, is composed of a module support structure with major modules for (1) communications and data handling (C&DH), (2) electric power, and (3) attitude control. In addition, there are adapter structures to attach to the payload and launch vehicle and a standard Tracking and Data Relay Satellite System (TDRSS) antenna. An optional propulsion module is used as required by the user mission. There are mission-unique subsystem elements which can be added to each module, such as a tape recorder or additional batteries. Antennas and solar arrays are considered to be mission-unique.

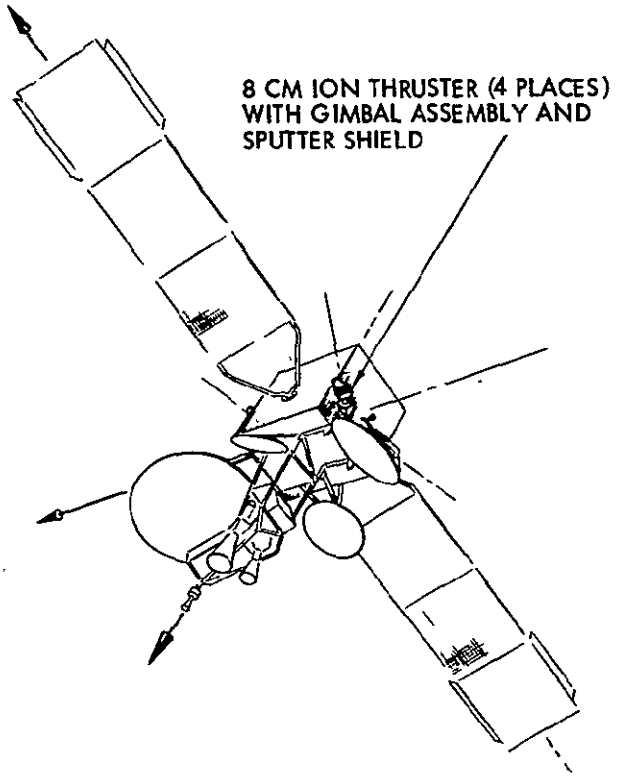

Figure 2. Advanced Communications Satellite with Ion Auxiliary Propulsion

There are two propulsion/actuation modules now included in the standard MMS equipment list. Both use monopropellant hydrazine. The basic small impulse spacecraft propulsion subsystem (SPS-I) is sized to provide orbit adjust and reaction control for a typical spacecraft mission. SPS-I is expanded to the large impulse SPS-II for missions that require orbit transfer or north-south stationkeeping. SPS-II uses the same rocket engine modules as SPS-I, but has a larger propellant tank and two additional thrusters for orbit transfer. A high-performance propulsion module, using ion engines, would be smaller and much lighter than the hydrazine system for most of the SPS-II applications.

Two potential MMS payloads have been used in the study to examine the use and advantages of ion propulsion. These are (1) a geosynchronous mission with tight pointing accuracy requirements, represented by StormSat (NASA

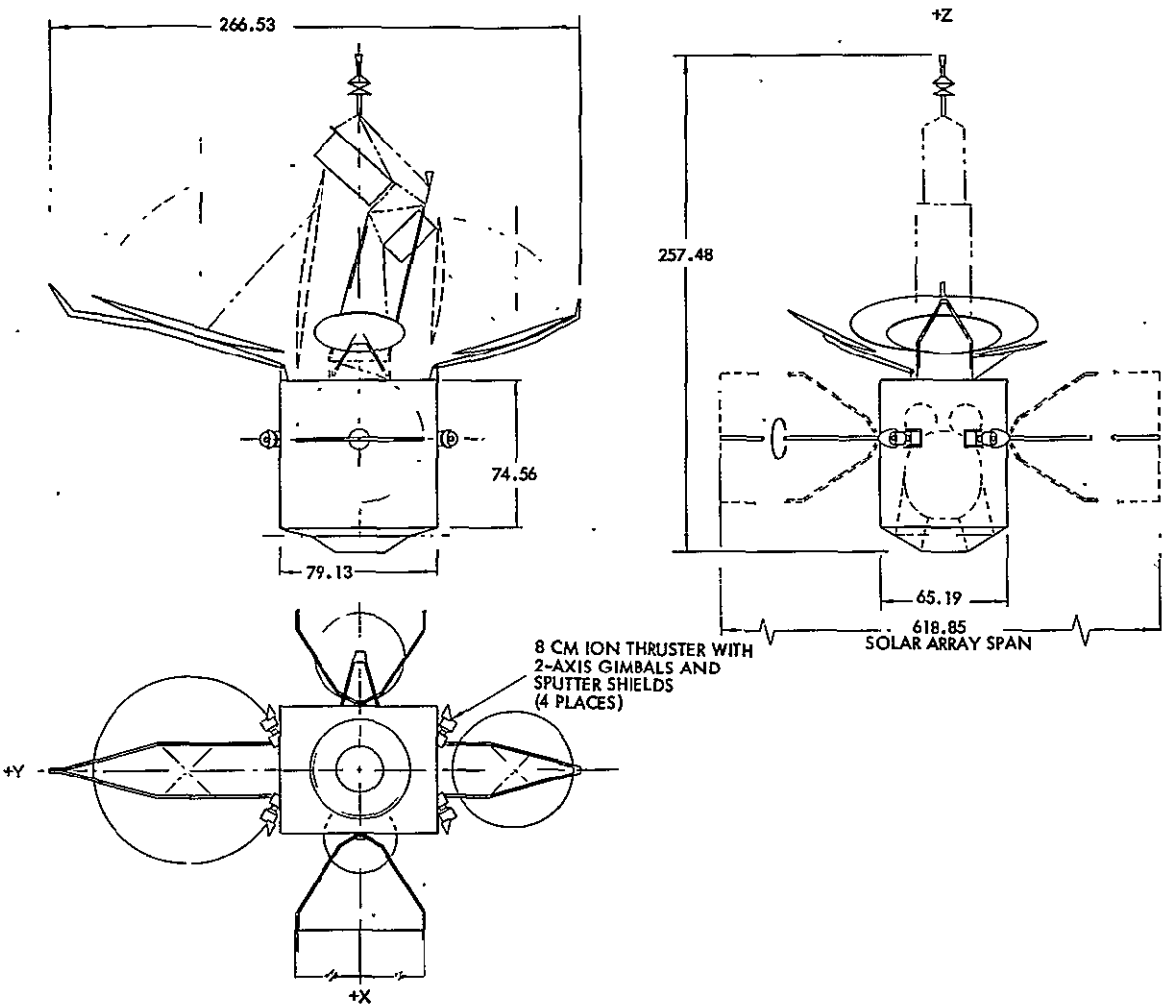

Figure 3. Location of Ion Thrusters on Advanced Communications Satellite

Payload EO-15-A), and (2) a low earth orbit mission with significant orbital maneuvers or drag makeup, represented by an advanced LandSat (NASA Payload EO-08-A). The mission descriptions and ground rules used to design the high-performance propulsion module are shown in Table 6.

3.2 MISSION 1: ADVANCED COMMUNICATIONS SATELLITE

This section describes the Mission 1 satellite and identifies potential uses of ion propulsion. The key spacecraft integration issues for this mission are the impact on the attitude and velocity control subsystem, and the electrical power sources. Special attention is given to these subjects.

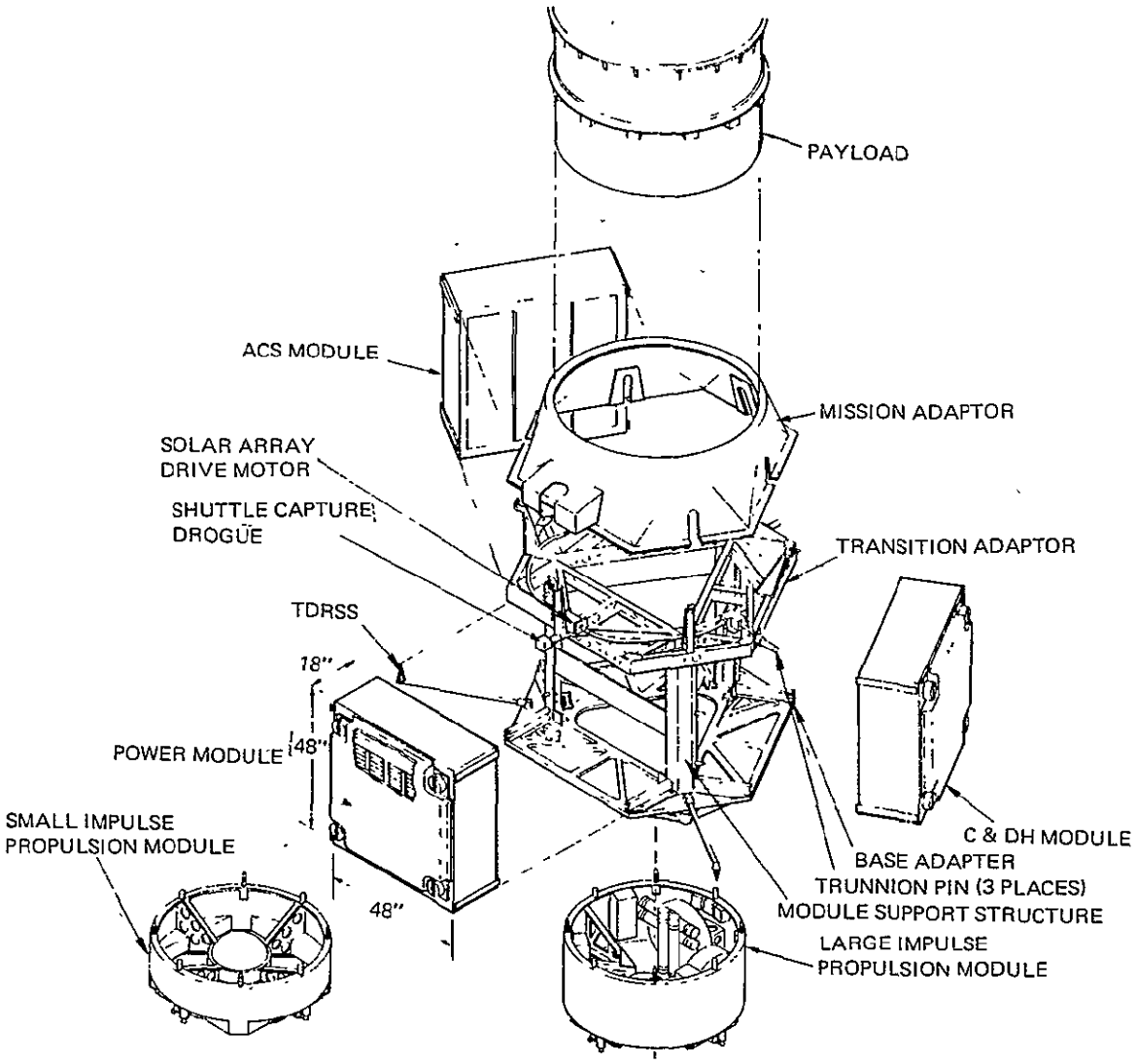

Figure 4. Multimission Modular Spacecraft Bus (Exploded View)

3.2.1 Ion Engine Auxiliary Propulsion Functions

The major payoff for the ion engine auxiliary propulsion subsystem on the Advanced Communications Satellite is in performing north-south station-keeping. However, the ion thrusters can also be used for many other orbital propulsion functions and even completely replace the standard hydrazine subsystem.

Table 6. Mission 2: High Performance Propulsion Module for Multimission Modular Spacecraft (MMS)

Description	MMS Geosynchronous Orbit Mission (e.g., StormSat)	MMS Low Earth Orbit Mission (e.g., LandSat)
Payoffs with ion propulsion	• More payload mass • Lower launch costs	• More payload mass • Lower launch costs • Increased lifetime
Orbit	Geosynchronous	705 to 914 km
Spacecraft mass (beginning of life)	1000 kg (assumed)	1700 kg
Mission life	3 yr	2 yr
Total north-south station-keeping ΔV requirement	150 m/sec	217 m/sec*
North-south stationkeeping	±0.1 deg	---
Spacecraft ACS mode	3 reaction wheels plus propulsion	3 reaction wheels plus propulsion
Control functions	• Acquisition • N-S and E-W stationkeeping • Momentum dump • Safehold backup mode	• Acquisition • Drag makeup and maneuvers • Momentum dump • Safehold backup mode
Spacecraft power load	400 to 600 watts	• 261.8 watts minimum for 93 minutes • 450 watts average • 2200 watts peak for 10 minutes
Pointing accuracy	• 10^{-2} deg accuracy • 10^{-6} deg/sec drift rate deviation • 6×10^{-4} deg attitude jitter • Safehold peak error of 10 deg	
Bus voltage	28 ± 7 volts	
Spacecraft power sources	• Hybrid solar cells • Lightweight nickel-cadmium batteries	

*for orbital maneuvers

The required spacecraft propulsion functions for this mission are:

- Transfer orbit attitude control
- Apogee boost
- Initial station acquisition
- N-S and E-W stationkeeping
- Attitude control and momentum dump
- Change of station

Three possible propulsion subsystem configurations were examined to perform all these functions. These are:

- Baseline – a liquid apogee boost motor, with its own cold-gas attitude control subsystem, plus an ion engine auxiliary propulsion subsystem.

- Alternate 1 – a solid apogee boost motor, a hydrazine auxiliary propulsion subsystem, and an ion engine auxiliary subsystem. (The first two items are on the current Intelsat V.)

- Alternate 2 – the Space Shuttle Interim Upper Stage plus an ion engine auxiliary propulsion subsystem.

The baseline represents the minimum spacecraft weight design. Alternate 1 has the least impact on Intelsat V and alternate 2 represents a future design when Space Shuttle launches are commonplace.

Table 7 shows how the six propulsion functions would be performed for each configuration. As can be seen, ion engines can provide a significant contribution for any of the options.

Each of the spacecraft propulsion functions are discussed in detail below, featuring the use of ion propulsion in the baseline configuration.

3.2.1.1 Transfer Orbit Attitude Control and Apogee Boost

NASA and commercial geosynchronous communications satellites are placed into an inclined elliptical transfer orbit by the boost rocket (Atlas-Centaur or Thor-Delta). The satellite itself must provide the attitude control and propulsion required to change this orbit into the desired geosynchronous orbit. This is done with an apogee boost motor (ABM).

Communications satellites currently employ high thrust level solid rocket ABMs. Since this high thrust level induces very high disturbance torques, the satellite attitude is controlled by spinning the satellite up before

Table 7. Propulsion Functions for Advanced Communications Satellite

CONFIGURATION	(1) TRANSFER ORBIT ATT. CONT.	(2) APOGEE BOOST	(3) INITIAL STATION ACQUISIT.	(4) N-S & E-W STATION-KEEPING	(5) ATTITUDE CONTROL AND MOM. DUMP	(6) CHANGE OF STATION
BASELINE	LIQUID ABM	LIQUID ABM	LIQUID ABM	ION ENGINE	ION ENGINE	ION ENGINE
ALTERNATE 1	HYDRAZINE	SOLID ABM	HYDRAZINE	ION ENGINE	ION ENGINE	ION ENGINE OR HYDRAZINE
ALTERNATE 2 (FUTURE)	INTERIM UPPER STAGE	INTERIM UPPER STAGE	ION ENGINE	ION ENGINE	ION ENGINE	ION ENGINE

firing and relying on gyroscopic stiffness to maintain control. Slit-type spinning sun and earth sensors are used to update estimates of the spin vector and hydrazine thrusters are used to spin the satellite up, precess the spin vector as required, provide a source of active nutation damping should the satellite mass properties provide an unstable inertia ratio, and despin the satellite. Ion propulsion cannot be used for these functions due to its low thrust levels and inability to operate in a high-frequency pulse mode of operation.

Some upcoming missions will use low thrust level (~100 to 200 lbf – 500 to 1000 N) liquid bipropellent engines for transfer orbit. The combined advantages of a higher specific impulse, large expansion ratio nozzles, and restartability of the engine offer significant weight-saving potential over a solid rocket ABM. The liquid engine nozzle can be gimballed for active control or a very slow spin rate used. In either case, cold gas or ion propulsion are attractive alternatives to hydrazine for the auxiliary propulsion functions. These functions include control of the thrust vector axis for active control of engine axis swirl torques and to provide satellite spin-up and despin. The baseline propulsion subsystem configuration consists of a gimballed nozzle and cold gas for auxiliary propulsion. The attitude sensors would be gyros (for inertial reference) updated by sun and earth sensor data.

The important conclusion here is that ion propulsion has little application in transfer orbit unless a liquid ABM is used. If ion propulsion is used for all other functions, a simple and inexpensive cold gas system can replace hydrazine for attitude control with the primary propulsion system.

3.2.1.2 Acquisition and Initial Station Positioning

After the satellite has been placed into geosynchronous orbit, it is despun and three-axis attitude control must be provided. Also, if some failure has occurred, the satellite may lose its earth reference and reacquisition is required. This is generally performed by using sun sensors as a reference to point and some combination of gyros, earth sensors, or reaction wheels to provide the third axis reference. Hydrazine is atractive for this maneuver due to the relatively high torques available – enabling acquisition within 15 minutes. Acquisition can be performed with ion engines, but the acquisition time may increase to as much as 3 days. Though this is an

undesirable period of time, it is acceptable and this function does not require a hydrazine subsystem.

After the apogee boost motor has inserted the satellite into a nominal geosynchronous orbit, the satellite has residual drift due to dispersions of the thrust vector and an intentional bias which allows the satellite to drift to its final orbital station. The satellite auxiliary propulsion subsystem must provide the final corrections if the apogee boost motor is a solid. If the ABM is a restartable liquid bipropellant, all final velocity corrections can be made with the apogee motor itself. The correction will include an east-west velocity component and a north-south component. For example, the Intelsat V with a solid ABM requires an orbital correction capability of 33.5 m/s east-west correction, 42.7 m/s north-south correction, or a vector total of 54.9 m/s.

The baseline ABM for this study is the liquid bipropellant. Should a solid ABM be required, the auxiliary propulsion subsystem must make up for these dispersions. This could take as long as 80 days of continuous thrusting with the ion engines and may not be acceptable. Hydrazine or some other auxiliary propulsion subsystem would then have to be provided for orbital correction.

3.2.1.3 North-South Stationkeeping

The primary role of the Advanced Communication Satellite ion thrusters is to provide stationkeeping forces. Stationkeeping is required to correct for the significant out-of-orbit-plane gravitational forces exerted on a geosynchronous satellite by the earth, sun, and moon. These forces cause the satellite orbit to precess and, if not corrected, the satellite antenna patterns will trace out ever-lengthening figure-eights on the earth. Ground-based tracking antennas would have to be programmed to compensate for this daily motion. In order to use simple, fixed-based ground antennas, a stationkeeping requirement is often imposed on the spacecraft.

North-south stationkeeping is an expensive operation, in terms of propulsion impulse, because it requires rotating the satellite orbit plane. The perturbations are of a complex oscillatory nature with component periodicities of 12, 12.5, 24, 25 hours, 1 month, 1, 2, 18, 53 years, etc. However, all the periodic terms of less than a year cause peak orbital precessions of less than the required 0.1 degree stationkeeping accuracy and need not be

ORIGINAL PAGE IS
OF POOR QUALITY

corrected. The longer term perturbations do need correcting. These long term effects cause orbital inclination changes which can be approximated by

$$di/dt = 0.8475 + 0.0985 \cos (0.0533t - 2.149) \qquad (1)$$

where di/dt is the rate of change of inclination in deg/year, t is the modified Julian date in years (counted from May 24, 1968), and the cosine argument is in degrees. This translates to yearly rates ranging from 0.75 to 0.95 deg/year or changes in orbital velocity (out of the orbit plane) of from 40 to 51 m/s/year.

Ideally, stationkeeping maneuvers are accomplished by applying an impulse each time the satellite crosses the line of nodes between its actual orbit and the desired goesynchronous orbit. The direction of orbital precession is nearly inertially fixed and the desirable place in orbit to fire pulses is a function of the time of the year. Figure 5 illustrates the phenomenon. The desired orbital time of day to perform stationkeeping is 6 a.m. or 6 p.m. at

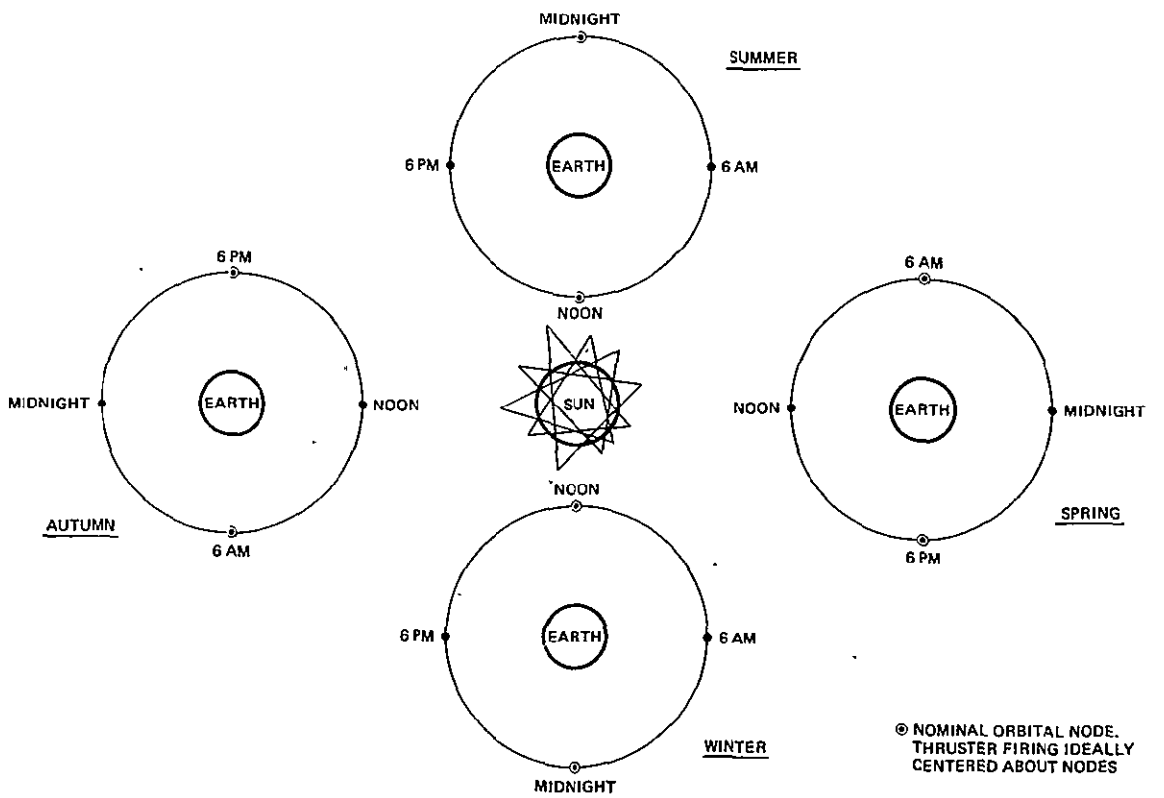

Figure 5. Geometry of Orbit Corrections

the spring and autumn equinoxes, noon or midnight in the winter or summer solstices, and at the same relative points in the orbit for other days during the year.

The thrust levels obtainable with ion thrusters are not large enough to provide an impulsive force. Therefore, they must fire for a finite period of time before and after the nodal crossing. The firing time depends upon the thrust level and a minimum thrust level is established when the firing time reaches 12 hours. At that point, the thrust force must change direction. If this is not possible (for instance, if the operating thrusters point in only one direction), thrusting can only be done once a day. Ideally, thruster forces will be applied in one direction at one node and in the opposite direction at the other node.

Inefficiencies due to off-nodal thrusting and thruster canting to avoid solar array impingement increase the total required thruster operational life requirements. For constant thrusting through an orbital arc centered around the nodal point, the orbital efficiency factor is $\sin \alpha/\alpha$, where α is the arc half-angle in radians. When the thrust vector is canted at an angle ϕ with respect to the north-south spacecraft axis, an additional cant angle efficiency factor, $\cos \phi$, is introduced.

Combining these factors, the required number of engine thrusting hours per node, t, is given by:

$$t = \frac{24}{\pi} \sin^{-1} \left[\frac{\pi}{24\,(3600)} \cdot \frac{1}{N_N N_D N_Y} \cdot \frac{M\Delta v}{F \cos \phi} \right] \tag{2}$$

and the total operating life per thruster is given by:

$$L = N_D N_Y t \text{ hr} \tag{3}$$

where

M = spacecraft mass, 1000 kg

Δv = total mission velocity increment, 350 m/s

F = thrust, newton

N_N = number of nodal firings per day, 1 or 2

N_D = number of days firing per year, 365

N_Y = number of years in mission, 7

The orbital efficiency factor and thrusting time per node are shown in Figure 6 for both one-node and two-node firing. The design points for this study are indicated. The ion thrusters have a cant angle of 30 degrees and are fired in pairs at both nodes in the normal mode of operation. If a thruster cannot fire, the other pair pointing in the opposite direction is fired at one node per day.

In summary, it can be seen that the propulsion subsystem must be capable of north and/or south thrusting directions. In the interest of maximizing thrust efficiency, it is desirable to thrust as often as possible near the nodes. This can be done by increasing the number of thrusters that fire at one time; firing in both north and south directions; and firing every day of the year. There may be some concern that firing at the node cannot be done during the eclipse season because of possible discharge of the batteries. However, it

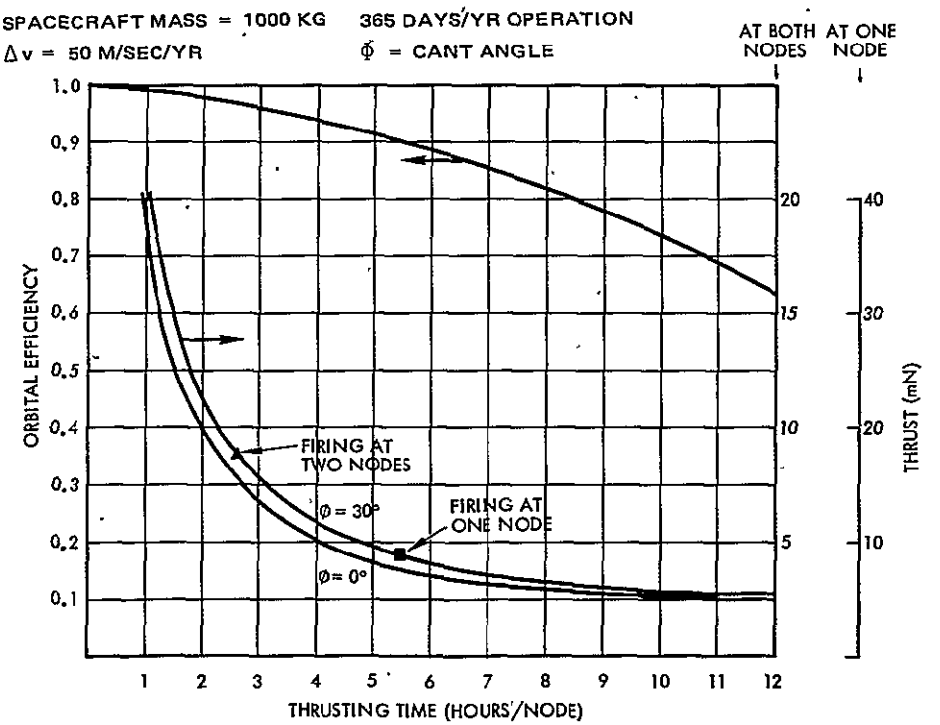

Figure 6. Orbital Efficiency and Thrusting Time for North-South Stationkeeping

can be seen from Figure 5 that during the eclipse seasons, the firing nodes occur at 6 a.m. or 6 p.m., permitting nearly 6 hours to recharge between ion engine firing and eclipse. Firing the engines for stationkeeping is never required during eclipse.

3.2.1.4 East-West Stationkeeping

The triaxiality of the earth's mass distribution exerts a small force east or west along the satellite velocity vector toward one of the gravitational equilibrium points. Figure 7 summarizes the annual drift as a function of spacecraft longitude. For example, for a mid-North American station at 240°E, the annual velocity drift is 0.70 m/s. Note that this correction varies with satellite location, is reasonably constant in value at its location, and is small (from 5% to 0% of the required north-south correction). Due to the low drift, corrections need not be made any more often than every 59 days to maintain the required 0.1 degree on-station accuracy. Since the total velocity increment is small, this correction need not be performed with ion propulsion. However, the baseline subsystem discussed below can perform this function simultaneously with north-south corrections and by use of ion propulsion, the overall propulsion subsystem is simplified in a fuel efficient manner.

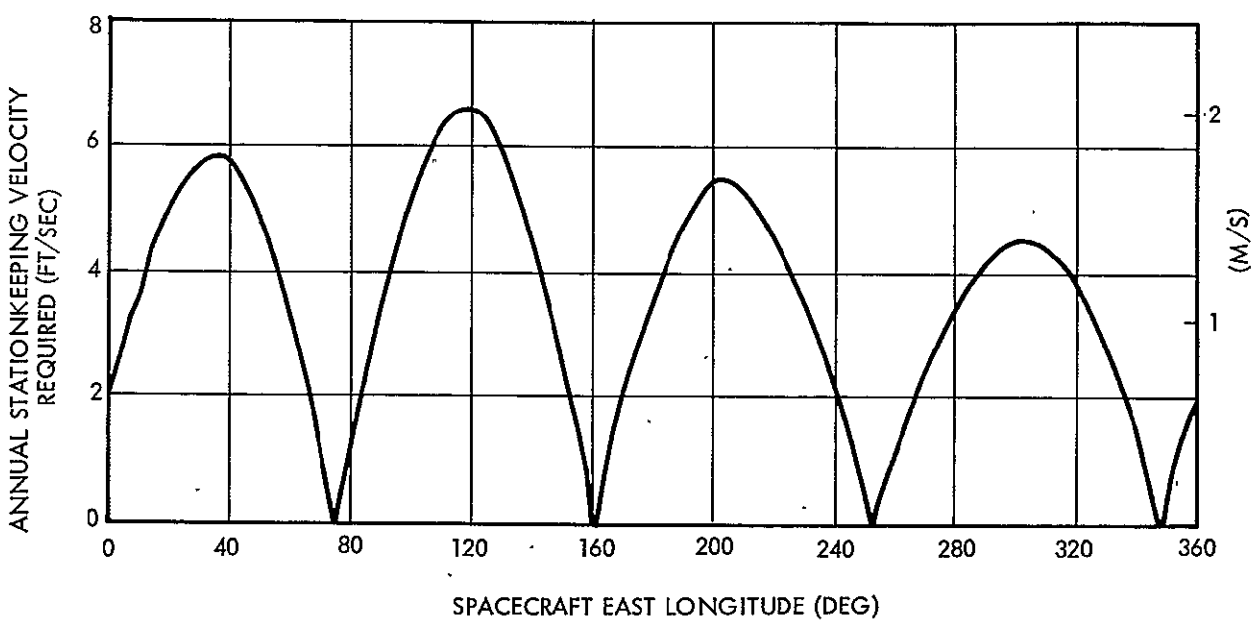

Figure 7. Annual East-West Stationkeeping Velocity Requirement

3.2.1.5 Attitude Control and Momentum Dump (Normal Mode)

The greatest percentage of the satellite time is spent on orbit, performing communications functions and not performing any special functions such as stationkeeping. This is called normal mode. The attitude and velocity control subsystem (AVCS) must only maintain pointing during this time.

Many alternatives which could also meet the attitude and velocity control requirements were considered in evolving the recommended AVCS configuration. These are discussed in Section 3.2.3. To summarize, the priorities in the selection process were:

- Develop a design that satisfies all pointing requirements
- Use well understood concepts with flight-proven components
- Maximize in-flight reliability by simplifying and minimizing equipment

Principal tradeoffs included:

- Biased momentum versus zero momentum bias control
- Number of axes of momentum storage

A biased momentum concept with a single body-fixed wheel (and typically a redundant wheel) was selected. The single body-fixed wheel is the simplest, generally lightest, and most reliable. Since thruster firings are generally in the secular torque direction, the technique is as efficient as others. However, impulse bit is limited by nutation of a single pulse, and the pulses must be separated so that roll attitude never becomes excessive (roll attitude error is an essential consequence of absorbing yaw torques without firing thrusters). This technique is mechanically the simplest and lightest that meets the basic mission requirements and was therefore selected for this study. It is the technique used on FLTSATCOM, Canadian Technology Satellite, the European OTS, and Intelsat V.

3.2.1.6 Change of Station

Communications satellites are typically designed to be placed into a specific station on orbit and not moved. If a failure occurs somewhere in the constellation of satellites, however, it may be desirable to move one or more satellites to a new station. The ion engines can accomplish this function, but

the low thrust levels involved mean that it takes a long time to move a significant distance. For example, an orbit station change of 120 degrees (1/3 of an orbit) would take about 80 days.

If the change of station maneuver must be done rapidly, such as on a military mission, hydrazine or solid rocket engines would be required. The baseline propulsion configuration selected for this study assumes that the ion propulsion change of station capability is adequate.

3.2.2 Ion Propulsion Subsystem

The basic Advanced Communications Satellite ion propulsion subsystem schematic is shown in Figure 8. There are two sets of two thrusters each. Each set of thrusters shares a propellant reservoir. North-south stationkeeping redundancy is obtained by operating one pair of thrusters at each nodal crossing, and, in the event that one thruster fails, by operating the remaining pair of thrusters at one node.

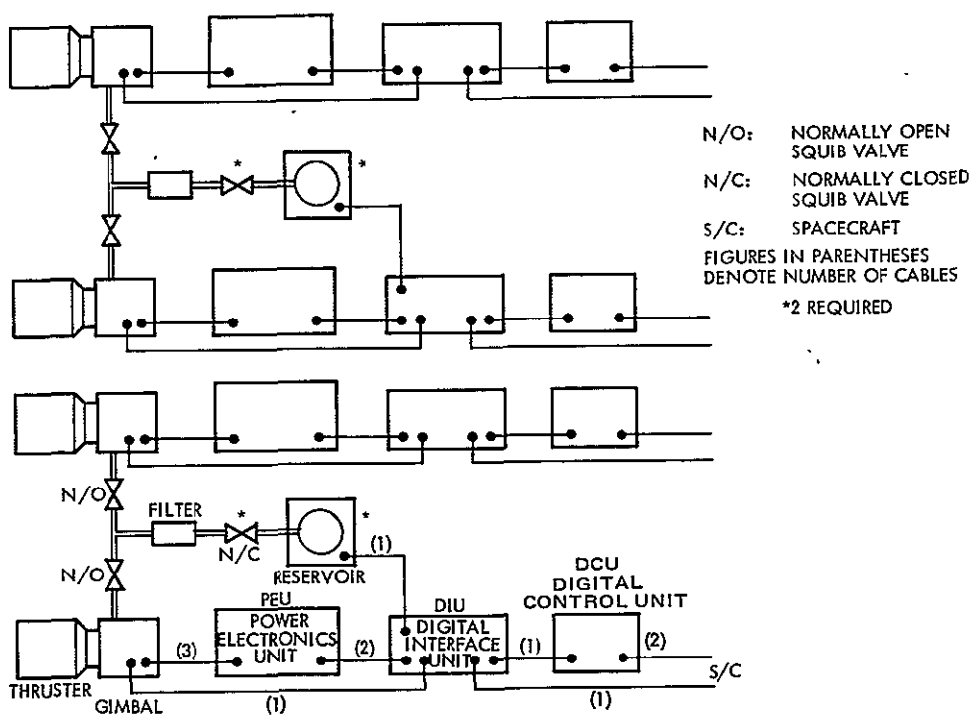

Figure 8. Ion Propulsion Subsystem Schematic

The dry weight summary for the Advanced Communications Satellite ion propulsion subsystem is given in Table 8. The electrical interface is summarized in Table 9 and the power requirements are detailed in Table 10.

The electrical interface with the satellite command and control subsystem is straightforward and does not require further comment. The interfaces with the attitude and velocity control and power subsystems are discussed in more detail in Sections 3.2.3 through 3.2.5.

The ion thrusters are located in pairs on the east and west faces of the central spacecraft body (see Figure 2). One of each pair points in the north direction and one in the south direction. They are tilted outward approximately 30 degrees, to reduce possible solar array contamination, and are gimballed. Mechanical interference with other spacecraft subsystems is minimized since the Intelsat V hydrazine thruster cluster is located at this point. Ion thrusters can fit next to the hydrazine thrusters and the subsystem electronics can be located inside the central body, as shown in Figure 9. Little spacecraft equipment rearrangement is required to accommodate the ion propulsion subsystem equipment. Smaller N_2H_4 tanks (16-inch diameter vs. the 20-inch diameter existing tanks—41 cm vs. 51 cm diameter tanks) are suggested since

Table 8. Ion Propulsion Subsystem Weight (Advanced Communications Satellite)

HARDWARE	UNIT MASS (KG)	NO. REQ'D.	MASS (KG)	WT. (LBM)
THRUSTER AND GIMBAL ASSEMBLY (a)	3.7	4	14.8	32.6
RESERVOIR (b)	1.2	4	4.8	10.6
POWER ELECTRONICS UNIT	7.0	4	28.0	61.7
DIGITAL INTERFACE UNIT	3.2	4	12.8	28.2
DIGITAL CONTROL UNIT	2.3	4	9.2	20.3
SQUIB VALVE	0.1	8	0.8	1.8
FILTER	0.1	2	0.2	0.4
PROPELLANT LINES	---	2	(c)	----
CABLES	---	44	3.1	6.8
TOTAL DRY WEIGHT			73.7	162.3

(a) INCLUDES TEMPERATURE SENSORS

(b) INCLUDES PRESSURANT, FILL VALVES, PRESSURE SENSOR, TEMPERATURE SENSOR

(c) LESS THAN 0.1 KG

Table 9. Ion Propulsion Subsystem Electrical Interface

POWER	320 WATTS AT 70 ± 20 VDC 14 WATTS AT 28 ± 1 VDC 7 WATTS AT 28 VDC FOR EACH GIMBAL MOTOR ACTUATION
COMMANDS	28 TOTAL

FUNCTION		TYPE	NO. REQ'D.
THRUSTER	IDLE	DISCRETE	4
THRUST	ON	DISCRETE	4
THRUST	OFF	DISCRETE	4
GIMBAL	-θ-	SERIAL	4
GIMBAL	Ø	SERIAL	4
RESERVOIR	VALVE	DISCRETE	4
THRUSTER	VALVE	DISCRETE	4

TELEMETRY — PER NASA STANDARD INTERFACE FOR DIGITAL DATA (SIDD)

Table 10. Ion Propulsion Subsystem Power Requirements

Table 10. Ion Propulsion Subsystem Power Requirements

CONDITION	28 ± 1 VDC	70 ± 20 VDC	TIME AFTER RECEIPT OF THRUSTER IDLE COMMAND	COMMANDS
STANDBY	14 W	0 W	--	
PREHEAT	14	214	0 - 7 MIN	THRUSTER IDLE
NEUTRALIZER ON	14	152	7 - 9	
CATHODE ON	14	90	9 - 10	
DISCHARGE ON	14	128	10 - 11	
BEAM ON	14	316	11 - 12	THRUST ON
FULL POWER	14	320	15 PLUS	
STANDBY	14	0	---	THRUST OFF

ADD 7 W OF 28 VDC POWER FOR EACH GIMBAL MOTOR ACTUATION

NOTE: FOR 2 THRUSTERS OPERATING SIMULTANEOUSLY WITH ASSOCIATED RESERVOIRS AND POWER PROCESSORS (PEUs, DIUs, DCUs)

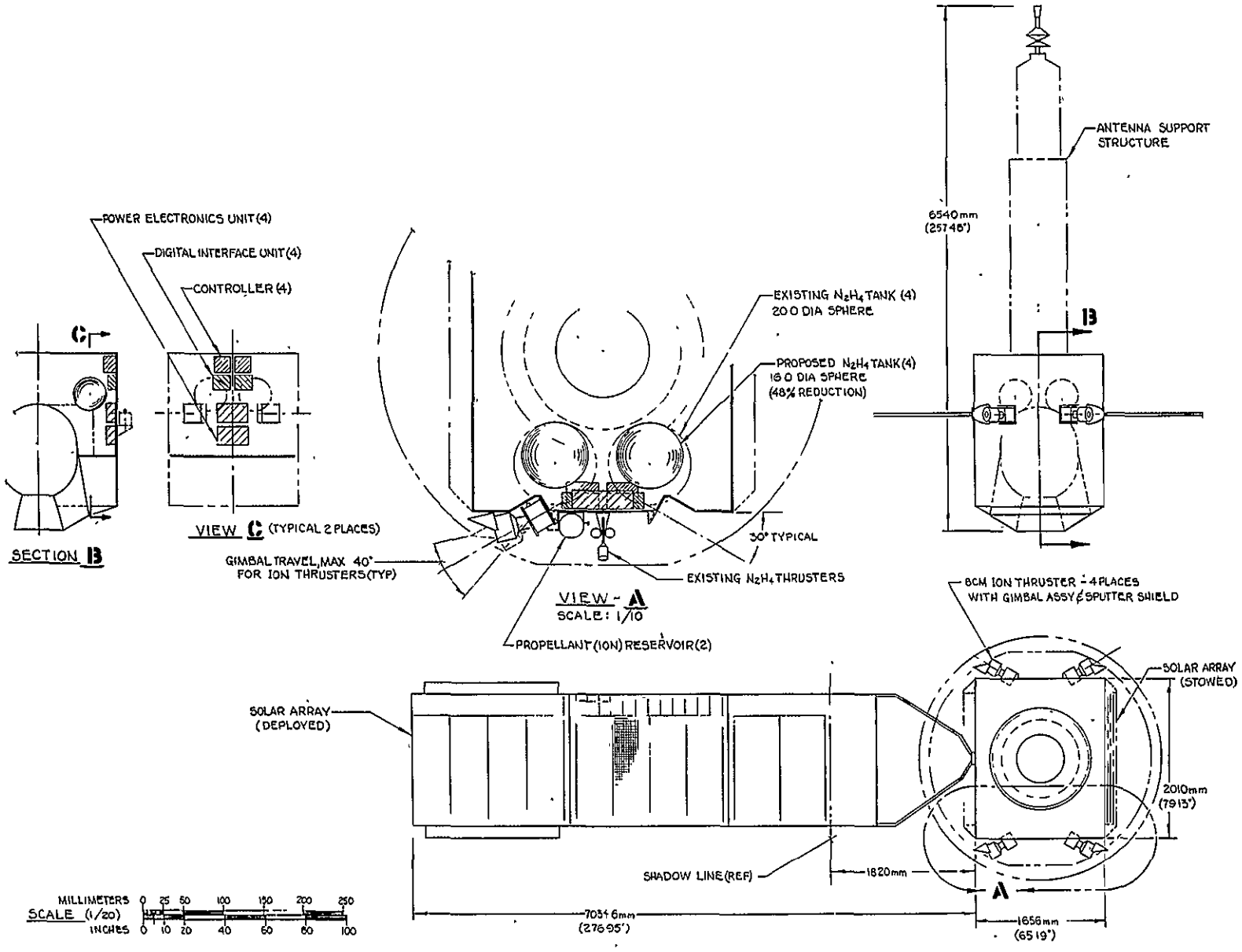

Figure 9. Integration of Ion Propulsion Subsystem with Intelsat V Design

ORIGINAL PAGE IS OF POOR QUALITY

not nearly as much hydrazine is required. If the ion propulsion subsystem completely replaces hydrazine, then there is a great deal of room available.

There is some potential for contamination of the east and west spacecraft faces by the ion engine efflux. These are not critical optical surfaces, however, and are only covered with thermal insulation. A thruster shield/thermal blanket material combination should be selected to minimize interactions.

Ion thruster efflux will impinge at wide divergence angles from the thruster centerline on the back of some of the communications antenna reflectors. TRW is building these reflectors as a subcontractor to Aeronutronic Ford for Intelsat V. There is little possibility of physical damage or degraded antenna performance occurring. The back of the reflectors is covered with an aluminized Kapton* insulation blanket of about 10 layers. Kapton, the outer material, is a polyimide film that is yellow in color. It is unlikely that mercury will react chemically with Kapton. The only effect might be a slight discoloration. This will not have a significant effect on the thermal distortion of the reflector since most of the thermal radiation is through the reflecting surface, not the back. The graphite face sheets of the composite reflector have a very low expansion coefficient.

3.2.3 Interactions with Attitude and Velocity Control Subsystem

This section presents an overview of the interactions of an ion auxiliary propulsion subsystem with a geosynchronous communications satellite attitude and velocity control subsystem (AVCS). The results are quite encouraging. Ion propulsion introduces few problems or needs for change in the basic AVCS design and provides significant benefits to the AVCS in terms of increased pointing accuracy and reduced stability problems.

In summary, it was found that the AVCS mission requirements are easily met with an ion propulsion subsystem substituted for hydrazine. This can be done with only changes in the control logic. No changes in sensors or torquers are required. The AVCS easily meets the mission pointing

*Trade name, DuPont.

requirements without excessive thruster on-off operations, which is the most critical ion propulsion parameter.

The AVCS controls satellite pointing at all times and thrust vectoring during orbital corrections. It consists of sensors (such as earth sensors or star trackers), electronics which provide the control logic to process the sensor data and provide corrective control commands, torquing devices for providing angular pointing control and some means of obtaining proper thrust vectoring. The AVCS relies on the propulsion subsystem for orbital correction thrusting, as well as a significant portion of the attitude torquing, even though it may also have its own torquers such as reaction wheels or magnetic torquers.

The AVCS depends on the propulsion subsystem to achieve part of its requirements and as such places requirements on the propulsion subsystem. Table 11 summarizes the significant ion thruster requirements for the Advanced Communications Satellite. Of concern are thrusting duration, number of thrust cycles, and total propellant consumed. It can be seen that the requirements are easily met by the NASA-LeRC 8-cm ion engine, which is designed for 20,000 hours of operation and 10,000 on-off cycles.

Table 11. Advanced Communications Satellite Ion Thruster Requirements

	Station Acquisition	N-S, E-W Stationkeeping	Momentum Dump	Total
Number of cycles (total)	1	5,110	5,110	10,221
Worst thruster	1	2,550	1,275	3,826
Hours used (total)	60	13,566	426	14,052
Worst thruster	60	6,783	107	6,950
Propellant used (kg)	0.1	18.7	1.2	20.0

The significant impacts of ion propulsion on AVCS performance for this mission are:

- Pointing accuracy is improved due to the low, vectorable torques available.
- Stability is improved due to distributed thrusting, rather than small pulses which can excite resonances.
- Nutation never builds up since engine pulses are long compared to the spacecraft nutation period.
- Because maneuvers are performed twice per day, stationkeeping accuracy is much better than 0.1 degree and is limited only by orbital determination accuracy.
- For currently estimated disturbance torques of 2×10^{-6} N m, ion engines need only fire for 10 minutes per day. Control torque capability exists for much larger disturbances.
- Yaw sensing is desired (not required) for the longer periods of time for north-south stationkeeping.
- Since reducing the number of thruster cycles is important, more elaborate disturbance torque estimation techniques must be employed — or another small reaction wheel added.

It should be stressed that pointing accuracies are very favorable when comparing ion propulsion to the more conventional hydrazine propulsion. This is due to the low thrust level, the vectorable nature of the gimballed thrusters, and the essentially steady-state operation. Transient pointing errors of less than 0.04 degree are predicted from computer simulation results for this mission. This advantage can be greater than the orbital correction propellant weight savings for certain missions requiring continuous high pointing accuracies.

The attitude and velocity control requirements for an Intelsat V type mission are summarized in Table 12. The satellite pointing requirements are moderate and are sized by the beamwidths of the antennas. Notice that shuttle launch is <u>not</u> assumed and transfer orbit attitude control and apogee boost to place the satellite into geosynchronous orbit are required.

3.2.3.1 Baseline AVCS and Propulsion Subsystem Designs

Defining baseline AVCS and ion propulsion subsystems for the Advanced Communications Satellite is difficult since so many AVCS options exist — each

Table 12. Attitude and Velocity Control Requirements for Advanced Communications Satellite

Functions	Δv
Transfer Orbit Attitude Control	
Apogee Boost	$\sim 2.3 \times 10^3$ m/s
Initial Station Acquisition	
N-S stationkeeping	~350 m/s over 7 yr
E-W stationkeeping	Up to 14 m/s over 7 yr
In Orbit Attitude Control and Momentum Dumping	
Station Change	Up to 50 m/s

Pointing Requirements During Payload Usage

Roll $\leq 0.2^\circ$, Pitch $\leq 0.2^\circ$, Yaw $\leq 0.4^\circ$

Stationkeeping Accuracy

N-S $\leq 0.1^\circ$, E-W $\leq 0.1^\circ$

one optimizing a certain class of requirements. The overriding considerations in selection of baseline designs are:

- Design similarities with existing satellite programs (such as Intelsat V)
- Design trends toward where satellite designs appear to be going (to reduce weight or slightly improve performance)
- Designs having features least suitable for ion propulsion, under the theory that if ion propulsion can be shown to be favorable here, then other designs will be more favorable.

In the interest of a concrete example, the proposed Intelsat V design was selected with modifications which seem likely or desirable.

The baseline AVCS and propulsion subsystem designs, plus some alternate designs, are summarized in Table 13.

Table 13. AVCS and Propulsion Subsystem Configurations for Advanced Communications Satellite

Function	Baseline	Alternates
Transfer orbit attitude control and apogee boost	• 100 lbf (500 N) liquid bipropellant motor, gimballed • Auxiliary cold gas propulsion • Sensors: gyros updated by sun and earth sensors	(1) • Solid apogee motor; • Auxiliary hydrazine propulsion; • Spin stabilized with sun and earth sensors (2) • Shuttle IUS
Initial geosynchronous orbital station acquisition	• Restartable bipropellant until velocity error <1m/sec, body rates <0.2°C • Ion propulsion for final control	(1) • Hydrazine (2) • Ion propulsion acquires from IUS
N-S and E-W stationkeeping	• Pair of ion thrusters, gimballed • Earth scanning IR sensor, sun sensor or rate gyros	
Attitude control and momentum dumping	• Body fixed, biased momentum wheel • Ion engine dumping • Earth sensor	• Small 1 N.m-sec roll axis wheel added
Change of station	• Ion propulsion	• Auxiliary cold gas • Hydrazine

The sensors are the normal mode pitch and roll axis sensor (an IR or RF earth sensor) and a sun sensor for yaw reference. Stationkeeping may be required at those times of the day when the sun does not provide a yaw reference. In this case, short term yaw reference is provided by a gyro or open loop estimation of the yaw disturbances induced by the ion engines. This latter option is available with ion propulsion due to the ability to control the induced disturbances so finely (due to low thrust levels and the gimbals).

High frequency torque control is provided by the normal mode control (momentum stiffness and wheel speed control). The ion engines are gimballed to provide low frequency torques which precess the momentum vector and properly adjust wheel speed.

The ion thruster layout, described in Section 3.2.2, consists of four thrusters, two on the east face of the satellite and two on the west face. They are canted with gimbal vectoring capability as shown in the layout.

The basic stationkeeping (north-south and east-west) thrusting firing logic is:

a) With no thruster failures

- Fire twice each day (one north and one south firing)
- A typical north firing is achieved with both north facing thrusters canted up with a nominal 30 degrees (the cant with respect to north)
- The thrusters are simultaneously turned on with θ and ϕ for each thruster finely controlled by the AVCS to assure proper pointing and unloading of the momentum wheel.
- Near the conclusion of the thrusting time, should an east or west correction be desired, one thruster is turned off and the other gimballed so its thrust vector goes through the nominal center of mass. This one thruster generates components of north and east or west velocity increments.
- This thruster is finely controlled by the AVCS to maintain proper pointing.
- The thrusting continues until the desired total north and east or west velocity increments are achieved.

- The mix of north and east or west velocity increments is controlled by the duration of two-thruster and single thruster thrusting. Nominally, a single thruster is firing for 8% of the thrust interval.

b) With a thruster failure

- The identical strategy is used, but firing is commanded just once a day (only north or south) in the direction that two thrusters are operative.

3.2.3.2 Momentum Bias

One of the most important factors affecting the on-orbit three-axes AVCS configuration is the use of momentum bias. In this approach, one or more continuously running wheels provide a net momentum vector perpendicular to the orbit plane. Gyroscopic stiffness is achieved in both roll and yaw axes and reduces attitude error buildup from disturbance torques. Rotation about the pitch axis is controlled by variation in wheel speed. The spacecraft rotates at orbit rate so that there is a kinematic coupling between roll and yaw errors. The momentum bias stiffness maintains attitude roll/yaw errors within required limits until the inertial error can be measured with a roll sensor and corrected. This approach obviates a yaw sensor.

The three-axes zero momentum approach uses three or more wheels. The wheels generate reaction torques to counter disturbance torques. This approach requires a yaw sensor as well as pitch and roll sensors.

Table 14 compares the biased momentum technique versus three-axes zero momentum bias. The latter uses three pairs (for redundancy) of small reaction wheels for interim momentum storage, and senses yaw using a gas bearing rate gyro that is updated twice daily with the sun sensor output. Both techniques are well understood and can meet mission requirements. However, biased momentum uses fewer rotating assemblies (two wheels versus three, plus the rate gyro), requires less onboard electronics (two axes of active control versus three), and avoids the need for a yaw sensor (other than the existing sun sensor). Hence, biased momentum is more reliable and less complex.

Biased momentum systems can be grouped based on which of the three spacecraft axes (pitch, yaw, or roll) require interim momentum storage.

Table 14. Biased Momentum Versus Zero Momentum Attitude Control Comparisons

Issue	Biased Momentum	Zero Momentum
Weight (reaction wheels, wheel drive electronics, control loop electronics and yaw sensor; including redundancy to protect against any single-point failures)	40 lb (18 kg weight is a function of solar disturbance torques and peak antenna slew rate requirements)	50 lb (23 kg weight could be reduced to 18 kg if three of four wheel redundancy is used)
Yaw sensor	None	Continuous yaw sensor required; assumed to be rate gyro updated by sun sensor. Could be RF plus IR earth sensor or star sensor
Number of wheels mechanically spun during control	Two	Four (would be reduced by 1 if alternate yaw sensor could be found)
Electronics complexity	Two axes of autonomous active control	Three axes of autonomous active control
Pitch and roll pointing	Capable of ≤ 0.17 deg	Capable of ≤ 0.17 deg
Yaw pointing accuracy	~0.33 deg for worst-case solar disturbance torques (4×10^{-6} ft-lb – 5×10^{-6} N.m	0.5 to 0.2 deg (dependent on yaw sensor accuracy)

Interim momentum storage has many usages: pointing error can be reduced without using propellant; momentum from periodic disturbance torques can be temporarily stored, so that no propellant is expended to offset these effects; and momentum from inertially fixed (secular) disturbance torques can be stored and periodically dumped, reducing the frequency of thruster firings.

The three basic types of systems are a single axis of momentum storage (pitch), two axes (pitch and yaw), and three axes (pitch, roll, and yaw). These are each shown in Figure 10 with two different methods for implementing three axes of momentum storage illustrated.

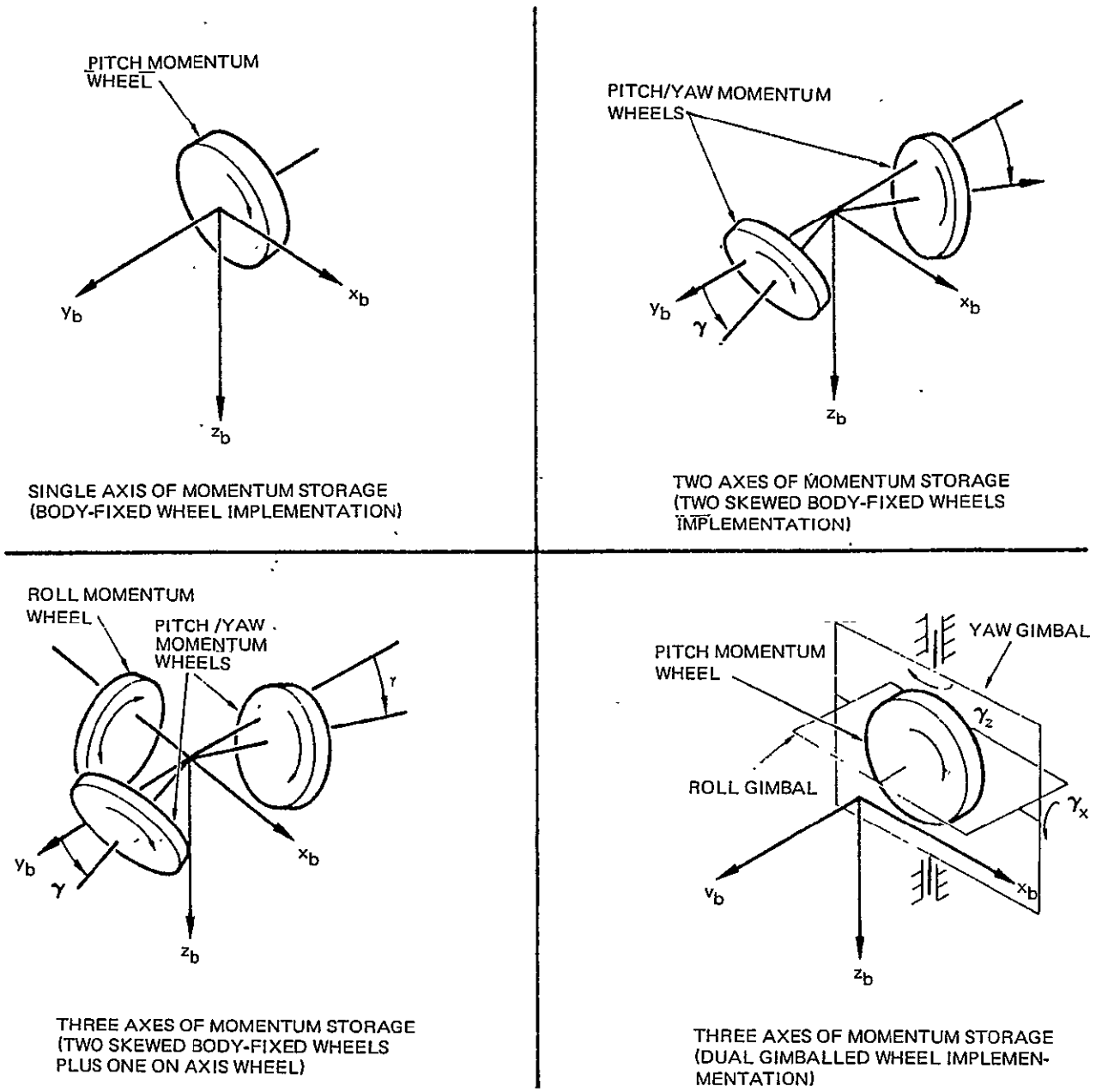

Figure 10. Schematic Representation of Various Biased Momentum Wheel/Gimbal Configurations

Single Axis of Momentum Storage (Pitch)

The simplest momentum biased system is a single, body-fixed wheel (and typically, a redundant wheel). This is used on FLTSATCOM, Canadian Technology Satellite, the European OTS, and Intelsat V.

Two Axes of Momentum Storage (Pitch and Yaw)

Pitch momentum is the same as for the single axis system. Roll torques precess the momentum vector in yaw, and yaw is passively controlled by the gyroscopic stiffness afforded by momentum bias, with periodic secular momentum dumps. External yaw torques precess the momentum vector in roll. Tight roll control in the presence of these torques is provided by a yaw momentum storage device. This allows a buildup of momentum without roll pointing error and infrequent momentum dumps, but at the expense of an additional momentum wheel and increased onboard electronics.

Nutation motion is damped by time phasing this pitch-yaw momentum interchange with respect to the nutation movement. The yaw momentum source can be a separate reaction wheel or a component of two skewed pitch wheels.

Three Axes of Momentum Storage

Pitch control is the same as in the other two approaches. Roll is controlled by a roll momentum source, and yaw by a yaw momentum source. Roll control is based on roll earth sensor data; yaw is controlled without yaw attitude data, using roll attitude and measurements of the stored roll/yaw momentum. This approach has all the capabilities of the others. In addition, yaw pointing error can be reduced to the extent that its motion can be predicted, and roll pointing errors from antenna slewing can be minimized by preemphasis commanded roll momentum changes. Roll and yaw momentum sources can be three or four skewed biased momentum wheels for the body-fixed case; a dual-gimballed biased momentum wheel can be used in the gimballed case.

Selection of Momentum Storage Technique

Table 15 summarizes the significant differences for five implementations of the three concepts. The single body-fixed wheel is the simplest,

Table 15. Comparison of Various Biased Momentum Attitude Control Configurations

Axes of Momentum	Configurations	Biased Momentum		Weight[1]		No. of Wheels (in normal use)	Relative Electronics Complexity	Peak Roll Dynamic Error[2] (deg)	Peak Yaw Dynamic Error[3] (deg)	No. of Thruster Firings/ Day	Wheel Failure Impact
		N.m-sec	ft-lb-sec	kg	lb						
1	Body-fixed wheel (plus 1 back-up)	20	15	16	35	2	1 wheel drive channel	0.23 (less with thruster firings)	0.5	≥10	Peak yaw pointing error increases by x2, thrusters used to damp large antenna slews
2	Two skewed wheels (plus 1 back-up)	20	15	18	40	2	2 wheel drive channels	0.04	2	<1	Momentum one half, therefore pointing errors double
2	Single gimballed wheel (plus back-up wheel and redundant drive)	20	15	21	47	1	1 wheel drive channel; 1 gimbal drive channel	0.04	2	<1	None
3	Four skewed wheels	22	16	24	52	4	4 wheel drive channels	0.04	0.2[4]	≤1	Momentum one-half, yaw pointing doubles
3	Dual gimballed wheel (plus 1 back-up wheel and redundant drives)	20	15	25	54	2	1 wheel drive channel; 2 gimbal drive channels	0.04	0.2	≤1	None

[1]Weight of wheels and drive electronics only (approximate).

[2]Alignment and sensor errors not considered.

[3]Solar torque assumed = 0.5×10^{-6} ft-lb secular and 7×10^{-6} ft-lb periodic (0.7 and 9×10^{-6} N.m).

[4]Solar torque assumed predictable within 10%.

ORIGINAL PAGE IS OF POOR QUALITY

generally lightest, and most reliable. Since thruster firings are generally in the secular torque direction, the technique is as efficient as others. However, impulse bit is limited by nutation of a single pulse, and the pulses must be separated so that roll attitude never becomes excessive (roll attitude error is an essential consequence of absorbing yaw torques without firing thrusters). This technique is mechanically the simplest and lightest that meets the requirements of a mission such as Intelsat V. This configuration has been selected for this study.

The two implementations of the two-axes momentum storage concepts meet all requirements, and are simpler than the three-axes systems. The difference between two skewed wheels and a single gimballed wheel is slight. Both are comparable in weight. The single gimballed system affords slightly better performance because the gimbals can be torqued at a higher rate and with less power than the momentum vector can be made to rotate by change of wheel speed. However, the skewed wheel concept uses off-the-shelf wheels with identical control electronic loops. The gimbal assembly must be designed, fabricated, and tested, with attendant development cost and risk.

Roll attitude error can be monitored at a ground station and corrected (typically no more than twice a day), or autonomously controlled from the spacecraft. Nutation can be actively damped either by timing the firing of the correction pulses to reduce the nutation, or by varying the wheel speed sinusoidally at the nutation period.

This technique is the most demanding on the propulsion subsystem. The propulsion subsystem must be used to precess the satellite when the roll error threshold is exceeded. Other techniques require thrusting only to unload stored momentum and the timing of the pulses is not critical. Also, this approach is sensitive to the nutation buildup due to thruster firing. For example, for hydrazine systems the pulse lengths are limited by the desire to limit all pulses to ≤ 0.04 ft-lb-sec (≤ 0.05 N.m-sec). This implies at least 200,000 pulses over 7 years. For ion propulsion, the torque is controllable and low so that the pulse duration can be distributed over the nutation period (on the order of 1000 seconds). Ion propulsion then shows mixed benefits. Since roll precession is governed by pointing error, and therefore phased with disturbance torques, precession may not be possible during the

ORIGINAL PAGE IS
OF POOR QUALITY

stationkeeping maneuvers, and added thruster cycles may be required. On the other hand, nutation worries are greatly reduced when making the precession maneuvers.

3.2.3.3 Pointing Accuracy

The pointing accuracy of the communications antennas in orbit is due to many factors. These include control subsystem transients, static internal satellite alignments and thermal deformations of the antennas. An example of an apportionment of error sources is presented in Table 16. It can be seen that, even to meet rather loose pointing requirements, the amount allotted to AVCS transients is rather small — on the order of 0.05 degree. The following discussion shows how this pointing accuracy might be satisfied with a body-fixed, biased momentum AVCS and an ion propulsion subsystem.

As will be shown, the time for corrective control torques is determined by the disturbance torques and, therefore, cannot necessarily be performed during stationkeeping. The stationkeeping times are ideal since torques can

Table 16. Antenna Pointing Error Sources (degrees)

Error Source	North/South (Roll)			East/West (Pitch)			Yaw		
	Fixed	< Daily Variation	≥Daily	Fixed	< Daily Variation	≥Daily	Fixed	< Daily Variation	≥Daily
Antenna									
RF boresight/mechanical and earth sensor alignment	0.05			0.05			0.05		
Thermal distortion			0.072			0.072			
Structural flexure	0.005			0.005					
Earth Sensor Assembly									
Alignment (internal)	0.0173			0.006					
Component variation		0.023			0.020				
Supply variation		0.01			0.01				
Radiance uncertainty		0.021			0.021				
Stationkeeping N/S & E/W (0.1 deg)		0.018			0.018				
Control System Errors									
Dynamics (transients included)			0.05			0.025			0.28
Electronics	0.02			0.02					
Yaw coupling error	0.006		0.036	0.008		0.042			
RSS Errors	0.057	0.037	0.095	0.055	0.035	0.087	0.05		0.28
Total Errors		0.189			0.178			0.33	

be provided with no added thruster cycles and insignificant propellant. The pointing error is based on the number of thrust cycles over a day. Techniques are shown which permit two or four thrust cycles per day. The two-cycles-per-day technique provides adequate performance and is selected as the baseline.

In geosynchronous orbit, the primary disturbance torques are either internally generated disturbances (such as from the propulsion subsystem) or are induced by solar pressure. These are all relatively low level disturbances and precess the body-fixed wheel relatively slowly. Therefore, its pointing error can be minimized by infrequent control actuation to realign the momentum vector.

In the satellite the axis of the body-fixed, biased momentum wheel (pitch) is nominally oriented normal to the orbit plane. This provides stiffness in the roll and yaw axis and permits accurate pointing by actively controlling only the roll axis. The yaw axis control is maintained by the kinematic coupling of roll and yaw during the 24-hour orbit (x is along the velocity vector and z is pointed toward the earth). Pitch control is achieved by torquing the momentum wheel. The present study analyzes the roll-yaw coupling under the influence of a secular disturbance torque and finds a proper control activation scheme to minimize the roll error. The momentum wheel unloading (pitch loop) is similar to that for Mission 2, which was analyzed by computer simulation. This is described in Section 3.3.3. Since necessary control laws are not yet defined for Mission 1, the emphasis here is placed on the theoretical capability. The following simplifying assumptions are made:

- Only the secular (constant) component of disturbance is studied
- Perfect roll/yaw attitude estimation is assumed
- The dynamics of the pitch axis are decoupled from roll and yaw.

Basic Concept

If an inertially constant (secular) disturbance torque vector lies in the orbit plane, the momentum vector normal to the orbit plane will precess about an axis in the orbit plane normal to the torque vector. A simple way

to demonstrate small precessional motions is to project the tip of the unit momentum vector onto the orbit plane. If an orbit reference coordinate frame is selected with torque vector along x and the body-fixed momentum vector along -y, the precession will be about +z. In the projected view, the motion will be along +x. Since the torque vector is constant in the inertial space, the projected motion on the xz plane rotating with the orbit will be an Archimedian spiral characterized in polar coordinates by:

$$r = \frac{M}{H} t \tag{4}$$

$$\theta = \omega_o t \tag{5}$$

where H is angular momentum, M is secular torque, t is elapsed time since error = 0, and ω_o is orbit rate.

A sample trajectory is illustrated in Figure 11. The solid lines show the xz plane projection of the precession of a momentum vector which is pointed out of the page. There will be a small nutation about this trajectory. However, this is neglected for the sake of simplicity. The applied torque is along +x when the attitude error is zero (t = 0). The locus is shown for a half orbit, since the control torque will be applied at least twice in one orbit. The magnitude is normalized to daily precessional angle δ due to the constant disturbance torque. If the disturbance torque is D and the body-fixed momentum is H, this angle is given by

$$\delta = 24 \times 3600 \times 57.3 \ D/H = 4.95 \times 10^6 \text{ deg-sec } (D/H) \tag{6}$$

If $D = 2 \times 10^{-6}$ N.m and H = 25 N.m-sec, $\delta = 0.396$ deg.

The dotted line in Figure 11 indicates the trajectory in the half orbit prior to t = 0. In a geosynchronous orbit, for example, $\phi = 0$ and $\psi = 0.5$ at t = -12 hr, $\phi = 0.25$, $\psi = 0$ at t = ±6 hr, $\phi = \psi = 0$ at t = 0, and finally $\phi = 0$ and $\psi = -0.5$ at t = +12 hr. The total precession is 1 during the 24-hour period. Thus, if the inertial orientation of the secular disturbance torque can be determined, the precessional motion can be predicted and hence

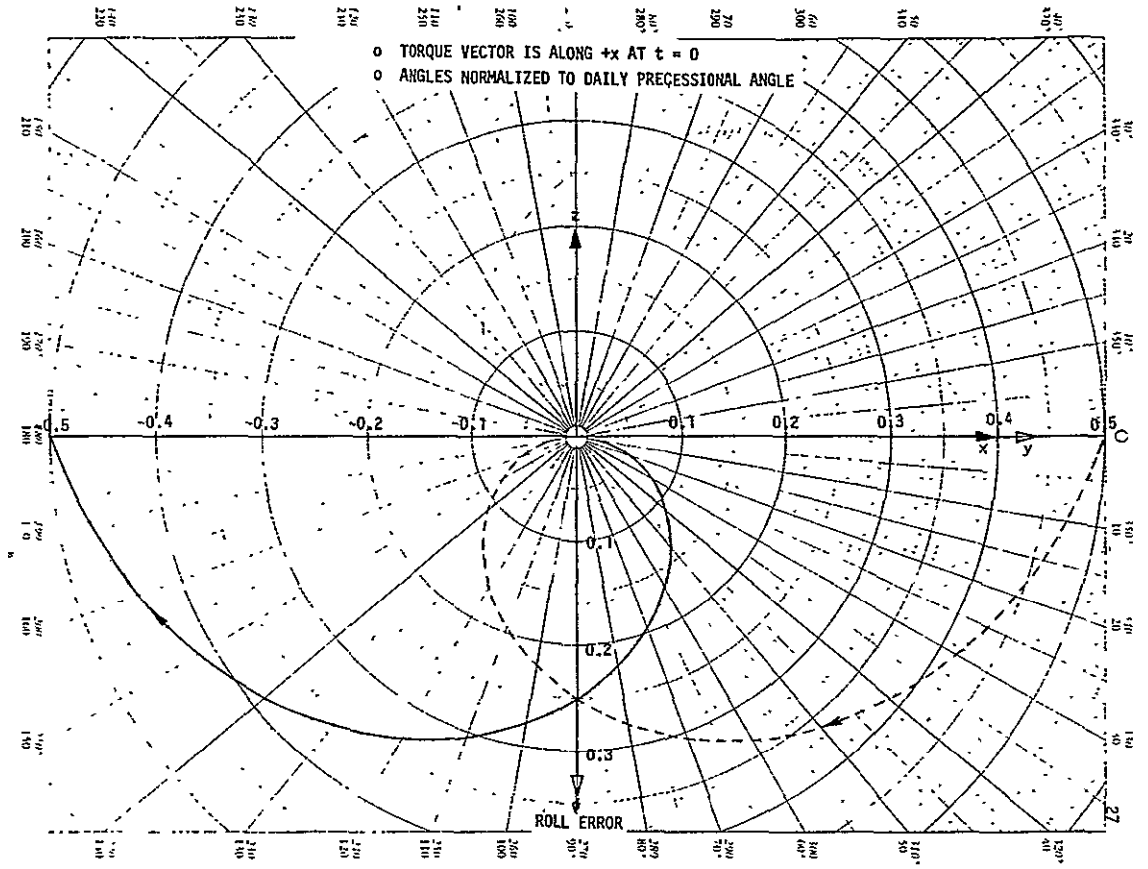

Figure 11. Precession Due to Inertially Constant Torque

managed by applying appropriate control torque. This will be demonstrated by a sample case. If a disturbance torque vector is oriented as shown in Figure 12a, and if a geosynchronous orbit is initiated with zero error at point A, the momentum vector (pointing out of the page) will precess as shown in Figure 12b. After 12 hours, the orbit position will be at B. If a control impulse is applied at this point (about x) such that the accumulated disturbance torque impulse is completely removed, the momentum vector will be driven back to the initial state of zero error, as shown by the dotted line. This trajectory is a cycloid due to nutation. The effect of orbital rotation during the control activation is neglected for simplicity. The deadbeat response is attained by equating the duration of the control to the nutational period of the satellite body. The process is repeated during the second 12-hour period with the control torque applied at A. It can be seen that the maximum error is ±0.29 in roll, ±0.5 in yaw. The error can be trimmed in this case by changing the timing of the control. The optimum position in orbit is found graphically to be C and D, approximately 27 degrees from A and B. Although the maximum radial error is still the same, the roll and yaw errors are reduced to ±0.22

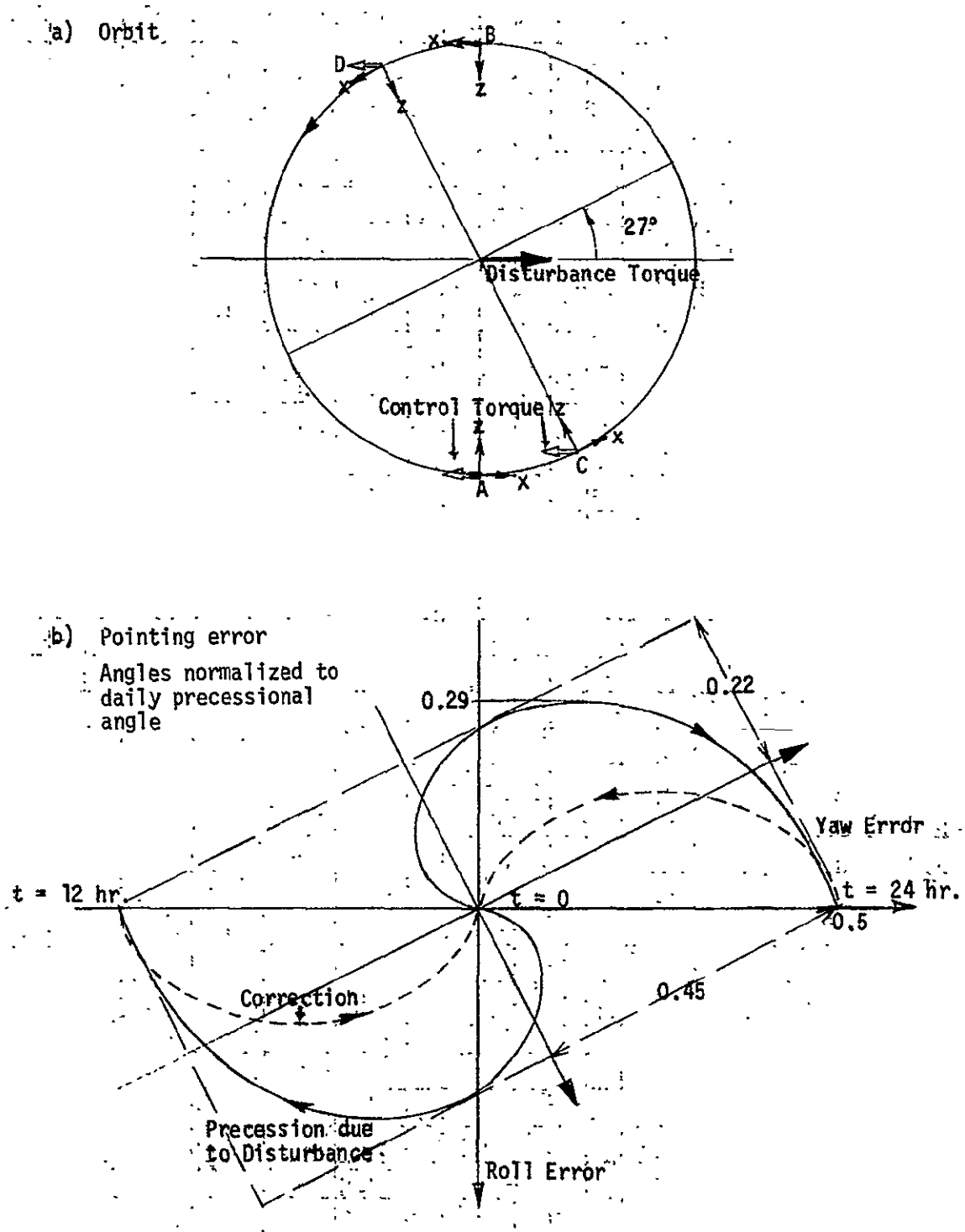

Figure 12. Precession Management — Sample Case

and 0.45, respectively, by changing the position of initialization. Note that the control torque is also shifted about 27 degrees from the x-axis in the body coordinates to be the opposite of the disturbance torque vector in the inertial space.

Optimum Precession Management with Two Control Pulses per Day

The error envelope can be further reduced if each control pulse precesses the momentum vector to the opposite direction past the zero error point. The minimum error envelope is obtained with the precession management scheme shown in Figure 13. This scheme is similar to the sample case (activating control at A and B). However, the orbital position of the initialization is 90 degrees out of phase with the sample case. In this way the semi-diurnal precession of 0.5 is centered about the zero error point. Thus the peak error is halved to 0.25. If this peak error point is aligned with the yaw axis, as shown in Figure 13, the peak roll error is 0.09. It is to be noted that control activation is extended over two nutational periods to reduce the nutation in the roll direction.

Thus, if the magnitude of the disturbance torque is D and the body-fixed momentum is H, the theoretically attainable pointing accuracy with two control pulses a day is given by:

$$\phi_{max} = 0.09\ \delta = 4.42 \times 10^{5} \text{ deg-sec } (D/H) \tag{7}$$

$$\psi_{max} = 0.25\ \delta = 1.24 \times 10^{6} \text{ deg-sec } (D/H) \tag{8}$$

In the earlier example, with $D = 2 \times 10^{-6}$ N.m and $H = 25$ N.m-sec, the peak roll and yaw errors are ±0.035 and 0.099 deg, respectively.

Optimum Precession Management with Four Control Pulses per Day

The effect of more frequent precession control is next shown by a scheme using four pulses a day. Using the graphical method as before, the optimum scheme was found to be the one illustrated in Figure 14. The maximum precession in this case is halved to 0.125. By a proper initialization, this error is reduced to 0.1 in both roll and yaw as shown in Figure 14. Extending each control activation to two nutation periods does not reduce the

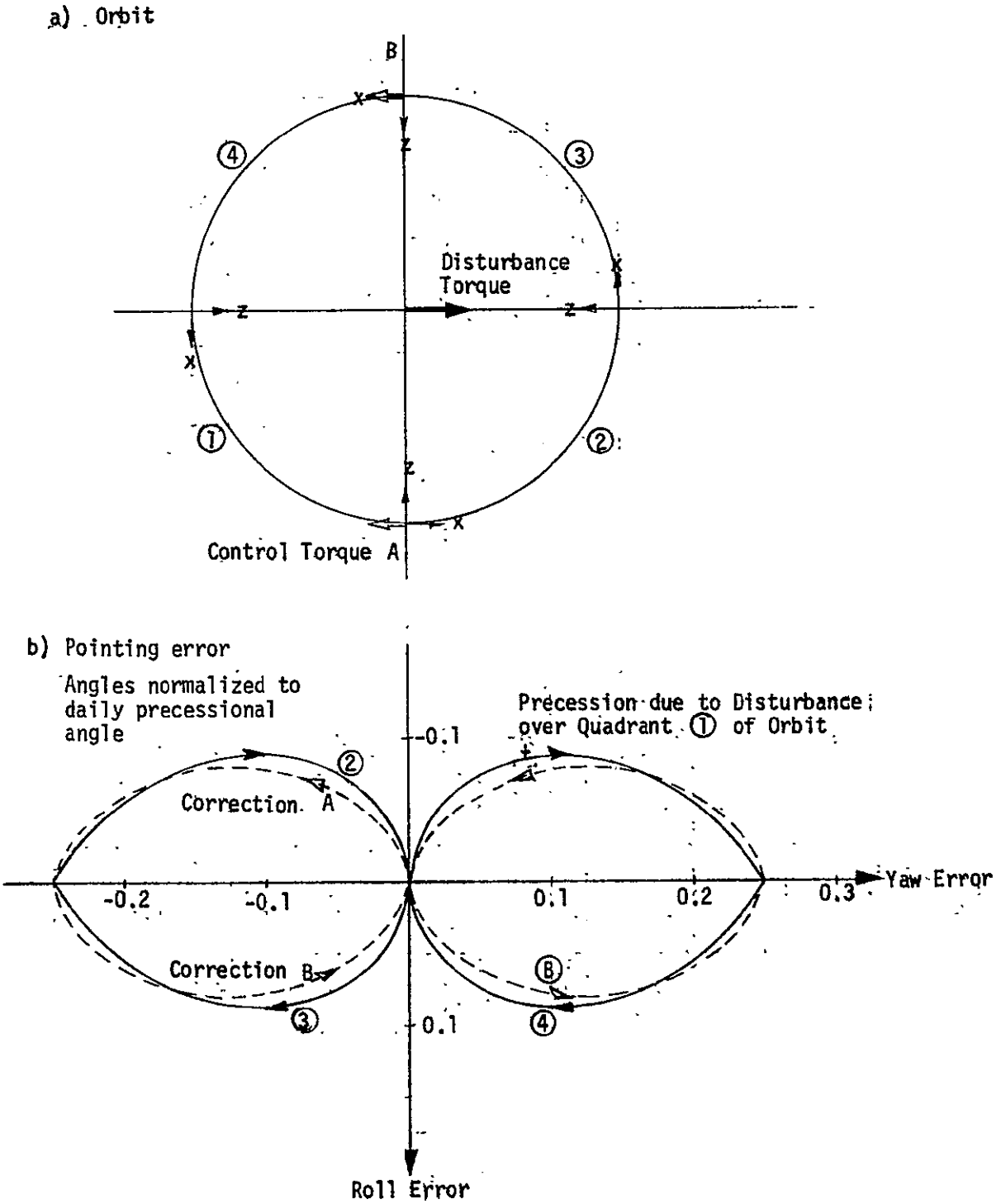

Figure 13. Optimum Precession Management with Two Control Pulses per Day

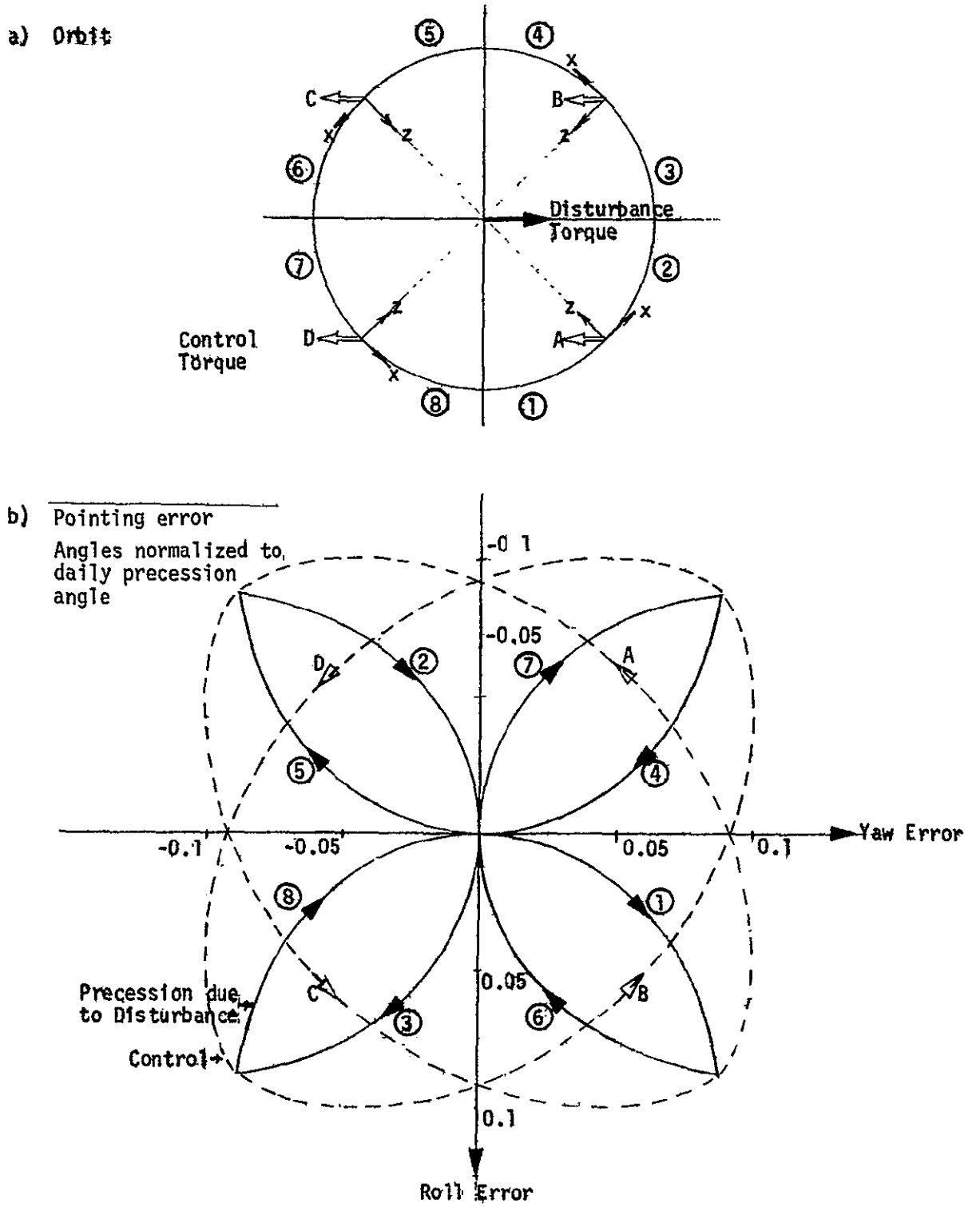

Figure 14. Optimum Precession Management with Four Control Pulses per Day

peak error substantially (0.095). With the same disturbance and momentum as before, the normalized error of 0.1 corresponds to peak pointing errors of 0.04 degree in roll and yaw.

Thus, unless a high pointing accuracy is required about both axes, the scheme with two daily control pulses is preferable because of its operational simplicity, fewer thruster activations, and slightly smaller peak roll error. The reduced actuation frequency is of course a significant factor to consider from the standpoint of ion thruster life.

Simulation and Results

The two schemes discussed above have been simulated on the TRW time share digital computer. Since the control laws are not yet designed, the selection, orientation, and activation of various control engines are preprogrammed in the simulation (this is equivalent to a perfect attitude estimation scheme on the satellite). The results are shown in Figure 15 for the scheme with two control pulses and in Figure 16 for the four pulse schemes.

In Figure 15, the performance characteristics are shown in terms of pointing errors, attitude errors, body rates, and body components of the disturbance torque and control torque over one orbital period of 24 hours. The major parameter values used in the simulation are as follows:

$$I_{xx} = 1903 \text{ kg.m}^2$$

$$I_{zz} = 2079.8 \text{ kg.m}^2$$

$$\tau_d = 2 \times 10^{-6} \text{ N.m (disturbance torque)}$$

$$\tau_c = 8.64 \times 10^{-5} \text{ N.m (control torque)}$$

$$T = 600 \text{ sec (nutation period)}$$

The control torque is calculated on the basis of the disturbance torque and 1000 seconds (= 2T) activation every 12 hours. As shown in Figure 13, the control torque vector is aligned with the body x-axis. The activation period of 1000 seconds is centered about the ideal time at 6 and 18 hours. This is evidenced by the openings at the top and bottom portions of the roll-yaw

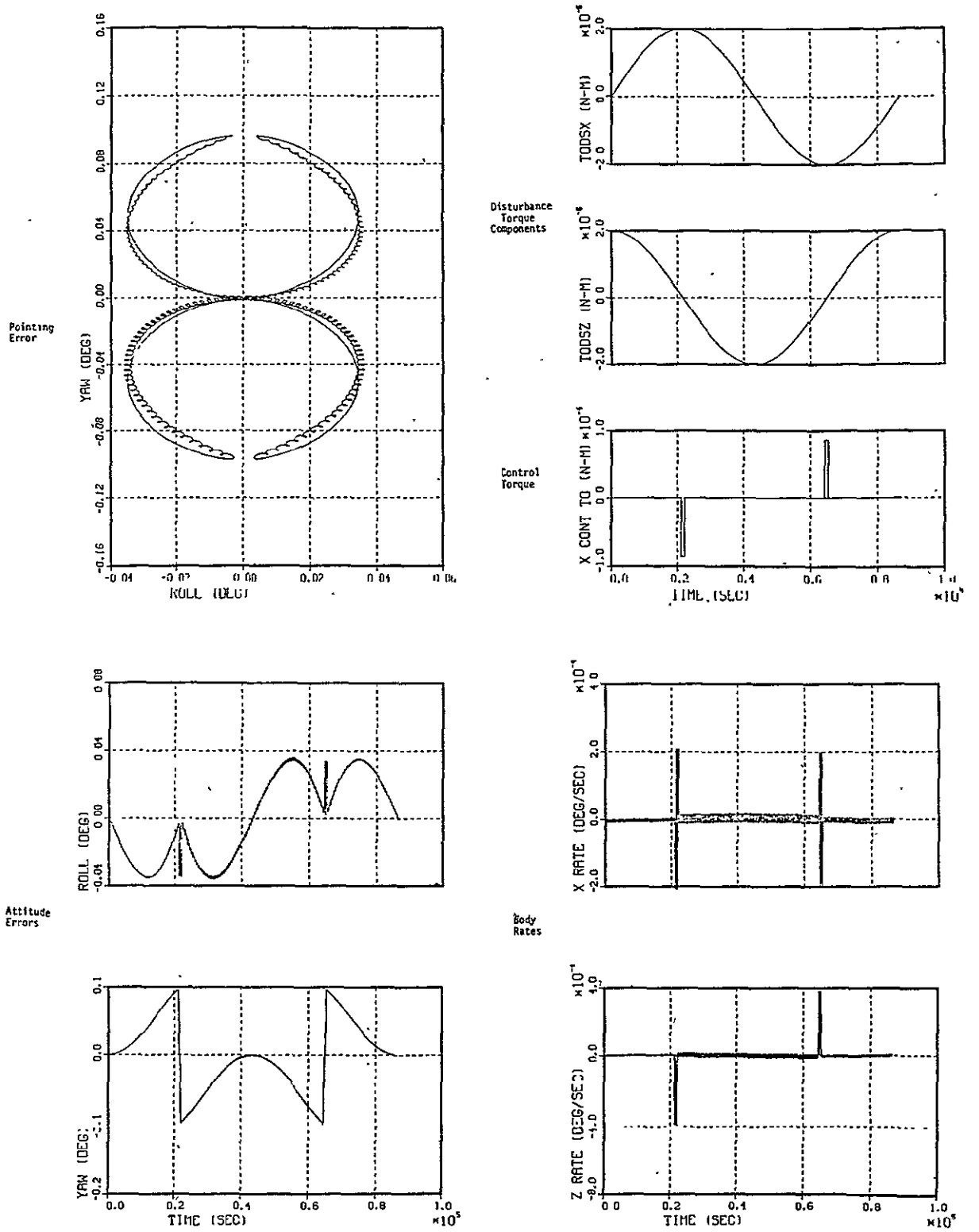

Figure 15. Performance Characteristics with Two Daily Control Pulses

ORIGINAL PAGE IS
OF POOR QUALITY

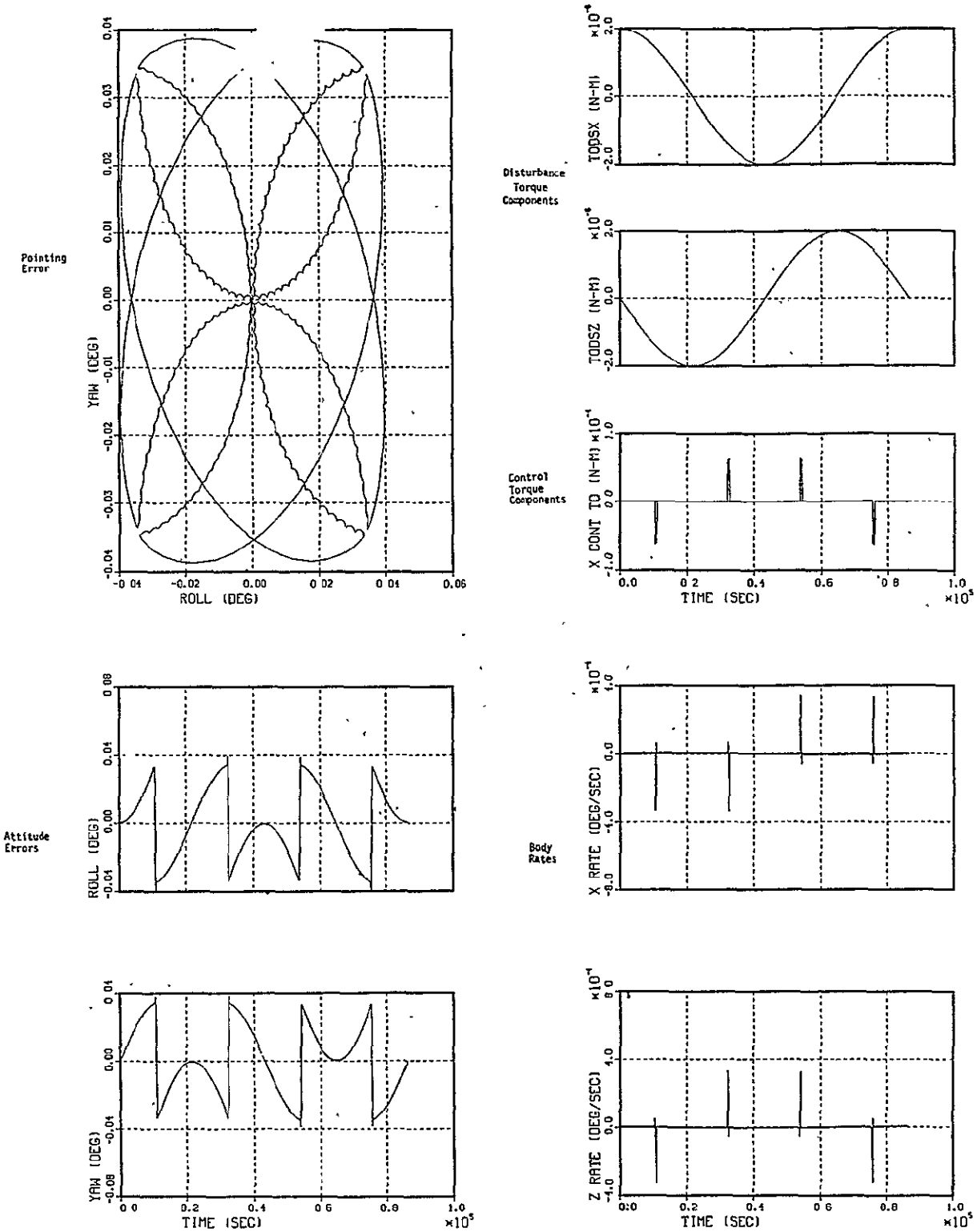

Figure 16. Performance Characteristics with Four Daily Control Pulses

pointing trajectory shown in the upper left plot in Figure 15. The ratio of the control torque to disturbance can be observed in the nutation associated with the control activation and the small nutation about the precession caused by the disturbance.

The performance characteristics are similarly shown in Figure 16 for the scheme using four daily control pulses. All the parameters used in the simulation are the same as before. The control torque is the same since the doubled number of activations is countered by the halving of each activation to one nutation period. The control torque vectors, however, are along the axes bisecting the x and z axes. (Only the x-component is shown in Figure 16.) It is interesting to note that the centering of activation period about the ideal time results in slightly smaller error envelope (about ±0.0395 degree in roll, ±0.0385 degree in yaw).

Practical Considerations

The simulation results validate the earlier discussion of the momentum management technique. However, these schemes are very ideal in that they demonstrate the theoretically attainable pointing accuracy for a given secular disturbance torque level. In actuality, the pointing will be affected by various factors such as:

- Accuracy of secular disturbance determination
- Magnitude of secular disturbance component normal to the orbit plane
- Magnitude of periodic disturbance
- Nonideal control initialization and activation

Thus, minimization of these effects will be important in developing control laws to effect the momentum management. Also a form of nutation damping must be studied to guard against large nutational motions resulting from unexpected disturbances or control activation not being exactly equal to some multiple of the nutation period.

3.2.3.4 Control System Stability

Control system stability problems usually arise in several ways. In order to meet tight pointing accuracies in the presence of large, high frequency

disturbances, the control loop gain is raised and lead compensation is added. Unexpected lags or phase shifts in the hardware can cause control loop instabilities. These instabilities are called rigid body instabilities since they are not introduced by satellite flexible bending modes but rather by the system behaving as a rigid body. Fortunately, the disturbances at geosynchronous altitudes have extremely low frequency content and low frequency control loops can easily be designed which counter the disturbances and are stable. This design is slightly more difficult for hydrazine propulsion than ion propulsion because the hydrazine engines are normally of high torque levels and nongimballed. This requires the thruster pulses to be pulse frequency modulated to approximate a linear torque capability.

In addition to the normal rigid body stability problems, a momentum stabilized satellite design must also be conscious of nutational stability. Nutation is coning action or wobble which is induced on the momentum vector when impulsive torques are applied to the satellite. The wobble couples motion between roll and yaw at the nutation period (between 500 and 2000 seconds, depending on specific satellite moments of inertia and the biased momentum magnitude). The nutation period is low with respect to control loop frequencies and the control loop will respond to nutation. This problem is compounded with a hydrazine subsystem which controls attitudes by short pulses. The problem is to ensure that the pulse train does not become synchronized with the nutation period and cause a growing or diverging nutation motion. The problem has been thoroughly studied and solutions are available, but nutation damping is an added expense in terms of analysis costs and electronic hardware implementation. Ion propulsion causes fewer nutation problems since the thrust intervals are long with respect to the nutation period. Section 3.2.3.3 describes how pointing accuracy can be improved and nutation controlled simultanesouly by thrusting integral multiples of the nutation period.

There are control loop stability concerns relating to flexible bending modes. The thrusting action of the propulsion subsystem can excite bending modes. If the thrust pulses are synchronized with the bending modes, the bending amplitudes will grow until limited by structural damping. It is of such concern that the control loop is designed insensitive to bending frequencies and the controlling action will not sense the resonances and

respond in an undesirable fashion. This can be done for geosynchronous satellites since bending modes are generally greater than 1/4 Hz and control loop responses can be much less. Gain stabilization is provided. This is easier than trying to tune the control system to damp the bending motions due to the inaccuracies of being able to precisely predict the bending frequencies.

Hydrazine subsystems introduce a different problem. For certain worst case disturbances, it is possible for the thrust pulses to be resonant with bending (even though the control loop is not sensing the bending motion). The peak oscillations are limited by the period of time the particular disturbance exists, thruster torque levels, and structural damping. Since the disturbance levels and structural damping are areas of great uncertainty, hydrazine propulsion subsystems typically create much concern over bending stability. Ion propulsion has none of these problems since it is not pulse modulated and its low frequency control loop will not respond to bending frequencies (there is no source for pumping the resonances, as with hydrazine).

3.2.3.5 AVCS Conclusions

Ion propulsion interactions with the AVCS have shown improved pointing accuracy because of the low, vectorable torques available, improved stability because of distributed thrusting (rather than small pulses which can excite resonances), and no nutation build up because engine pulses are long compared to the spacecraft nutation period. Since maneuvers are performed twice a day, stationkeeping accuracy is much better than 0.1 degree and is only limited by orbital determination accuracy. Transient pointing errors of less than 0.04 degree are predicted from computer simulation results for this mission.

3.2.4 Electrical Power Sources

The basic strategy for supplying electric power to the Advanced Communications Satellite ion propulsion subsystem is as follows:

(1) For the first few years, use the excess power in the load and battery charge solar arrays

(2) When the array power degrades and there is little excess, start using the batteries when they are not supplying the spacecraft load

This strategy was developed by TRW in a study for Intelsat, using advanced nickel-hydrogen batteries (reference 10).

In the present study, it was shown that the same strategy can be used with nickel-cadmium batteries for the Advanced Communications Satellite mission. This allows the spacecraft designer to use the standard Intelsat V batteries. Nickel-cadmium batteries have a long history of successful service in low-earth and geosynchronous orbits.

3.2.4.1 Electric Power Subsystem Configuration

The electric power subsystem configuration used as a baseline for analysis of both missions is shown in Figure 17. The charge controls for one of its batteries are shown in detail in Figure 18. The baseline subsystem contains north and south solar arrays (each containing charge and load array sections), two or more nickel-cadmium batteries, and a power control unit. A shunt limiter may be required for control of voltage excursions at the input of the thruster power processors, depending upon which option is selected for the electrical interface between the ion propulsion subsystem and the spacecraft electric power subsystem. This is discussed in Section 3.2.4.2.

Each solar array-battery combination supplies an independent unregulated load bus. The load buses may be interconnected by ground command. For Mission 1, all switches are actuated by ground command, thereby avoiding the complexity of automatic controls.

The batteries are normally disconnected from the load bus during charging because the load bus voltage falls below the voltage of the charged batterie as the solar array degrades. The end-of-life steady-state array voltage at maximum power is approximately 30 volts in comparison to a maximum battery voltage of approximately 40 volts.

A battery tap ensures continuous power availability to the loads during the transition from solar array power to battery power upon entry into eclipse, and in the presence of transient loads which may exceed the array capability. Upon entry into eclipse, the bus voltage falls as array illumination decreases. Eventually, the battery discharges through its tap to support the loads. Upon closure of the discharge contactor, the bus voltage rises to the full battery level.

ORIGINAL PAGE IS
OF POOR QUALITY

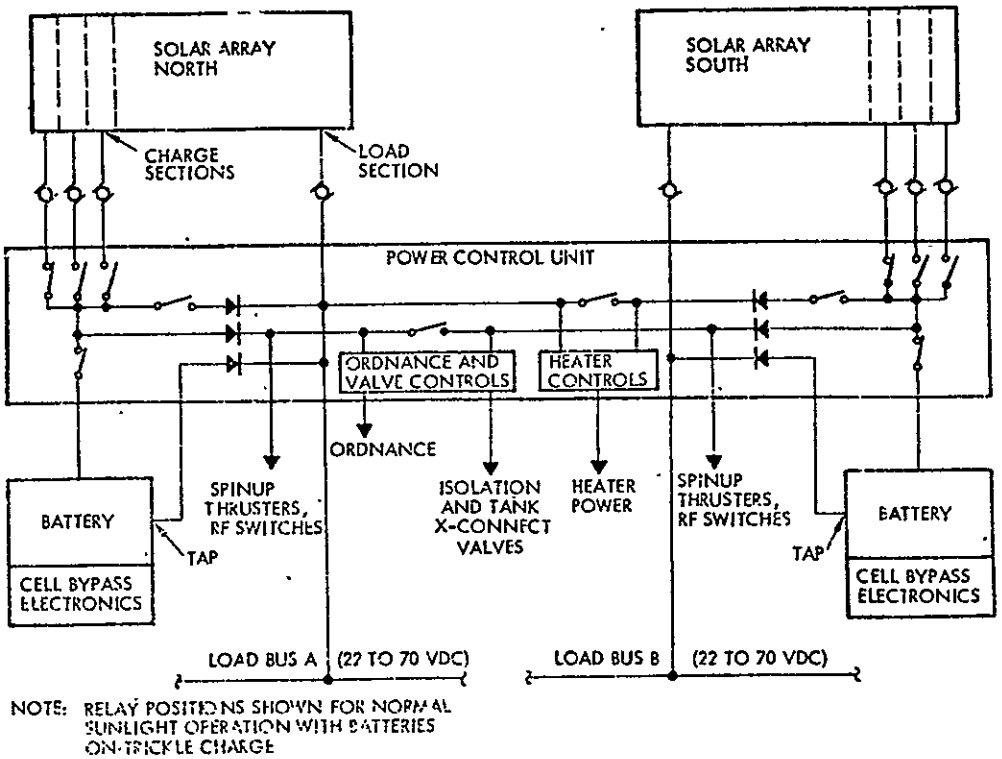

Figure 17. Advanced Communications Satellite Electric Power Subsystem

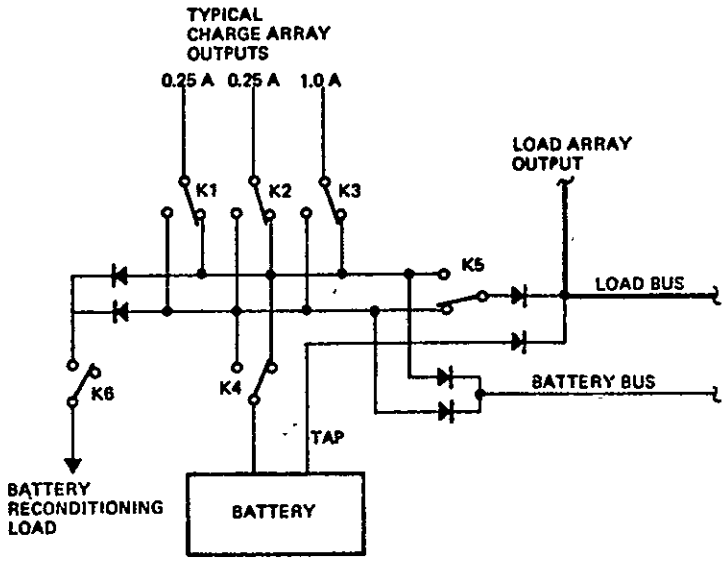

- RELAYS SHOWN IN NORMAL HIGH-RATE CHARGE MODE
- HIGH-RATE CHARGE SELECTION = 0.5, 1.0, 1.25, 1.50 A
- TRICKLE CHARGE RATE = 0.25 A (K1 OR K2)
- BATTERY TAP TO SUPPLY DISCHARGE POWER UNTIL COMMAND K4 OR K5 TRANSFER
- RELAYS OPERATE BY COMMAND ONLY

Figure 18. Typical Battery Controls

At eclipse exit, the solar array back-biases the battery discharge diode and assumes the full load at a voltage determined by the intersection of the load and array current-voltage characteristics. For a new array at minimum temperature (approximately -170°C) this is 70 to 75 volts. As the solar array warms to normal sunlight temperature, the bus voltage decreases to a steady-state level. If desired, the bus voltage excursion can be mitigated by leaving the solar array disconnected from the bus for a few minutes after eclipse exit. The battery must then be sized to provide this additional discharge.

Each battery is charged directly from combinations of dedicated charge array sections. Normal full charge of nickel-cadmium batteries is performed with combinations of charge array sections which provide a current corresponding to a 15-hour rate at the end of 7 years. When approximately 115% of the discharge capacity has been returned, the charge current is reduced by command to a trickle rate in the vicinity of 80 to 120 hours.

Charge array sections not connected to the battery automatically contribute power to the load bus at its operating voltage, as shown in Figure 18. This feature is utilized during thruster operation to reduce the magnitude of the increment which must otherwise be added to the power source to support the increased electrical load.

3.2.4.2 Integration of Power Processor with Spacecraft Power Sources

Two power sources are required for the 8-cm thruster power processor presently being developed by Hughes for NASA-LeRC. As described in reference 4, these are:

(1) 70 ±20 Vdc for the main thruster operation
(2) 28 ±1 Vdc of auxiliary power

Neither of the voltages are standard in the present or planned spacecraft for communications applications. Therefore, three design options were considered to make the two subsystems compatible:

Option 1: Add a dedicated 70-volt solar array to the spacecraft, plus dc-dc converters from the spacecraft bus for the auxiliary control power.

Option 2: Add boost line regulators and dc-dc converters to the standard spacecraft bus

Option 3: Modify the ion propulsion subsystem power processors to operate directly from an unregulated 28-volt input

Option 1 – Dedicated 70 Vdc Solar Array

Figure 19 presents the electric power subsystem diagram for Option 1, where a dedicated 70-volt solar array is used to supply power directly to the power processor and ion engine. Four power processors and ion engines are used. A redundant dc-dc converter is used to provide 28-volt regulated power to the different ion engine/power processors.

The characteristics and design impacts of Option 1 are:

- A fault clearing network must be developed (within existing technology, 0.34 kg (0.75 lb) weight penalty).
- Requires a 28-volt dc-dc converter to supply 16.8 watts of auxiliary control power for power processors (penalty of 1.8 kg (4.0 lb), 350 parts, and 4 watts)
- Extra weight penalty incurred for the dedicated 70-volt solar array (13.2 kg (29 lb) weight penalty).

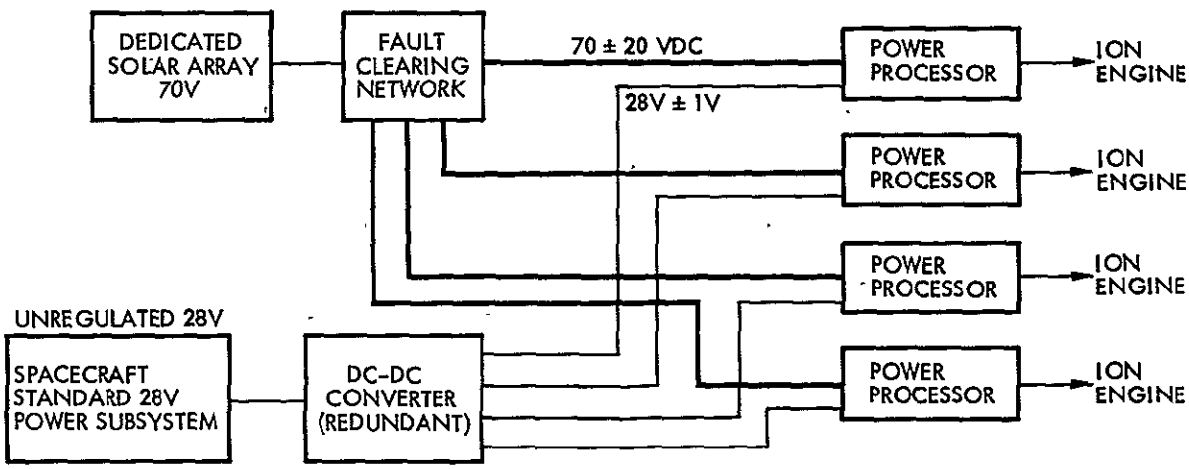

Figure 19. Option 1 – Dedicated 70 Vdc Solar Array for Electric Propulsion

Option 2 – Boost Line Regulators

Figure 20 presents the electric power subsystem diagram for Option 2, where the standard spacecraft power bus is used for the electric propulsion subsystem. DC-DC boost regulators are used to step up the standard 28 Vdc bus to a 55-volt bus at the ion engine power processor. To optimize the ion engine power processor efficiency, 55 volts was chosen since the

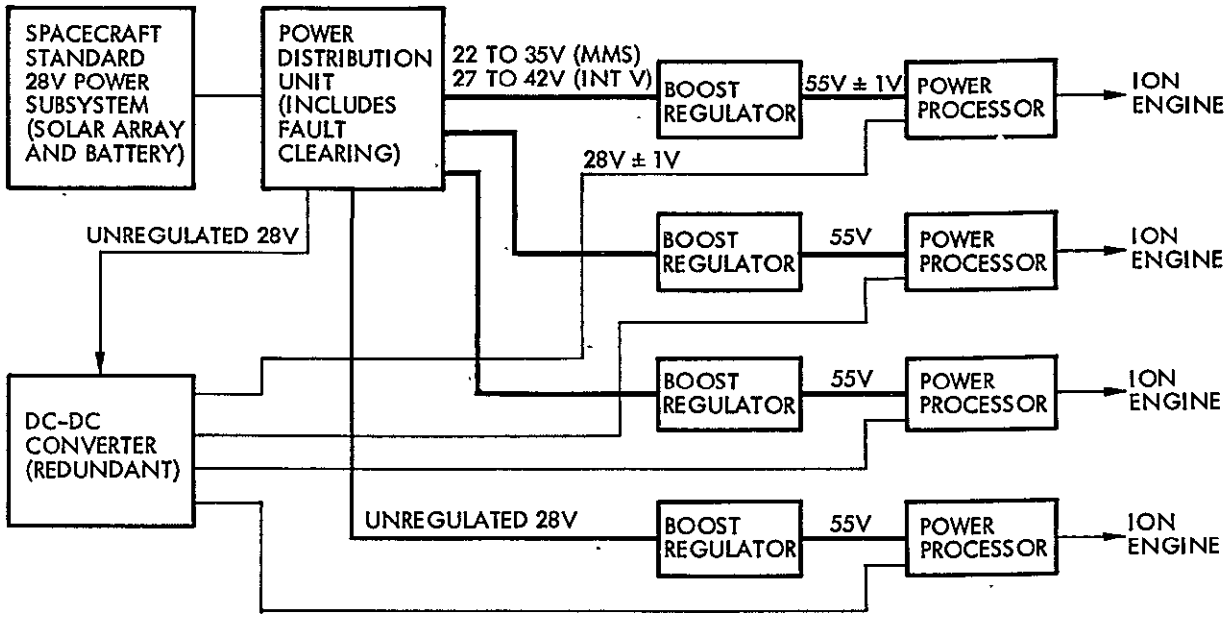

Figure 20. Option 2 – Add Boost Regulators to Standard 28-Volt Spacecraft Bus

power processor is capable of operation between 50- and 90-volt inputs. The 55-volt output also reduces the weight of the boost regulator. A redundant dc-dc converter is used to provide regulated 28-volt power to the power processor.

The characteristics of the boost regulator are summarized in Table 17 and described in detail in Appendix B.

This option can be implemented at a reasonable cost, although a total of about 1400 parts will be added in the boost regulators and converters.

Option 3 – Modify Power Processor

Figure 21 presents the block diagram for Option 3, where the ion engine power processor is redesigned to operate directly from the unregulated 28 Vdc power bus.

The basic design changes necessary for the power processor to operate at a lower dc input voltage and the penalties involved in the redesign are:

- Power transistors will have twice the present collector current
- Power transformers must be redesigned with new turns ratio
- Input filters redesigned for twice ac current ripple

Table 17. Characteristics of Boost Regulator

• Output Power	175 watts
• Input Voltage	27-40 volts (Intelsat V) 22-35 volts (MMS)
• Output Voltage	55 volts
• Efficiency	94%
• Weight (packaged)	1.4 kg (3 lb) 5.5 kg (12 lb) total for subsystem
• Parts Count	260 each
• No input/output ground isolation	

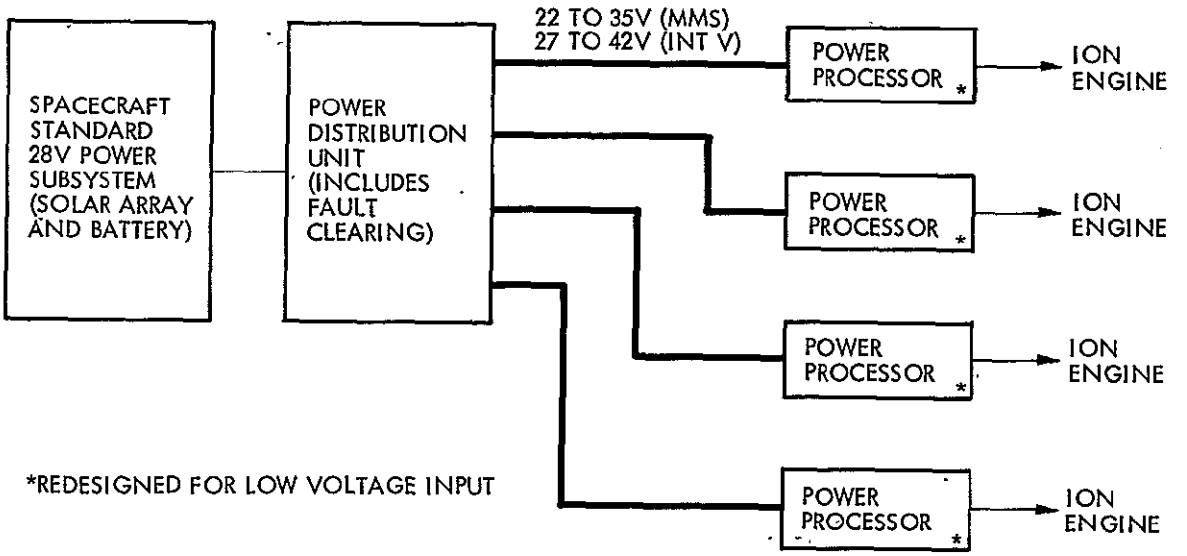

Figure 21. Option 3 — Modify Power Processor to Operate from Standard 28-Volt Power Subsystem

- Auxiliary power redesigned to accept unregulated dc
- Penalty of 1.0 kg (2.2 lb) each and 2% efficiency
- Parts count remains the same (no change in reliability)

Design changes are required in the power switching transistor due to higher current, the power transformer and its higher turns ratio and therefore higher reflected transformer capacitance, and the input filtering to meet the spacecraft electromagnetic interference specification limit.

Option Comparison

An overall comparison of the proposed three power subsystem options is shown in Table 18.

Option 1 (dedicated 70-volt array) carries a weight penalty of about 16 kg (34 pounds) since it does not permit sharing the main array. Option 3 has the lowest weight penalty (about 4 kg—9 pounds) and no increase in parts count, but it would be very expensive to implement.

Option 2 was chosen for further consideration in the study. Option 2 has a weight penalty of 7.3 kg (16 pounds), mostly for the boost regulators, an efficiency reduction of 7%, and will add about 1400 parts.

3.2.4.3 Analysis of Power Source Requirements

The spacecraft load power, P_{sc}, is the sum of the power requirements for each of the following subsystems:

- Communications
- Command, telemetry, and ranging
- Attitude and velocity control
- Propulsion (exclusive of thruster requirements)
- Thermal
- Electrical power distribution (exclusive of battery charge requirements)

P_{sc} remains essentially constant as the seasons change, although small differences may actually exist due to variations in heater power requirements. A 5% contingency is added to P_{sc} for analytical purposes and it is assumed that the solar array is sized to provide a power output at the end of 7 years of at least 110% of the satellite load power requirements.

For a body-stabilized spacecraft in a geosynchronous orbit with a nominal 1160-watt load array section output at equinox after 7 years, it is assumed that $1.1\ (1.05\ P_{sc}) = 1160$ watts, resulting in $P_{sc} = 1004.3$ watts.

Table 18. Comparison of Proposed Options for Electrical Interface Between Ion Propulsion Subsystem and Spacecraft

Option	Weight Increase		Efficiency Change	Parts Count Change	Relative Cost
	lb	kg			
(1) High voltage solar array	33.5*	15.5	-1%	+350 parts (redundant unit)	High
(2) Boost line regulators	16	7.3	-7%	+1040 parts (boost regulator) +350 parts (28 V converters redundant)	Low
(3) Redesign power processors	8.8	4.0	-2%	0	High

*Power subsystem array weight penalty of 13.1 kg (28.7 lb) included.

The analysis of power source requirements for the Mission 1 satellite is based on the following assumptions:

- Two thrusters fire simultaneously 4 hours per day, 365 mission days per year.
- Each thruster requires 220 watts of dc power at the input to its power processor.
- Boost regulators are added to the standard 28-volt spacecraft bus to transform power to the 70-volt input voltage level of the thruster power processors.
- Boost regulator efficiency is 94%.
- Nickel-cadmium batteries are utilized, with a maximum depth-of-discharge of 70% of rated capacity.

It is not necessary to add a shunt limiter to the baseline subsystem. The input to the boost regulator is constrained to a range of approximately 27 to 42 volts by delaying the connection of the load array to the load bus until the eclipse-exit solar array voltage transient has subsided.

Table 19 summarizes the in-orbit output power capability of the solar array sections of the Mission 1 satellite as a function of mission year. The output of the solar cells degrades with time in orbit due to radiation effects. This effect is reduced by careful design of the cell, its cover slide and the

Table 19. Mission 1 Solar Array Power Capability (watts)

Array	Nominal Operating Voltage (volts)	Season	Mission Year			
			0	3	5	7
Load	30	Equinox	1684	1318	1234	1167
		S. Solstice	1592	1246	1172	1112
Total Charge	40	Equinox	501	392	367	347
		S. Solstice	473	370	348	330
Total		Equinox	2185	1710	1601	1514
		S. Solstice	2065	1616	1520	1442

adhesive. Even so, the array power degradation over 7 years is on the order of 30%, as indicated in Table 19.

The solar array must be able to supply the required power all during the mission. Therefore, it is sized for end-of-life conditions. This means the array has the capability to supply extra power in the early years of the mission. It is this excess array power which is used to power the ion thrusters for the first few years of the mission. When there is no direct capability from the arrays, the batteries are used.

The table reflects the sizing of the solar array for P_{sc} = 1004 watts and without an added array increment to account for the thruster power requirement. Instead, an analysis of the impact of thruster programming on the size of the satellite power sources (performed as described in reference 10 under the section entitled "Battery Powered Thrusters") showed that the nickel-cadmium batteries had sufficient additional equivalent cycle life capability to support the thruster loads with no increase in their size. A summary of the highlights of the analysis procedure is given in the following paragraphs.

Array power capability varies sinusoidally as the seasons change. For the purpose of analysis, simplifying assumptions are made that, at the same mission point, the power output of the array is identical at the two equinoxes, and that the output at winter solstice is equivalent to that obtained at summer solstice. The average battery depth-of-discharge mission-time profile is then simply the average of the calculated equinox and summer solstice values. Stated differently, since thruster operation is performed during the equinox season, the effective depth-of-discharge reached at a particular mission point as a result of thrusting, d_T, is the average of the depth-of-discharge reached during equinox (d_{T_e}) and summer solstice ($d_{T_{ss}}$), subject only to the operational constraint that thrusting not occur during the 2-hour period immediately following the end of the satellite eclipse period. This constraint is imposed to ensure that the maximum depth-of-discharge limit of 70% is not exceeded.

Table 20 summarizes the values of d_{T_e}, $d_{T_{ss}}$, and d_T calculated as a function of mission year. Averaging the effective depth-of-discharge (d_T)

Table 20. Mission 1 Battery Depth of Discharge as a Function of Mission Year

Mission Year	(Fraction of rated capacity)		
	d_{T_e}	$d_{T_{ss}}$	d_T
0	0	0	0
3	0	0	0
5	0	0.076	0.038
5.55	0	0.187	0.094
7	0.113	0.256	0.185

mission-time profile shown in Table 20 over the corresponding number of discharge-charge cycles yields $\bar{d}_T = 0.086$. The number of discharge cycles is $N_{\bar{d}_T} = 1095$.

The next step in the analysis is the conversion of the effective depth-of-discharge mission-time profile to a profile equivalent to equinox-season cycling to the maximum allowable depth-of-discharge. The maximum allowable depth-of-discharge is taken as the design limit for equinox season cycling. This is nominally 0.7 for nickel-cadmium batteries. Reference 11 presents data from two accelerated geosynchronous orbit nickel-cadmium battery cycling tests conducted by TRW which provide background and justification for the selection of this depth-of-discharge limit. The battery configuration assumed is similar to the tested battery in that it contains cell protection circuitry which results in cell-level rather than battery-level redundancy.

It is assumed appropriate to maintain ampere-hour equivalency between the total capacity discharged throughout the effective mission-time profile and the total capacity discharged during equivalent equinox season cycling. With a nickel-cadmium battery system, this approach would be representative of the tendency of active material in the cadmium electrode to become permanently electrochemically unavailable (due to solubility, migratory or morphological processes) as the total time spent at a deeply discharged state increases.

The accelerated life test conducted by TRW simulated the eclipse season discharge-charge profile. The profile produces an average depth-of-discharge of 0.584 over the 45-day eclipse season when the maximum depth-of-discharge is limited to 0.7. Based upon the ampere-hour equivalency assumption discussed previously, the number of equivalent discharge-charge cycles (N_e) with an average depth-of-discharge of 0.584 is obtained from

$$N_e = \frac{\overline{d}_T}{0.584} N_{\overline{d}_T} \tag{9}$$

Substitution of previously-calculated values of $\overline{d}_T$ and $N_{\overline{d}_T}$ into the expression yields $N_e = 162$. Since the total number of expected cycles equals N_e plus 630 eclipse season cycles (7-year mission) plus 40 (an estimate) prelaunch cycles, it follows that the nickel-cadmium system must be capable of providing a minimum of 832 discharge-charge cycles to a maximum depth-of-discharge of 0.7.

Reference 12 is the traditional source for cycle life data (circa 1972) on nickel-cadmium batteries. It indicates that with a 70% depth-of-discharge a nominal capability of approximately 550 cycles can be expected. However, data from TRW's accelerated battery test at 73% shows over 1400 discharge-charge cycles have been experienced with little discharge voltage or capacity degradation (Reference 11). It is concluded that for conditions of this design case, the nickel-cadmium battery system has sufficient capability to support the additional discharge profile introduced by the ion thrusters with no increase in battery size or in solar array size.

3.2.5 Thermal Control

Most of the ion propulsion subsystem equipment for Mission 1 is located within the spacecraft central body, as shown in Figure 9 (section 3.2.2). Here temperature control is performed by the central spacecraft thermal control subsystem and the ion propulsion equipment should not tax its capacity.

The critical thermal integration consideration is for equipment located external to the central body. This is not a problem for the ion thrusters and

gimbals, but could be if the mercury propellant reservoirs are externally mounted. Mounting these tanks externally reduces the interference with other internal equipment, especially if the hydrazine propellant subsystem is not removed.

A simple thermal control concept has been developed to keep the propellant temperature within the allowable range of -5° to $+75^{\circ}$C. The tank has an insulation blanket consisting of 10 layers of 1/4-mil aluminized Teflon* with a 2-mil outer layer. In addition, the tank is thermally isolated from the spacecraft structure. These features ensure that the 75°C maximum temperature is not exceeded. The average temperature in sunlight is estimated to be $+35^{\circ}$C.

The 5-watt heaters are required for each external tank when there is no solar illumination. The heaters are turned off in sunlight.

3.2.6 Net Mass Savings with Ion Propulsion for Mission 1

An important reason to use ion thrusters for auxiliary propulsion applications is that they provide a significant mass savings over hydrazine thruster

To quantify the possible savings, Table 21 shows the mass properties of a hydrazine propulsion subsystem for a 1000-kg spacecraft as scaled up from the subsystem for the 939-kg Intelsat V, and the equipment required to perform the same functions with ion propulsion. In addition to the ion propulsion subsystem, provision is included for boost line regulators and converters as well as the additional support structure. No additional array is required for this mission.

The net mass available for additional payload with ion propulsion is 108 kg (237 lb) when the hydrazine subsystem is completely replaced.** It should be noted that Intelsat V uses electrothermally heated hydrazine, which has a much higher specific impulse than ordinary hydrazine. The savings noted are compared to the enhanced hydrazine subsystem.

---

*Trade name, DuPont

**A reliability/weight tradeoff is presented in Section 3.2.7.

Table 21. Additional Payload Mass Available with Ion Propulsion on Advanced Communications Satellite (1000 kg)

		kg	lb
With hydrazine			
Propulsion subsystem (electrothermal thrusters)	Dry	32	71.4
	Propellant	181	398.9
Total Mass Removable		213	470.3
With ion propulsion			
Ion propulsion subsystem	Dry	74	162.3
	Propellant	20	44.1
Boost line regulators and converter		7	16.0
Support structure		5	10.7
Subtotal		106	233.1
Mass Available for Additional Payload		108	237.2

If the hydrazine subsystem is retained on the spacecraft for initial station positioning and acquisition, about 29 kg of propellant will be required. A net mass savings of 46 kg (101 lb) is still possible by using ion propulsion for the other functions.

3.2.7 Reliability Analyses

3.2.7.1 Summary and Block Diagrams

Reliability analysis results for four candidate ion propulsion subsystem configurations are summarized in Table 22. Due to the scarcity of good failure rate data for mercury ion thrusters, all reliability assessments have been calculated for several assumed thruster failure rates. Currently available data indicate that an appropriate failure rate for the NASA-LeRC 8-cm mercury thruster lies somewhere in the range of 2500 to 25,000 bits (failures per billion hours), with 10,000 bits as a reasonable "most likely" value.

Table 22. Summary of Ion Propulsion Subsystem Reliability Assessments for Advanced Communications Satellite

Configuration	Reliability at 7 Years		
	Assuming Thruster λ = 2500	Assuming Thruster λ = 10,000	Assuming Thruster λ = 25,000
Non-Redundant	0.91671	0.83506	0.64731
Cross-Strapped DCUs	0.93323	0.86036	0.67628
Redundant Thrusters at Each Location	0.94062	0.93409	0.90307
Redundant Thrusters and Cross-Strapped DCUs	0.95236	0.94751	0.92271

Reliability block diagrams for the four candidate subsystem configurations are shown in Figures 22 through 25. The block diagrams make use of the following notation:

DIU Digital interface unit

PEU Power electronics unit

PSU Power switching unit

DCU Digital control unit

CSU DCU switching unit

λ_a Active (operating) failure rate in bits (failures per billion hours)

λ_s Standby (dormant) failure rate in bits

As implied by Figure 22 for the nonredundant four-thruster configuration, a failure of any single thruster is noncatastrophic, as is the failure of both north thrusters or both south thrusters. Any other pair failures, as well as any failures of three or more thrusters will be catastrophic to the system.

The actual failure rate of each box in the block diagrams is a function of duty cycle at which it operates. For any given duty cycle, D (where

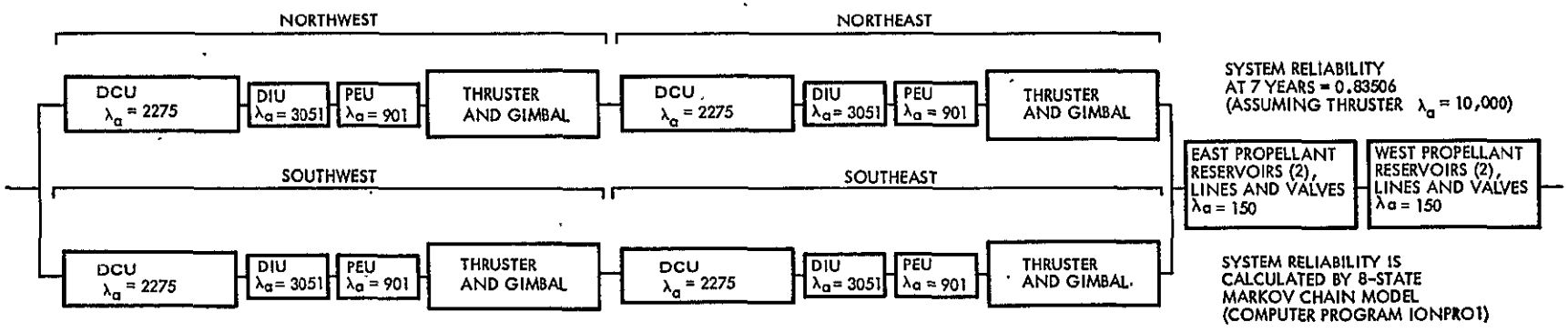

Figure 22. Reliability Block Diagram for Nonredundant Propulsion Configuration

ORIGINAL PAGE IS
OF POOR QUALITY

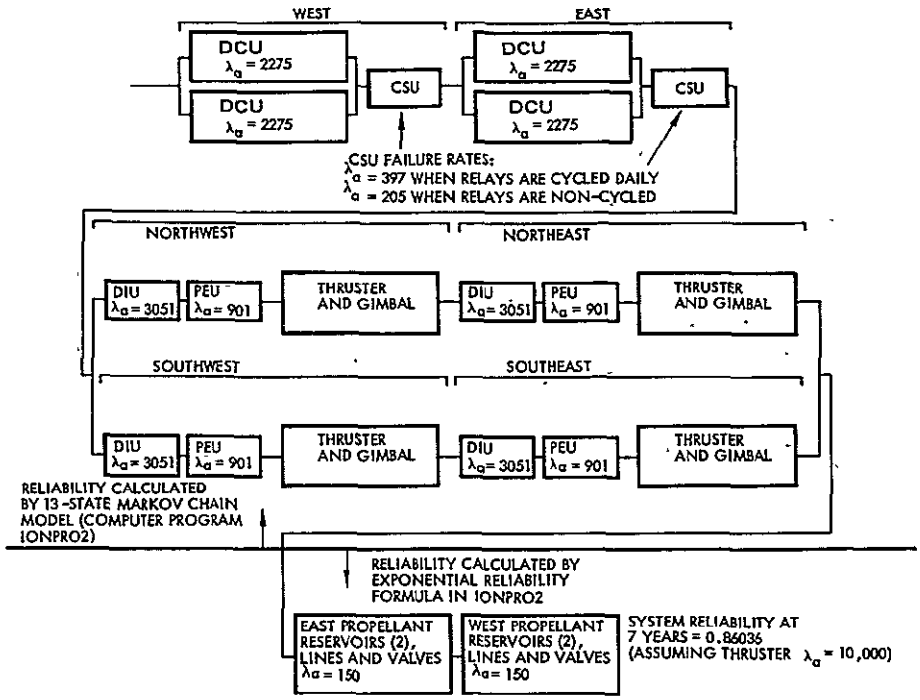

Figure 23. Reliability Block Diagram for Propulsion Configuration with Cross-Strapped DCUs

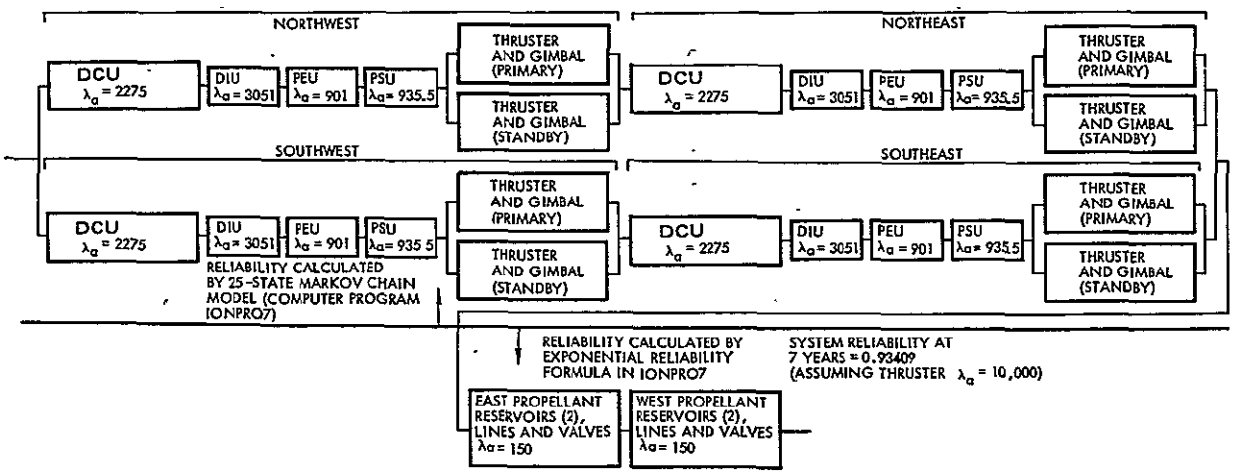

Figure 24. Reliability Block Diagram for Propulsion Configuration with Redundant Thrusters

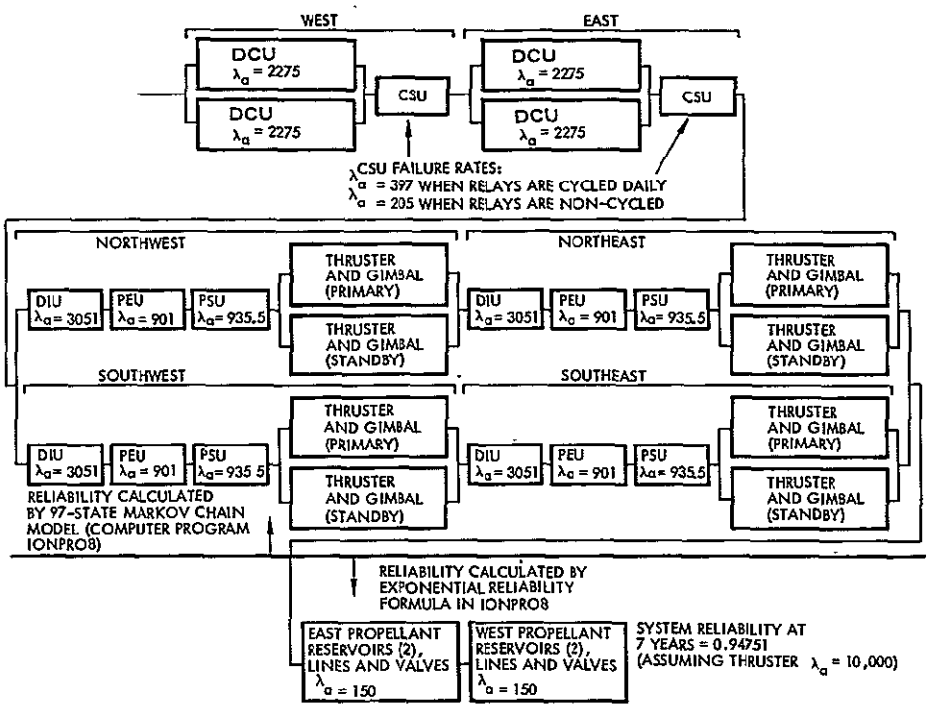

Figure 25. Reliability Block Diagram for Propulsion Configuration with Redundant Thrusters and Cross-Strapped DCUs

$0 \leq D \leq 1$), the box failure rate is calculated as a weighted average of the active and standby failure rates,

$$\lambda(D) = D\lambda_a + (1 - D)\lambda_s \tag{10}$$

Each DCU, DIU, PEU, and PSU is assumed to be duty cycled the same as its associated thruster (except that a small portion of each DCU's circuitry is assumed to be powered 100% of the time, to receive commands from the spacecraft). Each CSU is regarded as being powered whenever there is signal flow through it, and in addition its active failure rate is variable between two values depending on whether its relays are being cycled on a daily basis. Propellant reservoirs are assumed to be duty cycled 100% since they are pressurized all the time and experience no additional stress during times when the thrusters are operating.

The following relationships between standby and active failure rates are used:

- For all electronic equipment, $\lambda_s = 0.1\ \lambda_a$
- For thrusters, $\lambda_s = 0.05\ \lambda_a$
- For gimbals, $\lambda_s = 0.1\ \lambda_a$

The four candidate subsystem configurations involve two basic system designs (one with four thrusters, one with eight thrusters), together with an optional electronic cross-strapping arrangement for each basic design.

Pairwise north-south cross-strapping at the DCU-DIU interface can be accomplished by addition of the controller switching unit (CSU), a simple box which can be implemented by a few small, latching relays. One CSU would enable either DCU on the west side of the spacecraft to control both the northwest and southwest thrusters. Thus, the subsystem would be able to survive the failure of either of these DCUs with no loss of thrusting capability. An additional CSU for the two east DCUs provides the same redundancy for the northeast and southeast thrusters. This simple switching arrangement provides a significant increase in subsystem reliability, as shown in Table 22.

Subsystems incorporating eight thrusters appear to offer acceptable reliability along with significant weight savings relative to hydrazine subsystems. An eight-thruster subsystem consists of two thrusters (one primary plus one in standby) at each of the four locations on the spacecraft. A power switching unit (PSU) is required for each pair of redundant thrusters to permit a single PEU to operate either thruster of the redundant pair. The PSU would probably include ceramic vacuum relays to switch the high voltages involved, and thus appears to have a fairly high failure rate, but in most respects should be quite straightforward to implement. The vacuum relays currently qualified for spacecraft application are not magnetically latching. Thus, each PSU would require 12 to 18 watts to transfer to a standby thruster.

The last configuration studied combines the eight-thruster approach with the same DCU-DIU cross-strapping arrangement discussed previously. It enables the propulsion subsystem reliability to approach 0.95 at 7 years, for an assumed thruster rate of 10,000 bits. Table 23 shows the reliability

Table 23. Reliability Tradeoff Comparison (10,000 Bit Thruster Failure Rate, 7-year Mission)

Configuration	Reliability	Subsystem Dry Weight (lb)	Weight Available For Added Payload (lb)	(kg)
Nonredundant	0.835	162.3	237.2	108
Cross-strapped DCUs	0.860	163.5	236.0	107
Redundant thrusters	0.934	217.3	182.2	83
Redundant thrusters and cross-strapped DCUs	0.948	218.5	181.0	82

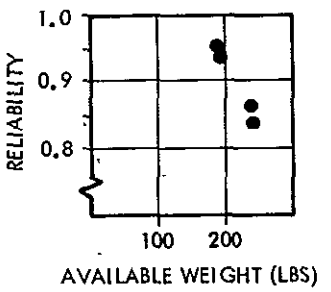

tradeoff comparison that was made for an assumed 10,000 bit thruster failure rate. The approximate weight available for added payload on the spacecraft is shown as a function of reliability for the candidate configurations. The thruster complement for the last configuration is shown schematically in Figure 26 (using nomenclature from Figure 8, Section 3.2.2). Its weight summary is given in Table 24.

Another possible eight-thruster configuration would be to provide eight dedicated PEUs and DIUs (i.e., one PEU and one DIU dedicated to each thruster, and with no power switching units). This candidate configuration was analyzed and found to have a reliability of 0.97005 at 7 years, assuming a thruster failure rate of 10,000 bits. However, this configuration was heavy compared to the others.

The reliability analyses were conducted under the assumption that the propulsion equipment was being qualified, and that internal configurational

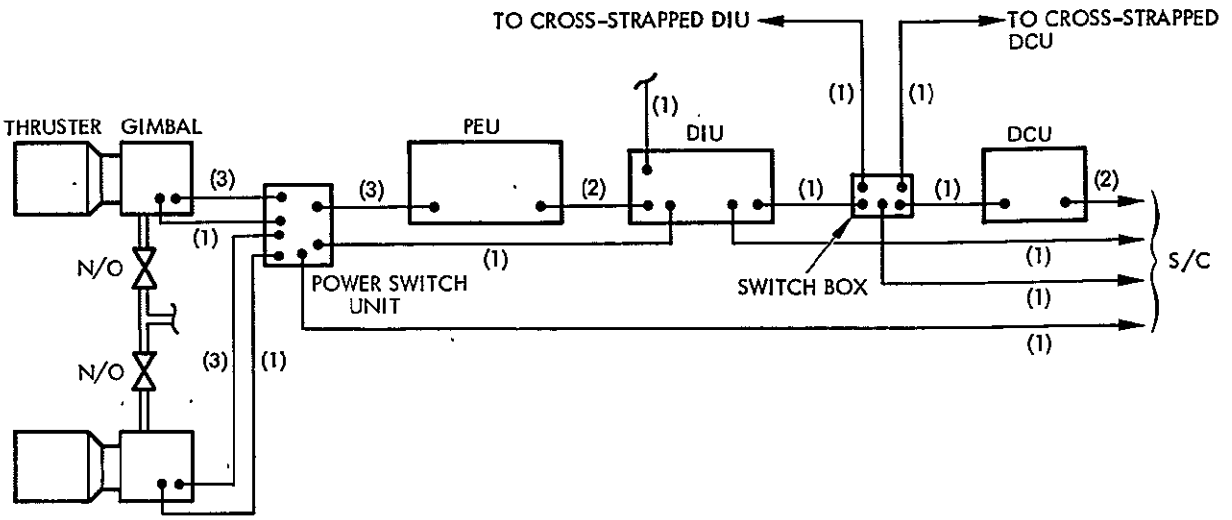

Figure 26. Propulsion Subsystem with Redundant Thrusters and Cross-Strapped DCUs

Table 24. Propulsion Subsystem Weight with Redundant Thrusters and Cross-Strapped DCUs

Hardware	Unit Weight (kg)	No. Required	Weight (kg)	Weight (lbm)
Thruster and gimbal assembly (a)	3.7	8	29.6	65.2
Reservoir (b)	1.2	4	4.8	10.6
Power electronics unit	7.0	4	28.0	61.7
Digital interface unit	3.2	4	12.8	28.2
Digital control unit	2.3	4	9.2	20.3
Squib valve	0.1	12	1.2	2.6
Filter	0.1	2	0.2	0.4
Propellant lines	---	2	(c)	---
Cables	---	86	5.8	12.8
Power switch unit	1.8	4	7.2	15.9
Controller switch unit	0.2	2	0.4	0.9
Total dry weight			99.2	218.5

(a) Includes temperature sensors

(b) Includes pressurant, fill valves, pressure sensor, temperature sensor

(c) Less than 0.1 kg

changes were too expensive to implement. It should be mentioned, however, that additional reliability improvements may be obtained by:

- Using one DCU (plus its redundant unit, if needed) for all thrusters. This eliminates several DCUs from the reliability chain.
- Eliminating noncritical functions in the electronics to reduce parts count and failure rates.
- Incorporating internal redundancy to reduce the effective failure rates of unreliable components.
- Increasing the propellant reservoir capacity to reduce the number of reservoirs needed.

3.2.7.2 Markov Models for Reliability Calculations

In calculating the reliability of systems shown in the block diagrams, it is not computationally valid to apply simple reliability models to each box and then multiply the box reliabilities across the block diagram in the usual manner. The difficulty arises from the fact that duty cycles at which each box operates (and therefore its failure rate) is dependent upon the good/failed status of other boxes in the system. This implies that box failure occurrences within the system are not statistically independent, the essential condition which makes multiplying box reliabilities across the diagram a valid procedure.

In order to accurately take into account the significant duty cycle and failure rate perturbations which result from failure occurrences, a Markov process model has been developed for each candidate system configuration. The Markov models developed for this study are of the discrete state, continuous time variety, sometimes referred to as continuous time Markov chains. Markov models of this type provide a means of analyzing the behavior of systems which can be regarded as always existing in one of several discrete states, and which are subject to random disturbances or hazards which cause the system to change states at unpredictable times. In Markov reliability models the states correspond to various numbers and kinds of failures, and the state transition probabilities are determined by the failure rates of the various parts of the system. Good textbook type material on Markov models is readily available.

The Markov model which has been developed for the nonredundant four-thruster system is shown in the state transition diagram of Figure 27. As the figure shows, each Markov state is a specific combination of thruster complement good/failed states, each thruster complement consisting of one thruster with its associated gimbal, PEU, DIU, and DCU. The letters G (good) and F (failed) are grouped in a north-south-east-west arrangement, with each letter pertaining to a specific thruster complement. This notation for Markov states is illustrated in Figure 28. As suggested in Figure 27, the system begins the mission in state 1, remains there for some random amount of time, then makes a transition into one of the single failure states (2, 3, 4 or 5), remains there for some random amount of time, then makes another transition, and so on. The reliability of the system, at any given time is the probability that the system has not entered state 8 by that time. Failure rate data for the various boxes of the system enter into the Markov model in the form of transition rates, denoted by A12, A13, ..., in Figure 27. The magnitudes of these transition rates define the state transition probabilities, as well as the probability distribution of the amount of time spent in each state. Since the transition rate between each pair of states may be specified independently, the dependency of box failure rates upon the good/failed status of other boxes is easily incorporated. Thus, the transition rates out of state 1 are calculated based on the pattern of duty cycles associated with thrusting at both nodes of the satellite orbit, while the transition rates out of states 2, 3, 4 and 5 are calculated per duty cycles associated with single node thrusting (with the attendant loss of thrusting efficiency taken into account).

Table 25 shows the daily hours of thruster operation required of each thruster for the Advanced Communications Satellite. These data are tabulated for each Markov state (i.e., for each noncatastrophic combination of failures) and thus show the thruster and electronic box operating time interactions resulting from failure occurrences. Thus, the duty cycle at which a given thruster and its associated electronics operate when in a given Markov state may be calculated by dividing the corresponding number in the table by 24. Since thrusters and their associated electronic boxes are at their active failure rates only during times when the thruster is operating, the failure

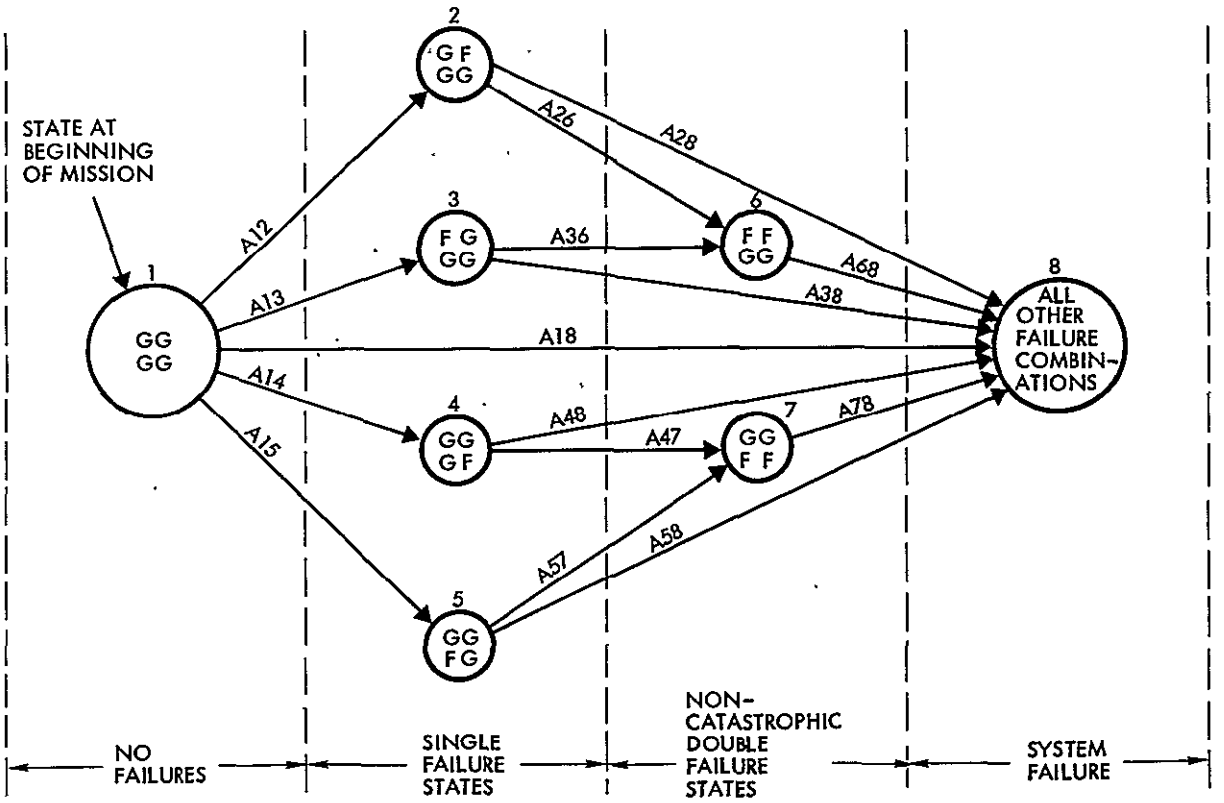

Figure 27. Markov State Transition Diagram for Nonredundant Propulsion Subsystem

G = GOOD

F = FAILED

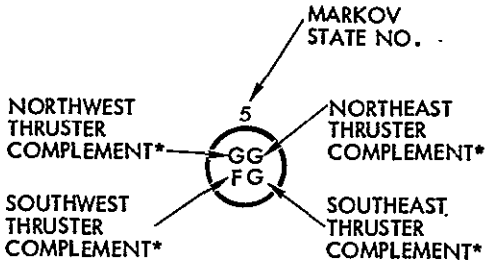

*INCLUDES THRUSTER. GIMBAL, PEU, DIU AND DCU

A12 = MARKOV TRANSITION RATE FROM STATE 1 TO STATE 2

= TOTAL FAILURE RATE (IN BITS) OF NORTHEAST THRUSTER COMPLEMENT WHEN DUTY-CYCLED IN ACCORDANCE WITH TWO-NODE THRUSTING

Aij, FOR ALL OTHER i AND j, ARE DEFINED SIMILARLY

Figure 28. Interpretation of Markov States

Table 25. Daily Hours of Thruster Operation for Advanced Communications Satellite with Ion Propulsion

System Markov State*	Thruster Hours per Day			
	Northeast	Northwest	Southeast	Southwest
1	2.695	2.483	2.695	2.483
2	(Failed)	0.167	5.80	5.30
3	0.167	(Failed)	5.80	5.30
4	5.80	5.30	(Failed)	0.167
5	5.80	5.30	0.167	(Failed)
6	(Failed)	(Failed)	5.883	5.383
7	5.883	5.383	(Failed)	(Failed)
8	SYSTEM FAILURE			

Assumption: Orbit is such that all east-west stationkeeping is performed by the east thrusters.

*This state numbering pertains to the system Markov model for the nonredundant configuration (see Figure 22). The data are also valid for all other configurations, with appropriate modifications to the state numbering.

rates of the various components of the system change in response to failure occurrences by amounts which are approximately proportional to the numbers shown in Table 25.

The transition rate data for a Markov model is normally presented in the form of a matrix in which the transition rate (failure rate) from state I to state J is contained in the row I, column J location of the matrix. The Markov transition rate matrix for the nonredundant configuration, assuming a thruster failure rate of 10,000 bits, is shown in Figure 29. A transition rate of 0 indicates an impossible single transition, although it may be possible to get from the row state to the column state in two or more transitions.

Beginning State \ Ending State	1	2	3	4	5	6	7	8
1	12749.2	3328.7	2895.9	3328.7	2895.9	0.0	0.0	300.0
2	0.0	11979.8	0.0	0.0	0.0	1744.8	0.0	10234.9
3	0.0	0.0	11979.8	0.0	0.0	1744.8	0.0	10234.9
4	0.0	0.0	0.0	11979.8	0.0	0.0	1744.8	10234.9
5	0.0	0.0	0.0	0.0	11979.8	0.0	1744.8	10234.9
6	0.0	0.0	0.0	0.0	0.0	10338.9	0.0	10338.9
7	0.0	0.0	0.0	0.0	0.0	0.0	10338.9	10338.9
8	0.0	0.0	0.0	0.0	0.0	0.0	0.0	0.0

*Based on an assumed thruster active failure rate of 10,000. bits.

Figure 29. Markov Transition Rate Matrix for Nonredundant Configuration

ORIGINAL PAGE IS
OF POOR QUALITY

The numbers on the main diagonal of the matrix have been calculated as the sum of all other transition rates in the corresponding rows of the matrix.

Systems of greater complexity having higher levels of redundancy and/or cross-strapping generally require larger Markov models (i.e., with greater numbers of states). Thus, while the Markov model for the nonredundant configuration has eight states, the Markov models for the other configurations have 13, 25 and 97 states.

Markov processes are defined mathematically by a system of linear, first-order differential equations. For an N-state model there are N differential equations in N unknown probability functions, and the Markov transition rates (e.g., Figure 29) define the coefficients of these differential equations. Reliability calculations are accomplished by solving these equations to obtain the system failure state probability as a function of time. In the model for the nonredundant configuration, state 8 represents system failure; therefore at any time, t, the reliability R(t) is simply $1 - P_8(t)$, where $P_8(t)$ is the probability that the system will be in state 8 at time t.

3.2.7.3 Failure Rate Data

The propulsion subsystem reliability assessments for this study were calculated parametrically over a range of assumed thruster failure rates. A brief investigation into currently available thruster life and failure rate data was conducted to provide a basis for choosing the range of assumed failure rates. The two sources of data will each be discussed:

> Electric Propulsion/Spacecraft Integration Study — This recent study by TRW for Intelsat contains an approach to thruster failure rate estimation based on a detailed, piece-by-piece analogy between the component parts of ion thrusters and traveling wave tubes (TWTs). Both components share manufacturing and electrical design factor similiarities. By considering the relative severity on the ion thruster as opposed to the TWT for each factor, an overall severity factor representing the factor by which a TWT failure rate must be weighed is obtained. This approach leads to a failure rate in the range of 4120 to 17,805 bits for 8-cm mercury ion thrusters.
>
> "Ion Propulsion Flight Experience, Life Tests, and Reliability Estimates" (reference 13) — This journal article develops thruster failure rates by estimating the failure rates of the thruster's component parts (including lengths of the welds, etc.) and adding up

the component failure rates. This has resulted in failure rate estimates for 5- and 30-cm mercury ion thrusters of 10,576 bits and 16,347 bits, respectively. These numbers, of course, represent active failure rates. The standby (dormant) failure rate of a thruster is taken to be 5% of the active failure rate.

The following active failure rates for the DIU and PEU have been obtained from the Hughes Failure Modes, Effects and Criticality Analysis (reference 14) for the 8-cm engineering model thruster system: DIU 3051 bits, and PEU 901 bits.

The DCU failure rate has been calculated based on the NASA-LeRC tabulation of part types and quantities, and has been found to be 2275 bits. This is shown in Table 26. The part failure rates used in this calculation have been adjusted downward somewhat based on the assumption that a moderate amount of internal redundancy exists in the DCU.

The following gimbal failure rates have been used:

λ_a = 450 when the thruster is doing both north-south and east-west stationkeeping

λ_a = 150 when the thruster is doing only north-south stationkeeping

The following reservoir failure rate has been used:

λ_a = 75

The following switching unit failure rates have been used:

λ_a = 205 for the CSU when the relays are not cycled

λ_a = 397 for the CSU when the relays are cycled daily

λ_a = 935 for the PSU

The gimbal, reservoir, and switching unit estimates were calculated on the basis of TRW failure rate data for flight hardware and of preliminary designs for the switching units.

Table 26. DCU Parts List and Failure Rate Calculation

Part Type	Quantity	Failure Rate per Part (bits)	Total Failure Rate (bits)
Microprocessor	1	935	935
RAM Memory	2	155	310
ROM Memory	4	118	472
Four-stage shift register (1/2)	1	45	45
Divide by 10 counter	1	105	105
Quad latch	2	35	70
Hex buffer	1	20	20
Fourteen-stage counter	1	136	136
Four-bit D type flip-flops	1	30	30
Eight input NOR gate	1	22	22
Quad 2-input and gate	1	20	20
Input optoisolator	1	20	20
Four MHz oscillator	1	70	70
Resistor network 1K ohm	1	10	10
Resistor network 22K ohm	1	10	10
		Total	2275

3.3 MISSION 2: HIGH-PERFORMANCE PROPULSION MODULE FOR THE MULTIMISSION MODULAR SPACECRAFT

In this section, the High Performance Propulsion Module is described and its performance assessed for two representative Multimission Modular Spacecraft (MMS) missions. The key spacecraft integration issues for Mission 2 are the interactions with the Attitude Control Subsystem Module, the electric power sources, and compatibility with both the MMS and the Space Transportation System (Shuttle). Special attention is given to these issues.

3.3.1 High-Performance Propulsion Module Description

The ion propulsion subsystem schematic for the two Multimission Modular Spacecraft applications identified in Section 3.1.3 is shown in Figure 30. It is quite similar to the one for the Advanced Communications Satellite (Mission 1). The only differences appear in the number of reservoirs and isolation valves needed to contain propellant for the two different missions.

The high-performance propulsion module meets all the interface requirements for any MMS propulsion actuation module. As shown in Figure 31, it is cylindrical and has a standard set of latch mechanism screws and alignment pins. It can be mounted at the "bottom" end of the MMS, or between the housekeeping modules and the payload. Specific design features of the high-performance propulsion module are outlined in the figure. Details for a low earth orbit mission configuration are shown in Figure 32. For the geosynchronous StormSat mission, all four thrusters are on one side of the module and protrude through the side of the cylinder.

The module contains four thrusters, which will be fired in pairs or alone. Two thrusters will be fired together at one node per day for north-south stationkeeping or continuously for orbit sustenance or orbit maneuvers. They will be gimballed and time-phased for attitude control and other maneuvers. The other pair are in standby redundancy; either pair can drain the propellant reservoirs.

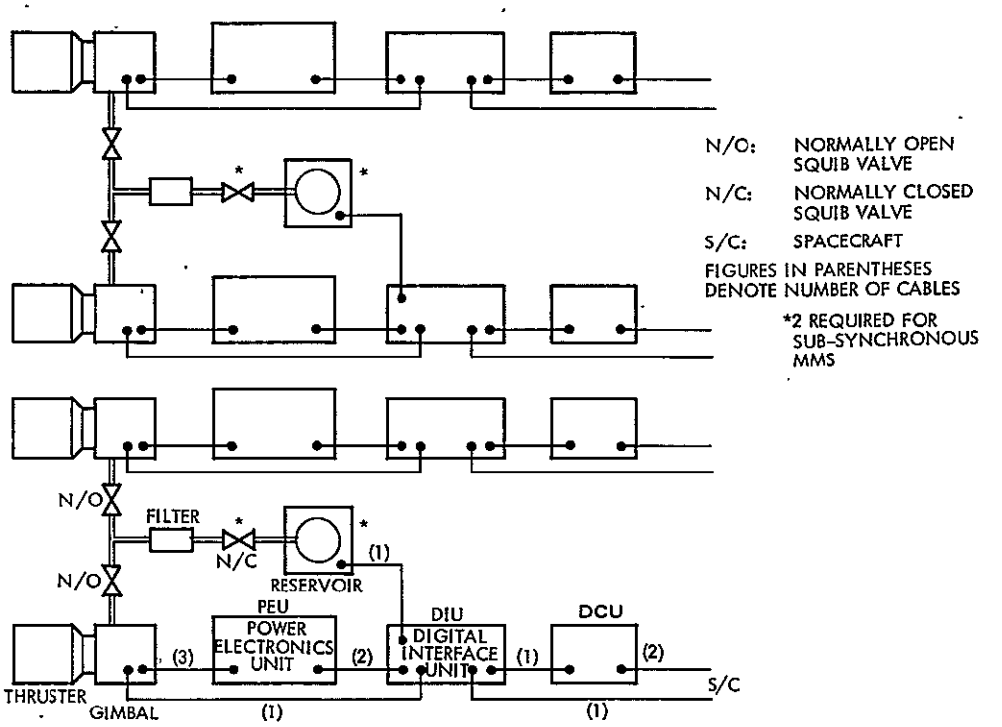

Figure 30. Ion Propulsion Subsystem Schematic for MMS Missions

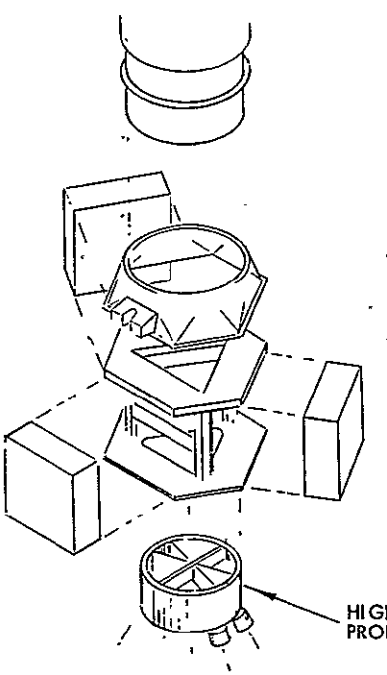

TOTAL NUMBER OF THRUSTERS	
NOMINAL THRUST LEVEL	1 MILLIPOUND EACH
SPECIFIC IMPULSE	>2500 SECONDS
TOTAL POWER REQUIRED	
OPERATING	400 WATTS
NON-OPERATING	20 WATTS
NOMINAL TOTAL IMPULSE (2 THRUSTERS)	6.4×10^5 NEWTON-SECONDS (144,000 POUND-SECONDS)
MODULE MASS	112 KG (247 LBS)
BASIC DIMENSIONS	50 INCH DIA. X 18 INCH LENGTH
INTERFACE	STANDARD MMS PATTERN

Figure 31. High-Performance Propulsion Module for Multimission Modular Spacecraft (MMS)

ORIGINAL PAGE IS
OF POOR QUALITY

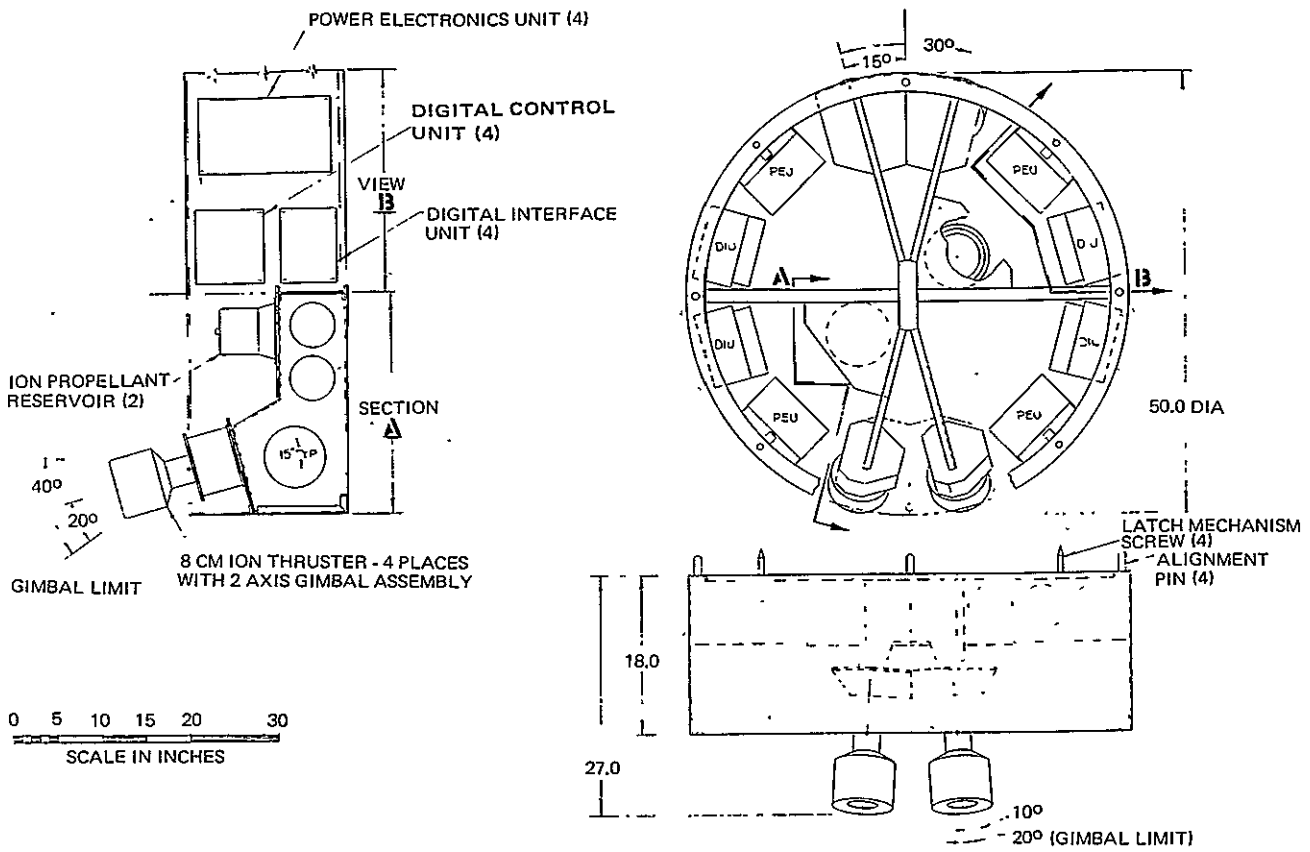

Figure 32. Layout of High Performance Propulsion Module with LandSat Configuration

The module in this form has enough propellant for two engines to thrust for 20,000 hours each. This is more than enough total impulse to satisfy any of the MMS missions under consideration. Propellant could be off-loaded for missions with lesser requirements.

The electrical interface problem with the MMS is similar to the one with the Advanced Communications Satellite (Mission 1). This was discussed in Section 3.2.4.2. The same solution, adding boost line regulations and dc-dc converters, has been used for Mission 2. With this solution, the propulsion subsystem electrical interface is the same as for Mission 1, shown in Table 9 (Section 3.2.2). The power requirements are also the same as for Mission 1.

The electrical interface with the satellite command and data handling subsystem is straightforward and does not require further comment. The

interfaces with the attitude control and power subsystems are discussed in more detail in Sections 3.3.3 and 3.3.4, respectively.

A spacecraft configuration for the geosynchronous StormSat mission is shown in Figure 33. Here the propulsion module must be located near the center of the spacecraft. For this application the four ion thrusters would protrude through the side of the module structure and all be located on the same side. The other equipment in the module can be easily shifted to accommodate this new thruster location.

Several factors have been considered to ensure that the high-performance propulsion module is compatible with the Space Transportation System (Shuttle). Some of the features in this area are:

- No single point failure will prevent retrieval of the spacecraft by the Shuttle. The spacecraft will go into a passive safehold mode which will allow retrieval.

- The propulsion module can be disconnected on orbit for servicing. The MMS is designed for on-orbit servicing and the complete propulsion module can be interchanged.

- The only module interface is with the rest of the spacecraft. There is no active tie to the Shuttle Orbiter or an upper stage. The module structure may be used as a structural load path, but this is a simple interface.

- There will be no mercury contamination of the Shuttle orbiter bay. The vaporizer and valves are designed so that two failures would have to occur before there would be spillage into the bay.

- The propulsion module is compatible with the Shuttle environment. Environmental data on the Shuttle Orbiter and/or upper stage will be used for detailed design of the module.

The short 0.46 meter (18 inch) length is a very attractive feature of the high-performance propulsion module (HPPM). This compares with more than 1.5 meters (5 feet) for the SPS-II Hydrazine propulsion module shown in reference 9. The pricing policy for the shuttle-launched spacecraft puts a premium on shorter-length spacecraft designs. At the currently quoted Shuttle launch price of $444,000 per foot of length, the HPPM could save $1-1/2 million per launch. Even if payloads are

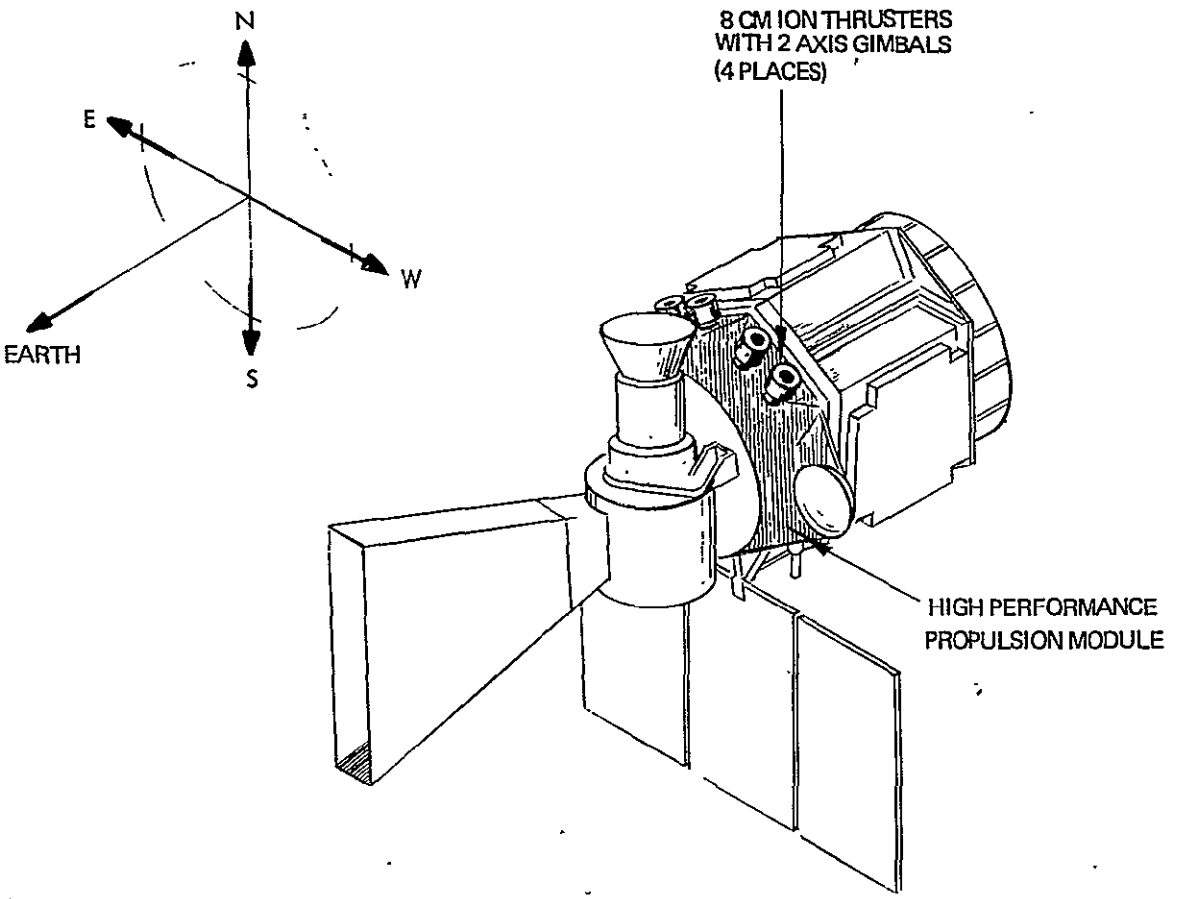

Figure 33. MMS StormSat Configuration with Ion Auxiliary Propulsion

launched side-by-side, the savings could be 3/4 million dollars per spacecraft. This is a significant factor above and beyond the weight savings possible from the use of ion propulsion.

The ion propulsion subsystem dry weight summaries for the geosynchronous and low earth orbit MSS missions are shown in Tables 27 and 28, respectively. The basic difference is that the low earth orbit configuration is sized to allow two engines to fire up to 20,000 hours each. This requires four reservoirs. Only two reservoirs, plus reduced lengths of lines and cables, are required for the geosynchronous mission. This is less than the Advanced Communications Satellite (Mission 1) requirement since the StormSat mission life is only 3 years, while it is 7 years for Mission 1.

Table 27. Ion Propulsion Subsystem Weight, Geosynchronous MMS Mission

HARDWARE	UNIT MASS (KG)	NO. REQ'D.	MASS (KG)	WT. (LBM)
THRUSTER AND GIMBAL ASSEMBLY (a)	3.7	4	14.8	32.6
RESERVOIR (b)	1.2	2	2.4	5.3
POWER ELECTRONICS UNIT	7.0	4	28.0	61.7
DIGITAL INTERFACE UNIT	3.2	4	12.8	28.2
DIGITAL CONTROL UNIT	2.3	4	9.2	20.3
SQUIB VALVE	0.1	6	0.6	1.3
FILTER	0.1	2	0.2	0.4
PROPELLANT LINES	---	2	(c)	----
CABLES	---	42	3.1	6.8
TOTAL DRY WEIGHT			71.1	156.6

(a) INCLUDES TEMPERATURE SENSORS

(b) INCLUDES PRESSURANT, FILL VALVES, PRESSURE SENSOR, TEMPERATURE SENSOR

(c) LESS THAN 0.1 KG

Table 28. Ion Propulsion Subsystem Weight, Low Earth Orbit MMS Mission

HARDWARE	UNIT MASS (KG)	NO. REQ'D.	MASS (KG)	WT. (LBM)
THRUSTER AND GIMBAL ASSEMBLY (a)	3.7	4	14.8	32.6
RESERVOIR (b)	1.2	4	4.8	10.6
POWER ELECTRONICS UNIT	7.0	4	28.0	61.7
DIGITAL INTERFACE UNIT	3.2	4	12.8	28.2
DIGITAL CONTROL UNIT	2.3	4	9.2	20.3
SQUIB VALVE	0.1	8	0.8	1.8
FILTER	0.1	2	0.2	0.4
PROPELLANT LINES	---	2	(c)	----
CABLES	---	44	3.1	6.8
TOTAL DRY WEIGHT			73.7	162.3

(a) INCLUDES TEMPERATURE SENSORS

(b) INCLUDES PRESSURANT, FILL VALVES, PRESSURE SENSOR, TEMPERATURE SENSOR

(c) LESS THAN 0.1 KG

3.3.2 Ion Propulsion Module Functions

The ion propulsion module on the MMS is used primarily for orbital corrections, such as stationkeeping or orbit change, where a large added velocity (Δv) is required. Ion propulsion also becomes an attractive vehicle for unloading wheel momentum and can be used for auxiliary control functions, such as acquisition and failure mode operation.

The fine level of control possible with ion propulsion permits it to be a backup to the reaction wheels for control of satellite pointing during an experiment. The ability of ion propulsion to provide stationkeeping or orbit sustenance with very low disturbances may be more significant than the weight savings resulting from the high specific impulse.

3.3.2.1 Geosynchronous Orbit MMS Mission

A representative MMS StormSat configuration using the high-performance propulsion module with ion engines was shown in Figure 33. The ion thrusters are oriented so that each thrust vector nominally points through the spacecraft center of mass. The pairs are symmetrically inclined with respect to the north-south axis by 15 to 30 degrees, depending on the spacecraft disturbance torque levels. The thrusters are oriented to point nominally through the center of mass, with a small cant angle to offset the solar pressure torques acting on the large solar array panel. The ion engines permit dumping of large amounts of momentum with very small propellant penalty. The various modes that ion propulsion may be used for on the geosynchronous MMS mission are discussed below. Note that the spacecraft is assumed to be orbited by the Space Shuttle and has no transfer orbit attitude control requirements.

Acquisition and Reacquisition

Acquisition with MMS is more efficient than with the Advanced Communications Satellite (Mission 1) because of three factors: (1) the tipoff rates from a Shuttle launch are smaller than the residual body rates due to despin experienced with expendable launch vehicle, (2) the spacecraft moments of inertia are lower, and (3) the MMS attitude control subsystem (ACS) is more sophisticated, with the equivalent of an inertial platform and elaborate computer-programmed search algorithms.

Acquisition with ion propulsion can be accomplished within several hours. Even though this is longer than is possible with hydrazine, it is acceptable. Two gimballed thrusters are fixed to provide sources of controllable torque.

Stationkeeping

On the geosynchronous MSS, north or south and east or west stationkeeping is performed only once per day, except when eclipse interferes with the operation. Two opposing thrusters are fired for north or south velocity increments (depending on satellite orientation). East or west velocity increments are achieved by turning off the west or east thruster near the end of a stationkeeping period. The thrusters fire approximately 5.3 hours per day. Firing starts with the thrusters vectored in a direction to minimize start-up torques.

For this mission, ion propulsion shows considerable advantage over hydrazine. The start-up transients from thruster misalignment are much smaller because of the lower thrust level and ability to produce very small torques. This advantage permits the consideration of performing experiments even during the stationkeeping maneuvers and maintaining the required attitude control. A single axis digital simulation was developed to study the transient magnitudes and is discussed in Section 3.3.3.3.

Momentum Dump

After the stationkeeping maneuver has started, the ion thrusters are gradually rotated in a direction which permits momentum wheel unloading. MMS currently is designed to use magnetic torquers or hydrazine thrusters to unload momentum. These are both unattractive for this application since the earth's magnetic field is undependable at geosynchronous orbit and hydrazine thrusters cause unacceptable attitude transients.

3.3.2.2 Low Earth Orbit MMS Mission

This class is representative of those scientific missions (earth pointing, or otherwise) which require an orbit altitude of 230 to 1000 miles with precisely controlled orbital parameters. Figure 34 shows a possible MMS configuration for this class of missions. Aerodynamic drag will cause the orbit to

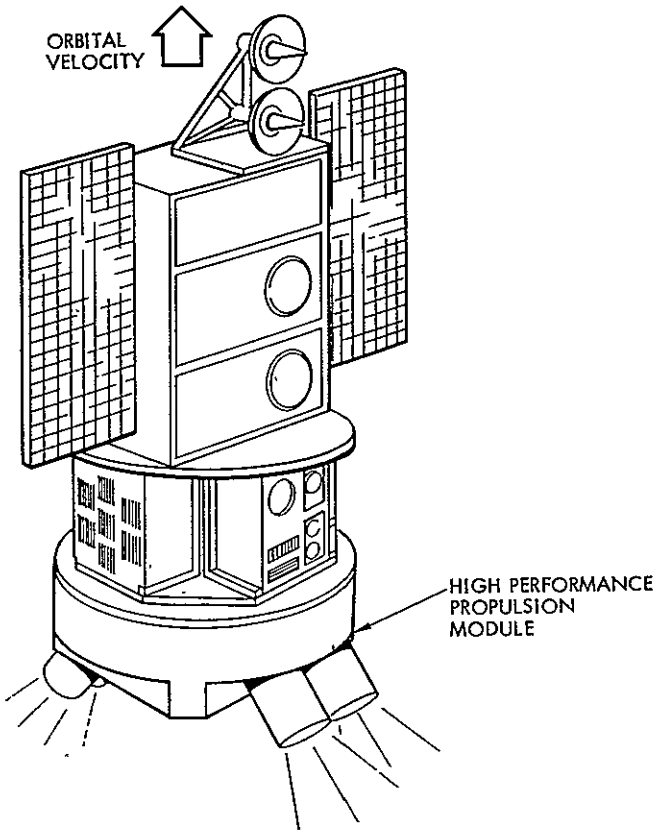

Figure 34. Possible Low Earth Orbit MMS Mission with Ion Propulsion

decay, especially at the lower end of the altitude range. Generally, orbital sustenance is not essential for mission completion, but it can simplify sensor data processing and may be highly desirable.

As with the geosynchronous mission, extremely tight experiment pointing is required. The ACS module is identical to the one used for the geosynchronous MMS. The propulsion subsystem is required to cycle much more frequently at this altitude because of the need for unloading the accumulated momentum of the wheels that the gravity gradient and aerodynamic disturbance torques create.

The layout of the propulsion module for the low earth orbit mission is shown in Figure 32. The thrusters are fired in pairs to produce a velocity increment along the bisecting line of the two thrusters and are differentially gimballed to produce the desired attitude control torques.

Acquisition and momentum dump for this mission are accomplished identically to the geosynchronous cases. The main function of the thrusters in low earth orbit is to achieve orbital control. This can be drag make-up or maneuvers to change orbits. The engines are intended to be fired continuously (or as continuously as possible) to achieve the desired velocity increment. The thrusters are symmetrically canted toward the bisecting vector or away from it to achieve the desired steady state acceleration. In this manner, a large range of steady state thrust levels can be achieved.

Continuous thrusting is desired because (1) this maintains high propellant efficiency since the weight penalty of continuous versus intermittent thrusting is small, (2) the 2-year mission life is easily met, (3) momentum dumping is continuously available, and (3) the number of thruster cycles is reduced. Momentum accumulation in low earth orbits is rapid due to the increased influences of gravity gradient, aerodynamic and magnetic disturbances.

3.3.3 Interactions with MMS Attitude Control Subsystem Module

The primary function of the MMS attitude control subsystem (ACS) is to orient and stabilize the spacecraft relative to a desired target. The basic approach applied to the ACS for the modular spacecraft has been to adapt proven techniques and, where possible, utilize flight qualified and/or NASA Low Cost Standard Office equipment. The basic control system element is an on-board computer that processes all sensor-derived information and, in conjunction with various types of stored information, generates the appropriate control signals to operate the reaction control devices. The on-board computer, which is shared with other spacecraft subsystems, is physically located in the communication and data handling (C&DH) module. The degree of flexibility provided by the on-board computer allows the use of a single ACS module design to meet the requirements of a diverse group of payloads with regard to both mission and configuration.

With the exception of coarse sun sensors on the solar array and mission-unique fine error sensors which may be incorporated in payload instruments, all control sensors are housed within the ACS module. The ACS includes the

reaction control devices that would be utilized during normal operations. These are the reaction wheels and magnetic torquers. Mass expulsion reaction control equipment, either ion engines or hydrazine, are housed within the propulsion/actuation module. The propulsion module should also be capable of accommodating large reaction wheels, large torquer bars and/or control moment gyros as may be necessary to complement the reaction control equipment in the ACS module for very large spacecraft with unique requirements.

Table 29 summarizes the significant ion thruster performance requirements for the two MMS missions used as examples. It can be seen that the NASA-LeRC 8-cm ion engine meets all the requirements.

Table 29. Ion Thruster Performance Requirements for MMS Missions

	Station Acquisition	N-S, E-W Stationkeeping	Orbit Maneuvers	Momentum Dump	Total
		Geosynchronous MMS*			
Number of cycles (total)	1	1,095	--	Included	1,095
Worst thruster	1	1,095	--	Included	1,095
Hours used (total)	.6	5,913	--	Included	5,914
Worst thruster	.6	5,913	--	Included	5,914
Propellant used (kg)	<.1	6.8	--	--	6.8
		Low Earth Orbit MMS**			
Number of cycles (total)	1	--	1 to 10	Included	2 to 11
Worst thruster	1	--	1 to 10	Included	2 to 11
Hours used (total)	.6	--	17,520	Included	17,521
Worst thruster	.6	--	17,520	Included	17,521
Propellant used (kg)	<.1	--	24.3	--	24.3

*3-year mission. Stationkeeping values shown scale linearly with time.
**2-year mission. Propellant usage calculated for worst case where thrusting is continuous.

The significant impact of ion propulsion on ACS performance for the MMS missions is:

- Experiment pointing accuracy can be maintained while performing stationkeeping, orbit maneuvers, or unloading momentum
- Magnetic torquers can be eliminated from the ACS module
- Care must be taken in selecting star sensors fields-of-view with respect to ion engine plumes.

As in Mission 1, pointing accuracies are very favorable when comparing ion propulsion to the more conventional hydrazine propulsion. Again, this advantage could be more important than the orbital correction propellant weight savings for missions requiring high pointing accuracies.

3.3.3.1 Mission Requirements

The two example MMS missions represent a geosynchronous mission requiring tight stationkeeping (StormSat) and a low to medium orbit mission requiring orbital changes and orbit sustenance (LandSat).

The ACS module on the MMS has a set of generalized requirements it must meet for any mission. These requirements are for accurate pointing in various modes and are summarized in Table 30. Mission-unique requirements for which the High-Performance Propulsion Module would have to be designed are summarized in Table 31.

3.3.3.2 Baseline Mission 2 Attitude Control Subsystem

The interfaces of the MMS attitude control subsystem are quite clearly defined. This is because of the modular concept of MMS where the same ACS module is used for all missions. Details of the ACS module, as defined by the RFP issued by NASA GSFC, are summarized in Table 32.

The basic ACS design concept is to maintain pointing via a gyro reference unit (updated with periodic star tracker measurements) and three reaction wheels. Should the payload sensor for the experiment provide a more accurate attitude reference, it is used for pointing error data. The accumulated momentum of the reaction wheels is periodically unloaded via either propulsion or magnetic torquing. The control logic resides in a satellite central processor.

Table 30. ACS Module Pointing Requirements for MMS

	Function	Requirement
Calibrated Inertial Hold Mode	Pointing accuracy	<0.01 deg (1σ)
	Average rate deviation	$<10^{-6}$ deg/sec
	Attitude jitter	$<6 \times 10^{-4}$ deg
Inertial Reference Unit (IRU) and Star Tracker Calibration	IRU drift bias	$<10^{-7}$ deg/sec
	IRU scale factor	<300 ppm
	Star tracker accuracy (ref. electrical null)	<15 $\widehat{\text{sec}}$

Other Pointing Requirements:

Mode	Pointing Requirement
Coarse sun acquisition	$<10^{\circ}$, rates <0.05 deg/sec
Fine sun acquisition	$<0.1^{\circ}$, rates <0.01 deg/sec
Transfer orbit	$<3^{\circ}$, rates <0.1 deg/sec
Orbit adjust	$<3^{\circ}$, rates <0.03 deg/sec
Ideal sensor error signal mode	$<10^{-4\circ}$, jitter $<10^{-6}$ deg
Safehold mode	$<10^{\circ}$, rates <0.1 deg/sec
Shuttle retrieval mode	$<1^{\circ}$, rates <0.1 deg/sec

Table 31. Mission 2 Attitude and Velocity Control Propulsion Requirements

Synchronous MMS Mission		Low Earth Orbit MMS Mission
FUNCTIONS	Δv REQUIREMENTS	FUNCTIONS
N-S STATIONKEEPING	50 M/SEC/YR	Δv FOR ORBITAL DRAG, MANEUVERS
E-W STATIONKEEPING	UP TO 2 M/SEC/YR	TORQUES FOR:
TORQUES FOR:		MOMENTUM WHEEL UNLOADING
MOMENTUM WHEEL UNLOADING		INITIAL ACQUISITION
INITIAL ACQUISITION		SAFEHOLD BACKUP MODE
SAFEHOLD BACKUP MODE		Δv REQUIREMENTS
TORQUE REQUIREMENTS		MISSION AND CONFIGURATION DEPENDENT
SUFFICIENT FOR REASONABLE ACQUISITION TIMES (10-20 MIN. DESIRED)		MODULE PROVIDES 2 MLB CONSTANT THRUST LEVEL AVAILABLE FOR DRAG MAKEUP OR MANEUVERING
BALANCE ANY SOLAR DISTURBANCE TORQUES (AS LARGE AS 5×10^{-5} N-M EXPECTED)		TORQUE REQUIREMENTS
POINTING ACCURACY		SUFFICIENT FOR REASONABLE ACQUISITION TIMES
10^{-2} DEG ACCURACY		BALANCE MOMENTUM BUILDUP FROM AERODYNAMIC AND GRAVITY GRADIENT TORQUES
10^{-6} DEG/SEC DRIFT RATE DEVIATION		POINTING ACCURACY
6×10^{-4} DEG ATTITUDE JITTER		SAME AS SYNCHRONOUS MMS
SAFEHOLD MODE WITH PEAK POINTING ERRORS OF 10 DEG.		

Table 32. Description of ACS Module for MMS

Missions:	Stellar, Solar and Earth Pointing Low Earth Orbit to Geosynchronous
ACS Equipment:	2 star trackers and shades
	3 reaction wheels (with the option of being able to add a 4th)
	1 inertial reference unit (no single point failure)
	1 2-axis fine sun sensor
	1 or more 3-axis magnetometer(s)
	3 magnetic torquers (orthogonal, redundantly wound)
	1 redundant interface assembly
	1 drive electronics assembly
	1 optical alignment cube
Physical Constraints:	Size 4' x 4' x 1-1/2' (1.2 x 1.2 x 0.5 meter)
	Weight 168 kg (370 lb)
	Power 170 watts average, 340 watts peak
Operational Modes:	Coarse sun acquisition (with and without thruster)
	Fine sun acquisition
	Stellar acquisition
	Inertial hold
	Flow
	Orbit transfer and adjust
	Calibration
	Equipment modes (stellar, solar and earth pointing with and without payload sensor)
	Safehold
	Shuttle retrieval

3.3.3.3 MMS Pointing Accuracies with Ion Propulsion

Worst-case pointing errors have been analyzed for a geosynchronous MMS mission with very high pointing accuracy (i.e., StormSat), using ion engine auxiliary propulsion. The specific situation considered is stationkeeping performed simultaneously with wheel momentum unloading. The results of a digital computer analysis show that pointing errors induced during these combined maneuvers are less than other ACS-induced transients, such as when the reaction wheel speed crosses zero. This result is possible with the gimballed thrusters which can produce simultaneous linear acceleration force and rotational torque. The low earth orbit mission case is analogous and ACS performance can be assumed to be comparable.

For the Advanced Communications Satellite (Mission 1) case, ACS disturbances were derived from some idealizing assumptions and a geometric analysis. The MMS (Mission 2) application has been studied by actually designing a control system and simulating its performance on a digital computer.

The attitude control subsystem used is the standard MMS three-axis stabilized concept utilizing reaction wheels. Accurate pointing is accomplished by means of integral compensation. Two sets of control parameters were analyzed for a satellite with an assumed yaw moment of inertia of 410 $kg\text{-}m^2$. Although the simulation is programmed for three-axis control, the analysis was made for yaw only, on a single-axis basis.

Of the two ACS designs, the one with higher bandwidth was used for the computer simulation. This subsystem has a closed loop natural frequency of 0.5 rad/sec and a design pointing accuracy of 8.4×10^{-8} degrees for a secular disturbance of 1.5×10^{-4} N.m, resolved between roll and yaw at the orbit rate. The daily accumulation of this torque corresponds to about 13 N.m-sec. The wheel friction is assumed to be of coulomb-type with magnitude of 0.01 N.m. When the wheel speed is reversed, this friction level, coupled with the integrator dynamics, will produce a maximum transient pointing error of 0.0032 deg.

Momentum Unloading Concept

Wheel momentum unloading is achieved by gimballing the ion thrusters to produce a linearly proportional torque during the stationkeeping maneuver. The torque level is selected to reduce the wheel speed. This added unloading logic results in an additional pole and zero in the basic control loop open-loop equation. (Appendix C gives a detailed explanation of the ACS design). The s-domain expression of this additional pair is given by

$$G(s) = \frac{s + \dfrac{2F\ell k_e}{57.3\, I_w}}{s} \triangleq \frac{s + \gamma}{s} \tag{11}$$

where

F = ion thruster force = 4.45×10^{-3} N

ℓ = thruster lever arm = 1.2 m

k_e = thruster angle gain = deg/rpm

I_w = RW motor inertia = $\dfrac{20 \text{ N.m-sec}}{3000 \text{ rpm}} = \dfrac{\text{N.m-sec}}{150 \text{ rpm}}$

When combined with the normal control loop poles and zeros, there will be four poles at the origin and three zeros on the left-hand real axis. By varying γ, the low frequency critical loop gain K_1 and frequency ω_1 can be defined along the imaginary axis in the s-plane where the two closed loop loci in the right-hand plane enter the left-hand plane. The results are shown in Figure 35. If $\gamma = 0.003$/sec is selected, $K_1 = 0.0244/\text{sec}^2$ and $\omega_1 = 0.173$/sec. Since the overall loop gain $K = 0.25/\text{sec}^2$ (see Appendix C), the low frequency gain margin is 10.25. This will yield $k_e = 0.1073$ deg/rpm. By letting $k_e = 0.1$ deg/rpm, $K_1 = 0.0227/\text{sec}^2$, and the gain margin = 11 (20.8 db). When the thruster gimbal movement is limited to ±10 degrees, the gimbal angle is proportional to the wheel speed up to 100 rpm. Thus the thrusters are deflected to the maximum angle during the most part of the unloading.

Computer Simulation

The momentum unloading concept described in the previous section has been simulated on a digital computer and the results are shown in Figure 36. The unloading was initiated at t = 100 seconds with the gimbal

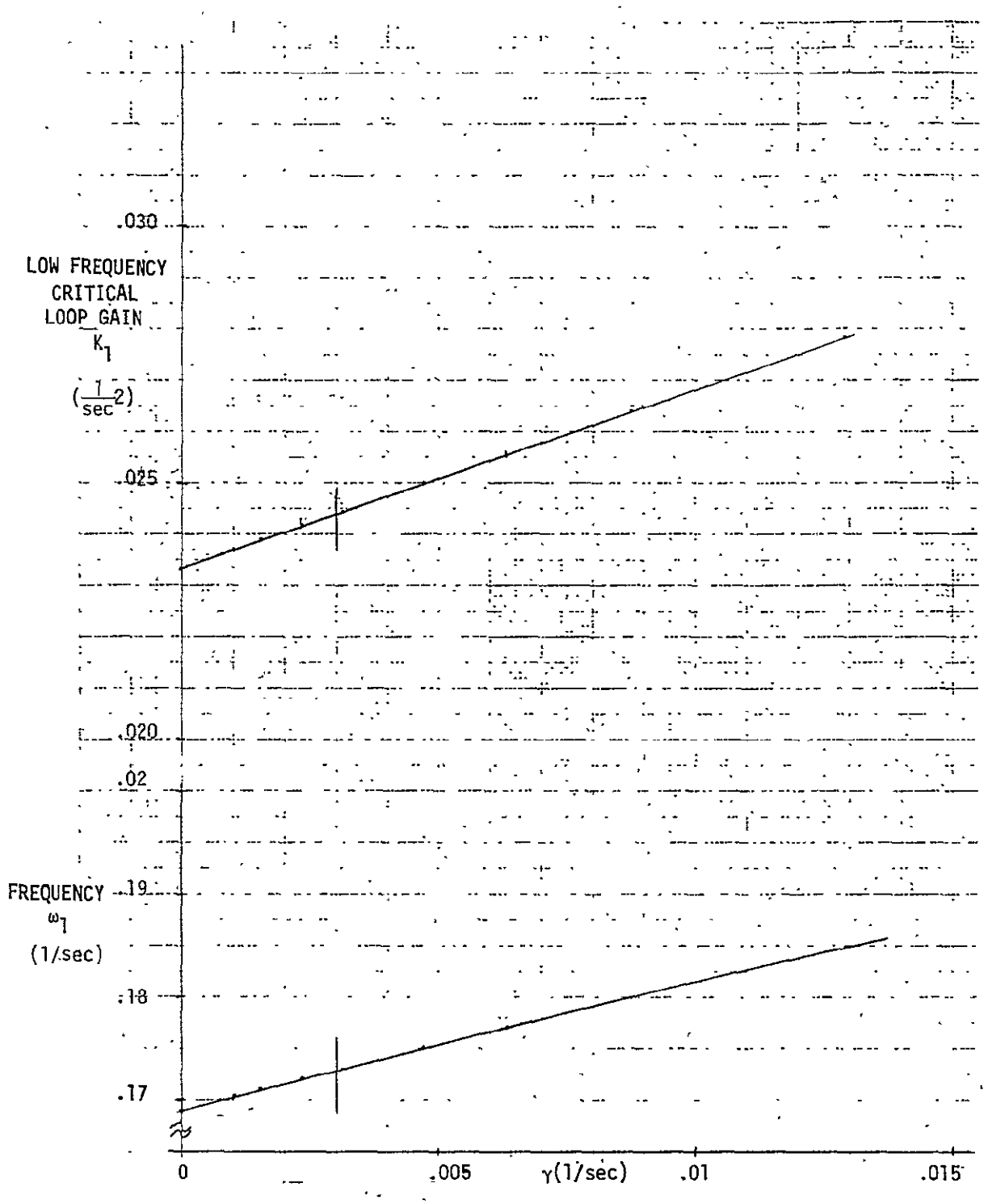

Figure 35. Effects of Momentum Unloading Loop Gain

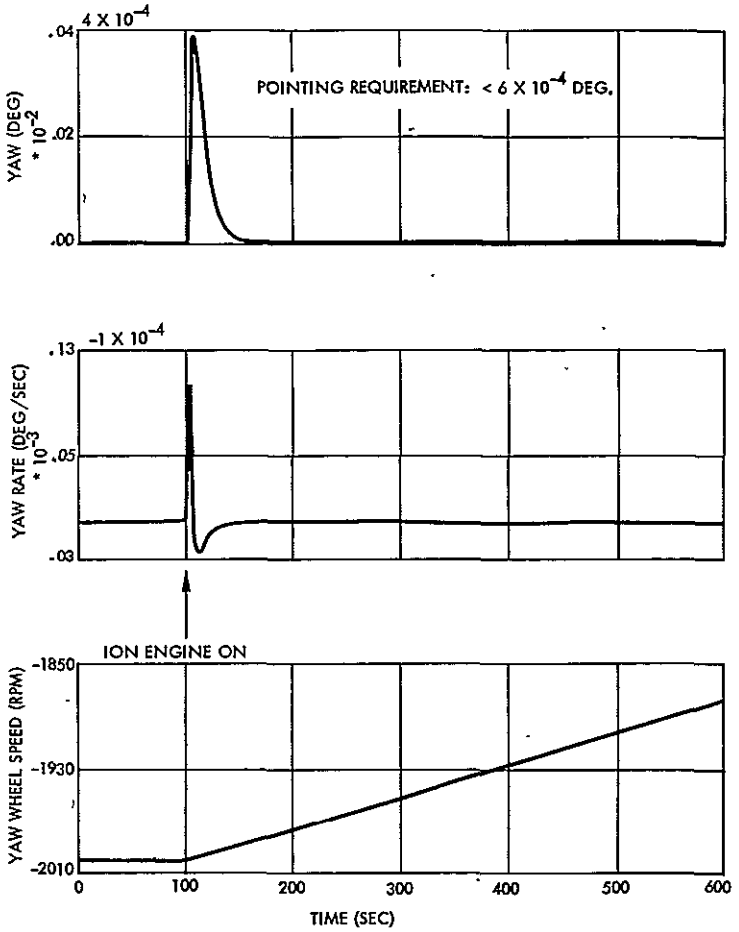

Figure 36. MMS Attitude Control Transients Due to Wheel Unloading During Stationkeeping

angle already deflected to 10 degrees. The thrusters are assumed to be in the x-y plane of the satellite body. The thruster vector produced by a pair of nominally oriented thrusters is along the y-axis. The z-axis torque is produced by rotating these thrusters in the same direction about the z-axis. The step torque input thus introduced into the reaction wheel control loop results in a yaw transient of about 3.9×10^{-4} degrees, which is an order of magnitude smaller than that caused by a wheel speed reversal. The peak transient rate is slightly over 1×10^{-4} deg/sec. The unloading rate is about 0.256 rpm/sec. This rate corresponds to unloading from 2000 rpm in about 2.2 hours. The slight increase in the wheel speed prior to the unloading is due to the disturbance torque.

Although the transient is sufficiently small, it can be further reduced by starting the loading by gradually increasing the gimbal angle. No further study was made, however, since the capability has been adequately demonstrated. The effect of the ion engine thrust vector offset will be also small. If the offset is 0.5 degree, the transient error will be approximately 5% greater (sin 10.5/sin 10 = 1.05).

Practical Considerations

The attitude control subsystem design parameters assumed in the analysis are fairly typical of geosynchronous satellites. The time required for momentum unloading, about 5 hours, is also compatible with that required for stationkeeping. Thus, the application of the ion thruster subsystem to stationkeeping and momentum unloading is feasible and straightforward.

The only critical design area identified is three-axis wheel unloading, particularly when a skewed wheel configuration is used. This configuration is to be used on the HEAO-B spacecraft and is a candidate for MMS. With limited thruster gimbal angles, the wheel-body matrix transformation in the control law will require careful consideration.

3.3.3.4 Other ACS – Ion Propulsion Interactions

Ion propulsion has been shown to have positive impacts on ACS pointing accuracy and stability, plus it reduces reliance on magnetic torquing for momentum dumps. The use of ion propulsion has other impacts, however. The satellite must be configured for properly locating the ion engine. This could impose constraints on solar array panel locations and ACS sensor field of view.

The baseline MMS designs show the solar array on the opposite side of the spacecraft center of mass from the ion thrusters. This nonsymmetric side design is possible since the ion engines can easily compensate for the solar pressure disturbance torques due to an offset array. The configuration can be advantageous from a satellite design aspect since only one solar array drive is required for oriented arrays and large payload appendices can be extended on the side opposite to the solar panel and not shade the array.

One possible limitation of ion propulsion is the interference of the ion plume on precision star trackers. The optical power density for photons emitted in the visible from the bombardment discharge is ~6 μwatts/cm^2 at a distance of ~35 cm from the discharge. The power density of the solar visible is ~100,000 μwatts/cm^2. It is, therefore, not likely that emission from the ion thruster will cause significant levels of interference in spacecraft optical detectors utilizing sun sensing for attitude control. If, however, advances in spacecraft design lead to the use of star trackers for spacecraft attitude control, the detector sensitivity levels will change by many orders of magnitude.

Recently Gates and McAloon (Ref. 15) have described a precision star tracker capable of responding to stars as dim as +10 Mv. The photon counting techniques used in this sensor dramatically extend the range of concern for possible interference between photons emitted from the operation of the ion thruster and the attitude control circuitry. Under these conditions, a variety of possible sources for photon release by the ion thruster, the ion thrust beam plasma, and the charge exchange ion plasma should be considered. These include:

1) Absorbed and re-radiated solar radiation in the plume.

2) Electron impact ionization in the plume.

3) Interactions between spacecraft outgassing products, the thrust beam plasma, and the charge exchange plasma.

Star trackers are nominally canted out of the orbit plane, to minimize solar interference, and away from solar panels. It appears desirable to point the field of view of a star tracker nominally parallel with the ion thrust vectors. The off-axis shielding of star trackers is controlled by their shade designs. Star tracker shade design factors are summarized in Figure 37. The allowable illumination of a typical two-stage shaded star tracker is shown in Figure 37.

3.3.4 Interactions with MMS Power Module

The standard MMS power module, defined in reference 9, uses a power regulator unit (PRU). As shown in Figure 38, its solar cell array is divided into "auxiliary" and "main" sections. The auxiliary section (which is optional to the user) is connected directly to the load bus and is sized to meet the

Table 33. Star Tracker Shade Design Factors

Requirements

Cut off angle: 60° (allows operation of tracker with sun or earth as close as 60 degrees to optical axis)

Off axis attenuation: 10^7 (ratio of incident power to that exiting shade)

Assumptions

Irradiance from sun: 0.07 W/cm^2 (in detector's spectral band)

Irradiance from star: 5.7×10^{-15} W/cm^2 (from 6th magnitude)

Off axis attentuation of optics: 10^3 (ratio of incident power to that at detector surface)

Ratio of total and instantaneous field of view: 2.7×10^3 (8 x 8 and 0.153 x 0.153 degree)

Configuration

Two-stage shade recommended (outer stage shadows inner stage such that no sunlit baffle edges are in view by optics aperture).

Shades now developed for CT401 tracker are one-stage shades (MIT SAS-C shade experiencing problems as far as 120 degrees off axis, AS&E is building shade for HEAO-A, and Honeywell is building shade for HEAO-B).

Shade will be truncated on one edge to conform to envelope limit for module (the truncation will allow sun to illuminate inner stage baffles for some sun angles, thus only providing one stage performance for those angles.)

minimum spacecraft load requirement. The balance of the solar cell array power is provided by the main section which is connected to the load bus through the PRU.

The PRU accepts unregulated dc power from the solar array main section, transforms the energy to the voltage level required by the batteries for controlled charging, and supplies the load requirements that are in excess of the capability of the auxiliary array section. Battery charging and discharging is accomplished in the parallel mode in all cases. The PRU also contains

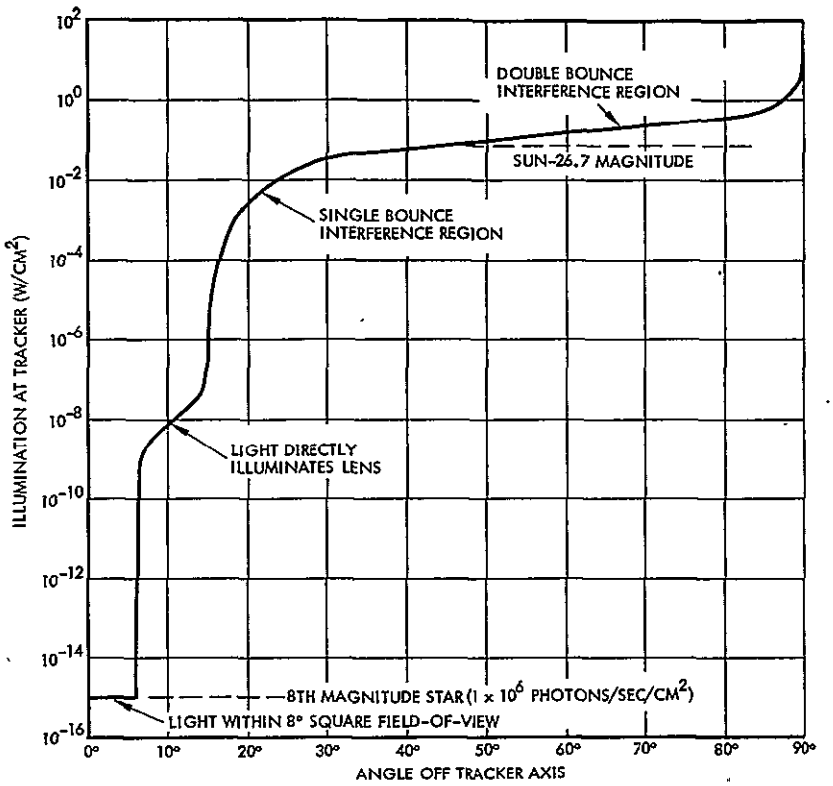

Figure 37. Allowable Illumination at Star Tracker (within 0.35 to 0.75 μ spectral band)

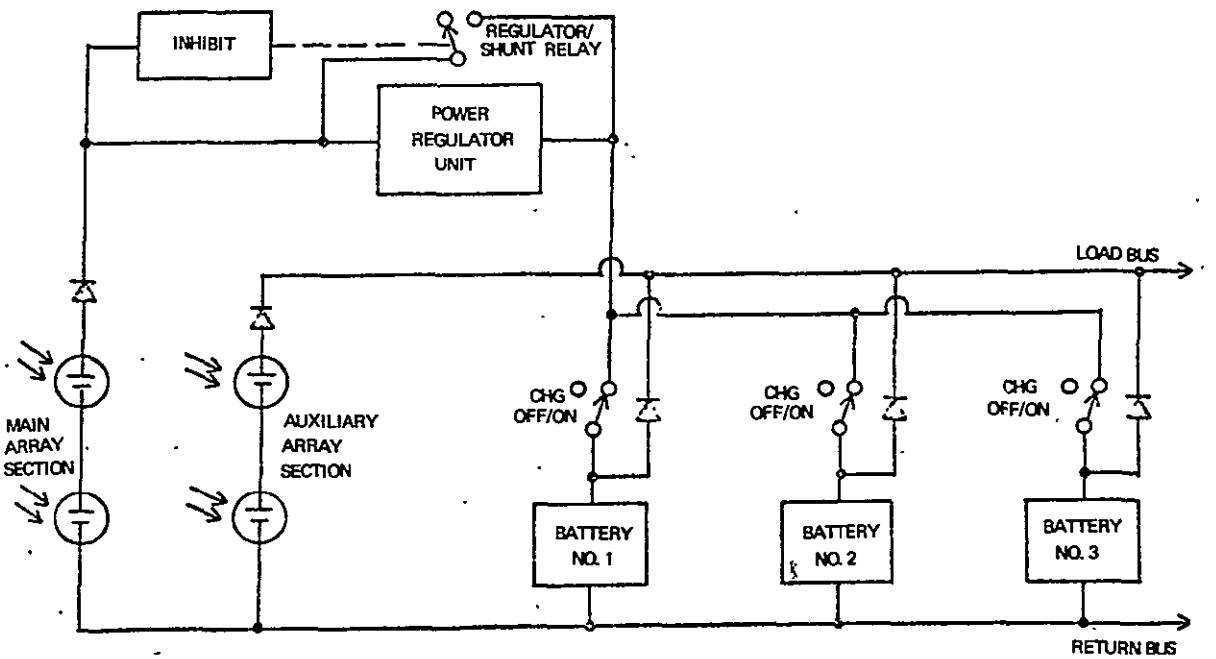

Figure 38. MMS Power Regulator Unit Power Module

a bypass relay whose function is to apply power from the main section directly to the load bus when high peak currents are planned. The relay is normally open and must be commanded closed. Relay closure is inhibited by a signal from the array bus when the array is illuminated. This prevents the relay from closing when high currents are present. The bypass function can also be used as a backup in the event of PRU failure.

Comparison of the network topology of the PRU subsystem (Figure 38) with the baseline power subsystem examined for Mission 1 (Figures 17 and 18) reveals the following comparisons:

- The "auxiliary" array of the PRU subsystem is analogous to the load array of the baseline subsystem.
- The "main" array is analogous to the aggregate of charge arrays of the baseline subsystem.
- The network consisting of the PRU and its bypass relay is analogous to the combined K1-K5 relay logic for all batteries in the baseline subsystem.
- The only dissipative circuit element in series between the battery and the load bus in either subsystem is a diode.
- A battery tap is not required by the PRU subsystem.
- If the PRU and baseline power subsystems are each sized to support a particular load power profile, the batteries of each subsystem will be of the same number and size.

The auxiliary and main solar arrays of the PRU subsystem will differ in size from their analogs in the baseline subsystem. Unlike the auxiliary array of the PRU subsystem, the load array of the baseline subsystem is sized to meet the total sunlight load at end of mission. The main array of the PRU subsystem will be different in size than the aggregate of the charge arrays of the baseline subsystem because: (1) there is an inefficiency in the PRU, and (2) unlike the main array, the aggregate of the charge arrays only supplies battery charge energy and is not required to supply the difference in power between nominal and minimum spacecraft load. The second effect will tend to mitigate the first, although not necessarily eliminating a difference in size between the main array and the aggregate of the charge arrays.

When the total solar cell array size of the two subsystem configurations is compared, the larger size of the array with the PRU subsystem will be due

to the losses introduced by the PRU. It is necessary, therefore, to modify the results obtained from the analyses of the baseline subsystems in Mission 1 for the Mission 2 applications by the addition of increments of solar cell array. The baseline Mission 2 power subsystem is therefore the Mission 1 baseline with minor modifications.

3.3.4.1 Synchronous Orbit MMS

The StormSat mission, used as the geosynchronous example, has a satellite load power requirement of 400 to 600 watts. With P_{sc} = 400 watts, the nominal load array section output at equinox after 3 years is 465 watts. With P_{sc} = 600 watts, the load array output under the same conditions is 697 watts.

Analysis of this mission is based upon the same subsystem and thruster system configurations and electrical interface option that served as the basis for the analysis of Mission 1. Identical thrusting scenarios are also assumed.

Table 34 presents the in-orbit output power capability of the solar array sections at beginning and end-of-mission for both satellite load power levels considered. Initial sizing of the solar arrays produced values which were insufficient to support both the satellite load and the thruster load profile. Specifically, 4-hour thruster operation, even when partially supported by charge array section power, was shown to have the effect of completely exhausting the batteries. It was therefore necessary to increase the load array section size by an amount sufficient to reduce the batteries' depth-of-discharge during thrusting to values consistent with the cycle life capability of the nickel-cadmium battery system. Table 34 shows the power increments that were added to achieve this objective.

The values of fractional battery depth-of-discharge calculated at beginning and end-of-mission for both satellite load levels are shown in Table 35. As a convenient approximation to the otherwise detailed calculation of the average of the effective depth-of-discharge mission-time profile (d_T versus time in Table 35), a conservative linear mission-time profile was assumed throughout the 3-year mission. For both cases of satellite load power, the average depth of discharge is approximately 0.070 and the number of discharge cycles is assumed to equal 1095.

Table 34. StormSat Solar Array Power Capability: Baseline Subsystem (Watts)

Mission Year	Satellite Load Power	Season	Load Power Increment Required for Thrusting	Total Array Section Capability	
				Load at 30 V	Charge at 40 V
0	400	Equinox	349	943	176
		S. Solstice	330	891	167
	600	Equinox	234	1126	265
		S. Solstice	221	1064	251
3	400	Equinox	273	738	138
		S. Solstice	258	697	131
	600	Equinox	183	881	207
		S. Solstice	173	833	196

Table 35. StormSat Battery Depth-of-Discharge* as a Function of Mission Year

Mission Year	Satellite Load Power (watts)	d_{T_e}	$d_{T_{ss}}$	d_T
0	400	0	0	0
	600	0	0	0
3	400	0.028	0.250	0.139
	600	0.074	0.250	0.162

*Fraction of rated capacity

Substitution of these values into the ampere-hour equivalency expression developed for Mission 1 (Equation 9) yields approximately 132 equivalent discharge-charge cycles for both cases of satellite load. To this must be added 270 eclipse discharge cycles over 3 years and 40 estimated prelaunch cycles. Thus, the nickel-cadmium batteries of either system must be capable

of providing at least 442 cycles to a maximum depth-of-discharge of 0.7 during the course of the 3-year mission. Since this is well within the capability of nickel-cadmium systems, it is concluded that an increase in the sizes of the batteries is not warranted, and the arrays used only increase by the increments of load power identified in Table 34.

Table 36 summarizes the end-of-mission capability of the solar array sections of the functionally equivalent PRU subsystem. It is assumed that the PRU regulates with an efficiency of 90%.

Table 36. StormSat Solar Array Power Capability after 3 Years: PRU Subsystem (watts)

Satellite Load Power	Season	Total Array Section Capability	
		Auxiliary at 30 V	Main at 42 V
400	Equinox	721	161
	S. Solstice	680	153
600	Equinox	855	242
	S. Solstice	806	229

3.3.4.2 Low Earth Orbit MMS

LandSat is a 2-year mission in low earth orbit. The orbit selected for analysis exhibits 35 minutes (maximum) of satellite eclipse and 68 minutes (minimum) of sunlight. As a worst case, it was assumed that these illumination characteristics hold for every orbit throughout the mission.

The LandSat load power profile has the following characteristics:

- 261.8 watts minimum power for 93 minutes
- 450 watts average power over the 103-minute orbit
- 2200 watts peak power for 10 minutes

The worst-case analysis assumes that the peak power period occurs during satellite eclipse. It is further assumed that the duty cycle of the thruster

system is 100%. (It was 16.7%, or 4 hours/day, for the geosynchronous orbit case.)

For this low earth orbit application, battery-level redundancy (2 of 3) is assumed. Accordingly, with two batteries supporting the mission, the design must be capable of providing 10,206 discharge-charge cycles plus 10% margin, plus 40 acceptance test cycles — 11,267 cycles, total.

Nickel-cadmium battery cell cycle life data, as presented in reference 12, indicate life of 12,000 cycles corresponding to a depth-of-discharge of 0.29. If this depth-of-discharge is obtained with two operative batteries, the depth-of-discharge with three batteries is reduced to 0.193, corresponding to a life of approximately 18,000 cycles.

The design of the nickel-cadmium batteries and the associated charge array section is based upon the following assumptions:

- The minimum battery recharge ratio (A-hr in/A-hr out) at end-of-mission is 1.05, corresponding to a battery temperature of $+5^{\circ} \pm 5^{\circ}C$.

- Normal full charge of two operative batteries at end-of-mission is accomplished with a current corresponding to a 3.5-hour rate.

Table 37 summarizes the effect of these two assumptions, as well as the previously stated assumption that the peak load be drawn from the batteries during eclipse, a power source capability. Table 37 also shows the differences in solar array section size and battery size resulting from the imposition of the constant thruster system electrical load. Unlike the geosynchronous orbit missions, an increment of solar array must be added to the charge array sections as well as to the load array sections to accommodate the peak spacecraft load.

Table 38 summarizes the end-of-mission capability of the power sources of a functionally equivalent PRU subsystem designed to operate with or without the thruster loads. It is seen that, for this particular mission, incorporation of a PRU results in increased total array size for all cases considered. However, for the post-eclipse case, the battery size is reduced since the PRU

Table 37. LandSat Power Source Capability after 2 Years: Baseline Subsystem

Power Source	Peak Load Event	Parameter	Parameter Value as Function of Thruster Load		Difference
			With	Without	
Solar Array	During Eclipse	Load Section at 30V	800 W	305 W	495 W
		Total Charge Section at 40V	1058 W	694 W	364 W
			1858 W	999 W	859 W
	Post-Eclipse	Load Section at 30V	800 W	305 W	495 W
		Total Charge Section at 40V	769 W	511 W	258 W
			1569 W	816 W	753 W
Batteries	During Eclipse	Total Capacity	120.1 A-hr	78.9 A-hr	41.2 A-hr
	Post-Eclipse	Total Capacity	101.0 A-hr	67.1 A-hr	33.9 A-hr

Table 38. LandSat Power Source Capability after 2 Years: PRU Subsystem

Power Source	Peak Load Event	Parameter	Parameter Value as Function of Thruster Load		Difference
			With	Without	
Solar Array	During Eclipse	Auxiliary Section at 30V	800 W	305 W	495 W
		Main Section at 42V	1233 W	810 W	423 W
			2033 W	1115 W	918 W
	Post-Eclipse	Auxiliary Section at 30V	800 W	305 W	495 W
		Main Section at 42V	876 W	581 W	295 W
			1676 W	886 W	790 W
Batteries	During Eclipse	Total Capacity	120.1 A-hr	78.9 A-hr	41.2 A-hr
	Post-Eclipse	Total Capacity	98.6 A-hr	65.5 A-hr	33.1 A-hr

is bypassed during the period of peak load and application of the larger main array section mitigates the amount of daytime battery discharge.

3.3.4.3 Summary of Impacts

The impact of the incorporation of electrical propulsion on the power sources of the satellites defined for the two MMS missions considered is summarized in Table 39. The geosynchronous mission requires no increase in nickel-cadmium battery size. However, the amount which the solar array size must increase is proportional to the ratio of thruster system power to satellite load power. Therefore, the relatively low-powered StormSat requires an increase in size of its load array section to help reduce the battery discharge profile resulting from thruster programming to within the capability of the nickel-cadmium battery system.

The low earth orbit mission (LandSat) is strongly influenced by its load power profile. If the peak power period is allowed to occur during the maximum satellite eclipse period, its batteries will be larger in size than if the peak is limited to the sunlight period. As battery size increases or decreases, the charge array sections also increase or decrease in size. If the peak discharge period begins at the end of the eclipse period, the charge array sections contribute to the peak load demand. Thus, it is necessary to write and solve an energy balance equation for the batteries as part of the solar array sizing procedure when peak loads are experienced during the sunlight period.

Table 39 defines the power source increments required when the PRU power subsystem is used instead of the baseline subsystem. The solar array increments are higher than those required for the baseline subsystem in the StormSat application due to the inefficiency imposed by the PRU.

In the LandSat application, the battery increment is unaffected when the peak load occurs during eclipse, but is reduced for the post-eclipse peak load case because the PRU is bypassed when the main array of the subsystem is switched to the load bus. Since the main array is sized to deliver charge power at 42 volts to the PRU, it can deliver slightly more power at 30 volts during the peak load period than would be available from an equivalently designed (40 volt) total charge array section. With less sunlight battery discharge, the PRU subsystem batteries are, accordingly, smaller in size.

Table 39. Power Source Area and Mass Increment Summary for MMS Missions

Mission	Orbit	Mission Length (yr)	Power Subsystem Configuration	Satellite Load (W)	Peak Load Event	Power Source Increments			
						Solar Array		Battery Mass (kg)	Total Mass (kg)
						Area (m^2)	Mass (kg)		
StormSat	Geo-sync	3	Baseline	400	--	2.91	8.57	--	8.57
				600	--	1.96	5.76	--	5.76
			PRU	400	--	2.97	8.61	--	8.61
				600	--	2.06	5.82	--	5.82
LandSat	Low Earth	2	Baseline	*	Eclipse	9.09	26.73	36.05	62.78
					Sunlight	7.97	23.48	29.66	53.14
			PRU	*	Eclipse	9.72	28.63	36.05	64.68
					Sunlight	8.36	24.62	28.96	53.58

*262 W minimum; 450 W average; 2200 W peak.

It is concluded that the integration of an ion propulsion subsystem of the type considered into satellites designed for these particular mission applications results in a small but acceptable penalty to the satellites' power sources except, perhaps, for the low earth orbit case involving a large peak load power requirement. The impact of the latter can be reduced somewhat by the restriction of the peak load event to sunlight periods. However, for all of the cases considered it has been determined that the cycle life capability of the nickel-cadmium battery system is not a constraining factor in the integration of the thruster system.

3.3.5 Other Design Considerations

3.3.5.1 Net Mass Property Impact

Dry weight data on the high-performance propulsion module are shown in Section 3.3.1 and the added solar array and battery requirements are in Section 3.3.4. In this section the net mass impact of the use of ion propulsion on the MMS will be developed.

In addition to the propulsion module dry weight and additional power source weights, there are three other items which must be included:

- Propellant. Sufficient mercury propellant is included in the geosynchronous mission to provide all ACS requirements, including stationkeeping, for 3 years.

  The low earth orbit configuration is sized to provide enough propellant to allow two engines to each fire 20,000 hours. This is the design life of the engines and provides a total impulse of 144,000 lb-sec (6.4×10^5 N/sec) at an I_{sp} of 2500 sec.

- Power Conversion Equipment. Two power sources are required for the ion propulsion subsystem power processor: (1) 70 ±20 Vdc for the main thruster, and (2) 28 ±1 Vdc of auxiliary power for the command bus operation. Neither of these voltages are directly available on the MMS.

  This is the same situation as was present in the Mission 1 study. The same solution (Option 2 of Section 3.2.4.2) is proposed — adding boost line regulators and dc-dc converters to the spacecraft bus. The penalties incurred in this option are 16 pounds of weight, 7% loss in efficiency, and the addition of 1400 parts.

- Structure. The high-performance propulsion module structure has been analyzed and is estimated to weigh 8.3 kg (18.3 lb).

The net mass property impact on the MMS, including all of the above effects, is shown in Table 40. The PRU power subsystem configuration of Section 3.3.4 has been used.

No attempt has been made to estimate the weight of a hydrazine propulsion module suitable for these two missions for comparison. Some of the necessary information is not available. However, the NASA Standard Equipment Announcement for the Multimission Modular Spacecraft lists a total weight of 586 kg (1290 pounds) for a hydrazine SPS-II with a total impulse capability of 231,000 lb-sec. (1.03×10^6 N/sec). A rough estimate of the weight of a high performance propulsion module using ion engines to produce this total impulse is 133 kg (293 pounds) for four thrusters operating 16,042 hours each. If eight thrusters are included, for redundancy or other considerations, the total weight impact would be about 162 kg (356 pounds). Thus, savings with ion propulsion can be as much as 454 kg (1000 pounds).

Table 40. Net Mass Impact of High Performance Propulsion Module on MMS

Item	Geosynchronous Mission		Low Earth Orbit Mission	
	kg	lb	kg	lb
Ion propulsion subsystem	71.1	156.6	73.7	162.3
Propellant	6.8	15.0	24.3	53.5
Boost Line Regulators and dc-dc converters	7.3	16.0	7.3	16.0
Module structure	8.3	18.3	8.3	18.3
Additional solar array	5.8*	12.8	28.6	63.0
Additional battery	--	--	36.1	79.5
	99.3	218.7	178.3	392.7

*Assumes 600-watt spacecraft load array

3.3.5.2 Thermal Control

The ion propulsion subsystem is completely contained within the propulsion actuation module. Therefore, thermal control is a localized problem and will be handled with the subsystem thermal control devices.

3.3.5.3 Reliability

No detailed ion propulsion subsystem reliability analyses were conducted for the Mission 2 configurations. The reliability models are highly dependent on configurational details, and these two missions are less critical than the Mission 1 Advanced Communications Satellite. Data from the detailed Mission 1 reliability analyses (Section 3.2.7) can be used as a guide in predicting the geosynchronous MMS subsystem reliability.

The ion engines on the Advanced Communications Satellite fire twice a day for 7 years. On the geosynchronous MMS they fire once a day for 3 years. For either mission the total firing time for a given engine is well within its design life of 20,000 hours. Therefore, predicted failures will be random. The firing time per engine over a year is quite similar for the four-engine, nonredundant Advanced Communication Satellite configuration and the baseline four-engine geosynchronous MMS configuration. Therefore, the 3-year reliability data generated in the Mission 1 analysis can be used as an approximation for the geosynchronous MMS mission.

Currently available data indicate that an appropriate failure rate for the NASA-LeRC 8-cm mercury thruster lies somewhere in the range of 2500 to 25,000 bits (failures per billion hours), with 10,000 bits as a reasonable "most likely" value. Using the Mission 1 data, Table 41 lists the predicted geosynchronous MMS ion propulsion subsystem reliability for various values of thruster reliability. The predicted reliability values shown in Table 41 are high enough that redundant thrusters at each location will not likely be required.

Table 41. Predicted Geosynchronous MMS Ion Propulsion Subsystem Reliability

Thruster Failure Rate (bits)	2500	10,000	25,000
Reliability at 3 years	.978	.957	.897

The operation of the high performance propulsion module for the 2-year, low earth orbit mission is quite different than for the other two missions. The number of firing cycles is much lower (11 cycles versus 3826 for Mission 1 and 1095 for the geosynchronous MMS). At the same time, the worst-case engine firing duration is much larger (up to 20,000 hours each, versus 6950 hours for Mission 1 and 5914 hours for the geosynchronous MMS). Therefore, reliability predictions from Mission 1 are not pertinent. Reliability is not considered to be a problem but detailed predictions must wait until a specific mission is defined.

4. THRUSTER INTERFACES

The 8-cm thruster was examined in a series of diagnostic measurements. These measurements included the angular and energy dependence of both charged and neutral particle fluxes from the thruster with and without a sputter shield present. Other measurements examined sputtering of the shield itself, transport of sputtered material from the shield, optical emissions from the thruster, thruster magnetic fields, and neutralization of differentially charged surfaces by charged particle transport from the thruster's plasma discharge neutralizer.

4.1 THRUSTER TEST CHAMBER

Most of the interface measurements were obtained in the 5- by 10-foot test chamber illustrated in Figure 39. The diagnostic array in that chamber varied from test to test. For charged particle efflux measurements, the diagnostic array illustrated in Figure 40 was utilized. Specific details of the various Faraday cups and retarding potential analyzers are given in Figures 41 through 44. Figures 41 and 42 show the outer case, grid, and collector configuration for the Engine J_+ and 1-1/2-inch J_+ probes, respectively. Figure 43 shows the outer case, grid, and collector configuration of the swinging J_+ probe, as well as the probe orientation and motion with respect to the thruster. Figure 44a shows the overall layout and orientation of the 4-inch J_+ and piggy-back J_+ probes. Figures 44b and 44c give the outer case, grid, and collector configurations for these two probes. Figure 45 is a view along the thrust beam axis locating the radial distance and azimuthal positions of the diagnostic probe mounting rods. This figure also indicates probe motion for the Engine J_+, 1-1/2-inch J_+, and swinging J_+ probes, as well as the radial position of the 4-inch J_+ and piggy-back J_+ probe assembly.

Charged particle efflux measurement procedures were the same as those used in previous thruster efflux analyses (e.g., ref. 16). The procedures used for the other measurements, together with the special diagnostic instrumentation employed, are presented in the following sections which discuss those measurements in detail. The coordinate systems employed are shown in Appendix D, Figure D-1.

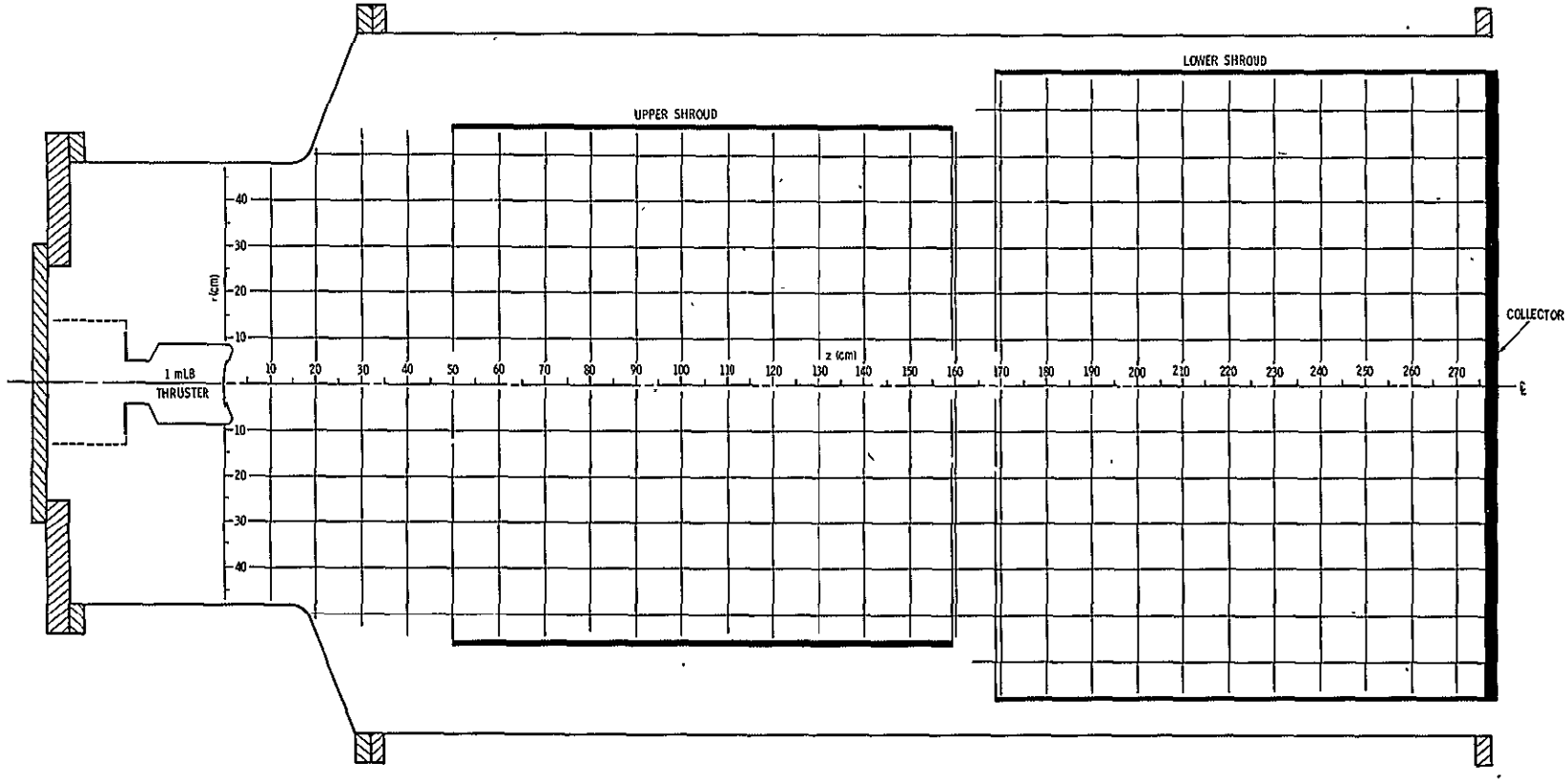

Figure 39. 5- by 10-foot Test Chamber Dimensions

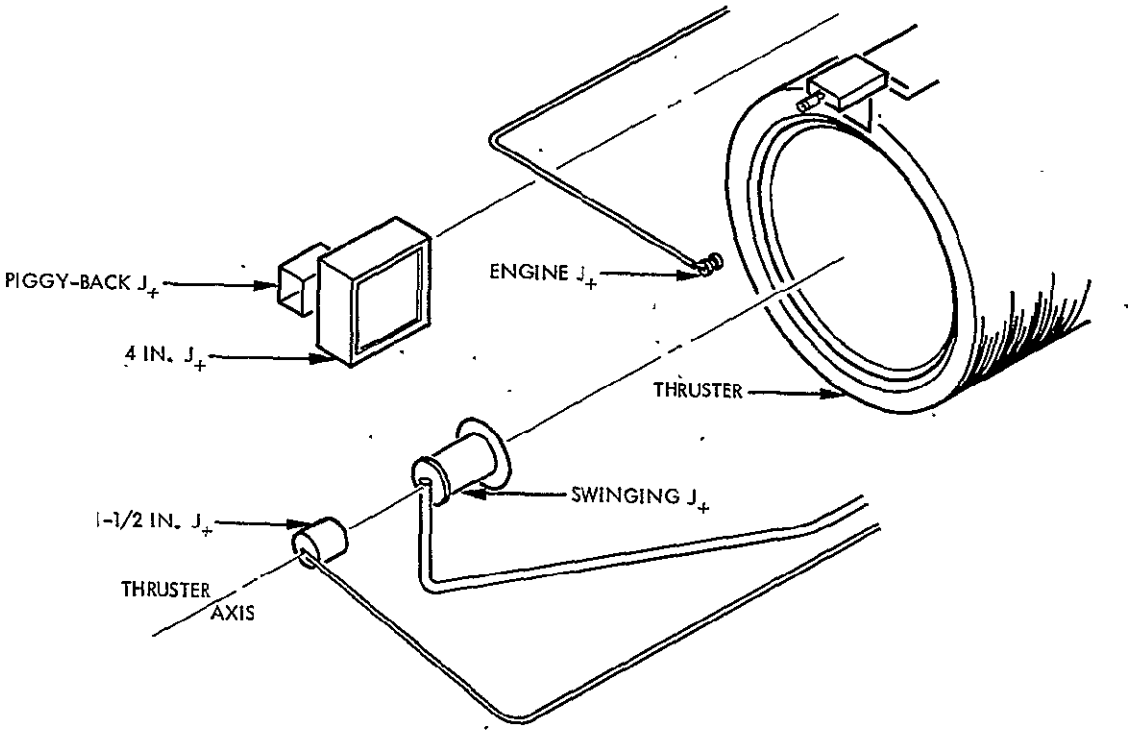

Figure 40. Diagnostic Instrument Array

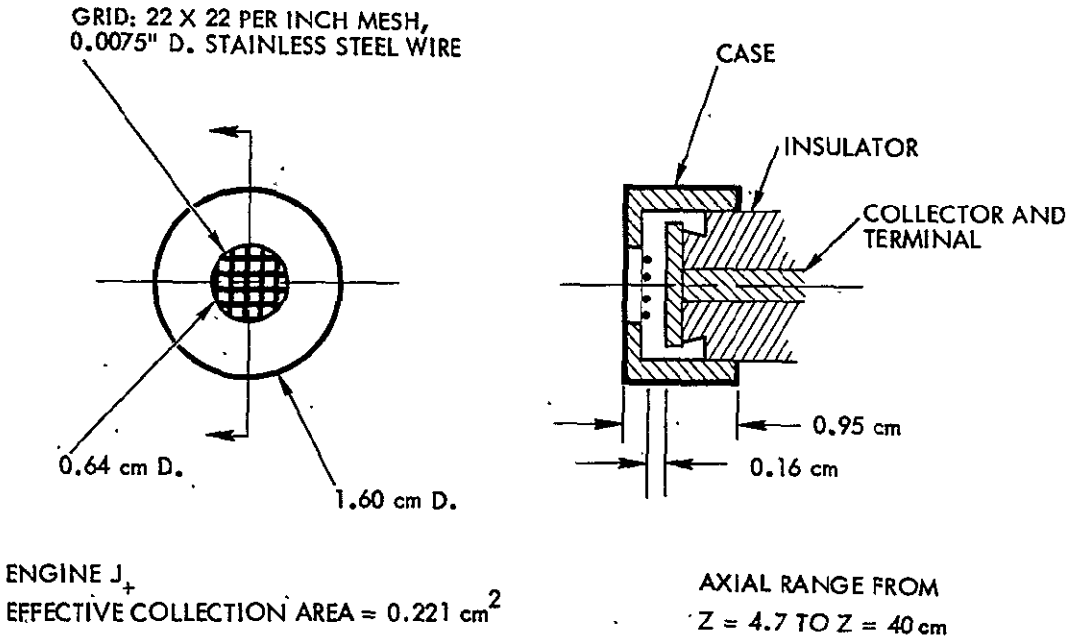

Figure 41. Engine J_+ Probe Dimensions

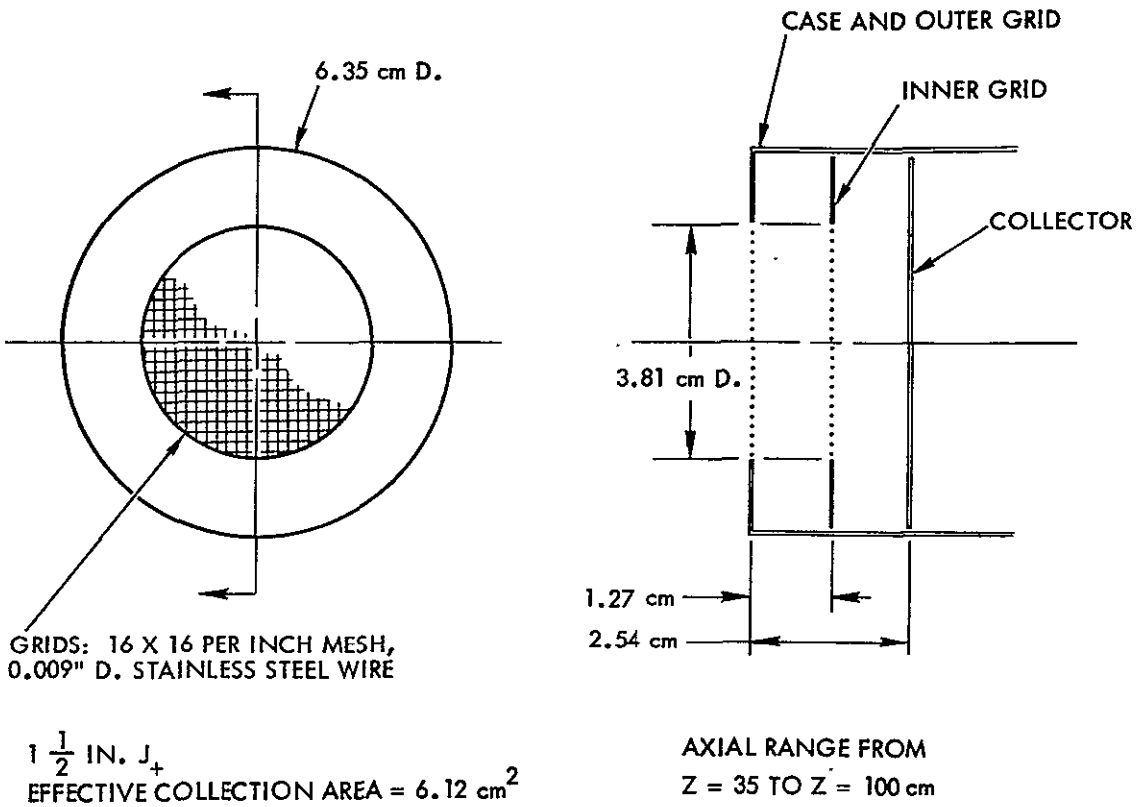

Figure 42. 1-1/2 inch J_+ Probe Dimensions

4.2 UNSHIELDED CHARGED PARTICLE EFFLUX

Ion flux measurements were taken as functions of Faraday cup position and Retarding Potential Analyzer (RPA) setting for the various diagnostic probes illustrated in the preceding section. The data were analyzed in terms of normalized efflux parameters, which will be defined later.

4.2.1 Charged Particle Measurements

The lower trace in Figures 46 through 50 shows the Faraday cup current density for the Engine J_+ probe at various probe rotation angles and axial distances from the thruster face. The upper trace given in these figures is the floating potential of the Engine J_+ probe when used as a floating probe with its case and collector connected to each other and both electrically isolated from ground by an 11 MΩ isolation resistor. The radial position of the probe in a cylindrical coordinate system (r, z, ϕ) whose z axis is the ion thruster axis is given by $r = 2\ R\sin\alpha/2$ where R is the probe arm length (34.3 cm) and α is the probe rotation angle.

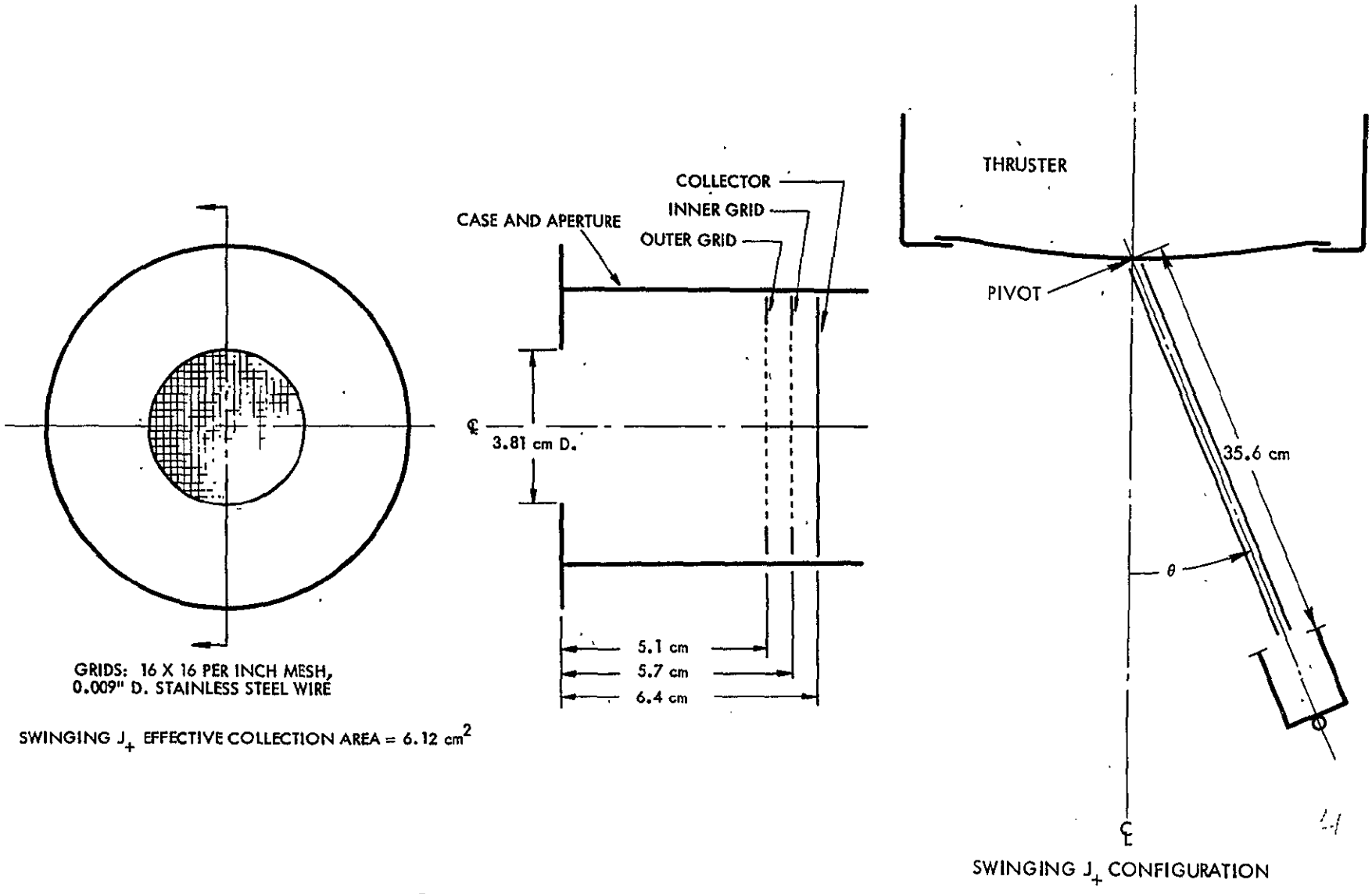

Figure 43. Swinging J_+ Probe Dimensions

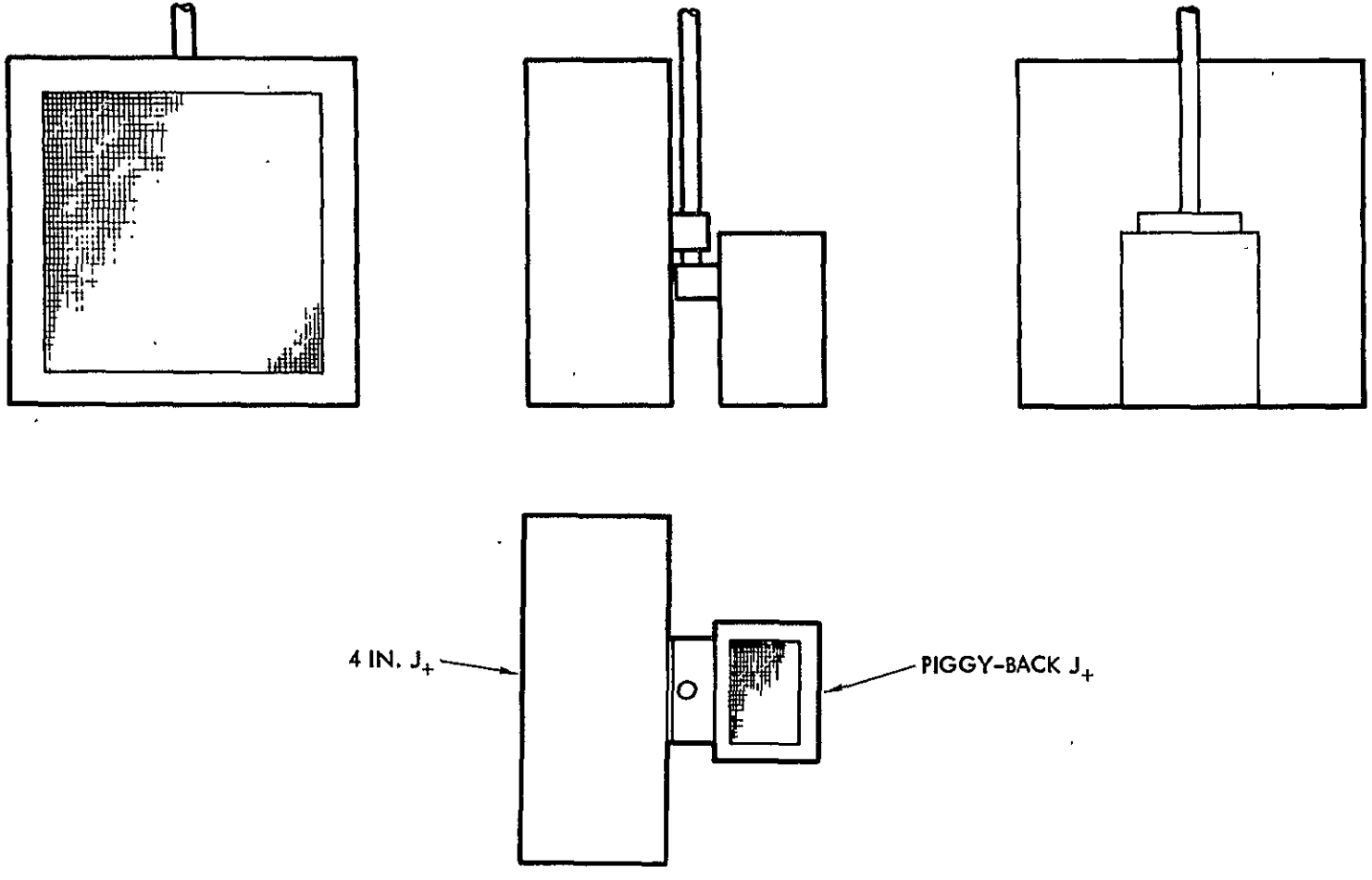

(a) Overall Layout

Figure 44. 4-inch J_+ and Piggy-Back Probe Dimensions

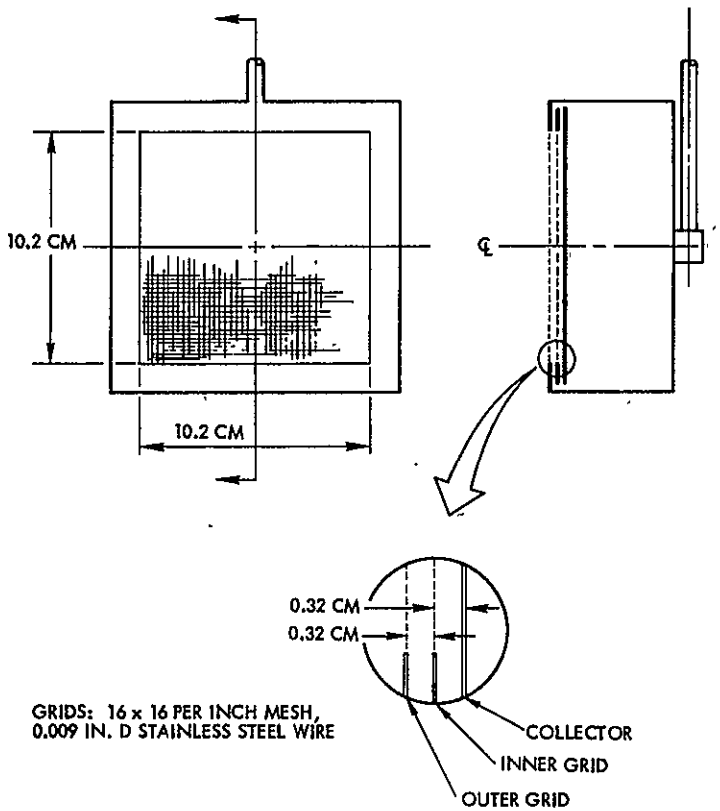

(b) 4-inch J_+

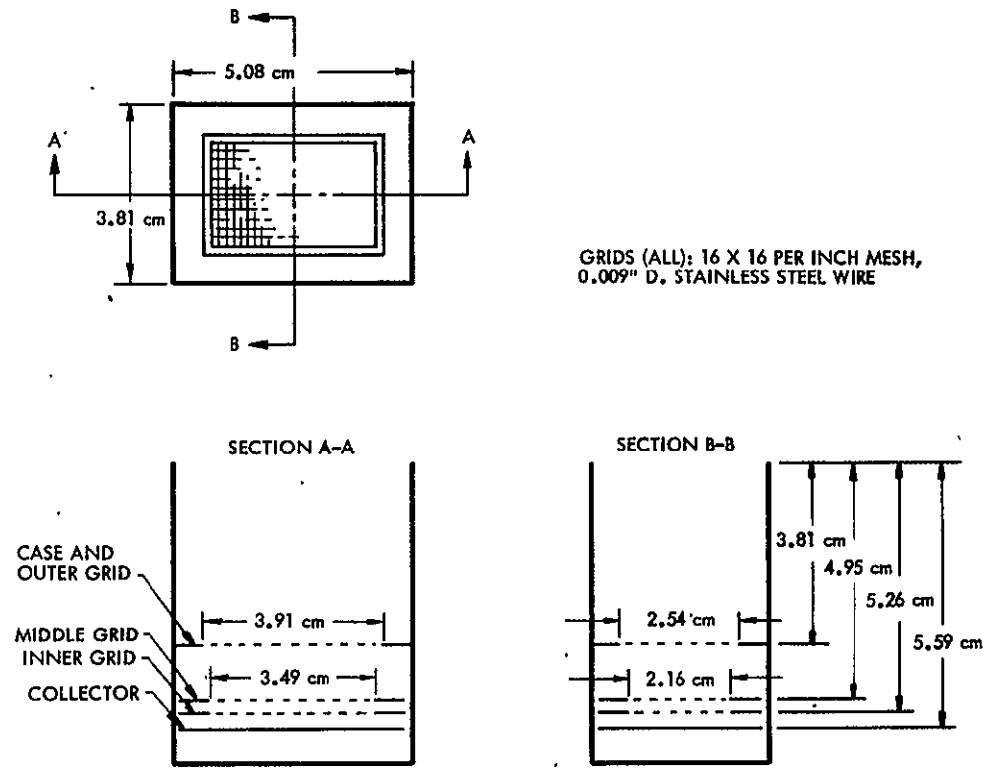

(c) Piggy-Back J_+

Figure 44. 4-inch J_+ and Piggy-Back J_+ Probe Dimensions (Continued)

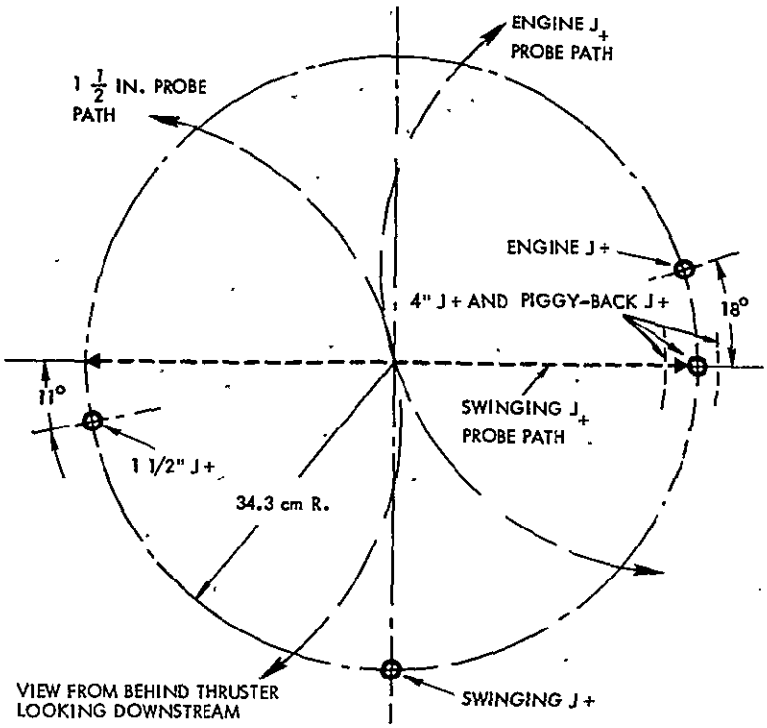

Figure 45. Probe Motion and Mounting Rod Locations

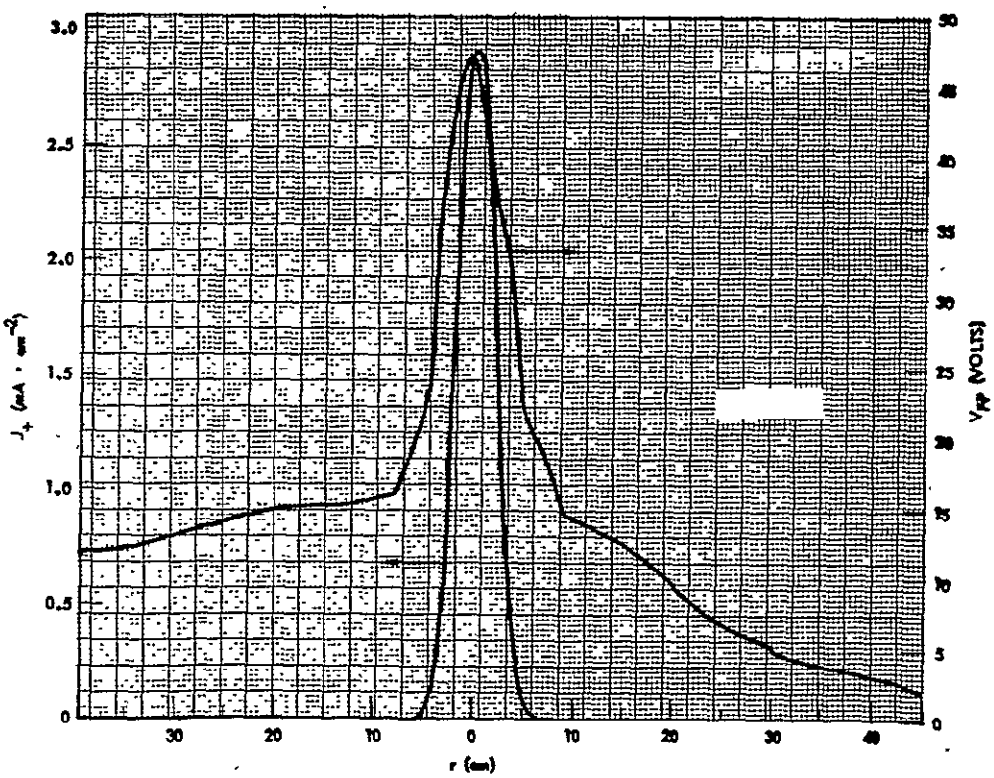

Figure 46. Engine J_+ Probe Data 5 cm Downstream

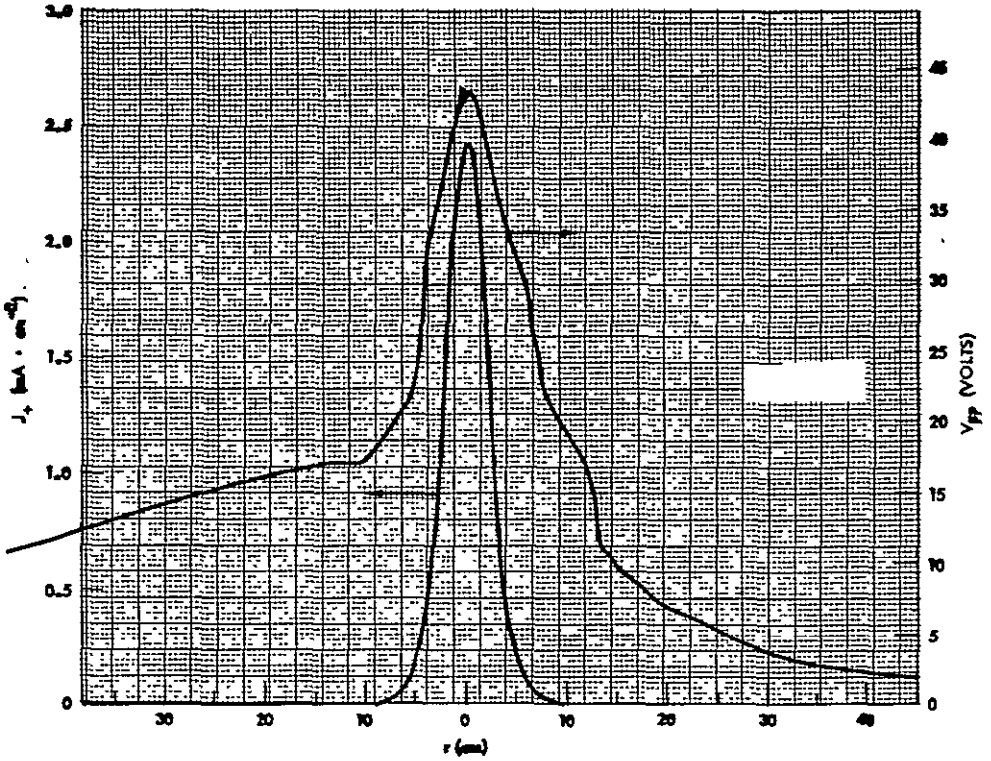

Figure 47. Engine J_+ Probe Data 10 cm Downstream

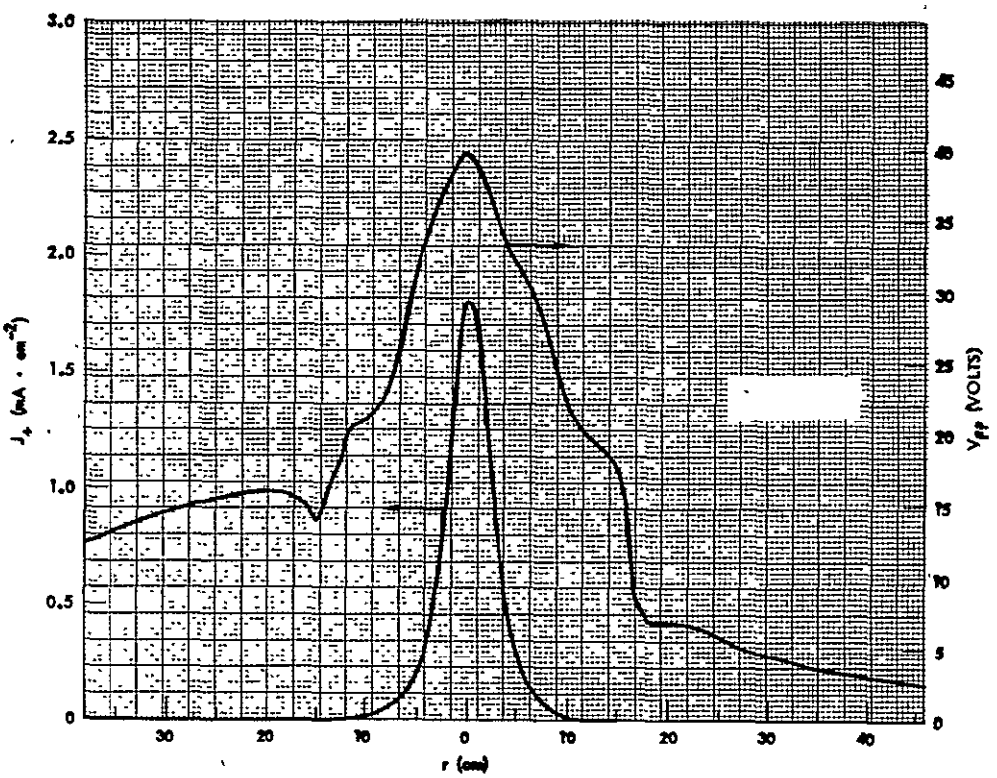

Figure 48. Engine J_+ Probe Data 15 cm Downstream

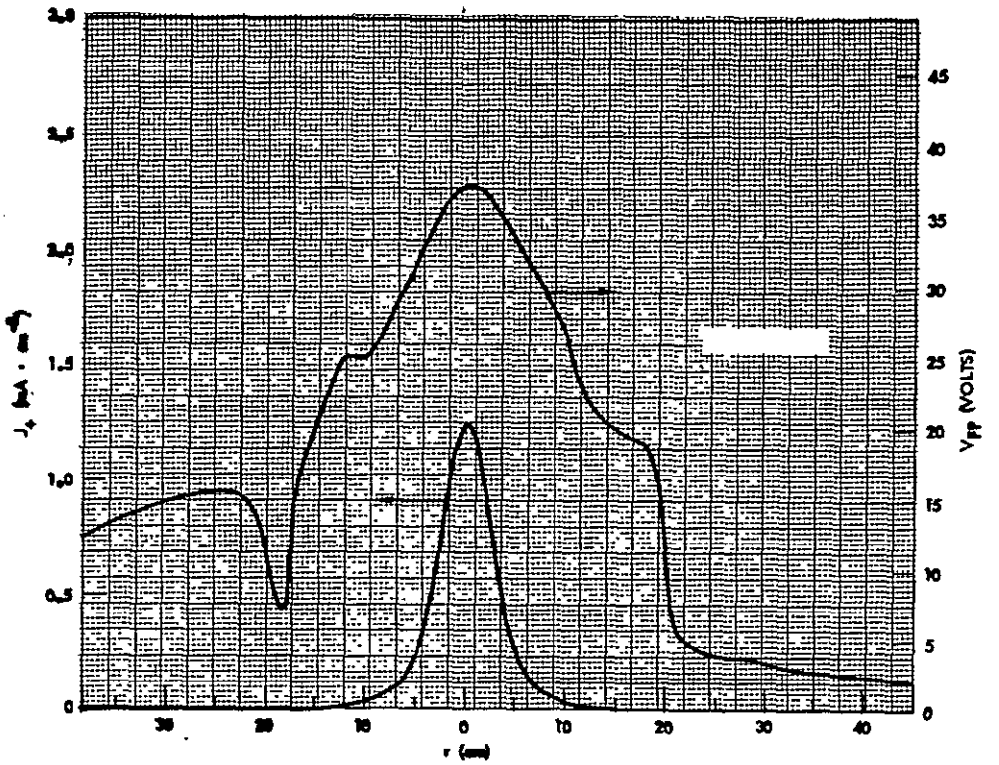

Figure 49. Engine J_+ Probe Data 20 cm Downstream

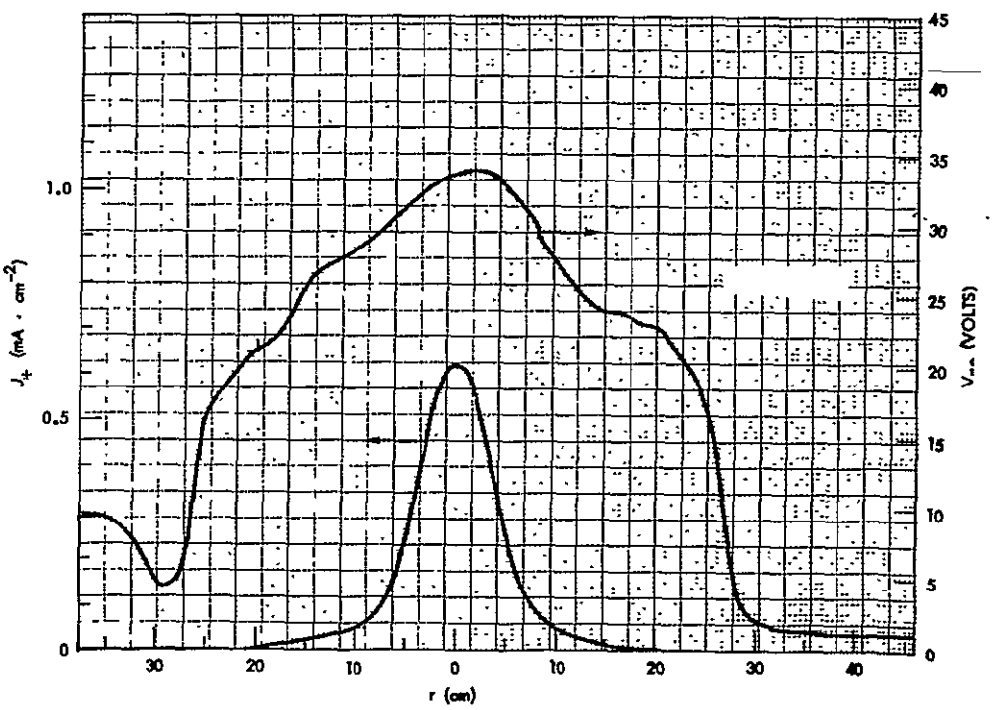

Figure 50. Engine J_+ Probe Data 30 cm Downstream

Figure 46 illustrates $J_+(\alpha)$ at z = 5 cm (z = 0 is the face of the ion accelerator grid at r = 0). The succeeding J_+ curves are at 10, 15, 20, and 30 cm in z. The J_+ probe traces reveal a narrow beam with sharply diminishing J values on either side of the beam axis. The broadening of the current trace for increasing z is evident, with expected fall-offs in the peak value of J_+ at r = 0 for increasing z. (Note change of scale for J_+ at z = 30 cm to provide additional sensitivity in these reduced current density regimes.)

The floating potential, V_{FP}, of the Engine J_+ in the floating probe mode provides a reasonably accurate determination of $V_p - kT_e$ where V_p is the plasma potential at the probe location prior to probe insertion, k is Boltzmann's constant, and T_e is the temperature of the neutralizing electrons in the thrust beam. The combined result of a finite electron temperature and plasma density gradients is a variation in the plasma potential in the thrust beam. For the 30-cm ion engine, the neutralizer coupling to the thrust beam is very strong, and electrons are transported from the neutralizer to the thrust beam with very modest acceleration potentials, usually less than 1 volt. As a result of this small ΔV, the temperature of the neutralizing electrons remains at values of ~1/2 eV. For the 8-cm thruster, however, the reduction in charge exchange ion plasma coupling between the thrust beam and the neutralizer (a likely source of the strong coupling observed in the 30-cm engine case) is no longer present and injection voltages are increased considerably. Other factors which may contribute to the reduced coupling for the 8-cm thruster are the decreased beam divergence and neutralizer plume. In Figure 46, V_{FP} at r = 0 is ~48 volts which is ~34 volts above the keeper potential. It should be noted that the injection voltage between r = 0 (at z = 5) and the neutralizer exceeds this 34 volt figure by ~kT_e since $V_P \sim V_{FP} + kT_e$. To estimate kT_e, the Boltzmann equation may be used ($kT_e = e\Delta V \ln \rho_1/\rho_2$) where ΔV is the potential difference between regions of the plasma thrust beam at density ρ_1 and ρ_2. From the Figure 46 data, the formula above leads to $kT_e \sim 13$ eV. The true plasma potential at r = 0, z = 5 cm then is ~(48 + 13) volts which is ~61 volts. For a keeper voltage of ~14 volts, the injection potential to r = 0, z = 5 is ~47 volts. Using the rule that $kT_e \sim V_{inj}/3$ determined earlier by Bernstein and Sellen (ref. 17) should lead to $kT_e \sim 15.6$ eV, is in comparatively good agreement with the reduced value of 13 eV.

The radial divergence of the ion flow for increasing z leads to plasma density gradients in the z direction, which, in turn, lead to observed gradients in the probe floating potential for axial rotation of the probe. In Figure 47 (z = 10 cm) at r = 0, V_{FP} is ~43 volts, and continuing declines in V_{FP} can be observed from the data in Figures 48 through 50.

The floating probe data discussed above serves to illustrate the problems facing a determination of static electric fields in the plasma beam. Potentials change from one point to another in the plasma beam. In addition, there are changes in the apparent electron temperature resulting probably from the fact that complete Maxwellianization does not occur in the injection region. As the electron distribution moves to regions less positive than (r = 0, z = 0), retardation of the distribution at those points results in a constantly changing and usually diminishing electron temperature.

Other features of the floating potential data in Figures 46 through 50 include asymmetries which are probably the result of the neutralizer positioning and, occasionally, "troughs." The very low values of floating potential in the trough regions are probably in error and result because of reduced ion flux at these points. Those reduced levels of ion flux are insufficient to provide the probe isolation resistor with enough ion current (~0.09 μA per volt of floating potential) and the probe ceases to act as an electrically isolated body. In most of the regions of the plasma thrust beam, the value of $J_+ A_p$ where J_+ is ion flux density and A_p is probe area exposed to the flow, is sufficiently large to maintain the isolation condition (drainage current through the 11 MΩ isolation resistor is small compared to intercepted ion flux), but in the distant wing regions this condition fails. For those regions, probe circuitry must be altered to require even less drainage current or, perhaps, larger area may be introduced into the measuring probe.

Figure 51 illustrates the total ion current signal to the swinging J_+ probe as a function of probe rotation angle θ, where θ is also the polar angle in a polar coordinate system in which θ = 0 is the thrust beam axis. As shown in Figure 51, the ion flux into the probe aperture falls by more than four orders of magnitude in moving from the beam axis to the 90-degree region.

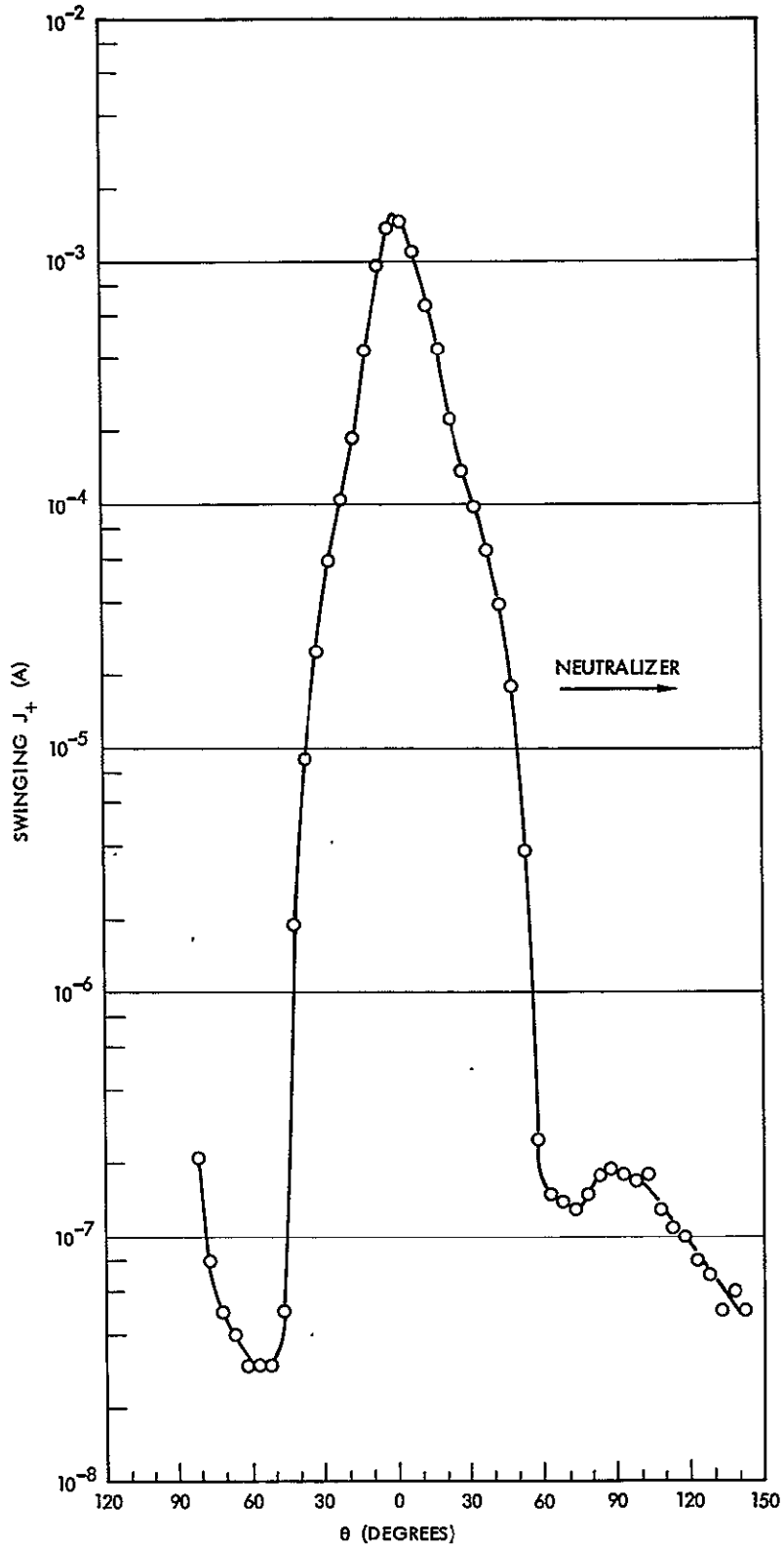

Figure 51. Ion Current Versus Polar Angle

The high angle regions of the swinging J_+ probe have been examined on each side of the beam for total ion flux, and for the hard and soft ion components. These latter measurements are obtained through the use of the probe as a retarding potential analyzer. These ion component scan data are illustrated in Figures 52 and 53. The ion flux groups there are (1) total ion flux for all energies, and with zero volts retardation, (2) hard ions whose energy exceeds 100 eV, and (3) soft ions whose energy lies in the range from 0 to 50 eV. As may be seen in Figure 52, the hard ion component drops rapidly until $\theta = 50$ degrees, and then commences on a "shelf-like" structure. At probe $\theta \sim 70$ degrees, the soft ions from charge exchange in the beam become comparable to the hard ion flux (Group IV comparable to Group II) and for further increases in θ, the soft ion predominance continues. Using the known area of the probe aperture (6.12 cm^2) leads to values of hard ion current density of 10^{-9} amp/cm^2 at $\theta \sim 82$ degrees. Using ϵ notation

$$\epsilon_i = \frac{J_i}{J_B}$$

leads to a location of the ϵ_{+II} contour value of 10^{-8} cm^{-2} at this location. The deposition analysis will generally be concerned with all ϵ contours at values in excess of 10^{-8} cm^{-2} and, on occasion, at the 10^{-9} cm^{-2} level.

Figure 53 illustrates the total, hard, and soft ion components in the swinging J_+ at the other side of the beam. The hard ion shelf, following a precipitous dropoff of J_+ with θ is evident here as it was in the data of Figure 52. Above a θ reading of 68 degrees, the Group IV charge exchange flux predominates. As was observed in the data of Figure 52, the ϵ_{+II} contour at 10^{-8} cm^{-2} is encountered at high θ (~90 degrees).

The data of Figures 52 and 53 bear both similarities and differences. The thrust ion beam was not expected to be without asymmetries and some of these are evident in the data given here. The hard ion shelf (believed to be Group II ions) appears on both beam edges and has approximately the same slope ($\partial J_{+hard}/\partial\theta$) on both edges. The Group IV ion plume appears to have edge-to-edge asymmetries.

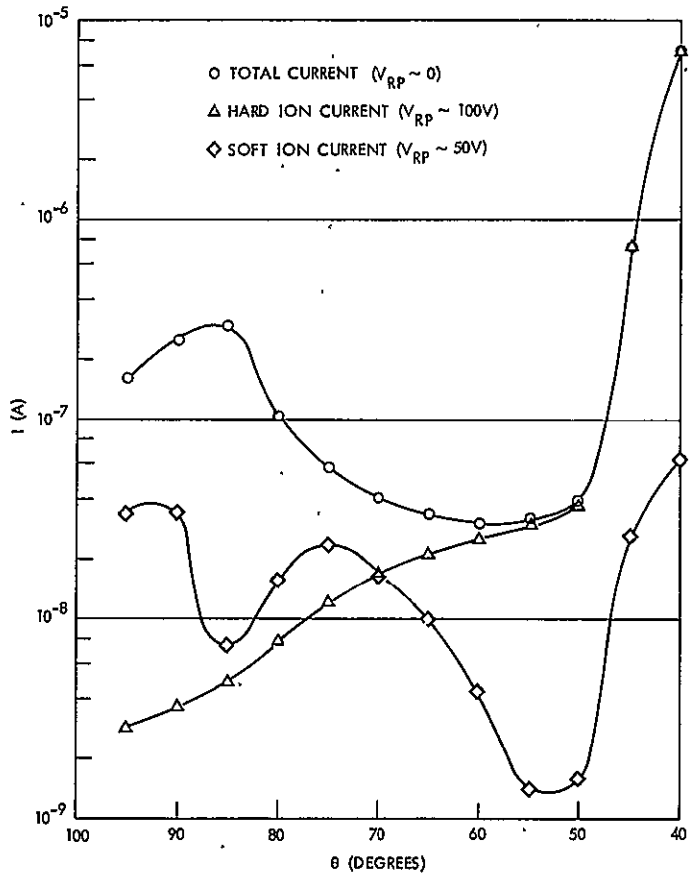

Figure 52. Swinging J_+ RPA Probe Data

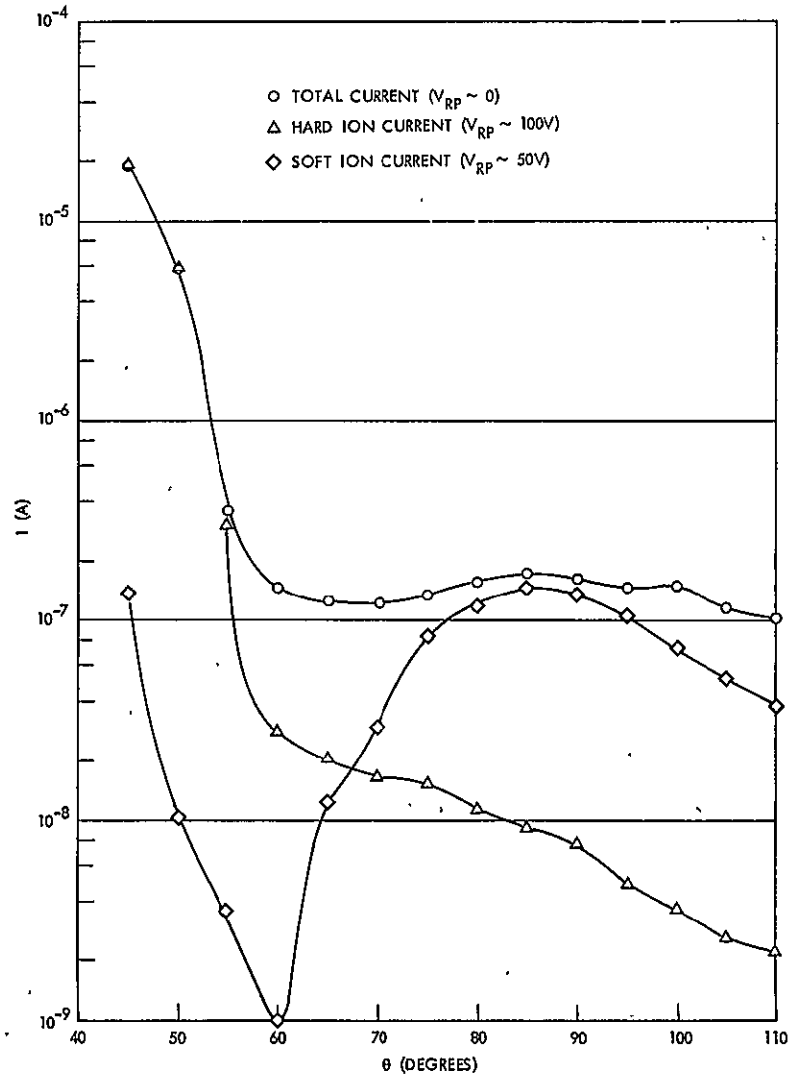

Figure 53. Swinging J_+ RPA Probe Data on Other Side of Beam

ORIGINAL PAGE IS OF POOR QUALITY

Two other probes used in the efflux measurements were the 4-inch J_+ and the Piggy-Back J_+. These probes move in both the forward and backward hemispheres, and, used as retarding potential analyzers, provide measurements of total ion flux and the hard and soft ion flux components. Figures 54 and 55 illustrate the results of these two Faraday cup, retarding potential analyzers.

The 4-inch J_+ signal is predominantly a hard ion signal until z diminishes below ~25 cm (this corresponds to a polar angle of ~48 degrees since the location of the 4-inch J_+ probe surface is at ~28 cm). The hard ion fall-off observed there is the Group II shelf postulated for the swinging J_+ data and perceived somewhat differently here because the present cup motion is along the z direction, and hence alters both θ and R (except for $\theta \rightarrow 90$ degrees). The Group IV ion plume is particularly evident for diminishing z values, with peak soft ion flux at z ~ 10 cm (θ ~ 70 degrees).

The 4-inch J_+ probe continues to record incoming ions for probe motion into the backward hemisphere. It should be emphasized, however, that the currents and current densities are very minute. At z ~ -10 cm (θ ~ 110 degrees) the hard ion signal is 10^{-8} amperes over a cup area of ~100 cm^2 for a $J_{+,hard}$ of ~10^{-10} A/cm^2 which corresponds to an ϵ contour of 10^{-9} cm^{-2}. The soft ion fluxes are considerably larger. Caution should be exercised in probe data interpretation, bearing in mind that the solid angle of acceptance for ion flow may become complicated in these backward hemisphere regions.

Figure 55 illustrates the Piggy-Back J_+ data. This probe accepts ions traveling primarily in the backward direction and has a solid angle for ion trajectory acceptance of ~π steradians and a probe aperture area of ~7.5 cm^2. The ion fluxes observed by the probe are generally considered to be the result of facility effects, but a positive demonstration of this condition remains to be formulated. Regardless of whether the effects are of facility origin or are genuine, the flux levels are at such reduced values (~10^{-10} A/cm^2 for hard ions, z ~ 0) that deposition effects are likely to be insignificant.

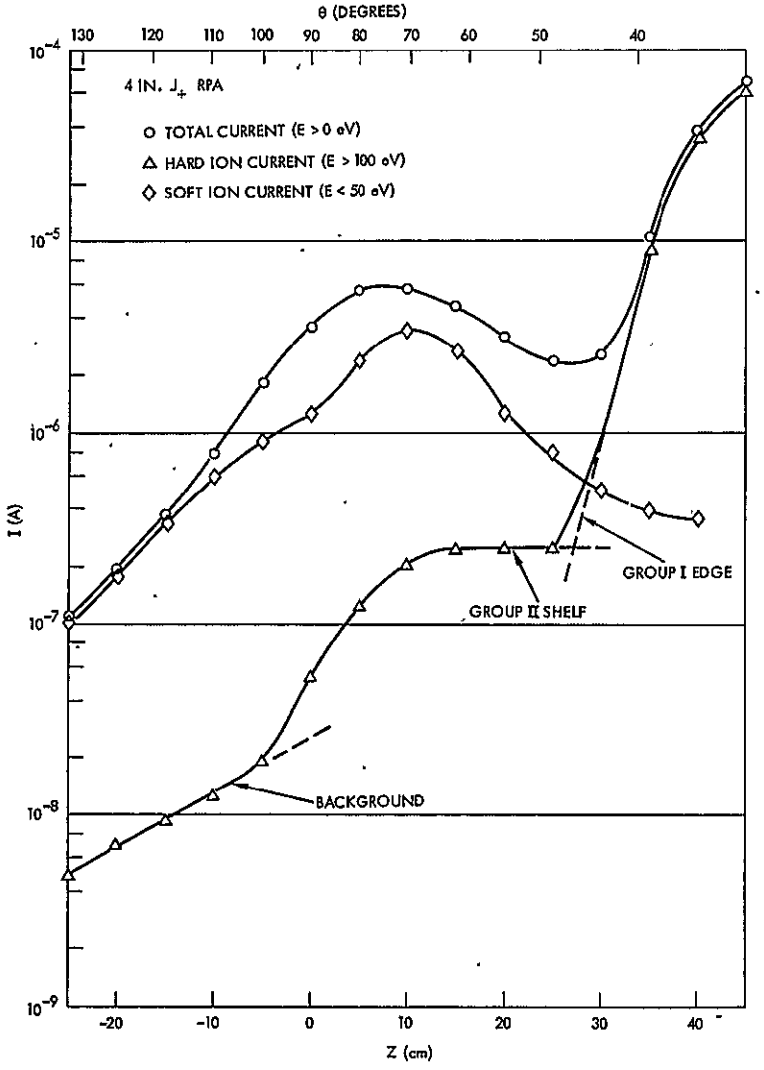

Figure 54. 4-inch J_+ Probe Data

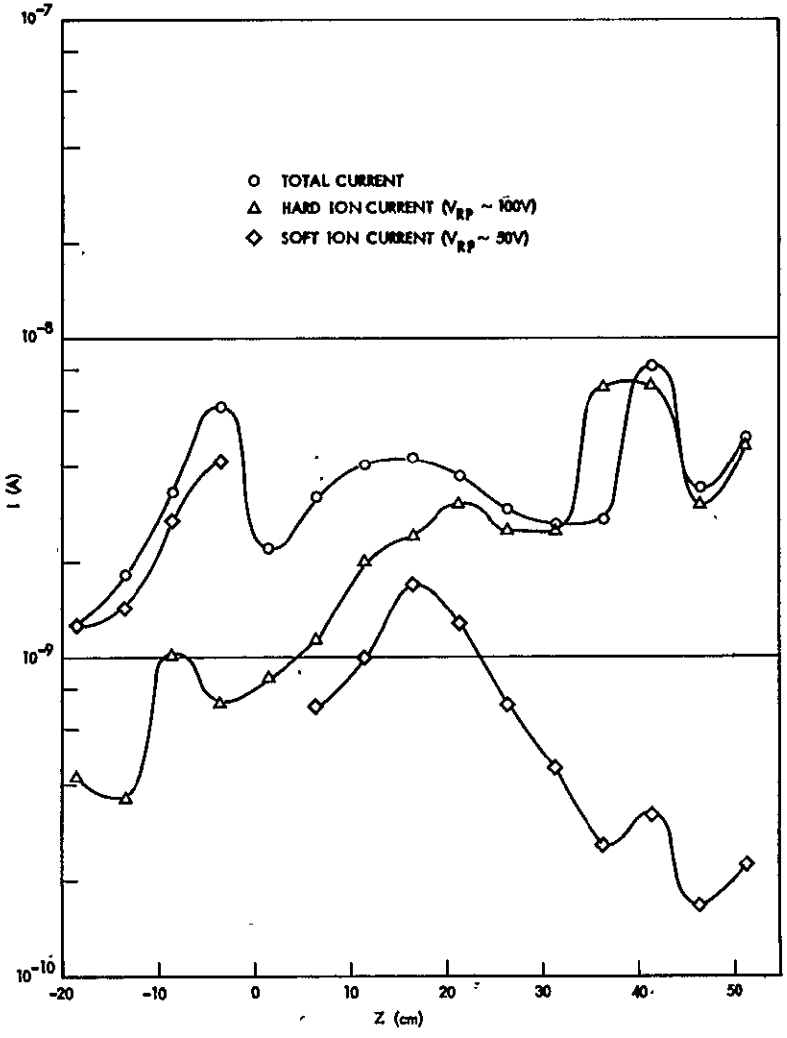

Figure 55. Piggy-Back J_+ Probe Data

ORIGINAL PAGE IS OF POOR QUALITY

4.2.2 Normalized Efflux Determinations

For the charged particles, the description of the particle flow is defined in terms of the normalized efflux. For thrust ions this normalized efflux is

$$\epsilon_{+,t} = \frac{J_{+,t}}{J_B} \tag{12}$$

where $J_{+,t}$ is the current density of thrust ions in amperes per square centimeter at a given point in space and J_B is total thrust beam current in amperes. The units of $\epsilon_{+,t}$ are in cm^{-2}, and the expression in Equation (12) is similar to that given in the other reports except for the change of notation of total thrust ion current to J_B, following the convention for the 8-cm thruster. For the Groups II and IV ions the normalized efflux is

$$\epsilon_{+II} = \frac{J_{+II}}{J_B} \tag{13}$$

and

$$\epsilon_{+IV} = \frac{J_{+IV}}{J_B} \tag{14}$$

where J_{+II} and J_{+IV} are Group II and Group IV flux density in amperes per square centimeter. The specific energy and angular ranges used in specifying either Group II or Group IV ions are described in the separate sections relating to these effluxes.

4.2.2.1 Thrust Ions

Thrust ion efflux contours were calculated from the swinging J_+ probe data. In the analysis given here, the point at which the polar angle, θ, is assumed to be zero is at the peak value of $J_{+,t}$ measured by the probe. In this analysis, there are no corrections for probe backlash, $\Delta\theta$, encountered in the right-angle gear box drive, so that the efflux contour has some θ spreading and tends to overestimate the thrust ion current at high angles. There are, in addition, θ broadening effects due to the finite size of the ion source (8-cm width of the thruster face). In later comparisons of swinging J_+ probe data to current measurements from other probes

(Group II and Group IV measurements), it is seen that $\Delta\theta$ at high angles can be of the order of 10 degrees. This conservative overestimate of the high angle thrust ion flux is preferable to underestimates because some of the thruster wear actions may tend to produce spreading in the thrust ion flux patterns.

Figure 56 illustrates the calculated $\epsilon_{+,t}(\theta)$ at R = 1 meter from the thruster face center. The polar system (R, θ), is used wherever possible and meaningful for data presentation. The presentation in Figure 56 is logarithmic, i.e., the distance from the central point of the plot = $K_1 \log_{10} \epsilon_{+,t} + K_2$ with $K_1 = 1$ division per decade and K_2 adjusted to provide appropriate range. In Figure 56, the peak value of $\epsilon_{+,t} = 4.0 \times 10^{-4}$ cm^{-2} and the range of the plot extends from 10^{-3} cm^{-2} to 10^{-8} cm^{-2}. Values of $\epsilon_{+,t}$ below these levels have not been calculated because of the presence of other current signals which are further examined in the sections that follow.

The 4-inch J_+ probe moves in the axial direction at constant radial position of r = 28.3 cm in an (r, z, ϕ) cylindrical coordinate system. Since this probe is located in the plane containing the thrust beam axis and the neutralizer, and in the plane containing the motion of the swinging J_+ probe, current measurements obtained by the 4-inch J_+ cup can be used as a check against the swinging J_+.

The comparison between the 4-inch J_+ probe and the swinging J_+ probe has three limitations. The first of these is in the solid angle of acceptance for particle trajectories. The 4-inch J_+ admits particle trajectories over $\sim 2\pi$ steradians of solid angle, while the swinging J_+ solid angle of trajectory acceptance is much smaller, of the order of 1 steradian. In principle this variation in solid angle should not be important if the measured flow is directed along the probe axis, as is the case, for example, in the measurement of thrust ions from the thruster. For thrust ion measurements and for Group II ion measurements, the more limited solid angle of the swinging J_+ is, in point of fact, an advantage compared to the 4-inch J_+ whose larger acceptance cone results in an increased acceptance of spurious current signals. For the measurement of Group IV ions, however, the swinging J_+ is probably too narrow in its acceptance cone because of the volume source nature of the Group IV ion

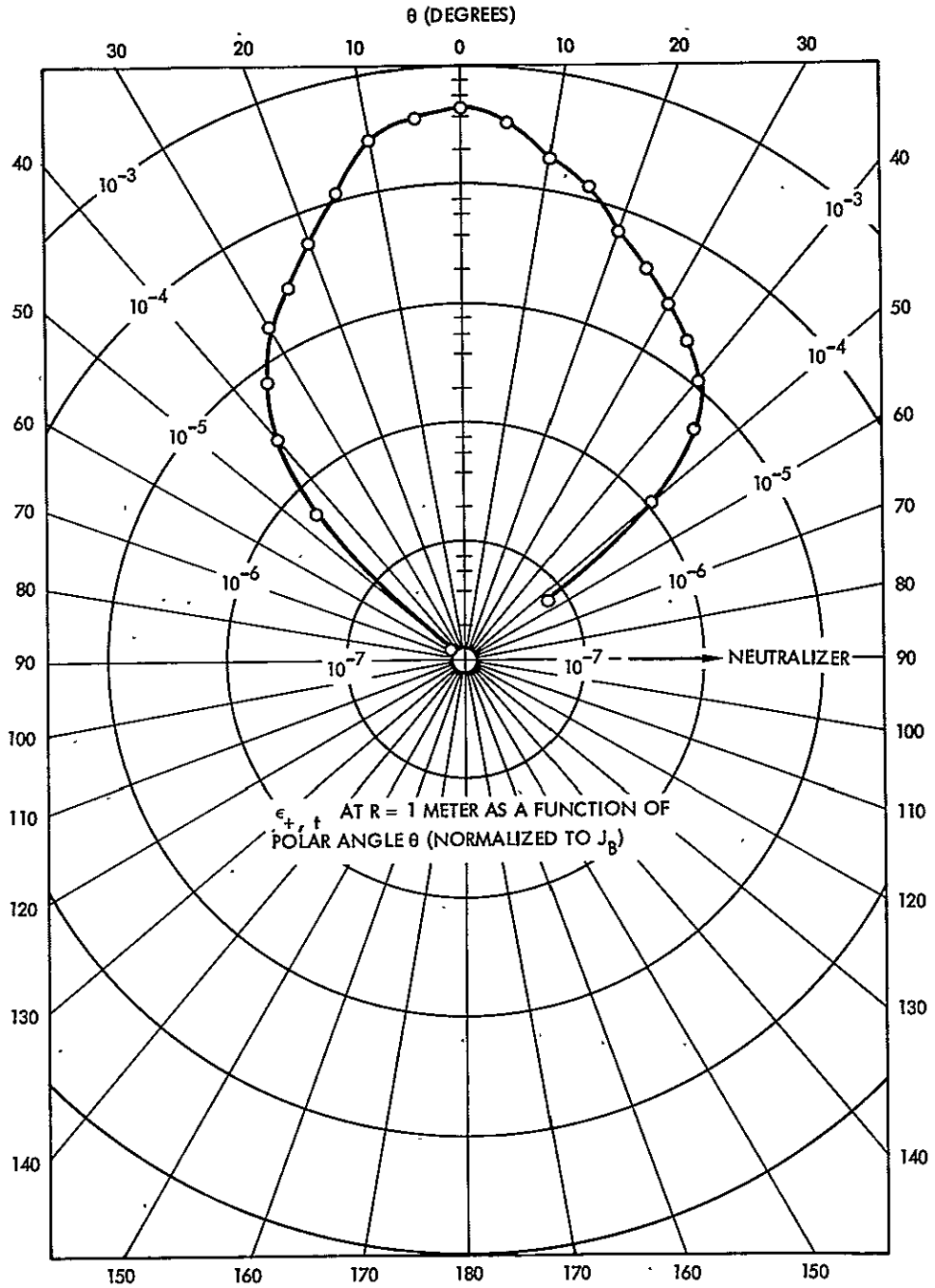

Figure 56. Normalized Thrust Ion Efflux at R = 1 Meter

production. It may, thus, indicate smaller Group IV fluxes than are actually present.

A second difference between the two probes is in the pointing direction of the acceptance cone axis. For the swinging J_+ this axis is always directed through the center of the thruster while for the 4-inch J_+ the probe axis points back through the thrust beam axis. Only for a 4-inch J_+ probe position at $z = 0$ ($\theta = 90$ degrees) will the two probe axes coincide.

A final limitation in the comparison of results from the two probes is in the cup opening area. Here the 4-inch J_+ is much broader than the swinging J_+ and is, thus, subject to some error in interpretation of measured current because of finite detector size effects. In spite of the limitations discussed above, it will be of interest to compare the results from the two probes in certain angular regimes (principally at high angles) and for certain ion species (in particular, for Groups II and IV ions). Probe thrust ion signals were not compared because of the very rapid falloff at higher angles of the thrust ion flux and because of the detector width in the 4-inch J_+. The 4-inch J_+ probe is more appropriately used for comparisons in swinging J_+ on Groups II and IV fluxes where the rates of change in z (or in θ) are less rapid and, hence, do not result in excessive errors in interpretation because of finite detector size.

Figure 54 illustrates the total current in the 4-inch J_+ probe as a function of axial position, and the hard and soft components of that current. The soft component is primarily charge exchange Hg+ (Group IV) while the hard component is either Group I (thrust ions) or Group II ions, depending on the z value of the probe. Figure 54 also illustrates certain interpretations of the probe signal. The precipitous decline in the hard component of the ion current for decreasing z (but $z \gtrsim 28$ cm) is considered the exponential wing of the Group I (thrust) ions. Near $z = 28$ cm there is a major change in the character of the hard ion current as it moves from precipitous decline to a flat shelf. This structure is believed to be Group II ions from a variety of experimental findings and is termed a Group II shelf. For diminishing z, these Group II ions will gradually fall away, leaving a background signal which is believed to be hard ions resulting from facility effects. The probe data demonstrates the necessity for a cutoff in the $\epsilon_{+,t}$ contour in the angular range

above approximately 50 degrees. This cutoff is warranted not only because of a competition between two species of energetic ions but also because of the relatively large flux of soft ions whose turnaround in the interspace between the grids of this retarding potential analyzer can create a small, but nevertheless significant, noise effect if the ion specie under examination is much more dilute than these other ion signals.

Facility effects are not considered important for thrust ion measurements for two reasons. First is the comparatively high magnitude of the thrust ion signal over most of the angular regimes examined, thus making background signals of less importance. Second is that the swinging J_+ probe employed has a limited solid angle for the acceptance of ion trajectories and, hence, is less influenced by chamber effect ions.

4.2.2.2 Group II Ions

Figure 57 illustrates the normalized efflux contour, ϵ_{+II}, of the Group II ions as a function of θ at R = 1 meter using swinging J_+ probe data. The shelf-like structure above $\theta \sim 50$ degrees in the data is attributed to Group II ions. As may be seen from the curves in Figure 57, the ϵ_{+II} values are in the range from 10^{-8} cm^{-2} to less than 10^{-9} cm^{-2}.

The two portions of the contour also appear to be displaced somewhat relative to $\theta = 0$. Because it is possible to compare the results of the swinging J_+ probe with the 4-inch J_+ probe for this ion specie, there has been no attempt at θ correction in the data given in Figure 57. As is seen from other probe measurements, the θ values given in the figure for the "+θ" contour (neutralizer side) are probably high by about 10 degrees.

Figure 58 illustrates the normalized efflux contour, ϵ_{+II}, for Group II ions as a function of polar angle θ at R = 1 meter using the 4-inch J_+ probe data. The expression of ϵ_{+II} in a polar plot is in keeping with other data presentation. It should be reemphasized, however, that the 4-inch J_+ probe is primarily a radially viewing probe in a cylindrical coordinate system with an axial, z, motion and, although the probe results can be stated in any coordinate representation, the viewing directions of the probe are not precisely those desired for polar plotting. These considerations may not be overly

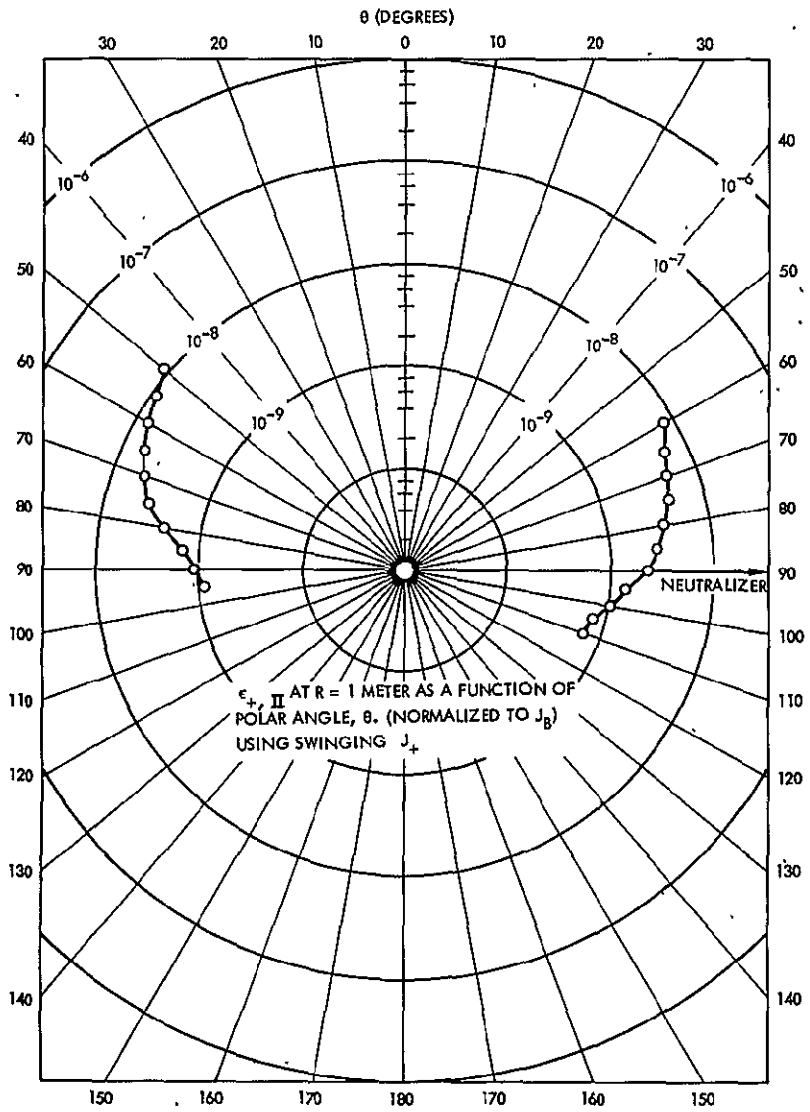

Figure 57. Normalized Group II Ion Efflux at R = 1 Meter from Swinging J_+ Probe Measurements

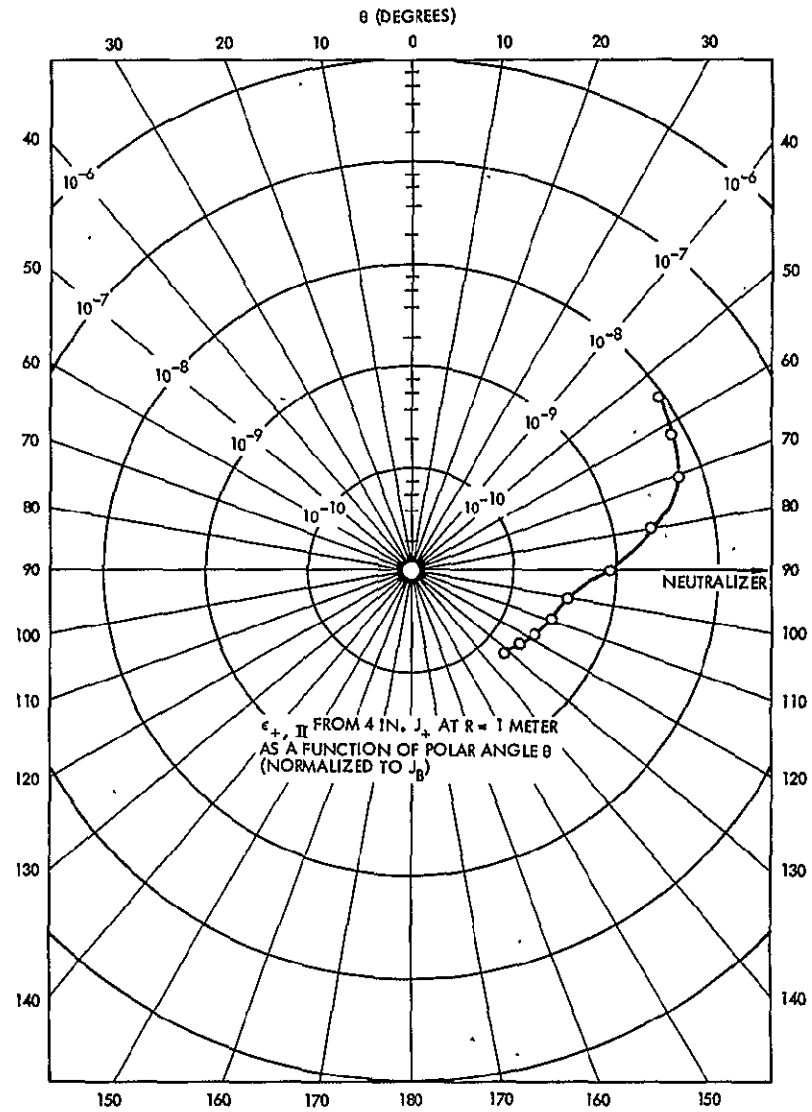

Figure 58. Normalized Group II Ion Efflux at R = 1 Meter from 4-inch J_+ Probe Measurements

important, however, because the 4-inch J_+ probe does possess a large cone of acceptance directions.

When the results of Figure 58 are compared to those of Figure 57, two features are evident. To assist in this comparison, Figure 59 presents the $\epsilon_{+,II}$ values from both the swinging J_+ (+θ side) and the 4-inch J_+. From the data given there it may be seen that near θ = 90 degrees a downward shift of the swinging J_+ probe θ is required to bring both probe results into agreement. This required θ shift of ~10 degrees appears to be a proper action. If this θ shift is done, however, the $\epsilon_{+,II}$ values are no longer in agreement at smaller θ values. As noted above, it is expected that the 4-inch J_+ will be more susceptible to facility effect signals than the swinging J_+ (because of the large cone of acceptance directions in 4-inch J_+), and, thus, the determined values of $\epsilon_{+,II}$ from the 4-inch J_+ should exceed those of the swinging J_+. The precise amount of extra signal in 4-inch J_+ compared to swinging J_+ because of facility effects cannot be stated. Some of these facility effects are discussed in greater detail below. For present purposes it appears reasonable that the θ value of the $\epsilon_{+,II}$ data from swinging J_+ should be displaced ~10 degrees downward and that the $\epsilon_{+,II}$ curve so obtained is then somewhat below the $\epsilon_{+,II}$ curve from the 4-inch J_+ by relative amounts of ~10% to ~20%.

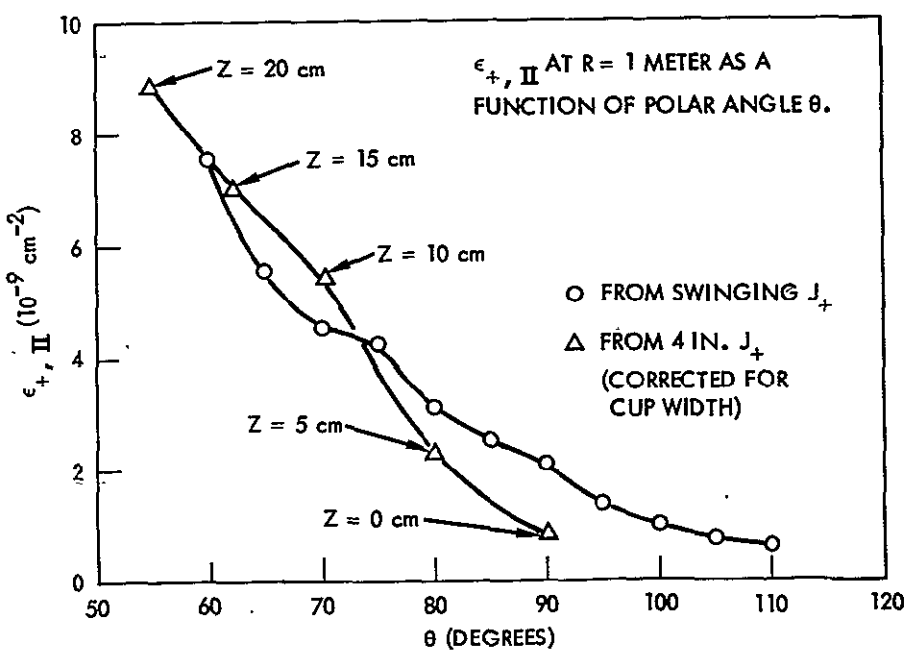

Figure 59. Comparison of Normalized Group II Ion Efflux from Swinging J_+ Probe and 4-inch J_+ Probe Data

In the 4-inch J_+ hard ion signal in Figure 54, and for $z < 0$ cm, it is apparent that energetic ions are present which cannot be accounted for by line-of-sight motion from the face of the thruster to the probe. Piggy-back J_+ probe data also acknowledge measureable levels of hard ion signal in the backward direction. There is, thus, a ubiquitous hard ion signal at comparatively low levels which requires explanation.

Before attempting explanation, it should be noted that the ϵ values for these suspected facility effects are in the range below 10^{-9} cm^{-2} and, hence, could result from comparatively improbable processes. For example, if a current of thrust ions, J_B, encounters a distant metallic collecting surface and if a fraction, β, of these ions reflect with a retention of at least 10% of the incident ion kinetic energy, then this collector is a virtual source of βJ_B facility effect hard ions. If these ions expand into π steradians of solid angle in moving in the backward direction, their current density at the location of the thruster would be

$$J_{+,\,refl} \sim \frac{\beta J_B}{\pi L^2} \tag{15}$$

where L is the distance from the collector to the thruster. These spurious hard ions would have an ϵ value of

$$\epsilon_{+,\,refl} \sim \frac{\beta}{\pi L^2} \tag{16}$$

and, for $\beta = 10^{-4}$, and $L = 2 \times 10^2$ cm, $\epsilon_{+,\,refl}$ would be $\sim 10^{-9}$ cm^{-2}. Such a value is not markedly different than those indicated in the data of Figures 54 and 58. This is not to state that such a reflection process is present at the level of 10^{-4} of the incident ions, but merely to note that, because the current measurements have been carried out to very sensitive levels, even an improbable process can contribute detectable signal levels.

Another possible process to consider is that of the sputtering of an energetic neutral from the thrust beam collector surface. If 10^{-3} energetic Hg^o atoms are sputtered from the target for each incident Hg^+ ion, and if 10^{-1} of

these energetic neutrals charge transfer to Hg^+ in their backward passage through the ion beam plasma, then, again, a hard ion, facility effect signal at the $\epsilon \sim 10^{-9}$ cm^{-2} level would be present.

There is no direct evidence that either of the two discussed reactions above is, in point of fact, responsible for the spurious hard ion signals. Perhaps some other mechanism is the cause of these energetic ions. The signal level of facility effect hard ions can, however, be estimated and, for the 4-inch J_+ probe is probably at less than 10^{-9} cm^{-2} at 1 meter and $\theta = 90$ degrees. For the swinging J_+ probe, whose cone of acceptance directions is of smaller size than that of the 4-inch J_+, these facility effect ϵ values are probably less than 5×10^{-10} cm^{-2}.

4.2.2.3 Group IV Ions

Figure 60 illustrates the normalized efflux contour $\epsilon_{+,IV}$ for the Group IV ions as a function of polar angle θ at R = 1 meter for the swinging J_+ probe data. Two features of the data given in Figure 60 are of interest. The first is the marked asymmetry in the Group IV efflux, with substantially larger ion signals at $+\theta$ (neutralizer side) than at $-\theta$. This is clearly the result of an additional neutral Hg^o emission with which the thrust ions may charge transfer. Another soft ion generating process is direct Hg^+ emission from the neutralizer plume.

A second feature of interest in the Figure 60 data is the magnitude of $\epsilon_{+,IV}$ which crests at values near 10^{-7} cm^{-2}. This high level of deposition, however, is probably of lesser concern that that experienced by $\epsilon_{+,II}$, because the lower energy Group IV ions are not capable of the sputtering damage of the more energetic Group II ions. If the interactive effect of concern, however, between a spacecraft and the thruster plasma plume is that of electron or ion drainage to exposed (or partially insulated) high voltage surfaces, then the Group IV deposition density becomes very much of concern. This possibility of plasma deposition effects is one of the factors indicating that the neutralizer placement should be in the deepest portions of the thruster sputter shield, thus blocking off much of this high level (neutralizer side) Group IV emission.

Figure 61 illustrates the normalized efflux contour $\epsilon_{+,IV}$ for the Group IV ions as a function of polar angle θ at R = 1 meter for the 4-inch J_+ probe data. When these data are compared to Figure 60, it may be seen that, again, the 4-inch J_+ signals for an ion specie predict higher ϵ values than for swinging J_+ measurements. The reason for this higher signal level is, again, a larger cone of acceptance directions in the probe. For the Group IV ions, however, it is more desirable to possess a larger acceptance cone because these particles emerge from a volume source and are not totally detected by more narrowly opening probe structures. In the instance of this ion specie, the 4-inch J_+ probe data are probably the more accurate of the two probes, in spite of larger expected facility effect signals.

The previous section on Group II ions has indicated that the θ values for the swinging J_+ probe should be reduced by ~10 degrees. With this θ shift, it may be seen that the peak in $\epsilon_{+,IV}$ would occur at approximately the same place for both probes (θ_{max} ~ 75 degrees for SJ_+, θ_{max} ~ 70 degrees for 4-inch J_+) and that the peak ϵ values differ by a factor of ~2. Because some of the 4-inch J_+ signal is expected to be an increased level of facility effect ions, an average of the two probe signals may be appropriate. That signal average would then be expected to be within 25% to 30% of the actual Group IV ϵ values.

Group IV facility effect ions result primarily from the charge transfer reaction between Hg^+ thrust ions and ambient chamber mercury atoms. The relative abundance of engine neutrals to chamber neutrals will depend upon the propellant utilization efficiency of the thruster and the pumping effectiveness of the thruster test facility. For the 30 cm thruster in the 5- by 10-foot facility, the 1 to 2 ampere levels of operation result in chamber ionization pressure gauge readings in the range from 2×10^{-6} to 4×10^{-6} torr. For the smaller beam levels of the 8-cm thruster, lower readings of chamber pressure of the order of 4×10^{-7} torr are obtained. While these ion gauge readings are of some interest, it should be noted that other chamber gases are present in addition to Hg^o and that neither of the readings above is directly indicative of the level of chamber Hg^o.

In addition to the factors discussed above, there are many configurational aspects to the facility effect signal relative to genuine signal. For example, the engine Hg^o rapidly reduces in density as the atoms move away

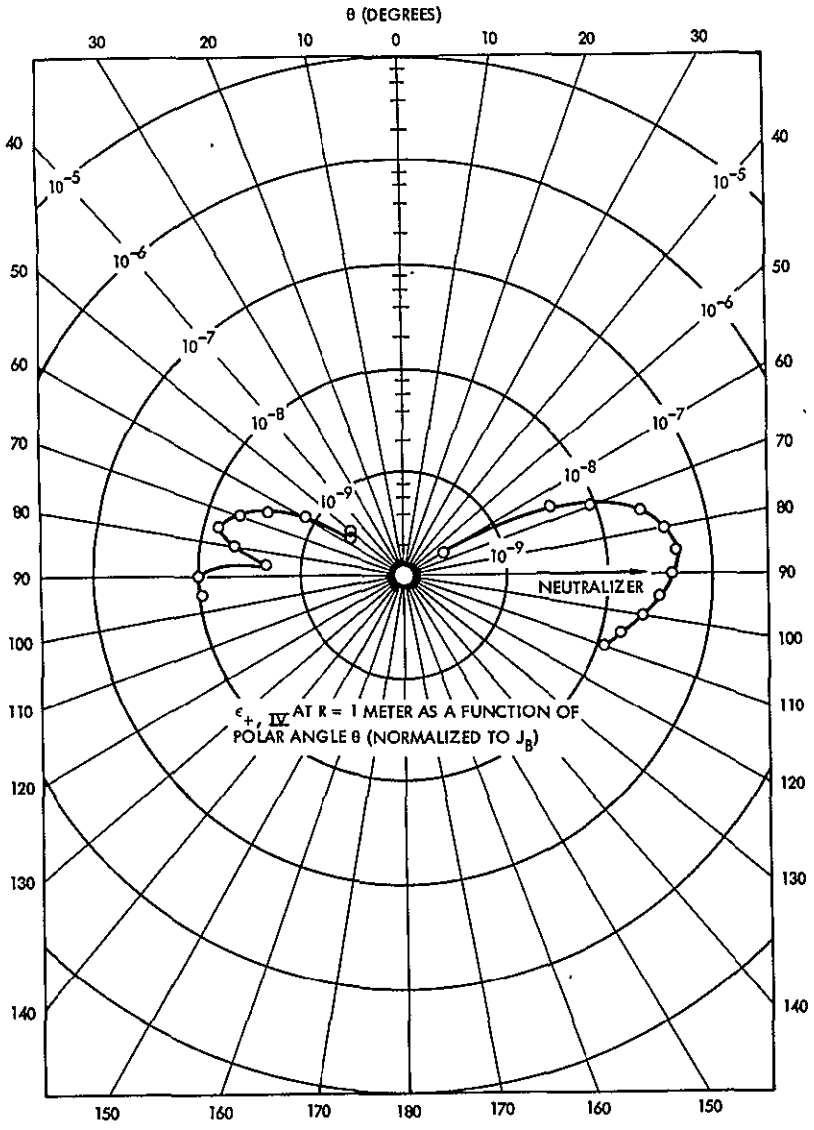

Figure 60. Normalized Group IV Ion Efflux at R = 1 Meter from Swinging J_+ Probe Measurements

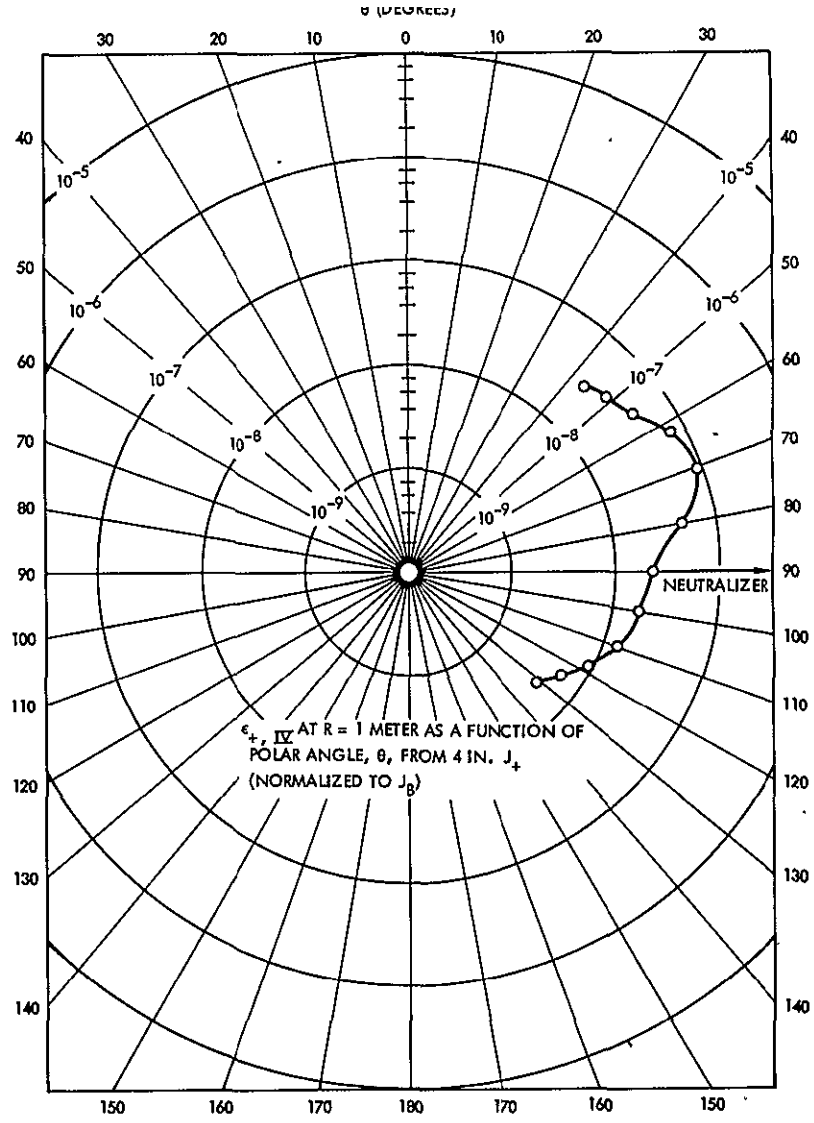

Figure 61. Normalized Group IV Ion Efflux at R = 1 Meter from 4-inch J_+ Probe Measurements

from the thruster. Thus, while engine neutrals may be much more dense than chamber neutrals near the thruster, for points more distant from the thruster these density ratios may be reversed. To reduce facility effect noise levels, then it is recommended that measurements of Group IV ions be carried out in the regions near the thruster.

Some estimate of facility effect Group IV signals can be obtained by an examination of probe readings in the backward hemisphere ($\theta > 90$ degrees). It should be emphasized, however, that Group IV ion motion can occur over a broad range in directions (as distinguished from Group II ions and thrust ions). From an examination of the 4-inch J_+ data at $z = 0$ it may be estimated that the facility effect $\epsilon_{+,IV}$ at $z = 0$ ($R = 1$ meter, $\theta = 90$ degrees) is $\sim 1 \times 10^{-8}$ cm^{-2}.

4.2.2.4 Piggy-Back J_+ Probe Measurements

The discussion of Piggy-Back J_+ probe results does not follow the format used earlier for the 4-inch J_+ and swinging J_+ probe results. The reasons for this change in discussion are, first, because this probe examines primarily facility effect currents, and second, because a representation of probe data in a polar plot form is not appropriate. Instead, the data are given as a function of probe position, z, at the radial location of the probe entrance ($r \sim 36.8$ cm).

Figure 62 illustrates the value of $\epsilon_{+,hard}$ for hard ions (energies above 100 eV) for $-20 < z < 50$ cm. Although there is some scatter in the probe current data, the results can be generally fitted with a straight line ($\epsilon_{+,hard} \alpha \exp\{-kz\}$). The slope of this straight line is somewhat less than the slope of the line for the hard ion signal in the 4-inch J_+ for $z < 0$ (Figure 54). Nevertheless, both of these signals have approximately the same behavior and both are, apparently, a portion of the ubiquitous hard ion signal discussed earlier. From an examination of the data in Figure 62, the ϵ value of this hard ion facility effect is $\sim 3 \times 10^{-9}$ cm at $z = 0$. This estimate of facility effect level is generally consistent with the earlier estimate of facility effect $\epsilon_{+,II}$ of 10^{-9} cm^{-2} at $\theta = 90$ degrees, $R = 1$ meter.

The remaining Piggy-Back J_+ data are illustrated in Figure 63 where $\epsilon_{+,soft}$ is given as a function of z at the $r = 36.8$ cm (cylindrical) position of the probe. The peak levels of this signal are $\sim 10^{-8}$ cm^{-2} near $z = 0$ which is

generally consistent with the estimates of facility effect Group IV levels of 10^{-8} cm^{-2} from the 4-inch J_+ probe data for z = 0 (R = 1 meter, θ = 90 degrees). The dropoff in the facility effect soft ions in this probe for increasing z is not consistent, however, with the general notions of the production of those facility effect ions. It may be that the flow directions of facility effect Group IV are primarily radially outward (in a cylindrical coordinate system) in these z regions and, thus, would be only fractionally detected in the Piggy-Back J_+ whose principal viewing directions are for particles moving in the backward direction.

4.3 THRUSTER SPUTTER SHIELD

Factors in the design of a sputter shield for the 8-cm mercury bombardment engine are discussed in Appendix D. In the discussion there, three configurations of a sputter shield are examined. These configurations include a "slashed cylinder," a "truncated slashed cylinder," and a "rectangle." After a review by NASA-LeRC, the slashed cylinder design was selected, and a titanium sputter shield was fabricated and installed on the 8-cm mercury ion thruster. Figures 64 and 65 illustrate the sputter shield both separately and in its mounted position on the thruster. The orientation of the sputter shield relative to the thruster was specifically chosen so that the plasma discharge neutralizer is placed in the most enclosed portion of the shield. This orientation acts to prevent the deposition of sputtered metal atoms from the neutralizer on adjacent spacecraft surfaces. Other details and dimensions of the sputter shield are discussed in Appendix D.

4.4 SHIELDED CHARGED PARTICLE EFFLUX

The charged particle measurements taken without a shield were repeated after the shield described in Section 4.3 was installed on the thruster.

4.4.1 Engine J_+ Faraday Cup Measurements

The Engine J_+ probe was used for scans of thrust ion current density in an (r, z) cylindrical coordinate system in which r = 0 is the axis of the thrust beam. The probe elements were also used in an electrically floating mode to obtain the plasma floating potential in the neutralized plasma thrust beam.

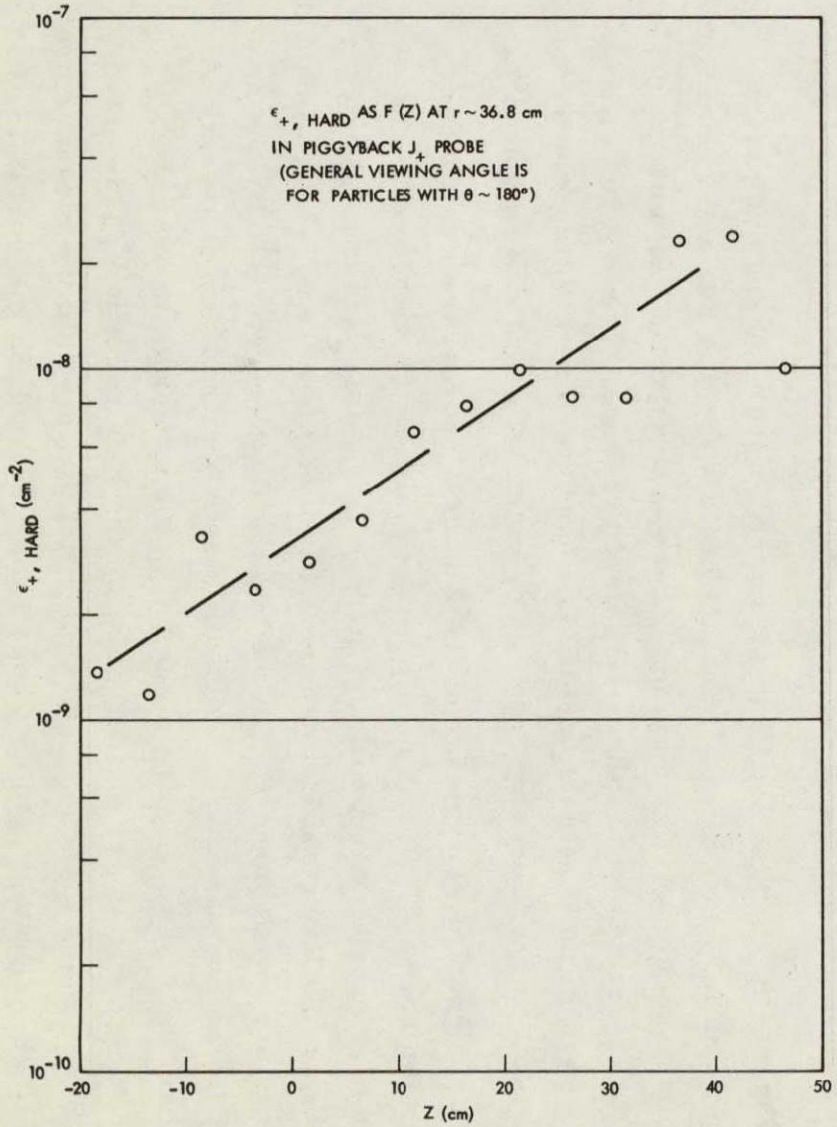

Figure 62. Normalized Hard Ion Efflux at the Piggy-Back J_+ Probe

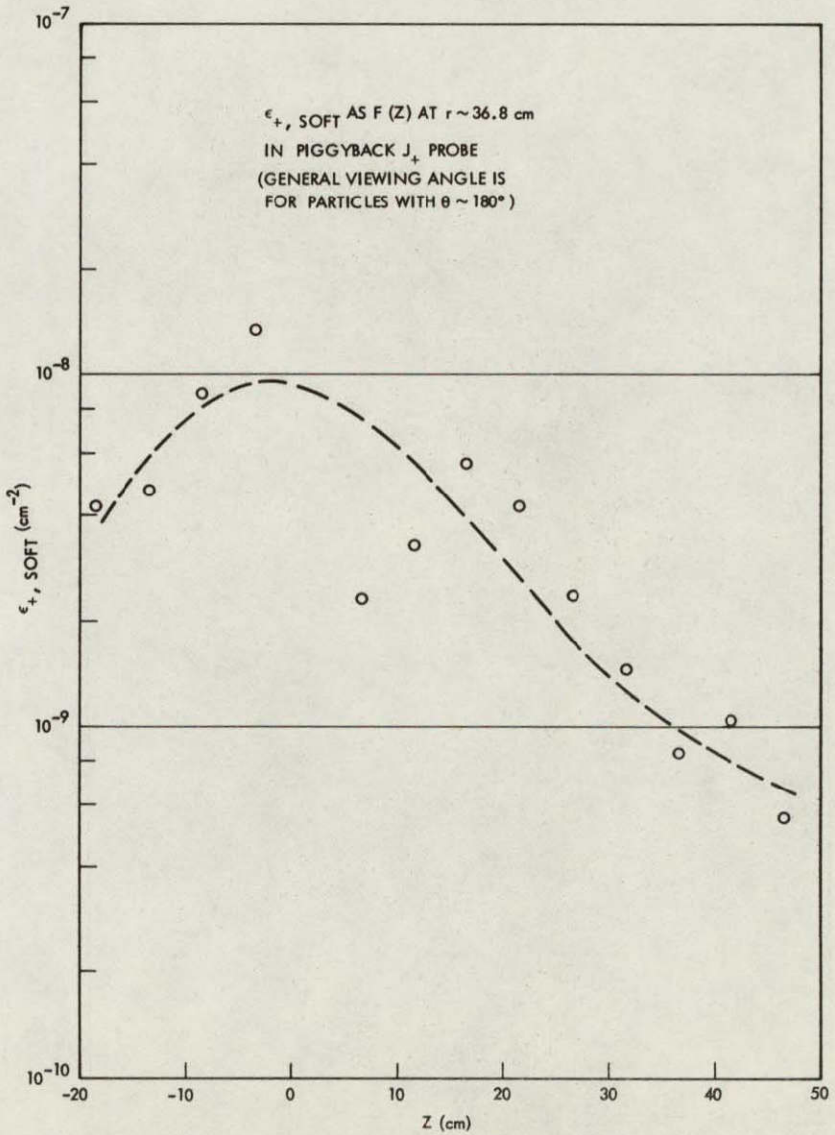

Figure 63. Normalized Soft Ion Efflux at the Piggy-Back J_+ Probe

ORIGINAL PAGE IS
OF POOR QUALITY

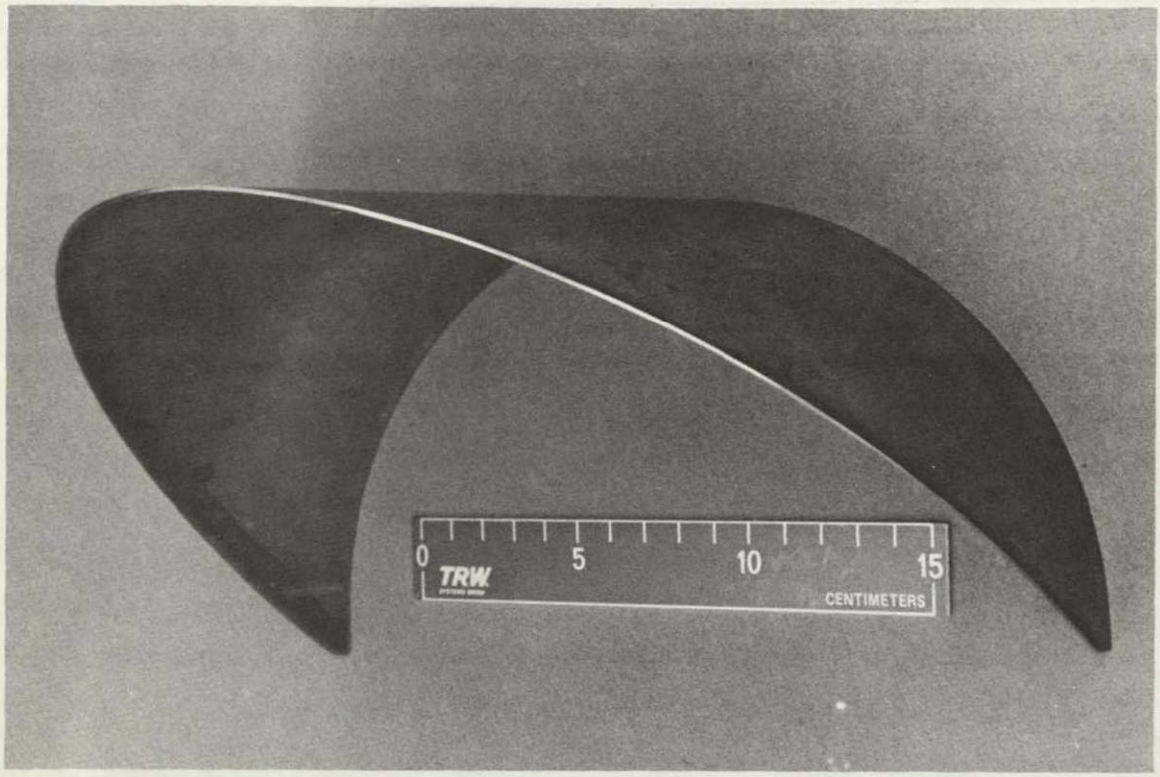

Figure 64. Thruster Sputter Shield

Figures 66 through 69 illustrate current density scans and plasma floating potential scans at axial distances of z = 20, 25, 30, and 35 cm from the thruster accelerator grid plane. These scans did not examine the regions of smaller z because of the thruster shield presence. For $z \geq 20$ cm, however, the arc of the Engine J_+ probe does not interfere with the sputter shield and complete current density and floating potential scans can be obtained.

The current density scans of the Engine J_+ reveal the narrow 8-cm thruster ion beam. There is no significant shift of the measured thrust ions in these near axial regions with the sputter shield installed from those current density profiles obtained with the sputter shield absent. A significant difference is observed, however, in the plasma floating potential for the sputter shield present compared to the measurements obtained with it absent. At z = 20 cm, the plasma floating potential on the thrust beam axis clearly exceeds the 47-volt upper end set point on the X-Y recorder. It is only at the z = 30 cm plane that the floating potential drops within the measurement band of the present test setup. These values exceed the measured floating

ORIGINAL PAGE IS
OF POOR QUALITY

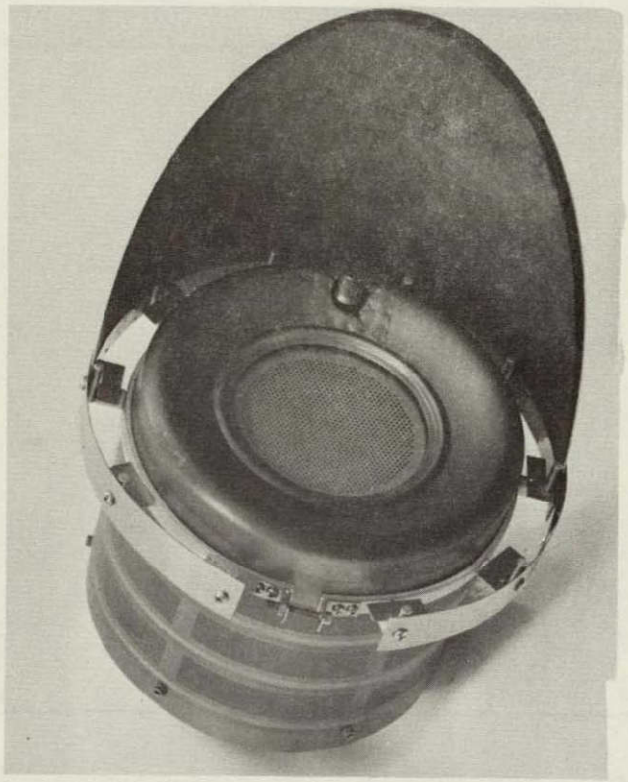

(a) Front View

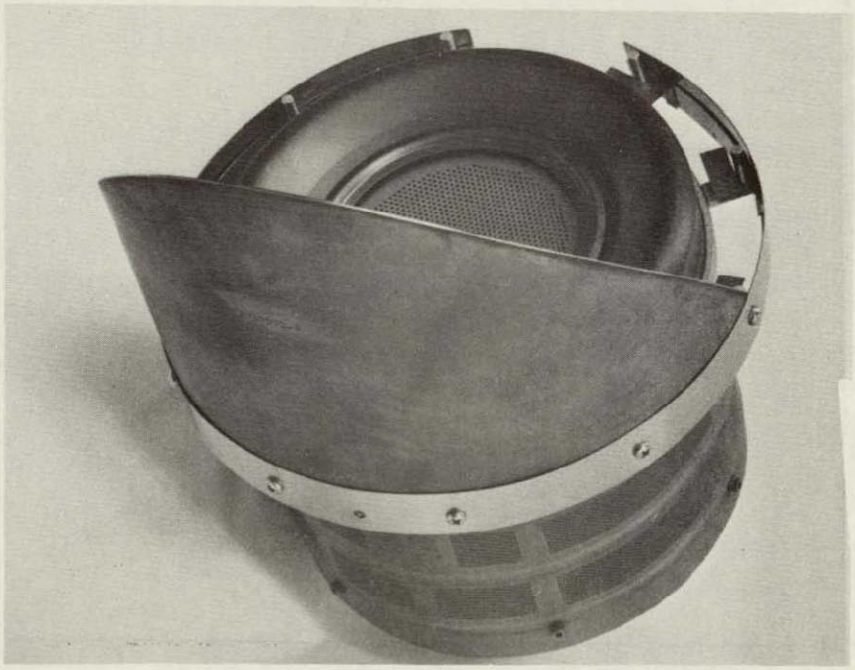

(b) Penumbra View

Figure 65. Sputter Shield Mounted on Thruster

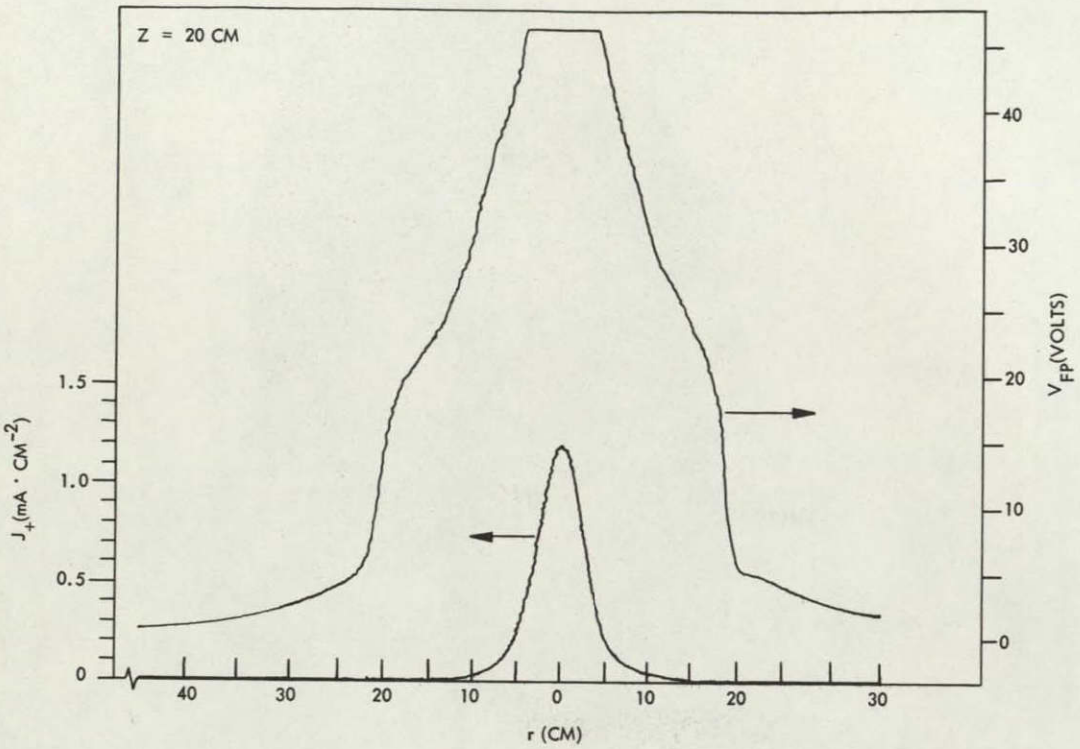

Figure 66. Engine J_+ Probe Data, 20 cm Downstream

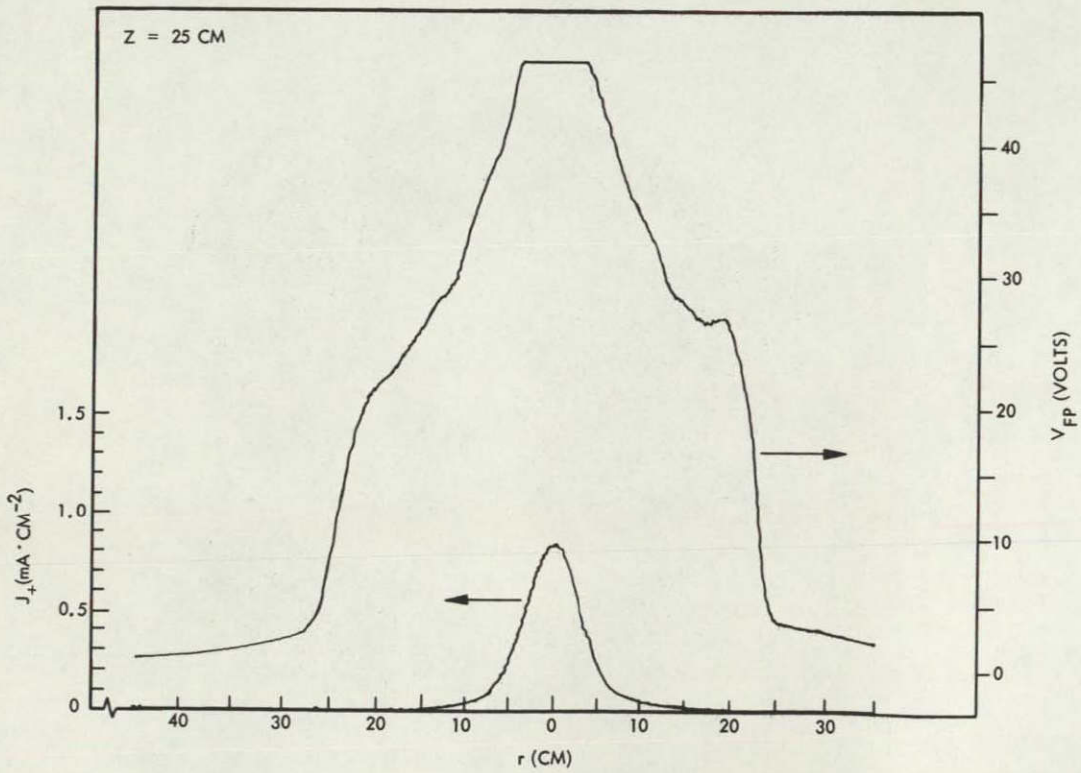

Figure 67. Engine J_+ Probe Data, 25 cm Downstream

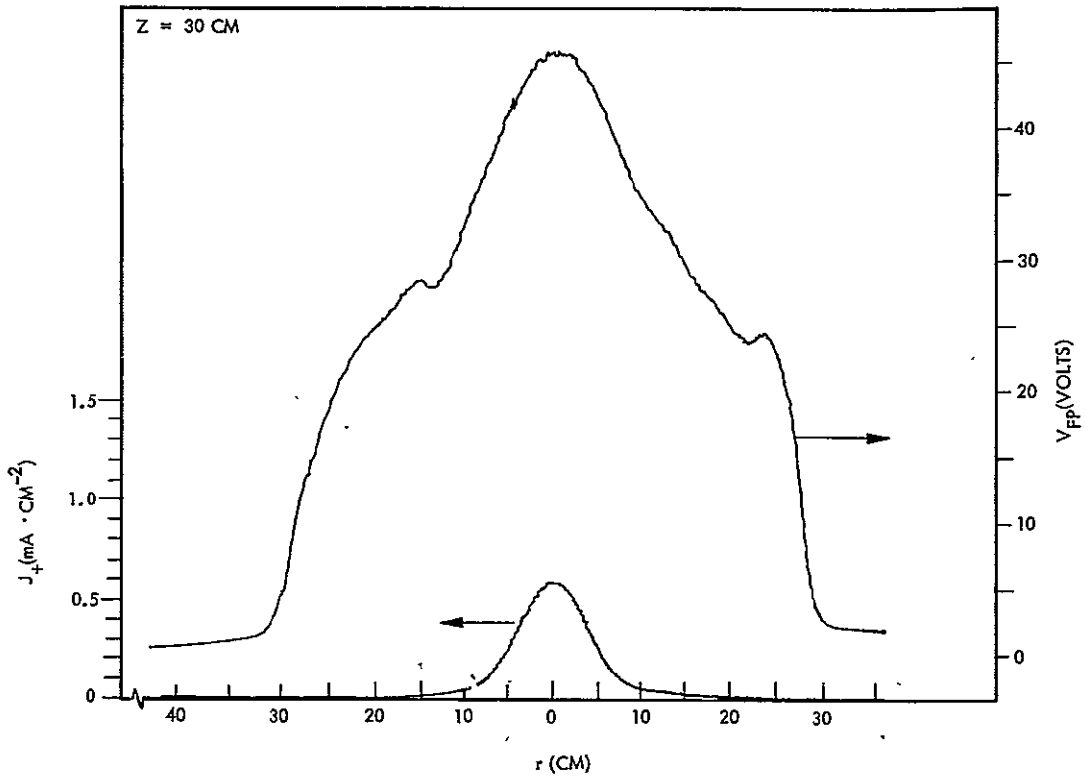

Figure 68. Engine J_+ Probe Data, 30 cm Downstream

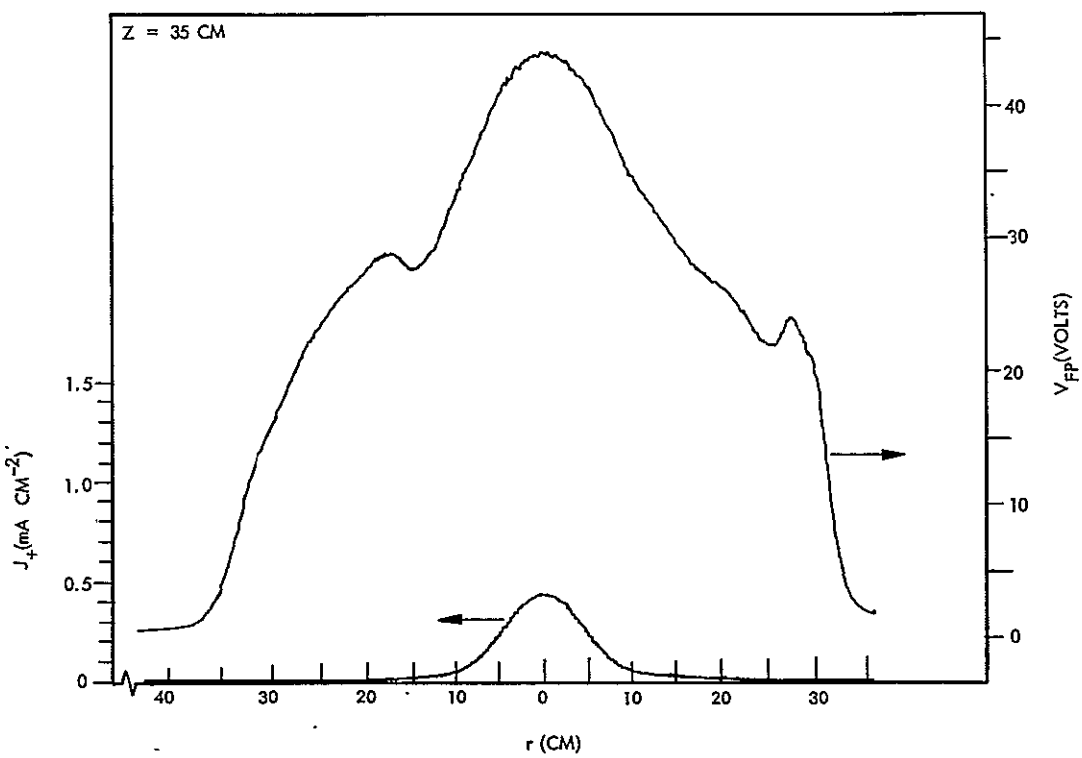

Figure 69. Engine J_+ Probe Data, 35 cm Downstream

potentials along the thrust beam axis for the case of the sputter shield absent (~37 volts maximum at z = 20 cm and ~33.5 volts maximum at z = 30 cm). Neutralizer conditions with the sputter shield absent were V(NK) = 13.9 v, J(NK) = 0.5 A, 5.4 mA flow rate, and 25.2 v target floating potential (i.e., floating potential of the upper shroud, lower shroud, and collector). With the shield present, V(NK) = 14.0 v, J(NK) = 0.5 A, 5.3 mA flow rate, and 27.9 to 28.2 v target floating potential.

A possible reason for this upward shift in the plasma floating potential as the sputter shield is added is that the presence of the grounded shield acts to reduce the electrical coupling between the plasma thrust beam and the discharge neutralizer, thus requiring an additional injection potential. While this upward shift in injection potential is not large, it does, nevertheless, move these potentials in a direction that is not generally desirable. The effects of increased injection potential include a higher eV per neutralizing electron cost as well as an upward boost in the energies of the Group IV ions (for Group IV ions formed in the near axial regions) as these ions move to nearby surfaces. Not only are there increased eV/ion losses to the Group IV colony, but increased ion impact energies upon surfaces leads to increased sputtering yields at those surfaces. While the observed increases in injection potential are not sufficient to cause major concern, the effect of the sputter shield as it is presently configured in decreasing the neutralizer to thrust beam coupling should be borne in mind for future iterations of the sputter shield design. It appears, in principle, that modifications of the sputter shield design can be undertaken which might restore the neutralizer to thrust beam coupling without reducing the extent to which the sputter shield protects the umbra and penumbra regions from direct thrust ion impact and without significant increases in the weight of the shield.

4.4.2 Swinging J_+ Faraday Cup Measurements

The swinging J_+ probe moves in an arc such that the probe is at constant radial distance, R, in a spherical coordinate system (R, θ, ϕ) in which $\theta = 0$ is the axis of the thrust beam. For the present experimental array, the plane of the swinging J_+ motion also contains the thruster neutralizer and the midline of the sputter shield. The swinging J_+ probe, thus moves from those regions which view the thruster face in a completely unobstructed

manner, into the penumbra regions (partial obstruction), and finally into the umbra region (total obstruction).

Figure 70 illustrates the total ion current density of the swinging J_+ probe. The lower end sensitivity limit of the probe ($\sim 10^{-10}$ A/cm^2) causes a cessation of probe measurements for $\theta \sim 55$ degrees in the umbra region. The most likely condition for the ion currents observed at this angle is that these very weak signals are "facility effects" signals. To demonstrate these umbra current collection conditions in a more thorough manner, a graphical model of the thruster, sputter shield, and the swinging J_+ Faraday cup (including aperture locations and allowable ion entrance trajectories) was fabricated and delivered separately to NASA-LeRC. An examination of this graphical model indicates that ion signals at $\theta \gtrsim 55$ degrees for the sputter shield side are due to very weak facility generated ions. The effectiveness of the sputter shield is, thus, even more dramatic than the high levels of current signal cutoff exhibited in Figure 70.

The data of Figure 70 is restated in Figure 71 in terms of a normalized total ion efflux, $\epsilon_{+,TOT}$, and for that radial arc at R = 1 meter. This presentation extends from a central point value of $\epsilon_{+,TOT} = 10^{-3}$ cm^{-2} to an outer wing value of $\epsilon_{+,TOT} = 10^{-8}$ cm^{-2}. The observed ion currents drop very rapidly as θ moves toward the penumbra and umbra regions indicating effective shielding by the sputter shield. The "bulge" in the ion current data at $\theta \sim 90$ degrees in the unshielded zone is the customary Group IV peak.

4.4.3 4-Inch J_+ Probe Measurements

While the data in Figures 70 and 71 are encouraging, it should be noted here that the goal of the efflux shielding, as generally derived from the integration analyses, is to reduce the normalized efflux values at 1 meter to values of the order of 10^{-9} cm^{-2}. Because such very small signals cannot be accurately measured by the swinging J_+ probe, an additional probe, the 4-inch J_+ probe, has been used to perform ion current density measurements in the umbra region.

The 4-inch J_+ probe moves in the axial direction, z, at a fixed radial location of the cylindrical (r, z) coordinate system (r = 0 is thrust beam axis). The present 4-inch J_+ probe is at r = 28 cm and moves along a line in that

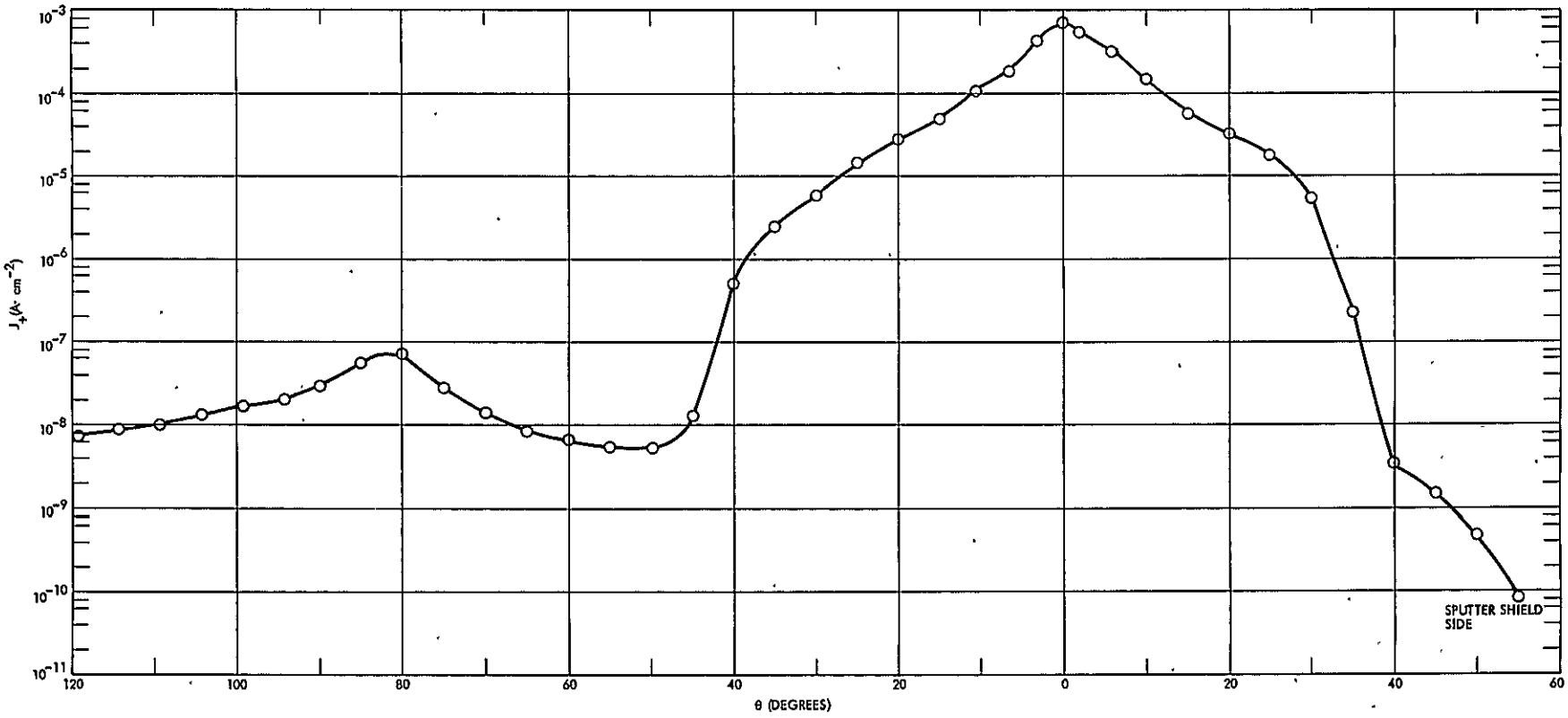

Figure 70. Ion Current Density Versus Polar Angle

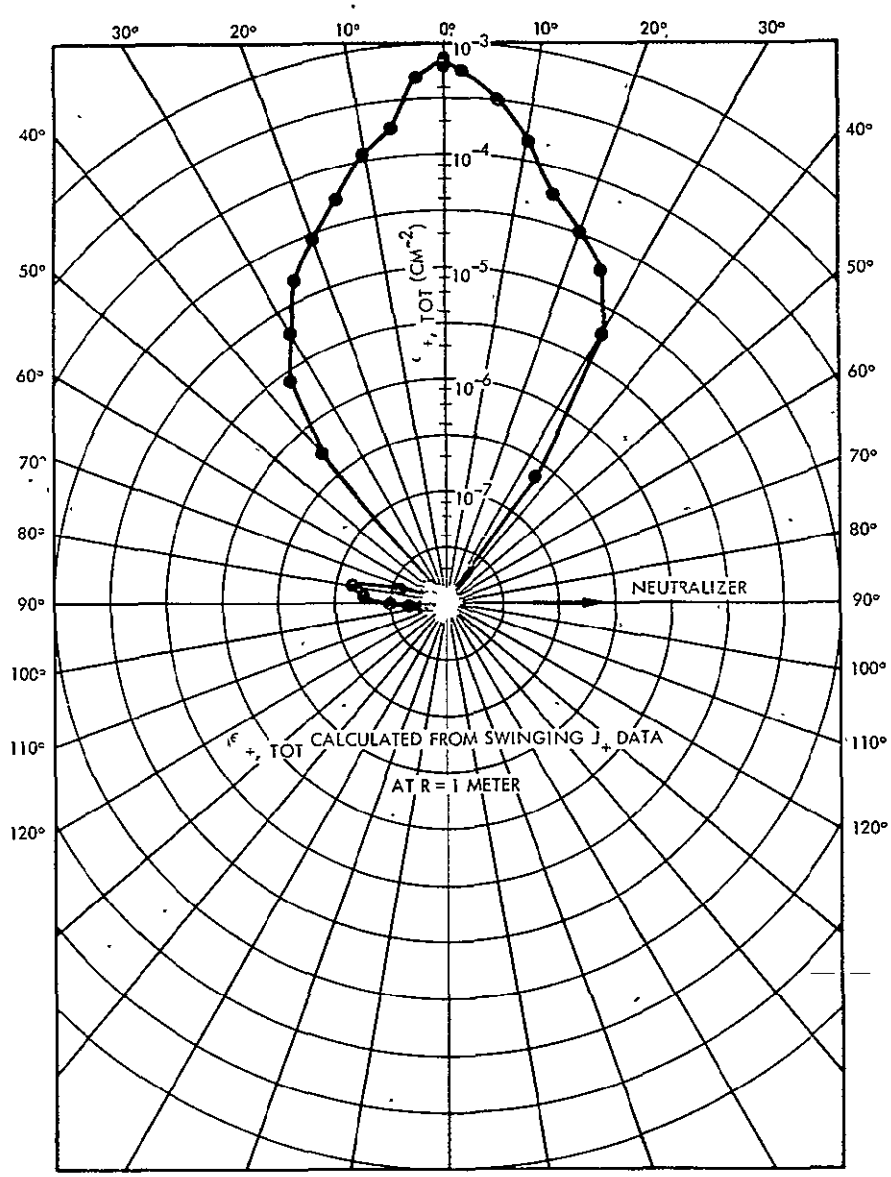

Figure 71. Normalized Total Ion Efflux at R = 1 Meter

plane containing the thrust beam axis, the thruster neutralizer, and the mid-line of the sputter shield. The probe is capable, thus, of making ion current density measurements in regions ranging from the unobstructed to the penumbra to the umbra. The increased measuring capability of this probe for weak ion current density signals results from its large opening aperture and its large acceptance cone (~2π radians) for incoming ion trajectories. While some of these features are desirable for probes measuring ion species whose

arrival directions are broadly distributed, it should also be noted that these features do result in an increased admittance of facility effect ions.

Figure 72 illustrates the total ion current obtained by the 4-inch J_+ probe as a function of probe position z. Also shown in Figure 72 are the currents of ions in various energy ranges obtained by using the probe as a retarding potential analyzer. The ion groups illustrated in Figure 72 are all ions ($E > 0$), weakly energetic ions ($0 < E < 50$ eV), hard ions ($E > 50$ eV) and energetic ions ($E > 100$ eV).

As may be seen in Figure 72, the currents of energetic ions are extremely weak for z dimension below 30 cm. This behavior is expected because the probe is proceeding into the umbra at this point.

Of specific interest in the data of Figure 72 are those ion currents with energies greater than 50 eV. Because the ion signals with $E > 100$ eV are very weak, it is apparent that the bulk of the ion signal with $E > 50$ eV is in the energy range 50 eV $< E < 100$ eV. Previous 4-inch J_+ probe scans without the sputter shield present have not revealed significant levels of ions in this energy range. It should be reemphasized, however, that the addition of the sputter shield resulted in an increase in the thrust beam potential (see the data in Figures 66 through 69). It would appear, thus, that the ions now observed in the 50 eV $< E < 100$ eV channel are primarily Group IV ions formed in the regions near the thrust beam axis entering into the 4-inch J_+ probe as it moves in the region from $z \sim 10$ cm to $z \sim 30$ cm. Because the bulk of these ion signals occur in the umbra, it is apparent that Group IV ions can move into these regions. These umbra-traversing Group IV ions result from a charge transfer reaction in the plasma thrust beam at downstream axial locations and subsequent motion in essentially radial (cylindrical radial, r) directions as a result of the thrust beam plasma potential gradients which are predominantly E_r with smaller levels of E_Z.

While the presence of Group IV ions in these umbra regions is not a facility effect (such ion formation and motion will occur in space), the magnitude of the observed ions can be influenced by facility presence. A specific concern here is the relative abundance at a given charge transfer location point of mercury atoms which have escaped from the bombardment discharge

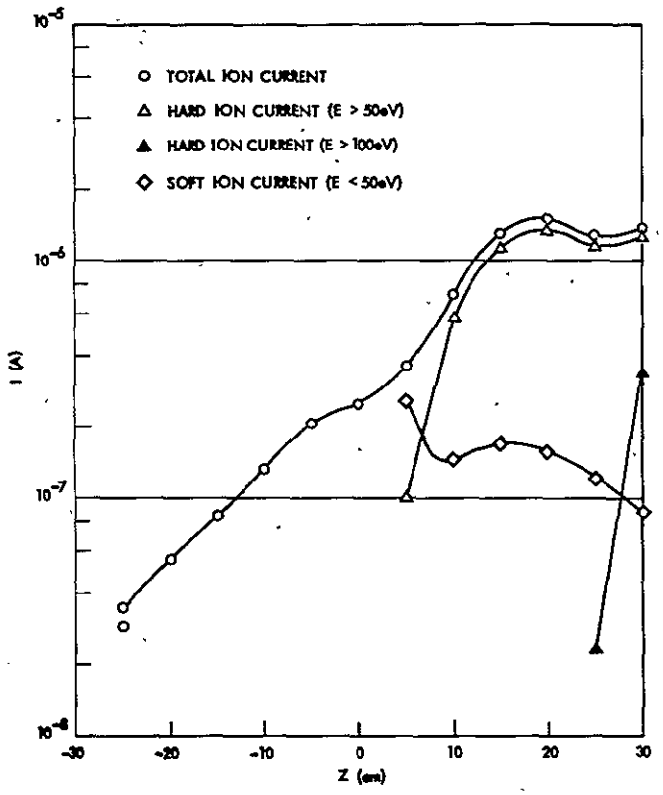

Figure 72. 4-Inch J_+ RPA Probe Data

without ionization (these atoms would also be present for ion thruster operation in space) and ambient mercury atoms whose presence is a result of the deposition of the mercury ion thrust beam on the various collectors and shrouds in the vacuum chamber. For locations very near the thruster accelerator plane, engine neutral density can exceed the density of ambient neutrals. However, engine neutrals rapidly dilute as they move away from the thruster face, and after a comparatively short expansion distance, the predominant neutral specie is the ambient mercury atom. It is not presently possible to rigorously estimate the extent of engine neutral atoms converted to Group IV compared to ambient neutral atoms converted to Group IV. The most likely condition is that the bulk of the ions observed in the umbra and with 50 eV < E < 100 eV are the result of a charge transfer involving an ambient neutral and that, in space and with only the genuine engine neutrals, this Group IV signal, would diminish significantly.

The data in Figure 72 have been reevaluated to provide a normalized Group IV efflux, ϵ_{+IV}, for a polar coordinate system and at R = 1 meter in this system. Figure 73 presents this normalized efflux signal. The significant aspects of the data are that ϵ_{+IV} values in the θ region >50 degrees are less than 10^{-8} cm^{-2} and diminish to values near the 10^{-9} cm^{-2} level. Thus, even though facility effects may still be present because of ambient chamber neutrals, the overall ion signal is at very low levels and does not present a significant thruster to spacecraft integration problem.

Some remaining aspects of ion current patterns with the sputter shield present are illustrated in Figures 74 through 76. These figures illustrate the total ion current in the 4-inch J_+ probe for both shield absent and shield present conditions, and soft ion signals (E < 50 eV) and energetic ion signals (E > 100 eV) for these two conditions. An inspection of these figures illustrates that the shield is effective in cutting off the energetic ion flux, but that weakly energetic ions still persist, largely as a result of facility effects.

4.5 SPUTTER SHIELD MATERIAL TRANSPORT

The function of the sputter shield is to protect spacecraft surfaces from energetic mercury ion impact, from the deposition of sputtered metal atom efflux from the thruster, and from neutral mercury atom deposition.

It is also important that the sputter shield should not, itself, be subject to excessive erosion by thrust ion impact nor be the source of metal atom deposition that will affect thruster operation or will affect the material properties of nearby spacecraft surfaces.

An examination was made of the effects of sputter shield erosion and of the deposition, at other points in space, of sputter shield atoms. For these measurements, the 8-cm mercury ion thruster was operated with the sputter shield described in Section 4.3.

4.5.1 Sputtering Plate Sample Measurements

Sputtering plate samples allow a measurement of surface erosion rate under the action of thrust ion sputtering at selected points in the thrust ion beam. The erosion rates are determined by the number of thin metallic layers removed during a known period of thruster operation. These sputtering

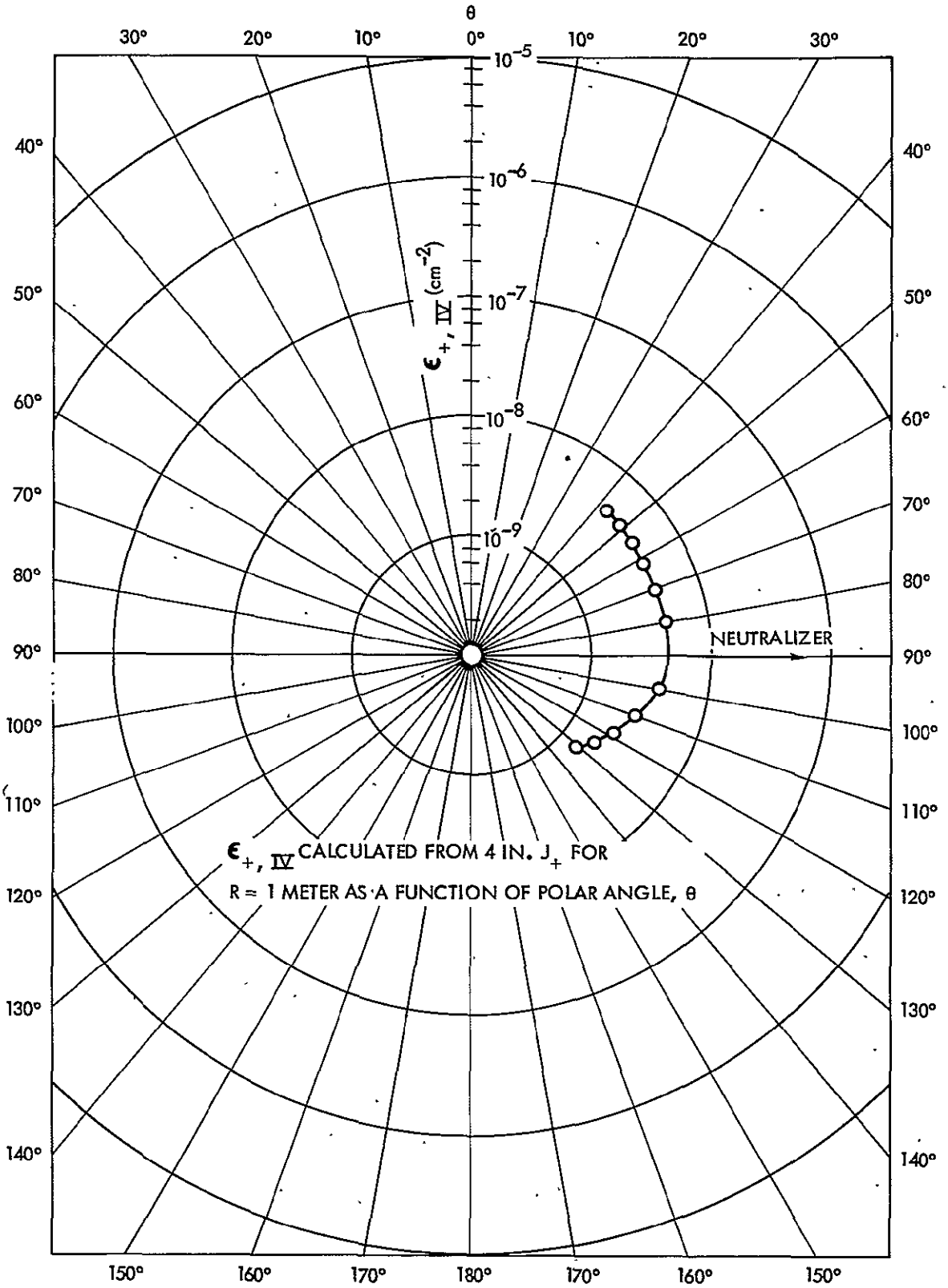

Figure 73. Normalized Group IV Ion Efflux at R = 1 Meter

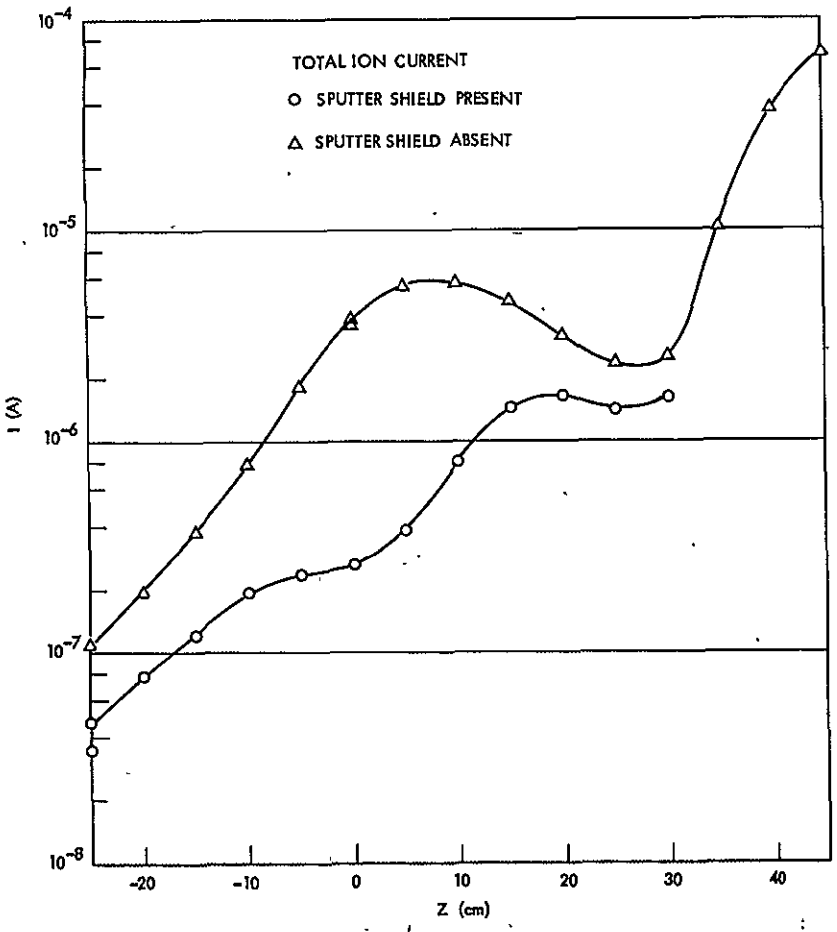

Figure 74. 4-Inch J_+ Current Measurements

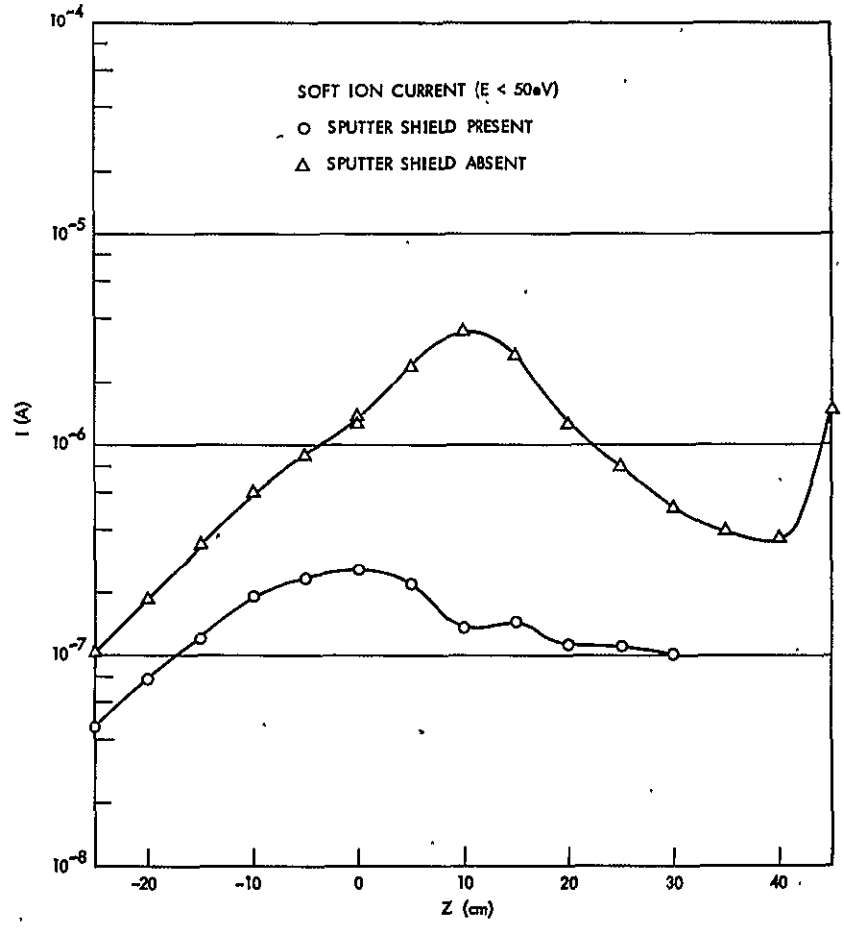

Figure 75. 4-Inch J_+ RPA Data, $E < 50$ eV

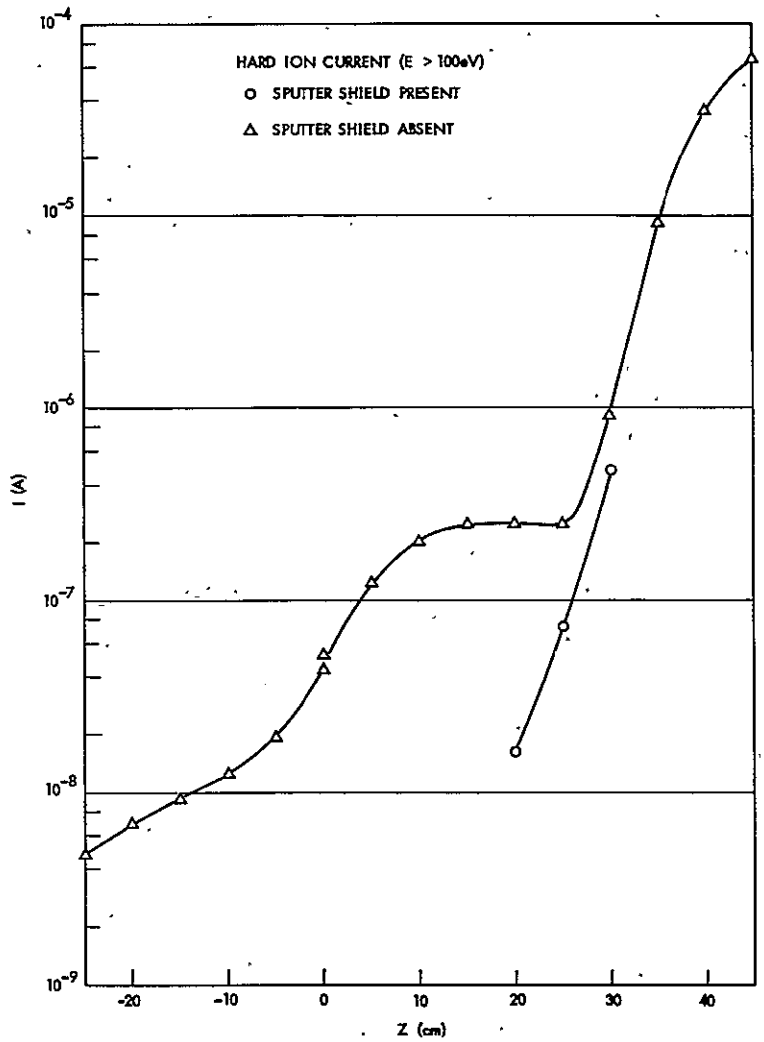

Figure 76. 4-Inch J_+ RPA Data, E > 100 eV

plate metallic layers are created by the alternate deposition of two metals whose colors are sufficiently distinct to permit later fringe counting as a means of determining the total erosion depth under thrust ion bombardment.

4.5.1.1 Sputtering Plate Layer Fabrication

For the present sputtering plates, the two dissimilar metals selected were chromium and copper. Vacuum deposition of these metals was carried out upon glass substrates to form a net 21 layer sandwich (11 layers of chromium and 10 intervening layers of copper) as is illustrated in Figure 77. The thickness selected was ~250 Å for both the chromium and copper layers, with total Cr thickness at 2870 Å and total Cu thickness at 2636 Å.

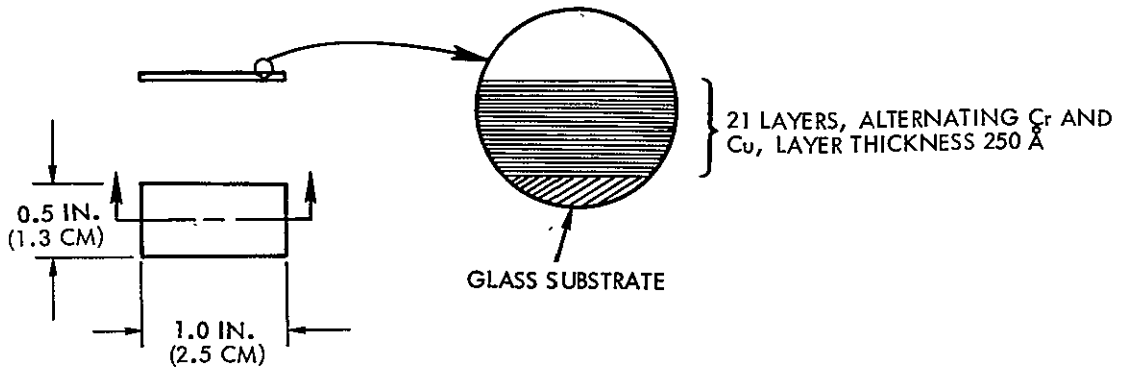

Figure 77. Sputtering Plate Sample

The alternate metallic layer sputtering sample approach utilized here has certain inherent limitations. If the sputtering does not proceed through the outer chromium layer, then no color fringes are formed and the only estimate of erosion depth that can be made is that the erosion is less than 250 Å of this outer material. This 250 Å level of uncertainty continues to be present regardless of the number of layers eroded, as long as some of the layers remain. The relative accuracy of the measurements increases, however, and can approach ~10% (relative accuracy) for erosion depths proceeding through the major portion of the total sandwich. If, on the other hand, the sputtering is sufficient to remove all of the deposited layers, then only a lower bound estimate can be made of the erosion depth of the thrust ion sputtering.

For experimental conditions of energetic, ~1200 eV Hg^+ ions incident on the sputtering sample, and using estimated sputtering rates for chromium and copper, the total Cr/Cu sandwich has an equivalent thickness of 3400 Å (~250 Å for each 250 Å layer of Cr, and ~60 Å for each 250 Å layer of Cu) of titanium. Through the use of these equivalency depths, the measured erosion of Cr and Cu can be used to estimate the thrust ion erosion of the present titanium sputtering shield. As noted above, the removal of the entirety of the Cr/Cu layers establishes only a lower bound estimate of ~3400 Å of titanium sputter shield erosion. There is no immediate and accurate method to improve this estimate, if all layers of the sandwich are removed, and it should be emphasized that conditions can be obtained in which this lower bound estimate can be substantially below the actual erosion depth.

4.5.1.2 Sputtering Plate Configuration and Mounting

Three sputtering plate samples, designated SS-1, SS-2, and SS-3, respectively, were mounted along the interior midline of the thruster titanium sputter shield. Figure 78 illustrates the ion thruster, the sputter shield, and the sputtering sample configuration. Because of the angular distribution of emitted thrust ions, the incidence of thrust ions at SS-1 is expected to be significantly larger than the ion incidence at SS-2, while only a very limited ion arrival rate is expected at SS-3. Under these ion arrival conditions it may be expected that erosion of SS-1 will be substantially above that of SS-2, and that only a comparatively minor erosion will occur at SS-3. This expected behavior was, in point of fact, obtained in the measurements.

Another important aspect of the sputtering plate array is the sample mounting to the sputter shield. This mounting was achieved with a spring clip which presses against the top and bottom edges of the sputtering plate glass substrate. Along the upper edge of the sputtering plate furthest from the thruster face, this mounting clip does not interfere with the incident ion arrival at sputtering layer surfaces. At the other edge, however, a tab extension of the mounting clip is interposed between the thruster and the sputtering layers. This protective tab allows a fringe count of the total number of eroded layers.

The mounting clip arrangement for the sputtering plate samples does result in the rear face of the glass substrate being slightly displaced away from the surface of the titanium sputter shield. It will be seen that this opening was sufficient to permit sputtered metal atom deposition on the rear of the substrate for one of the sputtering plate samples (SS-1).

4.5.1.3 Sputtering Plate Sample Properties After Exposure

Figure 79 illustrates sputtering samples SS-1, SS-2, and SS-3, after a thruster operational period of ~51.5 hours.

The appearance of sputtering sample SS-1 poses several apparent problems. Over the middle interior of the sputtering plate the thrust ion erosion appears to be complete, i.e., all layers of the sandwich removed. That area of Cr/Cu layers protected by the lower tab remains. In view of this total erosion (except for the protected area), the apparent material along the sides of

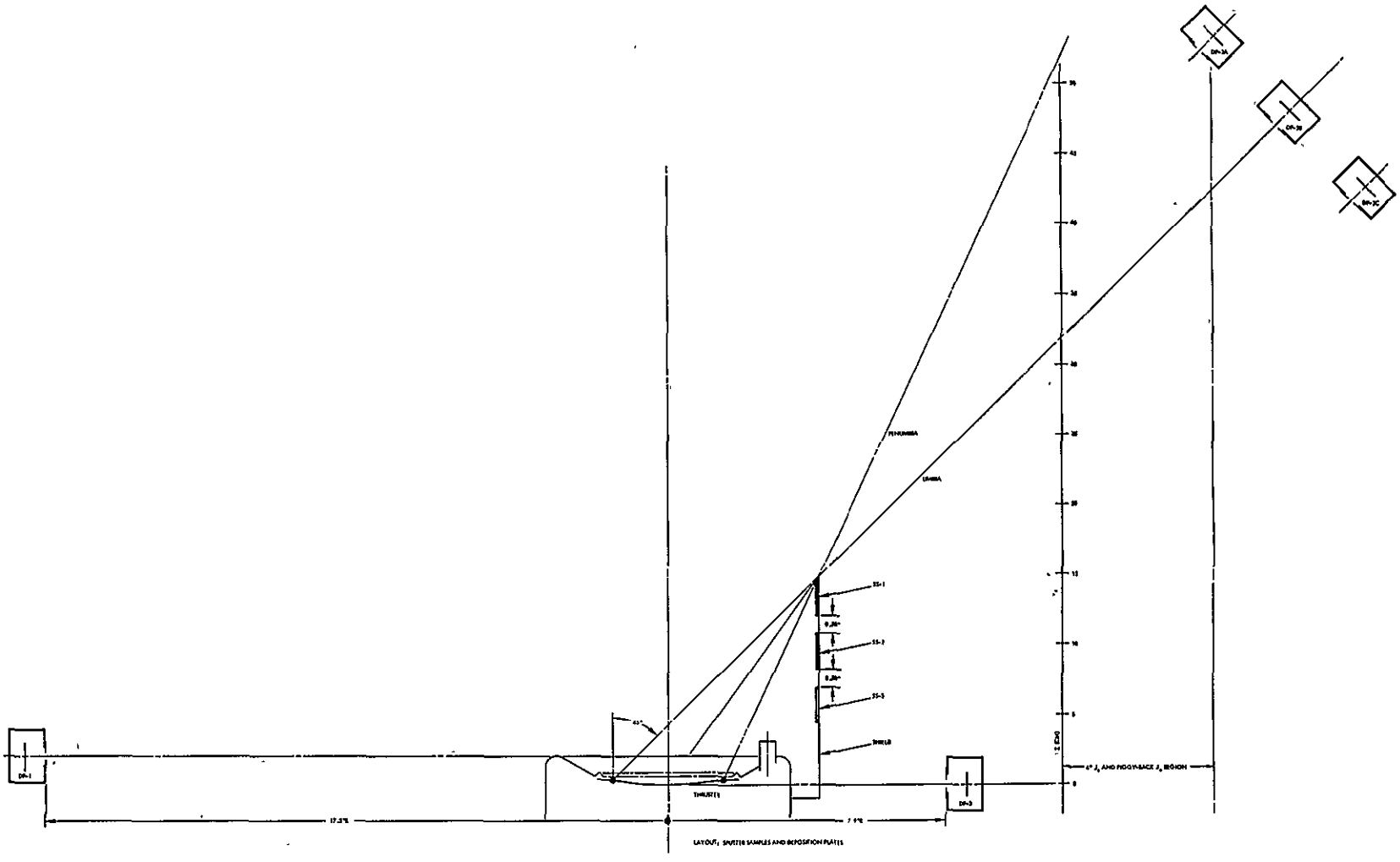

Figure 78. Thruster, Sputtering Sample Plates and Deposition Sample Plates; Test Configuration

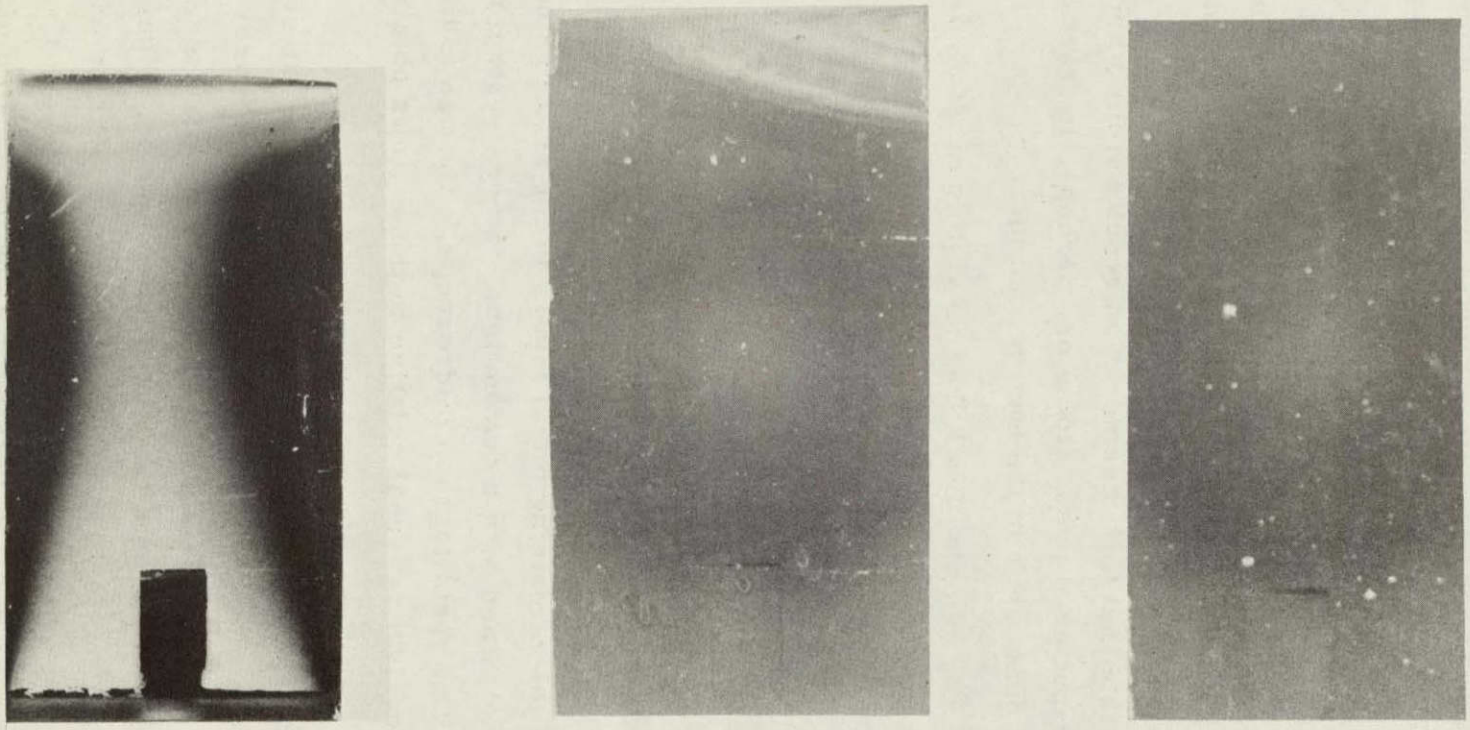

(a) (b) (c)

Figure 79. Sputtering Samples SS-1, SS-2, and SS-3 After Exposure

ORIGINAL PAGE IS
OF POOR QUALITY

the sputtering sample is difficult to explain. It will be seen that this material is not on the exterior surface of the substrate but is, rather, on the rear face of the glass and has resulted from sputtered metal atom deposition there. These rear face deposits and the color bands which appear at the upper portion of the sputtering sample are discussed below.

Sputtering sample SS-2 has a material removal pattern along the upper right hand edge which reveals erosion into the fifth Cr layer. Erosion beneath the outer Cr layer is not apparent over the remaining bulk of the surface area. Some discoloration is evident at the lower portion of SS-2 in the area protected by the tab. It is possible that this discoloration results from other material transports, either in sputtered metal atoms or, perhaps, in fractionated hydrocarbons from the residual vapor in the testing chamber.

The final sputtering sample, SS-3, has no visible erosion, i.e., erosion is less than the outer Cr layer thickness. There is, in addition, some discoloration around the area protected by the tab, as occurred for the protected area in SS-2.

Detailed Properties of Sputtering Plate Sample SS-1

Figure 80 illustrates details of sputtering sample SS-1. Figure 80a illustrates the area protected by the tab for SS-1 at somewhat greater magnification than used before. Figures 80b through 80e contain still further magnifications of portions of the remaining metal layers in the area protected by the tab. Figure 80a was obtained with a conventional camera system while the rest were obtained with a metallograph microscope. The use of the microscope causes a left-to-right reversal relative to those views obtained with the camera.

The upper right hand edge of the area protected by the tab and shown in Figure 80a has been examined in greater magnification in Figures 80b and 80c. The magnification in Figure 80b is 100X, and under the polarized light used there, the color fringes of the various layers may be seen. Figure 80c increases the magnification to 400X and retains the use of the polarized light for sample illumination. All eleven Cr layers of the 21 layers Cr/Cu sandwich are evident in Figure 80c, confirming that the ion erosion of the sputtering plate metallic layers was complete.

a. Tab Area

b. 100X

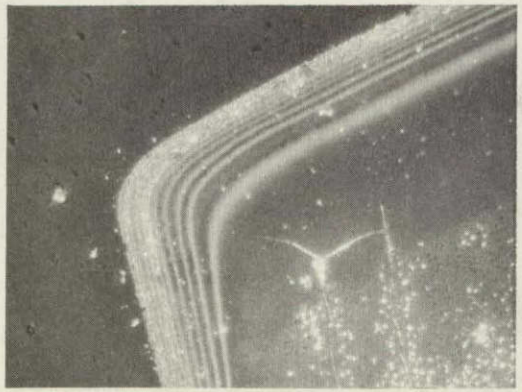

c. 400X

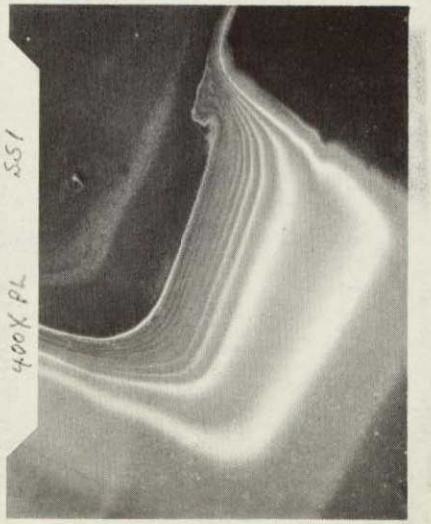

d. 100X

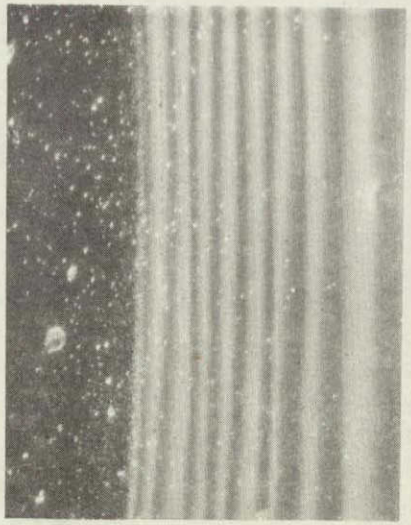

e. 320X

Figure 80. SS-1 Microphotographs

ORIGINAL PAGE IS
OF POOR QUALITY

Figure 80d is an enlarged view of the protected tab area at the lower right hand corner of the tab viewed in Figure 80a. Magnification in Figure 80d is 100X and polarized light illumination was used. Figure 80e examines (at 320X and with polarized light) the region along the side of the area protected by the tab. As before, total cut-through of the layers is confirmed and the effectiveness of the layer counting techniques is verified.

Figure 81 illustrates the rear face sputtered metal atom deposit (100X and bright field illumination). This deposition was possible because of the finite standoff of the sputtering plate sample rear surface from the titanium sputter shield and does seem to illustrate the complexities of material transport in these regions of the sputtering shield. It is believed that these rear face deposits are also responsible for the several fringes which appear near the upper middle of SS-1 (see Figure 79a).

Detailed Properties of Sputtering Plate Sample SS-2

Figure 82 illustrates details of sputtering plate sample SS-2. Figure 82a is an enlarged version of the view in Figure 79b and illustrates the cut-through to the fifth chromium layer in the sputtering plate sandwich. A still further enlargement (to 25X, and using polarized light) is provided in the metallograph microscope view in Figure 82b. Figure 82c illustrates the discoloration around the protected tab area at the lower portion of the sputtering plate sample. Because there is no evidence of any substantive erosion of the upper layer of SS-2 in the neighborhood of the tab, it is concluded that the coloration around this area seen in Figure 82c results from deposition of other materials, including both other sputtered metals and perhaps fractional hydrocarbons.

There are several important questions raised by the sputtering pattern observed at the upper edge of SS-2. The pattern is not uniform across the sample as might have been expected. The rate of gradation of the sputtering also raises questions, falling by a factor of ~4 over a surface traverse of only a few millimeters. There is no apparent reason for such rapid gradations in erosion when the extended source of the sputtering ions is considered and when considering the expected drop-off rates of ions for increasing polar angle from the various beamlets. In view of the differences between expected behavior and observed behavior, a tentative hypothesis may be advanced that the observed

ORIGINAL PAGE IS
OF POOR QUALITY

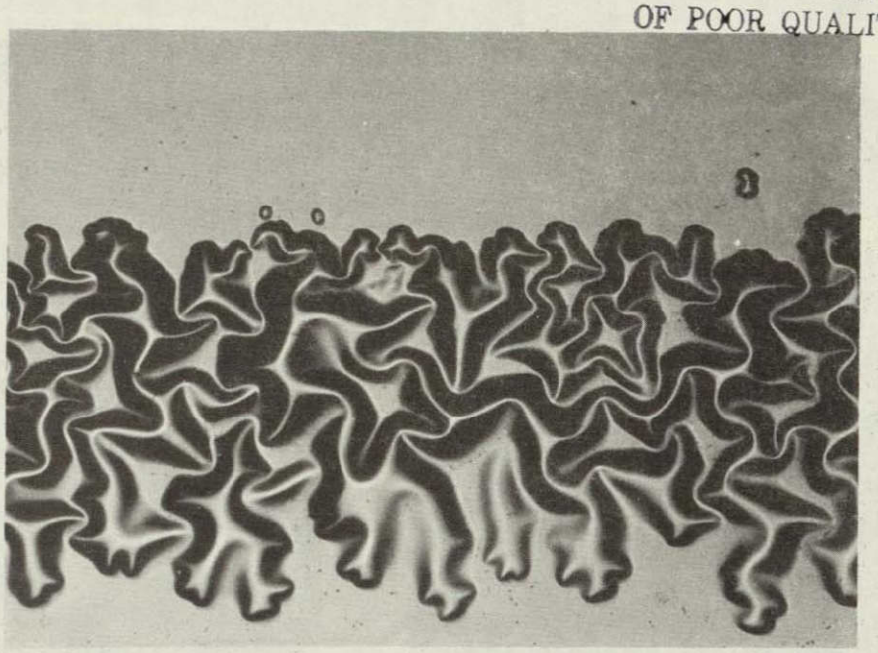

Figure 81. Rear Face Deposit

behavior results from an individual beamlet or perhaps a few beamlets with ion release patterns and ion divergence patterns which are not characteristic of the thrust beam as a whole. The present evidence for such individual beamlet variations is admittedly small, and suggests that further sputtering plate measurements may be required to determine the actual thrust beam sputtering patterns.

Detailed Properties of Sputtering Plate Sample SS-3

Sputtering plate sample SS-3 revealed no substantive erosion, i.e., less than 250 Å in Cr. The discoloration around the protected tab area observed in SS-2 and discussed above, also appeared for sample SS-3. No further examination of this sample was carried out.

4.5.1.4 Calculated Thrust Ion Erosion Rates

For sample SS-1 the erosion rate was equivalent to at least 3400 Å of titanium in 51.5 hours for a lower bound estimate of 66 Å/hr. Because there is no immediate method to impose an upper bound limit, and since cut-through was completed, this erosion rate lower bound estimate has indeterminable accuracy. A suggested procedure for better accuracies in rate determination is to

a. Upper Edge Enlargement

b. 25X

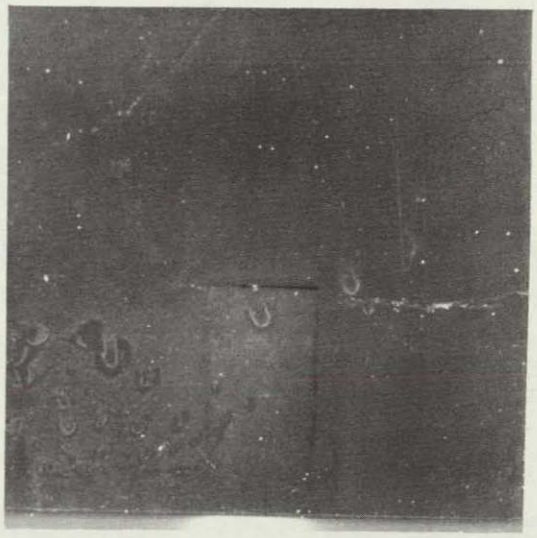

c. Tab Area

Figure 82. SS-2 Photographs

to narrow the range of examined area of the sputter shield and to specifically tailor the thruster run duration to the needs of these more localized areas.

For sample SS-2 the high end removal rate is ~30 Å/hr of titanium erosion for the area of maximum erosion and less than 5 Å/hr of titanium for areas of the least erosion.

4.5.2 Deposition Plate Measurements

Deposition plates allow a measurement of mass transport to and surface buildup upon surfaces in the regions surrounding the ion thruster and for those specific regions in which mass arrival exceeds the rate of mass removal by thrust ion sputtering. Section 4.5.1 has examined surface behavior in regions in which the predominant behavior is surface sputtering by the thrust ions. This section examines surface layer accretion in other regions around the ion thruster in which mass removal by sputtering is not the principal process. Here samples are taken by a series of copper deposition plates located in suitably shielded enclosures.

As a preliminary examination to the present deposition plate exposure, an earlier set of deposition plates was placed in the ion thruster vicinity and exposed during a suitable period of ion thruster operation. That earlier set of deposition plates was examined by an electron beam microprobe for evidence of molybdenum deposited on the plates by thrust ion erosion of the thruster accelerator grid. The electron beam microprobe analyses generally failed to detect molybdenum (small signals possibly attributable to molybdenum were seen on one plate), although there were strong signals for deposited Hg and of the deposition plate base material (copper). This experimental result was somewhat surprising in view of expected deposition levels of molybdenum and raised questions concerning the effectiveness of the electron beam microprobe approach to surface analyses. As a result of these questions, the analysis approach for the second (present) set of deposition plates was changed to the ESCA (electron spectroscopy for chemical analysis). The ESCA results obtained from the more recent analyses provide possible reasons for the previous inability of the electron beam microprobe to detect molybdenum.

4.5.2.1 Experimental Array

The experimental array of deposition plates is illustrated in Figure 78. The five plates shown there provide an examination of material transport in three principal areas. The first deposition plate (DP-1) allows an examination of titanium transport from the sputter shield under thrust ion bombardment. As a result of its placement, it is not likely that this deposition plate will record the buildup of any molybdenum sputtered by thrust ions from the accelerator grid. The second set of deposition plates (DP-2A, DP-2B, and DP-2C) are located across the penumbra-umbra boundary for the thruster sputtering shield. The most exposed deposition plate there (DP-2A) might be expected to have a net scrubbing (thrust ion erosion of the surface in excess of material arrival) while DP-2B and DP-2C, in succeedingly more sheltered zones, could have a net mass buildup with modybdenum and titanium as possible mass species in the layer accretion. A final deposition plate, DP-3, is located in a fully sheltered zone behind the thruster sputter shield and acts as a reference deposition plate against possible facility effect depositions.

4.5.2.2 ESCA Analyses of Deposition Plates

The ESCA is achieved by directing a known source of x-rays (in the work to be reported here, the 1253.6 eV x-ray from magnesium) into the surface material to be analyzed. The x-rays absorbed in the very uppermost surface layers create photoelectrons and Auger electrons whose kinetic energy is specific to a given atom where

$$h\nu = 1253.6 \text{ eV} = BE + KE + 4.3 \text{ eV} + V_s \qquad (17)$$

and BE (the binding energy) is specific to the atom involved in the photoemission process or Auger emission process prevalent and V_s is a surface charge-up term. The kinetic energy (KE) is determined by a retarding potential analysis of the emitted electron.

Uncertainties can result in the ESCA procedure as a result of chemical alteration of the binding energy and as a result of other extraneous energy losses. This uncertainty in binding energy can be as large as 10 eV.

Because the penetration depth of the x-rays into the surface is very small and because the analysis of the electrons is adversely affected by any electron energy loss in the passage through the uppermost layers, the ESCA procedure necessarily focuses attention upon the very outermost atoms on the surface. It is possible, thus, for the procedure to fail to detect a deposited mass species if other species are present and have been deposited on top of the specific mass element under examination. The results to be discussed will indicate that additional (facility effect) depositions did occur on the plates and have acted to mask the presence of the specific elements of interest to these thruster deposition processes. Under these circumstances, the masked species may be identified by briefly sputtering the outermost layers of the deposition plate sample. In neither instance above, however, can the ESCA procedure identify, absolutely, the layer depth (in atoms/cm^2) of the deposited species.

Results of the Deposition Plate Analyses

The initial ESCA scans were carried out on DP-2A. For this plate it would not be generally expected that either Mo or Ti would be detectable on the surface in that the sample is in a relatively strong scrubbing zone (by Hg^+ thrust ion bombardment). In the ESCA examination of DP-2A neither of these species was detected. The surface analysis did, however, reveal traces of what is believed to be Si and, in addition, there were strong emissions from carbon. The carbon signal was not unexpected because this species is almost universally present unless extraordinary methods of sample preparation are employed.

As a check against the DP-2A scan, a reference copper plate was examined. This reference plate had not been present in the chamber but was one of the original group of copper plates used in the deposition analyses. For this reference plate the Si (possible) line was observed and, again, a strong carbon emission.

The ESCA analysis then turned to DP-2B and DP-2C. The results of the scans of both of these plates was, again, traces of possible Si and strong carbon lines but neither Mo or Ti. These same results (no Mo, no Ti, possible

Si, and strong C) were also obtained for DP-3, the deposition plate for facility effects analysis, and DP-1, the plate which examines the material release from the sputter shield.

The results above indicated, generally, that carbon and silicon were present but that Mo and Ti were not. To determine if these contaminant layers were capable of complete obscuration of the substrate, a search was made for copper emission lines using the reference sample (no entry into the testing facility). For this plate, the copper emission lines were evident. A search for copper emission from DP-1 did not, however, reveal this element, thus indicating that the observed carbon contaminants on this plate could have been deposited-in-facility. DP-1 was then subjected to a 30-second sputtering by argon ions capable of approximately 1 monolayer removal. After this sputtering clean-off of DP-1, the copper emission was evident. An additional 2.5-minute sputtering of the sample resulted in a still larger emission of copper electrons, thus indicating still further cut-through of overlying contaminant layers. At this point, an ESCA was made for titanium and revealed the presence of this element. Figure 83 indicates these surface emissions both before and after the sputtering clean-up.

The results of the present ESCA analyses indicate that very minute surface layer accretions can be monitored. From the present results, however, it is not apparent that either the electron beam microprobe or the ESCA can be sufficiently definitive in an evaluation of total surface layer accretion for specific elements. An additional concern for these surface layers is the inadvertent deposition of other elements. These facility effect elements were present for the laboratory tests. Contaminant depositions may be expected to be present, however, even for deposition plate experiments in space, and significant questions remain to be answered for the effects of these additional contaminant materials on analytical results.

4.6 NEUTRAL MERCURY EFFLUX

The neutral mercury efflux release pattern from the 8-cm thruster was determined using a movable ion gauge. Figure 84 illustrates this experimental arrangement. A Bayard-Alpert gauge was used for the measurements. The

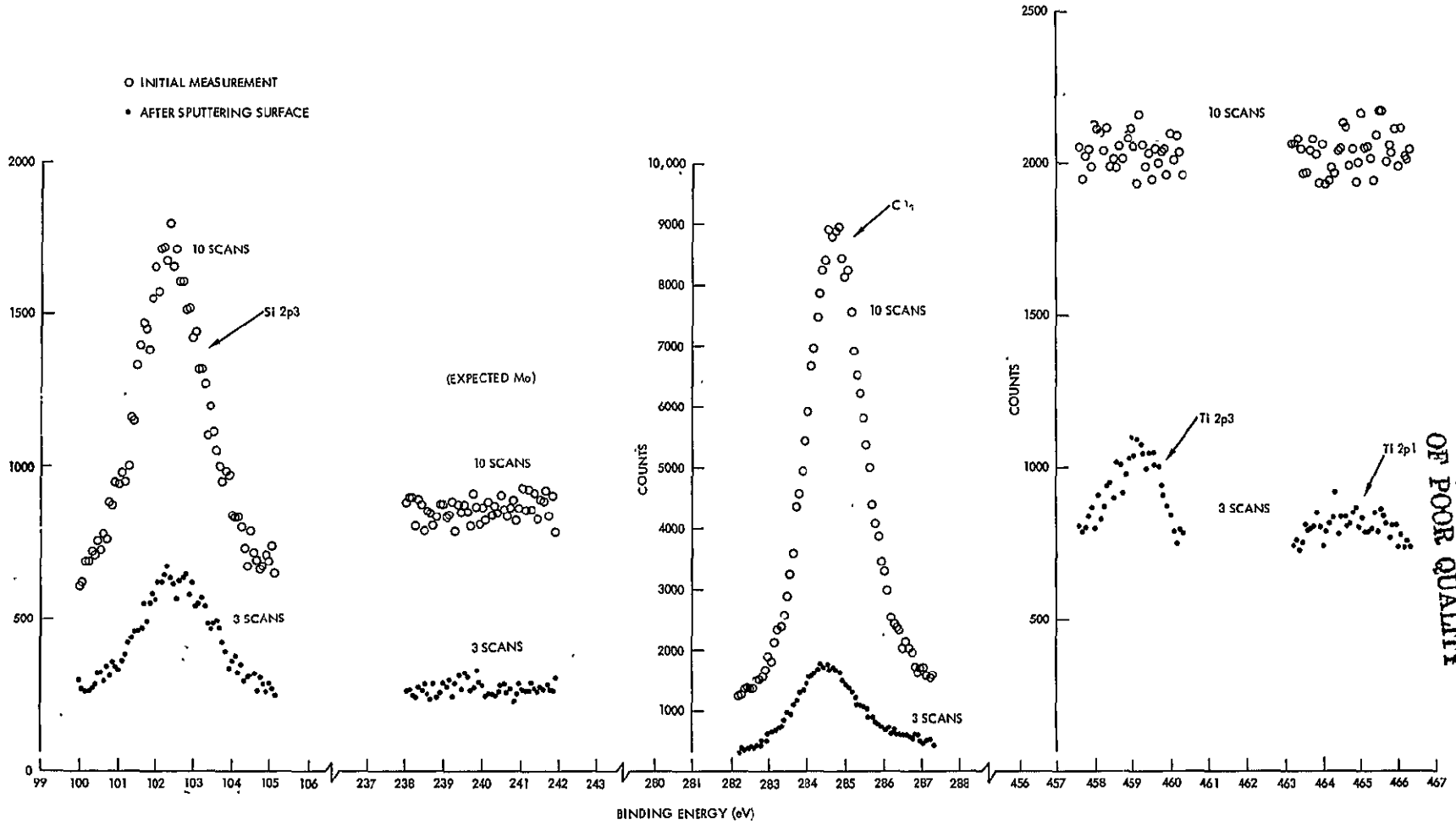

Figure 83. ESCA Data

ORIGINAL PAGE IS
OF POOR QUALITY

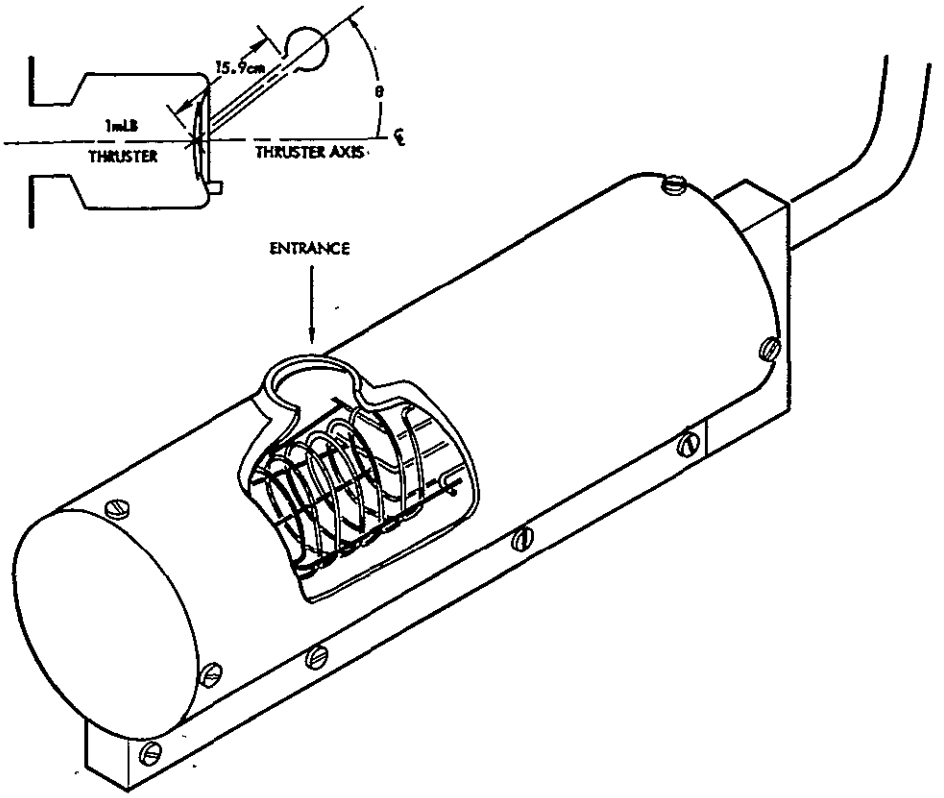

Figure 84. Movable Ion Gauge

gauge mounting arm causes the gauge opening to move at a constant radial distance; R, of ~16 cm where R is the radial coordinate in a spherical (R, θ, ϕ) coordinate system. Neutral efflux is measured as a function of polar angle θ. The gauge opening is an elliptical area ~1.9 cm (3/4 inch) in the major axis and ~1.6 cm (5/8 inch) in the minor axis.

The short R value used was for the purpose of increasing the signal-to-noise ratio between ion gauge response to Hg^o released from the ion thruster and the ambient chamber neutrals. As can be seen from the results in the sections to follow, the signal-to-noise obtained in the measurements ranged from 10 to 10^2 depending upon the source and strength of the Hg^o atoms. In retrospect, somewhat less shortening of the probe mounting arm would have been permissible and would have provided a larger ratio between the probe arm length and the thruster accelerator grid radius. However, a ratio of 4:1 generally reduces finite source size effects to tolerable levels. There are,

moreover, analytical procedures which can be applied which further reduce these finite source size effects.

Discharge Chamber (Cathode) Neutral Efflux

The measurements of Hg^o efflux from the discharge chamber (cathode) are illustrated in Figure 85. In this measurement the background chamber pressure is first obtained with all mercury vaporizer feeds deactivated. Following these background measurements, the bombardment discharge is then established and is operated for a period of several hours to provide a temperature equilibration of all thruster surfaces. At this juncture the discharge voltages and currents are extinguished. Mercury vapor is allowed to continue to flow, however, and the temperature of the mercury vaporizer for the cathode is held fixed. To assist in this constant temperature condition at the mercury vaporizer, additional heating is supplied to the tip of the cathode, following bombardment discharge extinction.

With Hg^o continuing to exhaust from the thruster face, the movable ion gauge is directed through the neutral plume, beginning at $\theta = -90$ degrees and moving to small positive values of θ, followed by recovering and rechecking at $\theta = -90$ degrees, after which the ion gauge is moved to +90 degrees (coinciding with $\phi = 0$ degrees in the cylindrical coordinate system at $z = 0$)* for a downward sweep in θ to small negative values with a final check on gauge reading at $\theta = +90$ degrees. The chamber gauge readings in Figure 85 indicate chamber pressure during the movable ion gauge measurements and for the movable gauge at position θ. The results illustrated in Figure 85 indicate a good side-to-side consistency and demonstrate that whatever cooling of thruster surfaces may occur during the measurement period is not sufficient to allow mercury inventory on those surfaces.

The measurements of Hg^o given in Figure 85 provide a determination of the angular distribution of emission of Hg^o for conditions in which no ionization takes place in the bombardment discharge region. To estimate the Hg^o plume density during thruster operation, the angular distribution function of Figure 85 is used with an estimated Hg^o flow (based here on propellant utilization efficiency) and an estimated thruster wall temperature.

*See Appendix D, Figure D-1, for the coordinate systems employed. Note that the plane of motion of the movable ion gage is the plane containing the thruster axis and the neutralizer axis.

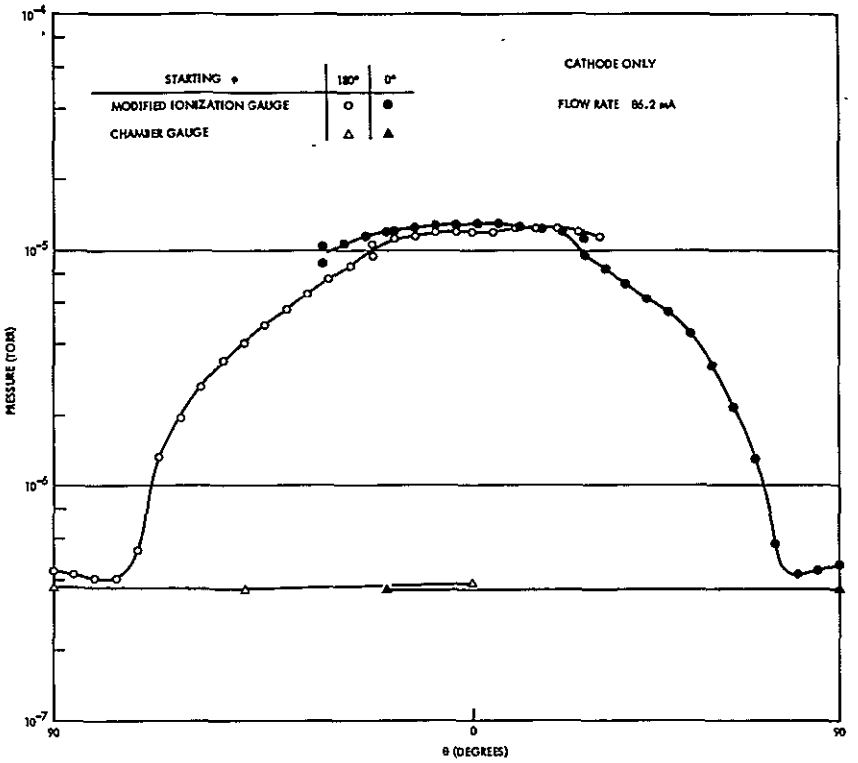

Figure 85. Movable Ion Gauge Measurement of Discharge Chamber (Cathode) Hg^o Release

Neutralizer Neutral Efflux

Figure 86 illustrates the measurements of Hg^o efflux from the thruster neutralizer. In these measurements, background pressure readings are obtained, as before, with all mercury vaporizer feeds deactivated. Following the background pressure readings, the neutralizer is placed in operation for a prolonged period prior to voltage shutdown. After the neutralizer discharge is extinguished, the movable gauge is directed through the plume in the same sequence discussed above. During these measurements, power is supplied to the tip heater and adjustments are made to the vaporizer power to maintain constant vaporizer temperature.

The asymmetry in the neutral mercury release in Figure 86 (and, also, to a much reduced relative magnitude in Figure 87 below) results from the off-axis placement of the neutralizer in the spherical coordinate system utilized here. As θ moves toward positive values ($0 \leq \theta \leq 90$ degrees) the gauge

ORIGINAL PAGE IS
OF POOR QUALITY

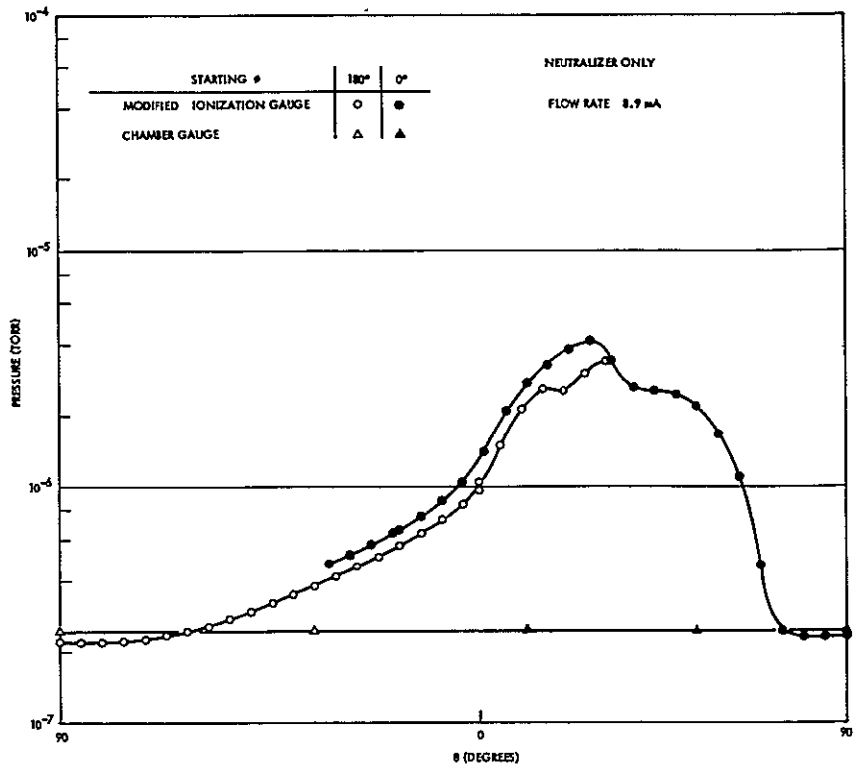

Figure 86. Movable Ion Gauge Measurement of Neutralizer Hg^{o} Release

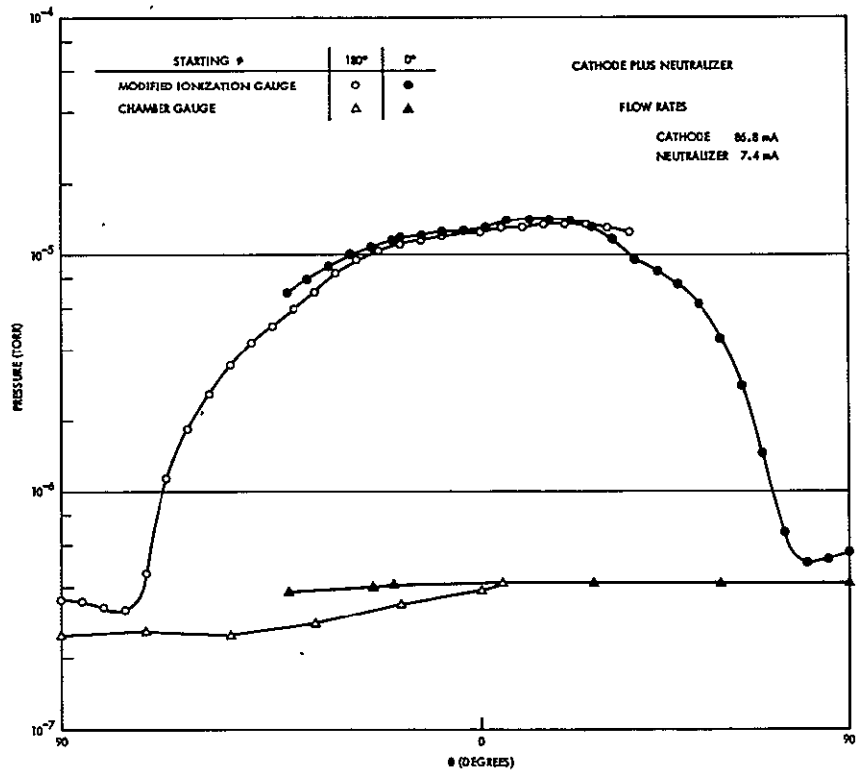

Figure 87. Movable Ion Gauge Measurement of Discharge Chamber (Cathode) and Neutralizer Hg^{o} Release

entrance moves over the neutralizer location and the signal strength of the released Hg^o increases. For more negative θ, the neutralizer position becomes increasingly distant from the gauge opening and the Hg^o signal strength diminishes.

The measurements of Hg^o given in Figure 86 provide a determination of the angular distribution of Hg^o emission from the neutralizer for conditions in which no plasma discharge is present. To estimate the Hg^o plume density during neutralizer operation, the angular distribution function of Figure 86 is used with an estimated Hg^o flow (based here on vapor feed to the neutralizer during operation and an estimated fraction of ionization of that vapor feed) and an estimated neutralizer tip temperature.

Combined Discharge Chamber (Cathode) and Neutralizer Neutral Efflux

Figure 87 illustrates the measurements of Hg^o efflux from the thruster discharge chamber and from the neutralizer under conditions in which both the bombardment discharge and the neutralizer discharge are extinguished. The measurement procedures used here are the same as those described above. The analytical procedures to derive Hg^o plume densities have also been described there.

4.7 OPTICAL EMISSION

Optical emission measurements from the bombardment discharge and from the plasma discharge neutralizer were carried out for both the optical power radiation and the spectral distribution of this radiation.

4.7.1 Optical Power Density Measurements

Figure 88 illustrates the mounting of the photodiodes used in the power density measurements and their relationship to the 8-cm thruster. The mounting allows the diodes to move over a polar angle range from -20 to +90 degrees at fixed R of ~35 cm in a spherical polar (R, θ, ϕ) coordinate system.

The photodiodes used for the optical radiation measurements are PIN-10DB/541 silicon photodiodes from United Detector Technology (UDT). The

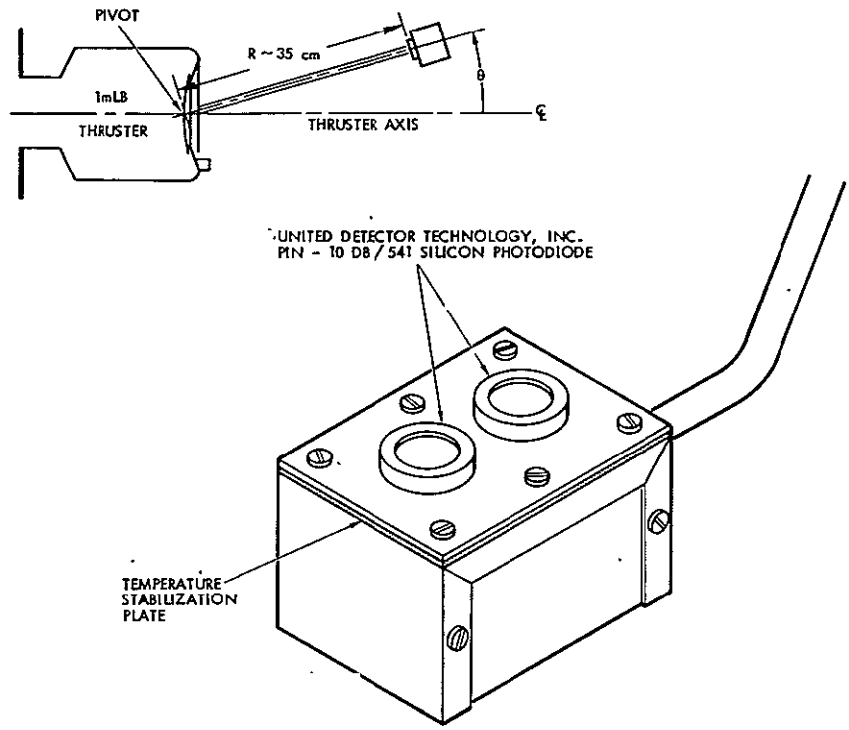

Figure 88. Photodiode Mounting Arrangement

diode response ranges from ~2750 to ~11,000 Å with a maximum output of 0.35 ampere per watt at 8000 Å. The response from 2750 to 8000 Å rises in an approximately linear fashion from 0 to the maximum and has an approximately linear decline in sensitivity from the peak at 8000 Å to zero response at 11,000 Å. This response does not extend into the UV at the 2536 Å line which may be expected to be present for a mercury discharge. The loss of measurement capability of 2536 Å is not crucial, because relevant optical detectors for spacecraft operate, in general, in the visible and cannot respond to the far UV mercury lines at either 2536 or 1849 Å. It will also be shown that measurements in the visible region for the Hg I emission permit an estimation of the UV power.

The two UDT photodiodes were mounted in a rotation arm normally used by the swinging J_+ probe. Some additional rotation constraints were encountered in order to include front surface mirrors for the mercury discharge spectral measurements. Thus, the motion of the diodes cannot proceed in the negative polar angle direction beyond approximately -30 degrees. For positive θ, however, the probe motion extends into the backward hemisphere.

Figure 89 illustrates a trace of the photodiode signal from an electron bombardment discharge at 30 volts anode potential and 1 ampere of discharge current. The peak intensity, at $\theta = 0$ degrees causes a diode current of 1.24 microamperes. Using an averaged diode sensitivity of 0.2 ampere per watt leads to a peak optical power density of ~6 microwatts per square centimeter for an electron bombardment discharge at 30 volts and 1 ampere. Although this discharge is at a somewhat elevated level, the radiation emission is considered sufficiently linear in discharge current to permit a statement of optical power density at 6 microwatts per ampere of discharge current at a radial (polar) distance of ~40 cm from the discharge region and for $\theta = 0$ degrees. Table 42 describes the angular dependence of the radiation power density per ampere of discharge current and at R ~ 40 cm for an assumed average diode response of 0.2 A/watt where the average is taken over the visible spectral range.

Figure 90 illustrates the photodiode response to the radiation for a nominal plasma discharge neutralizer. The radiation from this source is at lower power density levels compared to the electron bombardment discharge. The angular distribution of the radiation is asymmetric as might be expected because of the off-axis location of the neutralizer. The radiation from the neutralizer is also more narrowly confined than the emission from the bombardment discharge.

Table 43 describes the power density of the neutralizer radiation as a function of polar angle θ for R ~35 cm and for an assumed average photodiode response of 0.2 A/watt.

The principal feature of the measurements is that the optical power density is low. For the bombardment discharge and at approximately 40 cm from the discharge, the power density of ~6 microwatts/cm^2 is ~5×10^{-5} of the power density of solar radiation (which is ~100,000 microwatts/cm^2).

4.7.2 Spectral Measurements

Figure 91 illustrates the experimental apparatus used in the spectral measurements. The spectral analysis was carried out using a Jarrell-Ash 82-020 monochrometer located as shown in Figure 91. The optical radiation from the electron bombardment discharge was reflected by a 5 by 5 cm front

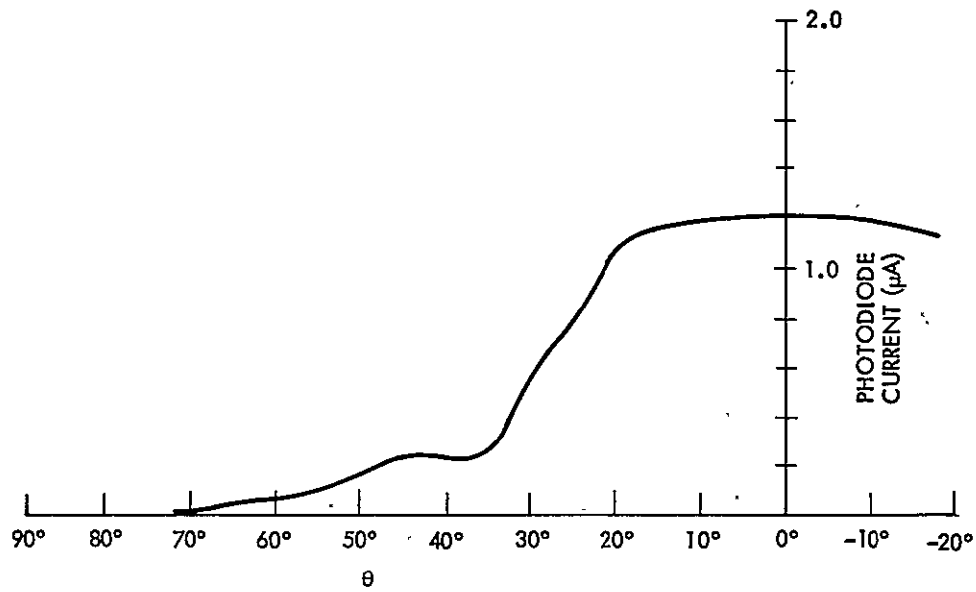

Figure 89. Electron Bombardment Discharge Emission as a Function of Probe Rotation Angle, θ

Table 42. Electron Bombardment Discharge Radiation Power Density

θ (degrees)	Power Density (μwatts/cm2)	θ (degrees)	Power Density (μwatts/cm2)
0	6.195	40	1.125
5	6.150	45	1.125
10	6.075	50	0.825
15	5.925	55	0.525
20	5.550	60	0.300
25	3.975	65	0.225
30	2.775	70	---
35	1.350		

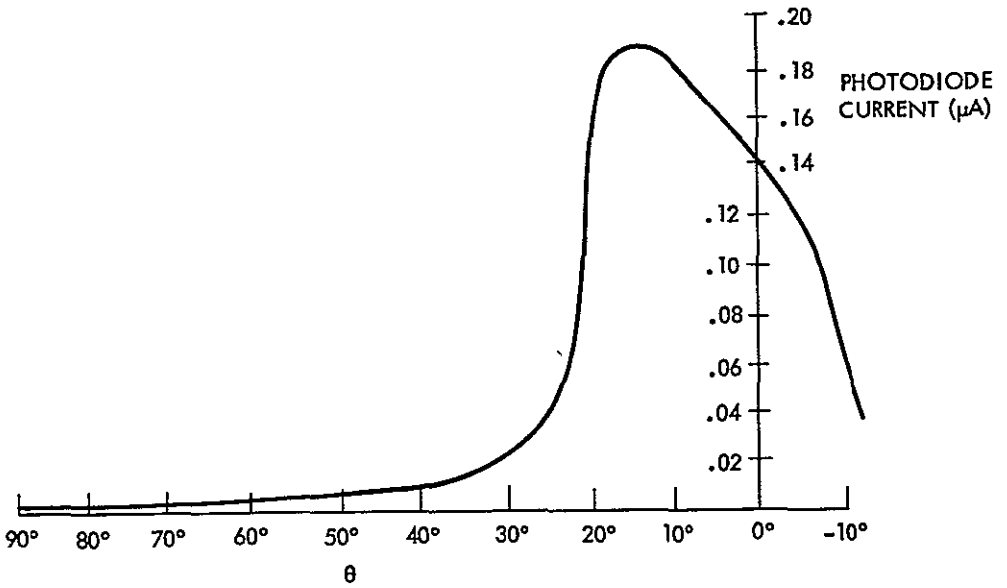

Figure 90. Plasma Discharge Neutralizer Emission as a Function of Probe Rotation Angle, θ

Table 43. Plasma Discharge Neutralizer Radiation Power Density

θ (degrees)	Power Density (μwatts/cm^2)	θ (degrees)	Power Density (μwatts/cm^2)
-15	---	20	0.780
-10	0.315	25	0.225
- 5	0.585	30	0.120
0	0.720	35	0.075
5	0.810	40	0.045
10	0.915	45	0.041
15	0.960	50	0.037

surface mirror which could be rotated into the region in front of the accelerator grid, and was then directed through a quartz window onto a second mirror exterior to the testing facility and then into the monochrometer. The photons at the monochrometer output were detected by an RCA 6199 multiplier phototube which had an S-11 response. The S-11 response curve extends from ~3000 Å at the short wavelength end to ~7000 Å at the long wavelength end.

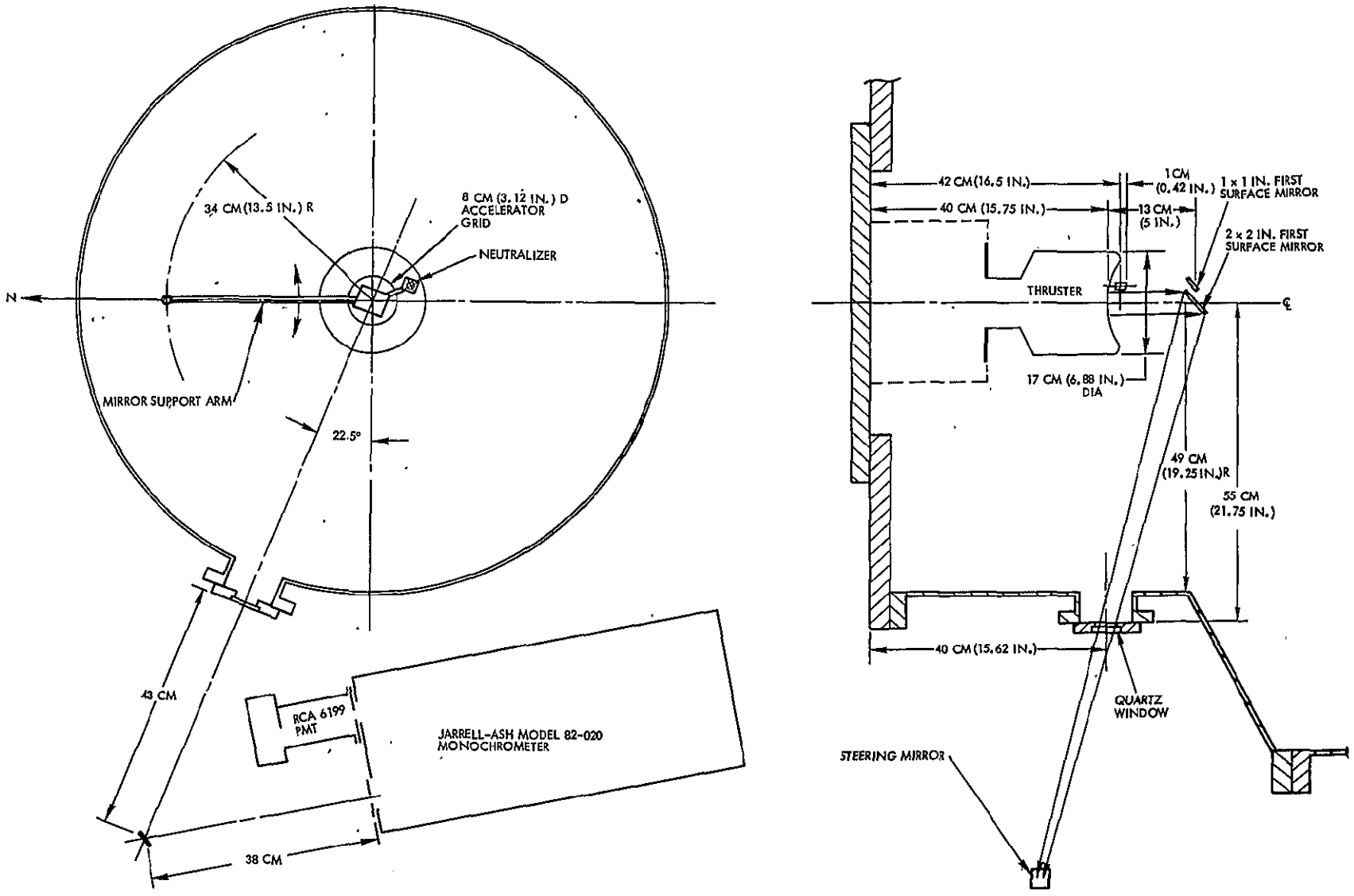

Figure 91. Spectral Measurements Apparatus

Spectral measurements of the radiation emitted from the thruster neutralizer discharge were obtained using a second movable mirror inside the testing facility. This second front surface mirror was 2.5 by 2.5 cm and was mounted on a rotation arm for appropriate placement to reflect the photons onto the optical axis of the monochrometer.

A final element of the experimental apparatus was a low pressure mercury arc (Ultra-Violet Products, Inc., Pen-Ray Lamp Model 11 SC-1C). This mercury lamp provides a calibration spectrum which can be used to verify the spectral sensitivities of the monochrometer detector. A description of the radiation from this source is given in reference 18.

Figures 92 through 94 illustrate the monochrometer output as a function of wavelength for the ion thruster bombardment discharge, the thruster neutralizer, and the mercury calibration lamp. Operating conditions of the bombardment discharge and the neutralizer are given in the figures. Also shown is the total dynode chain voltage of the photomultiplier tube. It should be noted that this photomultiplier voltage was increased during the neutralizer emission measurements compared to the setting used for the bombardment discharge emission measurements. There is, thus, no direct amplitude comparison of the neutralizer emission to the bombardment discharge emission from these monochrometer traces. Optical power densities of the two thruster elements, however, are obtained from the earlier photodiode measurements given in Section 4.7.1.

Tables 44 through 46 provide the measured monochrometer output at the various wavelengths recorded for the bombardment discharge, the neutralizer, and the calibration lamp. A correction term is applied to the photomultiplier outputs to account for the spectral response (S-11) of the RCA 6199 photomultiplier. The corrected outputs are then normalized to the emission at 4046 Å. Table 47 compares the normalized outputs of the bombardment discharge, neutralizer, and calibration lamp. Also given in Table 47 are the measured absolute outputs at various wavelengths for the calibration lamp (from Childs), and the normalized Childs output using 4046 Å as the normalization point. This final column in Table 47 can be compared to the column for the calibration lamp using correction factors for the S-11 response to verify that the correction factors are at the correct values. An inspection of these

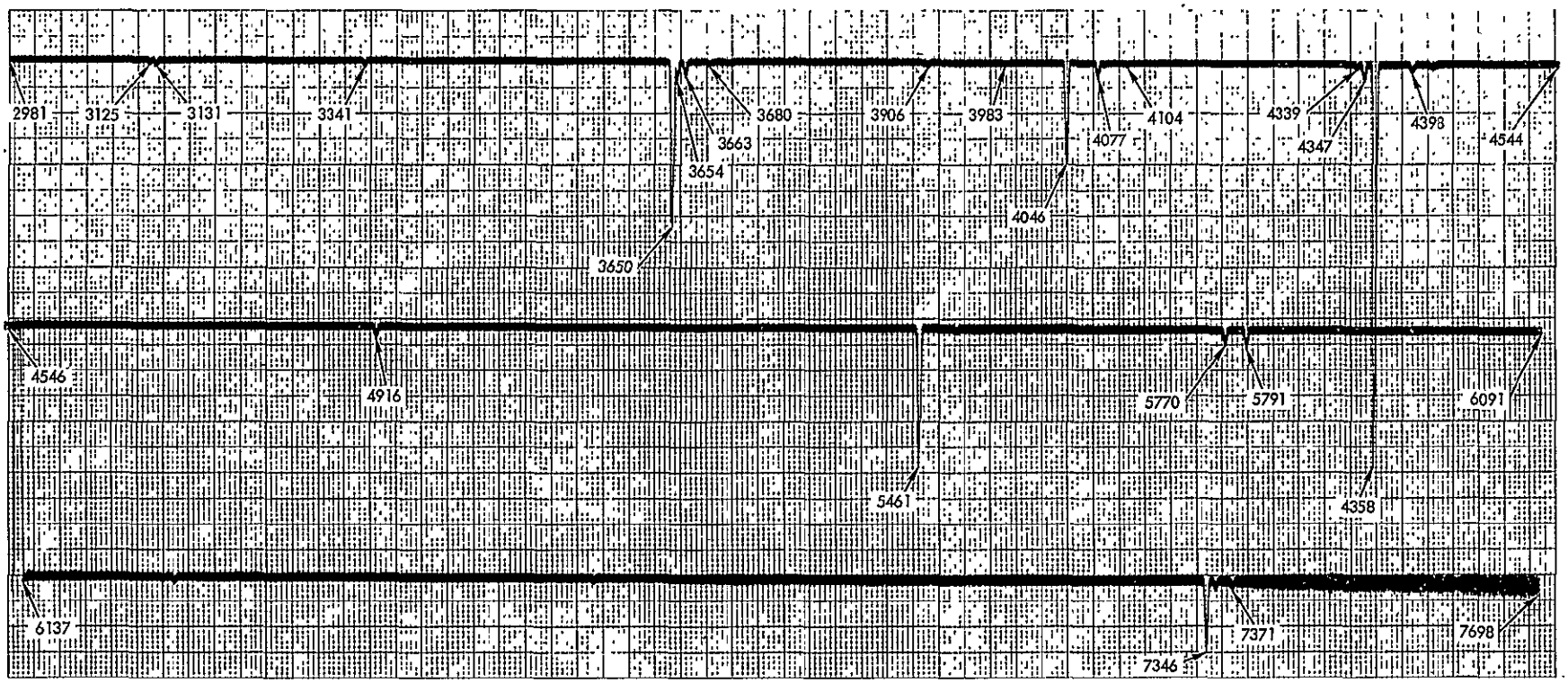

Figure 92. Monochrometer Output as a Function of Wavelength for the Electron Bombardment Discharge. [J(CK) = 0.55 A, V(CK) = 9.2 V J(E) = 1.01 A, ΔV = 30 V, Dynode Chain Voltage = 700 V]

ORIGINAL PAGE IS OF POOR QUALITY

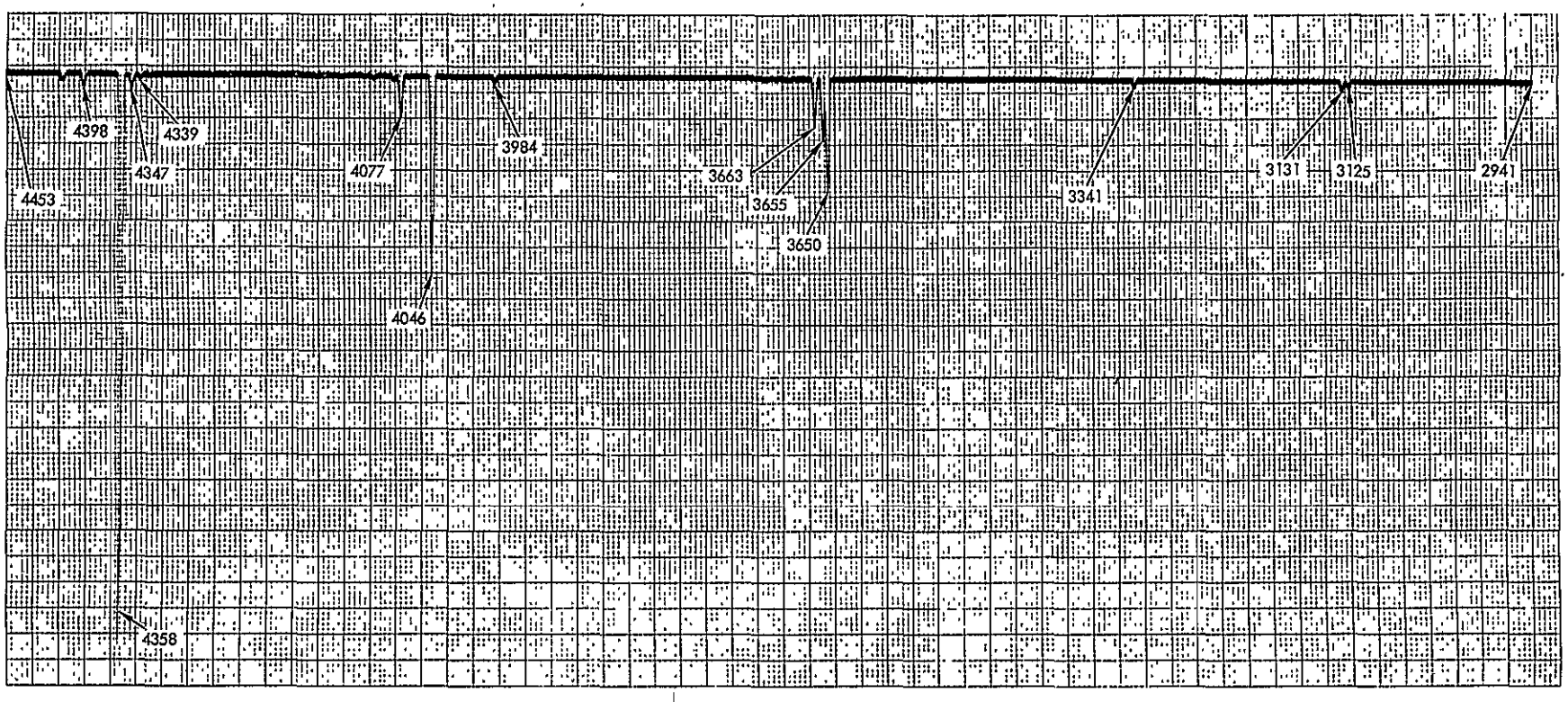

Figure 93. Monochrometer Output as a Function of Wavelength for the Neutralizer Discharge. [J(NK) = 0.5 A, V(NK) = 15.7 V, Dynode Chain Voltage = 900 V]

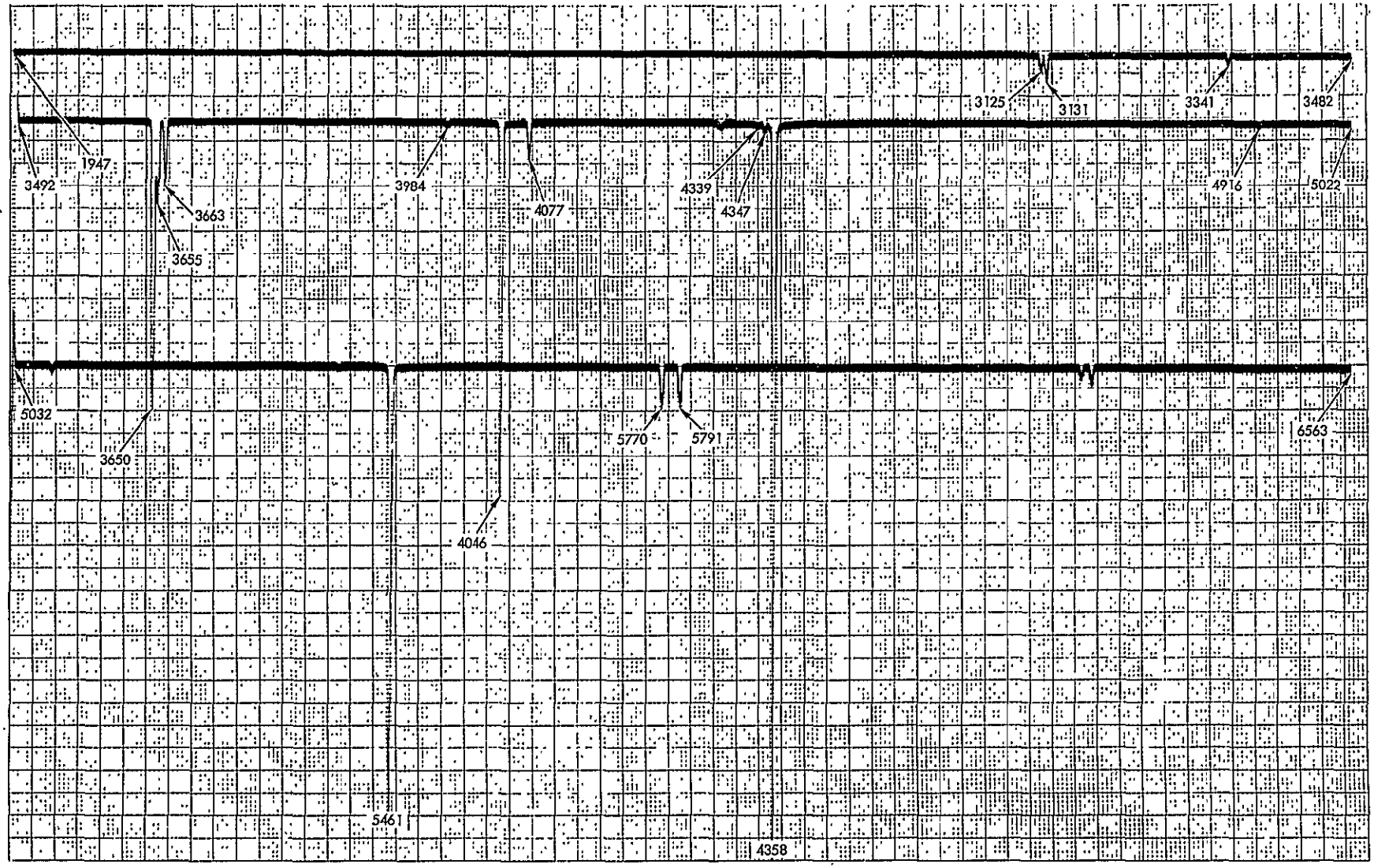

Figure 94. Monochrometer Output as a Function of Wavelength for Mercury Calibration Lamp

ORIGINAL PAGE IS
OF POOR QUALITY

Table 44. Electron Bombardment Discharge Spectral Measurements

Wavelength λ(Å)	Photomultiplier Current (nA)	Spectral Response Correction Factor	Corrected Amplitude	Normalized Amplitude	Spectral Assignment
3125	.12	33.3	4.00	.61	Hg I
3131	.18	33.3	5.99	.91	Hg I
3341	.18	5.5	.99	.15	Hg I
3650	9.60	1.25	12.0	1.82	Hg I
3654	1.02	1.25	1.28	.19	Hg I
3662	.60	1.25	.75	.11	Hg I
3906	.12	1.12	.13	.020	Hg I
3983	.06	1.12	.067	.010	Hg II
4046	6.00	1.10	6.60	1.00	Hg I
4077	.60	1.10	.66	.10	Hg I
4339	.12	1.00	.12	.020	Hg I
4347	.66	1.00	.66	.10	Hg I
4358	23.4	1.00	23.4	3.55	Hg I
4398	0.30	1.00	.30	0.05	Hg II
4916	.30	1.12	.34	0.051	Hg I
5461	8.10	1.61	13.0	1.98	Hg I
5770	.60	2.77	1.66	.25	Hg I
5791	.78	2.94	7.33	1.11	Hg I

Table 45. Neutralizer Discharge Spectral Measurements

Wavelength λ(Å)	Photomultiplier Current (nA)	Spectral Response Correction Factor	Corrected Amplitude	Normalized Amplitude	Spectral Assignment
3125	.18	33.3	5.99	.47	Hg I
3131	.36	33.3	11.99	.95	Hg I
3341	.24	5.50	1.32	.10	Hg I
3650	6.60	1.25	8.25	.65	Hg I
3654	3.60	1.25	4.50	.36	Hg I
3662	2.88	1.25	3.60	.28	Hg I
3983	.18	1.12	.20	.016	Hg II
4046	11.50	1.10	12.67	1.00	Hg I
4077	2.40	1.10	2.64	.21	Hg I
4339	.18	1.00	.18	.014	Hg I
4347	.42	1.00	.42	.033	Hg I
4358	33.0	1.00	33.0	2.60	Hg I
4376	.42	1.00	.42	.033	Hg I
4398	.30	1.00	.30	.024	Hg I

ORIGINAL PAGE IS
OF POOR QUALITY

Table 46. Mercury Calibration Lamp Spectral Measurements

Wavelength λ(Å)	Photomultiplier Current (nA)	Spectral Response Correction Factor	Corrected Amplitude	Normalized Amplitude	Spectral Assignment
3125	12.0	33.3	400	1.47	Hg I
3131	18.0	33.3	599	2.20	Hg I
3341	7.2	5.5	39.6	.15	Hg I
3650	192	1.25	240	.88	Hg I
3654	55.2	1.25	69.0	.25	Hg I
3662	42.6	1.25	53.3	.20	Hg I
3983	1.2	1.12	1.34	.005	Hg II
4046	248	1.10	273	1.00	Hg I
4077	24	1.10	26.4	.097	Hg I
4339	1.2	1.00	1.2	.004	Hg I
4347	3.0	1.00	3.0	.011	Hg I
4358	501	1.00	501	1.84	Hg I
4916	.6	1.12	.67	.002	Hg I
5461	296	1.61	477	1.75	Hg I
5770	28.2	2.77	78.1	.29	Hg I
5791	27.6	2.94	81.1	.30	Hg I

Table 47. Normalized Spectral Comparison

Wavelength λ(Å)	Spectral Assignment	Normalized Bombardment Discharge	Normalized Neutralizer Discharge	Normalized Calibration Lamp	Absolute Lamp — (Childs)	Normalized Lamp (Childs)
3125	Hg I	.61	.47	1.47	.0071	.80
3131	Hg I	.91	.95	2.20	.0110	1.24
3341	Hg I	.15	.10	.15		
3650	Hg I	1.82	.65	.88	.0089	1.00
3654	Hg I	.19	.36	.25	.0021	.24
3662	Hg I	.11	.28	.20	.0014	.16
3983	Hg II	.010	.016	.005		
4046	Hg I	1.00	1.00	1.00	.0089	1.00
4077	Hg I	.10	.21	.10		
4339	Hg I	.020	.014	.004		
4347	Hg I	.10	.033	.011		
4358	Hg I	3.55	2.60	1.84	.0170	1.91
5461	Hg I	1.98		1.75		
5770	Hg I	.25		.29		
5791	Hg I	1.11		.30		

two columns indicates that, in general, the response curve of the photomultiplier has been suitably accounted for. At the shorter wavelengths, however (i.e., at 3125 and 3131 Å), the correction factor used may be high by a factor of ~2. Note that in this spectral region a large correction factor (33.3) was used.

Examination of the data indicates that the emissions from the bombardment discharge, neutralizer discharge, and calibration lamp are primarily radiations from Hg^o, i.e., from transitions between various states of the mercury atom, and that only small amounts of radiation occur from transitions in the mercury ion, Hg^+. (In the tables, Hg I denotes emission from neutral mercury, and Hg II denotes emission from the singly ionized mercury ion.) An immediate question is whether this result is consistent with expected behavior in these discharges, and, in particular, with the electron bombardment discharge. The electron bombardment discharge is, after all, a region with energetic primary electrons capable of forming Hg^+ from the bulk of the Hg^o present and also capable of forming excited states of the Hg^+ ion. Two reasons appear to be responsible for the relatively small amounts of Hg^+ emission compared to emission from Hg^o. The first of these is the relative effectiveness of the thermal electrons in the bombardment discharge for excitation of Hg^o and Hg^+. The thermal electrons, in contrast to the primary electrons, have energies which are more capable, in general, of causing excitation in Hg^o than in Hg^+ (as may be seen from an examination of the term values for the excited states of the atom and ion). A second, and perhaps the major, reason for a relatively diminished Hg II emission is in the particle dwell time in the discharge. The Hg^o atoms traversing the discharge move at thermal velocities for which the relevant temperature is the temperature of the discharge chamber walls (500°K). Mercury ions, Hg^+, on the other hand, respond to the electric fields in the discharge region and, after their formation, rapidly acquire kinetic energies of the order of several electron volts and as a result remain in the discharge chamber region for periods of time estimated to be one order of magnitude less than the dwell times of the relatively cold (500°K) mercury atoms. Thus, there are sufficient reasons for an expected predominance of Hg I spectra over Hg II spectra for the radiation from the electron bombardment discharge. Since the neutralizer

discharge has a comparatively low electron temperature, it should be expected that this light source will also be mainly from excitations of Hg^{o}.

While the spectra of the bombardment discharge, the neutralizer discharge, and the calibration lamp are primarily Hg I emission spectra, an examination of the data in Table 47 does reveal quantitative differences between the various emissions. For example, emission at 3125 and 3131 Å is relatively stronger from the calibration lamp than from either the bombardment discharge or the neutralizer discharge. The emission at 4358 Å, on the other hand, is larger from the two thruster discharges than from the calibration lamp. These spectral variations raise questions as to the adequacy of using a calibration lamp as a thruster radiation emission simulator for possible spacecraft integration tests. Complete answers to these questions cannot be given, of course, unless the features of spacecraft optical sensors are more thoroughly specified as to absolute sensitivity and relative sensitivity in the various spectral regions. If simulation within factors of 2 is adequate for these hypothesized spacecraft integration tests, then the use of low pressure mercury arc light sources in place of an actively operating thruster would appear to be acceptable and also appears to provide considerable simplification and cost savings in such integration testing.

Another area of interest in the data is the presence of ultraviolet radiation. While the photomultiplier response (S-11) precludes a measurement of quanta at 2536 Å, and while the earlier measurements with the silicon photodiodes also were restricted to the visible band, the spectral data obtained in the visible can be used to estimate the strength of ultraviolet emission. Radiation at 2536 Å is prompt, because the excited state involved ($^3P_1$) is resonant. The lines in Tables 44 through 47 are frequently emissions in which the $^3P_1$ state results from the transition and, hence, the 2536 Å line will accompany the emissions observed in the visible. From the data of Childs with the low pressure mercury arc light source and from the relative similarity of this source to the thruster discharge, it may be estimated that the optical power in the ultraviolet at 2536 Å will be approximately 10 times the power contained in the visible band. The bombardment and neutralizer discharge thus have approximately 90% of their total emissive power in the hard ultraviolet region.

This emitted radiation may or may not be of any consequence in terms of integration of the thruster with spacecraft. For the majority of spacecraft optical detectors, the response at 2536 Å is absent and, thus, the detector is blind to these mercury resonance lines. If, however, an optical sensor with a response extending into the hard ultraviolet is contemplated for spacecraft use, the question of ultraviolet emission from the thruster discharges should be reexamined.

A final area of interest for the data in Table 47 is in the comparison of the normalized spectrum of the calibration lamp and the normalized spectrum of Childs. At 3125 and 3131 Å, the normalized calibration spectral outputs are 1.47 and 2.20, respectively, while Childs has 0.80 and 1.24 for these lines. This discrepancy tends to indicate that the factor of 33.3 used to correct for the S-11 response of the 6199 photomultiplier may have been too large by a factor of ~1.8 and that the abundance of thruster emission at 3125 and 3131 Å is too large by this factor of ~1.8. The consequences of these overestimates are not immediately apparent, because tolerable levels of radiation for a spacecraft integration with the thruster are strongly dependent on spacecraft configuration. Specific configuration requirements include not only the sensitivities of possible spacecraft optical detectors but also the placement and orientation of such detectors relative to the thruster. The spacecraft studied in Task I of this program, which typify near term missions for the 8-cm thruster, are not affected by these overestimates.

4.7.3 Ratio of Photon Generation to Ion Generation in the Electron Bombardment Discharge

Section 4.7.1 described the measurements of optical power density from the bombardment discharge and the neutralizer discharge. For the bombardment discharge the power density at zero polar angle (ion beam axis) is ~6 microwatts/cm^2 for photons in the visible range detected by the silicon photodiodes. For an assumed average photon energy of 2.5 eV and for assumed uniform emission over 4π steradians, it follows that ~1 photon in the visible range is created in the discharge region for each ion generated and accelerated into the ion thrust beam. From the spectral measurements

described in the earlier sections and from the known cross sections for photon production and ion production, it is possible to determine if the previous optical power density measurements are consistent with expected photon/ion generation ratios. Using the data in Table 47, it may be estimated that the photons at 4046 Å comprise ~7.5% of the photons emitted in the range from 3000 to 7000 Å and ~8.1% of the radiation energy in the 3000 to 7000 Å range. From the data of Jongerius (ref. 19) the differential cross section for photon emission at 4047 Å by 15 eV electrons is 1.0×10^{-19} cm^2/steradian measured at 90 degrees with respect to the direction of electron flow. If it is assumed that this photon generation cross section is uniform over the available 4π steradians, then the total cross section for photon generation at 4046 Å by 15 eV electrons would be $\sim 10^{-18}$ cm^2. The cross section for Hg^+ ion formation by electron bombardment has a threshold at 10.4 eV of electron bombardment energy and reaches a maximum value of 5×10^{-16} cm^2 at bombardment energies of ~75 eV. At 15 eV of bombardment energy, the Hg^+ formation cross section is $\sim 2 \times 10^{-16}$ cm^2. For 15 eV electrons, thus, the ratio of photon production at 4046 Å to ion production should be approximately 0.005 and the ratio of photon generation in the visible should be approximately 0.05.

The value obtained earlier of ~1 photon per ion is ~20 times the value of 0.05 obtained above at 15 eV electron bombardment energy. It should be emphasized that the electron bombardment discharge contains a wide range of electron energies, from the primary electrons (extending to ~30 eV) to the thermal electrons. It should also be emphasized that excitation of the 4046 Å line has a threshold energy of less than 8 eV and, thus, electrons in the lower energy range may be able to cause photon emission but will not be capable of ion formation. Considering the many unknowns in terms of electron energy distribution and in terms of the angular and energy dependence of the photon excitation cross sections, it is still possible to state that the experimentally observed ratio of one visible photon per Hg^+ ion formed is generally consistent with known behavior for electron bombardment of mercury atoms.

4.8 MAGNETIC FIELDS

Thruster magnetic measurements were taken. They showed that the thruster can be closely represented as a magnetic dipole. These measurements are described in detail below.

4.8.1 Experimental Apparatus for Magnetic Measurements

Figure 95 illustrates the experimental apparatus used in the measurements of the permanent magnetic moments of the 8-cm ion thruster. The permanent magnetic moments of the thruster are those magnetic fields present during periods of nonoperation for the ion engine and result from the use of permanent magnets in the field generation elements for the bombardment discharge. These fields are important because they are present for the entirety of the spacecraft on-orbit time. The permanent magnetic fields are also shown (Section 4.8.3) to be the major magnetic field contributions of the ion thruster.

The TRW magnetic test facility used for these measurements consists of a series of degaussing coils, a rotation table, and a variable position magnetometer. The degaussing coils, shown in Figure 95, consist of a vertically oriented Helmholtz coil pair and a horizontally oriented solenoid. The vertically oriented Helmholtz coil is adjusted to null the vertical component of the earth's magnetic field at the central point on the coil axis. The horizontal solenoid has its axis aligned in the direction of the earth's horizontal field (approximately north-south) and is powered with a current which causes cancellation of the earth's magnetic field at the central point on this solenoid coil. The central points of both coil systems coincide and the rotation table is placed at this central point location with the axis of the rotation table aligned with the axis of the vertical coil system.

The magnetic field of the earth, $\vec{B}_e$, is nulled precisely to zero at the central point of the coil system. For movement away from this central point, cancellation of the earth's field will no longer be exact, because of the finite size of the degaussing coils. However, for distances small compared to the coil scale size, the cancellation of $\vec{B}_e$ remains essentially complete. The relevant scale size in both vertical and horizontal systems is of the order of meters and, hence the volume occupied by the 8-cm ion thruster is essentially field free prior to introduction of the thruster.

The use of the degaussing coil system to cancel the earth's magnetic field at the location used by the ion thruster is important in that it permits the measurement of the thruster permanent magnetic moments without the

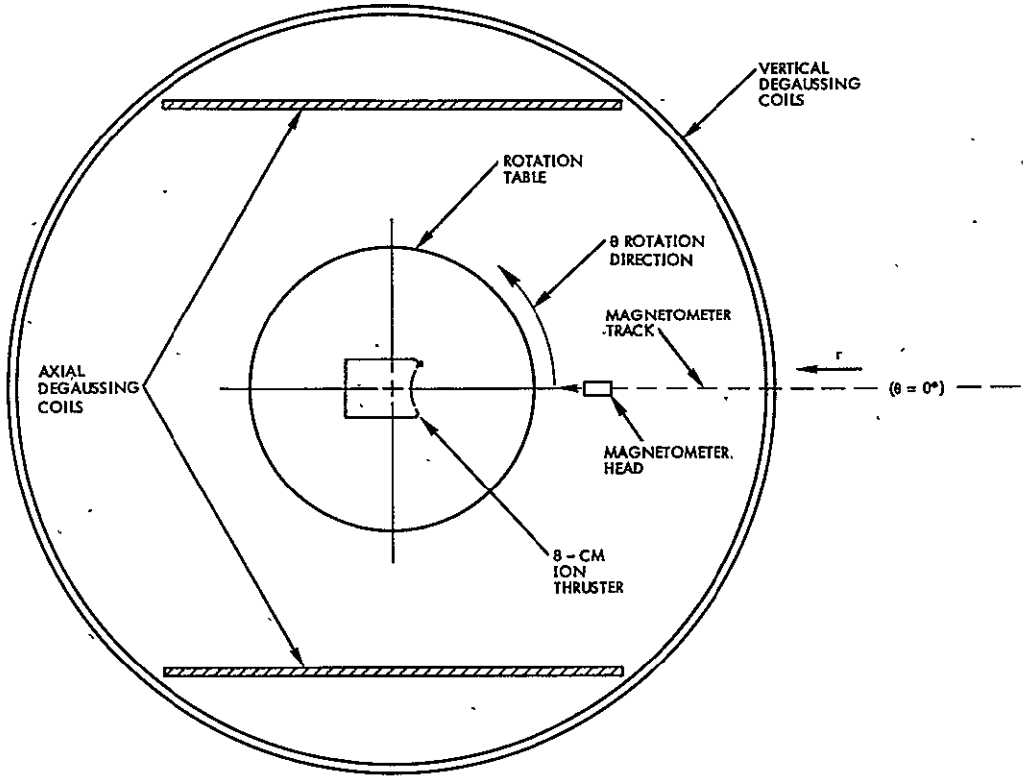

Figure 95. Permanent Magnetic Moments Test Apparatus

introduction of errors because of induced magnetic fields. It should be noted that the introduction at a point in space of material whose permeability, μ, is not identical to that of the permeability of free space, μ_o, causes alterations in the magnetic field patterns (for the case of nonzero B) as the lines move to accommodate the presence of such newly introduced magnetic material. A magnetometer located at some other point in space will observe $\Delta\vec{B}$ as the magnetic material is introduced. The observed $\Delta\vec{B}$, however, may derive from either induced $\Delta\vec{B}$ (alterations in B_e as the material is introduced) or permanent $\Delta\vec{B}$ (caused by permanent magnetic fields in the material). The cancellation of $\vec{B}_e$ at the location to be occupied by the thruster, however, eliminates any such field lines for possible reorientation and allows a direct, error-free, measurement of the permanent field effects.

The measurement of the permanent magnetic moments of the thruster is provided by the measurement of the <u>variation</u> in $\vec{B}$ at the magnetometer head as the thruster, mounted on the rotation table, is turned. A thruster dipole magnetic moment, for example, will be revealed by a variation of the form

B cos θ where θ is the rotation angle of the table. A magnetic quadrupole will display a dependence of cos 2θ and still higher magnetic moments will reveal even more rapid angular dependence (cos 3θ, cos 4θ, etc.). An additional aid in the identification of the moments is in drop-off as the radial separation distance between the magnetometer head and the test object is increased. The magnetometer head is, as noted, movable so that this variation of B as a function of separation distance can be determined.

The magnetometer utilized was a Forster-Hoover triaxial magnetometer with suitable bucking and bias coils. For the measurements of the ion thruster magnetic moment, only a single magnetometer head was required.

4.8.2 Thruster Permanent Magnetic Moment Measurements

Figure 95 illustrates the placement of the 8-cm ion thruster in the magnetic test facility and also the orientation of the magnetometer head and its direction of movement. For the orientation illustrated the magnetometer head determines $\vec{B}_r$ in a spherical coordinate system (r, θ, ϕ) in which θ is the polar angle and is the angle of rotation of the rotation table. The precise location of the point r = 0 for the magnetic system of the ion thruster is not known. This magnetic system consists of the soft magnetic material used for the formation of $\vec{B}$ in the bombardment discharge region and the permanent magnets used to power this system. An estimate of the point r = 0 for the magnetic system was that it lay on the central axis of the ion thruster and at a point ~3 cm upstream of the accelerator grid. The ion thruster was placed on the rotation table so that this assumed origin for the magnetic moment system lay at the central point of the degaussing coil system which is the point of rotation for the table.

Figure 96 illustrates $\vec{B}_r$ as the rotation table moves from θ = 0 degrees to θ = 360 degrees and as the magnetometer head moves from a separation distance of 0.406 to 0.610 meters. From the traces shown there, the permanent field of the thruster appears to be completely describable as dipolar (i.e., α cos θ). To test this conclusion, the variation of $\vec{B}_r$ from θ = 0 to θ = 180 degrees was determined as a function of r. The results of this measurement are given in Figure 97 in a log-log presentation. The straight-line drop-off in B_r is almost exactly of the form r^{-3} which is the radial dependence

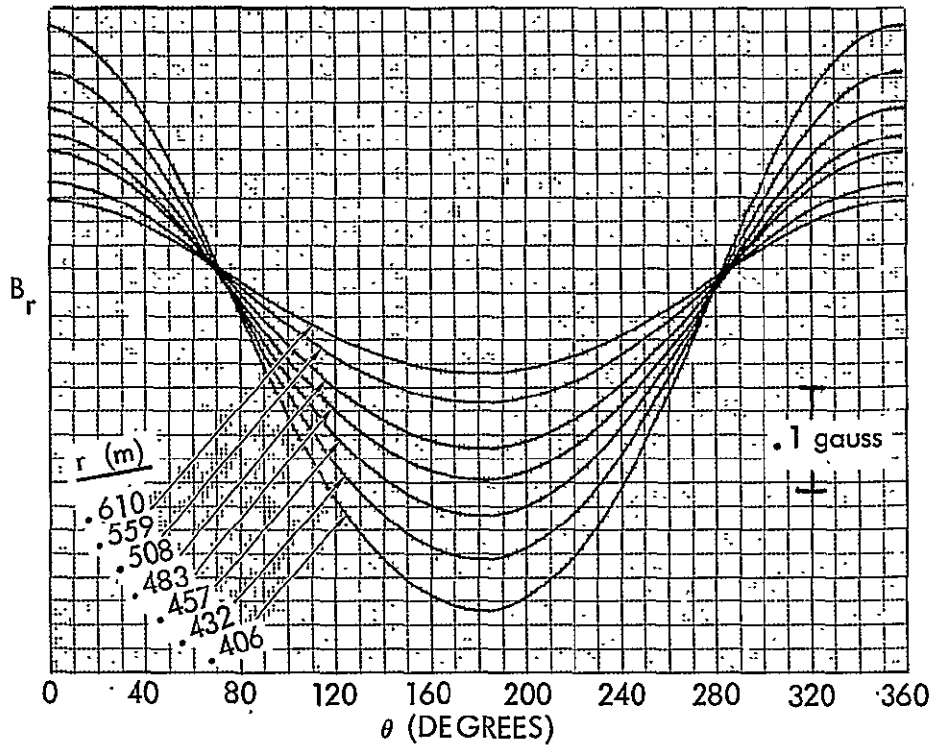

Figure 96. Magnetometer Signal (B_r) as a Function of Rotation Table Angle (θ) for a Series of Magnetometer-Thruster Separation Distances (r)

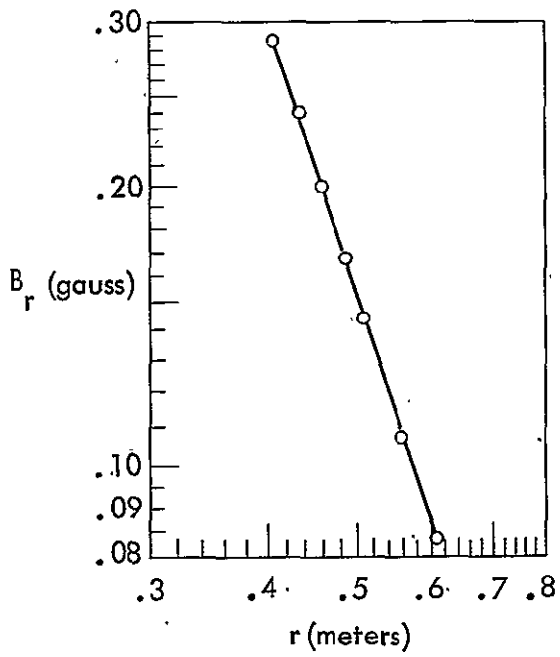

Figure 97. Maximum B_r as a Function of Magnetometer-Thruster Separation Distance, r

of a magnetic dipole. Table 48 provides additional detail for these measurements. Over the range in radial separation from r = 0.406 to r = 0.610 meter the drop-off in B_r and the drop-off in r^{-3} are within ~2% of each other, thus confirming that the permanent magnetic moment of the ion thruster may be accurately represented as dipolar. Using the calibrated outputs of the magnetometer head, this magnetic dipole may be stated as

$$B_r = \frac{1932 \cos \theta}{r^3} \tag{18}$$

and

$$B_\theta = \frac{966 \sin \theta}{r^3} \tag{19}$$

where B_r and B_θ are stated in γ ($1\gamma = 10^{-5}$ gauss) and r is in meters. The coordinate system, as previously noted, is a spherical polar system (r, θ, ϕ) in which $\theta = 0$ is the axis of the ion thruster.

Table 48. 8-cm Thruster Magnetic Moment Data

r(m)	$\vec{B}(0)-\vec{B}(180)$ (Relative)	$\vec{B}(0)-\vec{B}(180)$ (Normalized)	r^{-3} (Normalized)	Normalized $\vec{B}(0)-\vec{B}(180)$/Normalized (r^{-3})
0.406	123.2	1.0000	1.0000	1.0000
0.432	102.5	0.8320	0.8337	0.9980
0.457	85.6	0.6948	0.7023	0.9893
0.483	71.8	0.5828	0.5972	0.9759
0.508	62.0	0.5032	0.5120	0.9828
0.559	46.2	0.3750	0.3846	0.9750
0.610	35.8	0.2906	0.2963	0.9808

A final area of comment on the data given in Figure 96 is in the apparent shift in the level of B_r at $\theta = 90$ degrees and $\theta = 270$ degrees as the magnetometer head is moved from 0.406 to 0.610 meter. From the dipole equation (Equation 18) it is clear that this variation in B at $\theta = \pi/2$ and $\theta = 3\pi/2$ cannot be a contribution from the magnetic source itself. It should be recalled, however, that the cancellation of the earth's magnetic field by the degaussing coils is exact over only a limited volume of space. While that volume of complete cancellation is sufficiently large to enclose the ion thruster, the magnetometer head will, in general, be placed in regions of less than complete cancellation. As the magnetometer head moves from small radial separation distances to large separation distances the degree of cancellation of the horizontal component of the earth's magnetic field, $\vec{B}_{eh}$, diminishes and the level of signal from the magnetometer will vary. This magnetic signal shift is not significant, however, in that magnetic moments are determined by the variations in magnetometer reading as θ is varied and background level $\vec{B}$ (from uncompensated $\vec{B}_{eh}$) does not exhibit a dependence on this rotation angle.

4.8.3 Magnetic Moment Levels for an Operating Ion Thruster Compared to the Inactive (Nonoperating) Thruster

The magnetic moment measurements discussed in Section 4.8.2 were obtained with the thruster in an inactive state (zero current flows in all elements) and result from the permanent magnets and associated magnetic materials used to generate $\vec{B}$ in the electron bombardment discharge region. It is of interest to estimate the variance between the stray magnetic fields produced in the inactive state with those which are obtained when the thruster is in operation and current flows are present in the various elements.

Equations (18) and (19) are the determined B_r and B_θ for the magnetic dipole of the inactive thruster. In its general form the terms B_r and B_θ may be rewritten to

$$B_r = \frac{\mu_o I a^2 \cos\theta}{2r^3} \tag{20}$$

and

$$B_\theta = \frac{\mu_o I a^2 \sin\theta}{4r^3} \tag{21}$$

where μ_o is the permeability of free space and I and a are the current flow and radius of a single turn coil which produces the magnetic dipole. For MKS units, $\mu_o = 4\pi \times 10^{-7}$ webers per ampere-meter, I is in amperes, a and r are in meters, and B_r and B_θ are in webers/m^2 (1 weber/m^2 = 10^4 gauss = 10^9 gamma). For the inactive thruster

$$B_r = \frac{1932 \cos\theta}{r^3} \quad \text{gamma} \tag{18}$$

$$= \frac{1.932 \times 10^{-6} \cos\theta}{r^3} \quad \text{webers/m}^2 \tag{18}$$

so that

$$\frac{\mu_o I a^2}{2} = 1.932 \times 10^{-6} \quad \text{weber/m}$$

in Equation (20). Using $\mu_o = 4\pi \times 10^{-7}$ weber/ampere-meter leads to

$$Ia^2 = \frac{2(1.932)(10)^{-6}}{4\pi(10)^{-7}} \tag{22}$$

$$= 3.075 \text{ ampere-m}^2$$

for the single turn coil which is equivalent to the permanent magnetic field of the ion thruster. Alternatively, the result in Equation (22) illustrates that the substitution of a single turn current carrying loop for the permanent magnetic field elements would require a loop with 3.075 ampere-m^2 as the product of the current flow times the square of the loop radius.

Elements of the active thruster which have current flows as a result of engine operation will generate magnetic dipole moments proportional to the Ia^2 product (described above) where I is the current flow around a radius representative of the thruster current flow. A single turn of the heater element for the thruster neutralizer, for example, will have an Ia^2 product of $\sim 10^{-4}$ ampere-m^2 per ampere of heating current. This Ia^2 value is $\sim 3 \times 10^{-5}$ of the equivalent Ia^2 value of the permanent magnetic field elements. On this basis it is apparent that current flow in the heater elements does not produce magnetic fields which are significant, compared to those resulting from the permanent magnetic elements. This conclusion remains valid for other current carrying elements of the thruster, following a systematic examination of the various thruster elements. This situation results from both the comparatively low levels of current circulation in these low thrust ion engines and from the comparatively small sizes (of the order of a few centimeters in scale) of the current flow patterns.

4.9 NEUTRALIZATION OF DIFFERENTIALLY CHARGED SURFACES

The chargeup of spacecraft surfaces in geomagnetic substorms and at geosynchronous orbit altitudes is now a generally accepted condition for the electrical equilibration of spacecraft under such conditions. A particularly severe form of spacecraft chargeup, and, specifically, differential chargeup, occurs when the metallic frame of the spacecraft is photoemissively clamped to the ambient space plasma potential, while the dielectric outer surfaces of the spacecraft are charged negatively to high potentials by the deposition of energetic substorm electrons.

For spacecraft which include an ion thruster in the system complement, it is of interest to examine the possibility that charged particles from the ion thruster can be used to offset the effects of these differential chargeups on spacecraft surfaces. A specifically interesting possibility is that ions from the plasma plume of the plasma discharge neutralizer can be used to neutralize the deposited substorm electrons on spacecraft dielectric (insulating) surfaces.

It is not easily possible to duplicate, in laboratory facilities, the various charged particle flows and electrical equilibration phenomena which occur for electrically isolated spacecraft in the very dilute, but very energetic, charged particle environments of the magnetic substorms. It is possible, however, to

examine certain aspects of charged particle flow from the plume of the plasma discharge neutralizer to negatively charged surfaces, and from these drainage current measurements to infer the charged particle flow behavior for vehicles in space. This section describes such a series of measurements, beginning with the design of the experimental apparatus.

4.9.1 Experiment Setup

In the initial planning of the experimental tests, the principal requirement of the experimental array was that it should be capable of detecting relatively small drainage currents of positively charged ions to various surfaces at variable negative bias potentials. The notion that the positive ion current flow would be at small levels follows generally from the space charge and particle mass limitations on such flows. These space charge limitations in current flows in diodes causes the current density to diminish as the inverse square of the distance from the particle source to the particle collector. Because these distances can be comparatively large for spacecraft with ion thrusters, the experimental apparatus might anticipate that the currents over these large separation distances would be greatly reduced. A second major factor in the reduction of the current is the high mass of the Hg^+ ions in the discharge neutralizer plume (noting that the space charge limited current is inversely proportional to the square root of the charged particle mass). Another requirement of the experimental array is that it should be capable of detecting charged particle flows to several different surfaces which, if possible, should be at various distances from the thruster and its neutralizer.

Figure 98 illustrates features of the experimental array in these current drainage tests. The ion thruster was installed in the 5 by 10 foot test chamber as illustrated. The ion thruster sputter shield was in place in view of anticipated future spacecraft operation of the thruster with such a sputter shield in place. In the present experimental array the sputter shield was electrically isolated from the thruster and could be separately biased for charged particle extraction with appropriate measurement of that drainage current.

Also present in the experimental array in Figure 98 was an electrically isolated, cylindrical electrode, the upper shroud, the lower shroud, and thrust beam collector. The upper shroud is electrically isolated for drainage current measurements as is the combined lower shroud and thrust beam collector.

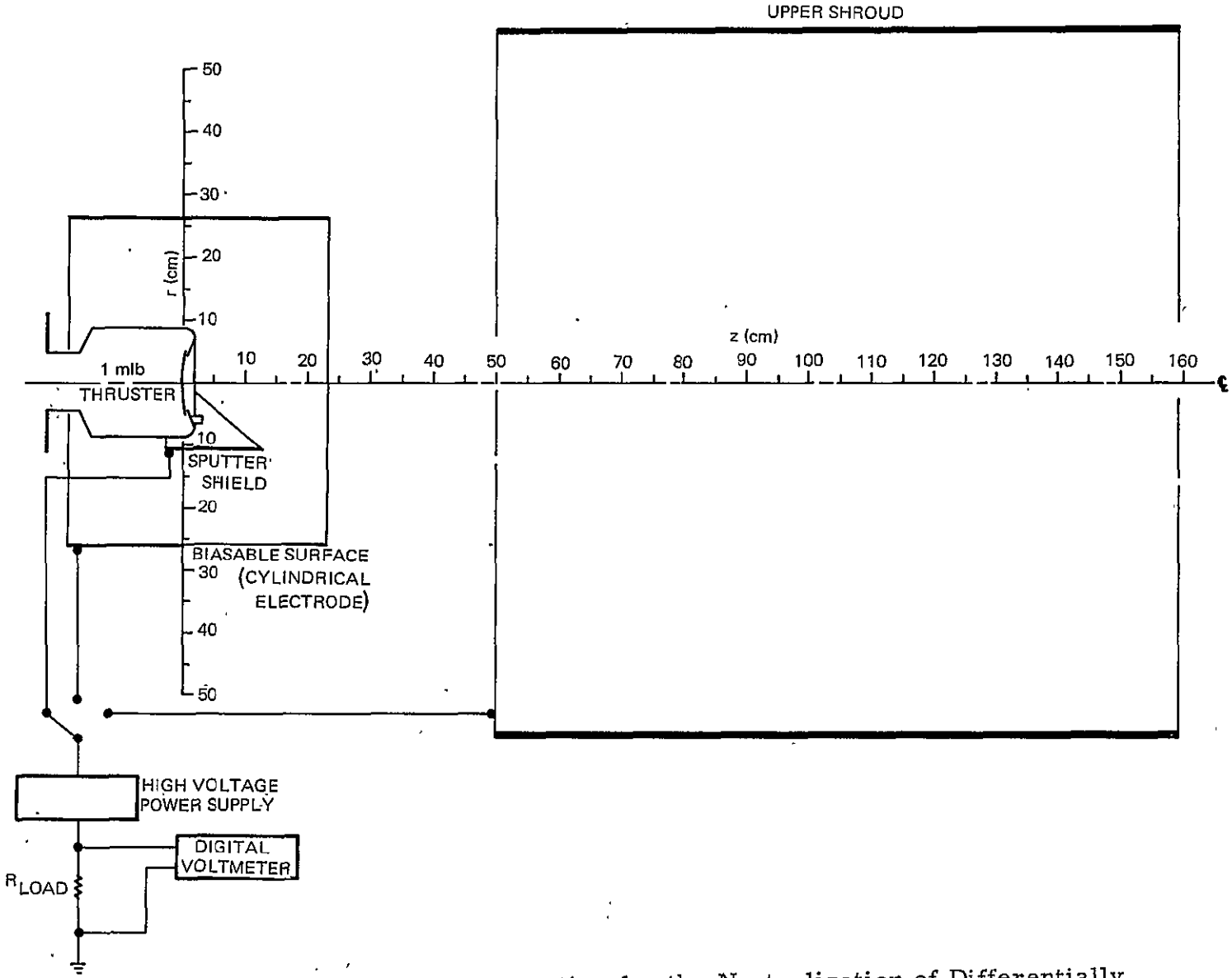

Figure 98. Overall Test Configuration for the Neutralization of Differentially Charged Surfaces Tests

4.9.2 Drainage Current Measurements

During test, drainage currents were measured as a function of bias potential to: the cylinder, the upper shroud, and the thruster sputter shield.

Measurements of Drainage Current to the Cylinder

When a negative bias potential is applied to the cylinder, a current of ions can be observed at this electrode. Figure 99 illustrates the ion current arriving at this electrode as a function of bias potential.

There are several features of the data in Figure 99 which are important. The first of these is the surprisingly high value of ion drainage current. For only small levels of bias (-10 volts), ion currents at the 40 microampere level can be observed. Such currents are clearly not consistent with a model of the ion current flow in which a physically small plasma cloud is the source of ions which emerge from this cloud to traverse the bulk of the separation distance from the thruster neutralizer to the electrode in a unipolar flow. The large values of ion current at low bias potentials, rather, indicate that the source of the ions is an extensive and dilute plasma cloud whose dimensions greatly exceed the dimensions of the thruster neutralizer proper and that ions moving from the neutralizer to the cylindrical electrode have the major portion of their traverse in plasma so that the space charge limitations of unipolar flow are not present.

The continued growth of the ion drainage current to levels of several hundred microamperes is also considered as an important feature. Because the deposition current densities in magnetic substorms are only at levels of a few nanoamperes per square centimeter, even spacecraft surface areas as large as 1 square meter may have electron deposition currents of only a few tens of microamperes. Ion drainage currents of several hundred microamperes, thus (as observed at ~300 volts of negative bias potential on the cylinder), could act to discharge differentially charged spacecraft surfaces of many square meters in area.

A third feature of importance in the data in Figure 99 is the abrupt cutoff in the ion drainage current to the cylinder for bias voltages more negative than 300 volts. As noted, the ion current falls abruptly to zero and remains

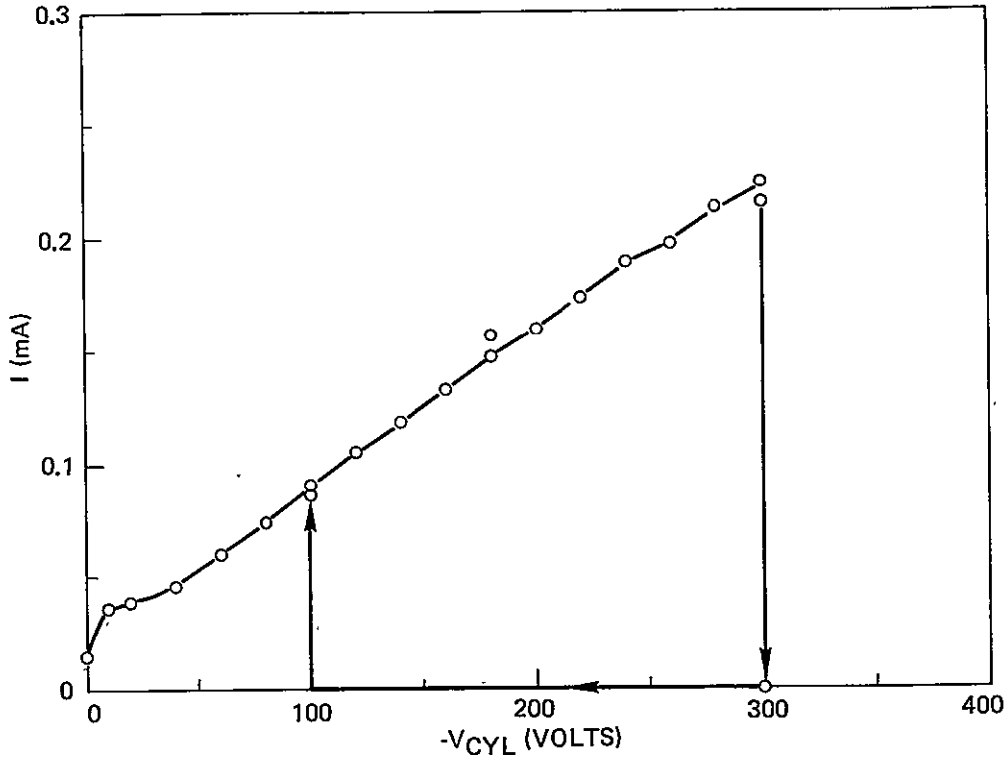

Figure 99. Ion Drainage Current to the Cylinder

at this low level for either positive or negative voltage motion of the extraction electrode. For more negative bias voltages, drainage currents remain small, even for bias potentials at several kilovolts (approximately -5 kV) of bias potential. For less negative bias voltages, drainage currents remain small until the cylinder potential approaches approximately -100 volts at which point the drainage current abruptly rises to the levels originally observed (for the I - V curve for the $0 < V_{CYL} < -300$ volt regime initially described).

The observed behavior suggests several possible processes described in the following hypothesized interaction. In the first regime, a dilute and extensive plasma cloud is hypothesized and ions diffusing outward in this cloud eventually move to the cylinder at only comparatively modest extraction potentials because most of the ion traversal is carried out <u>in plasma</u> (in the presence of electrons which mitigate the effects of ion space charge). As the cylinder bias is carried to more negative potentials, ion extraction current increases. At some upper bound limit on ion current, however, the plasma

cloud is dissipated, collapsing to a much smaller physical size. In this more compact plasma cloud condition, the ions must move large distances without accompanying electrons and would appear at very low current levels as was originally anticipated. After the collapse of the plasma cloud volume, relaxations of the bias voltage do not act to restore the ambipolar diffusion until considerable relaxation of this bias has been exercised. At this lower bias point the ambipolar diffusion is once again active and the plasma volume once again enlarges so that significant ion current transport to the cylinder can take place at even modest cylinder bias voltages.

The hypothesized behavior above does not explain the method by which the plasma cloud collapse is initiated. One possible line of explanation could be an ion-electron instability which destabilizes the plasma at some upper end ion current passage. A second line of explanation can be that only a limited ion generation rate exists in the plasma plume and that the extraction of the entirety of this generated current to the cylinder causes the dissipation and collapse of the plasma. Either method of explanation remains speculative, however, in view of the present comparatively limited experimental evidence.

As a final treatment of the data in Figure 99, the I - V curve is restated in Figure 100 in log-log form and using, as the voltage variable, the term $V_K - V_{CYL}$ where V_K is the potential of the neutralizer keeper (which is, presumably, the potential at which the dilute plasma cloud forms) and V_{CYL} is the cylinder bias. Over the larger part of the I - V characteristic, the relationship is $I_{drainage} \alpha k (V_K - V_{CYL})^n$. The implications of these data are not completely understood at present.

Measurements of Drainage Current to the Upper Shroud

The upper shroud of the testing array is illustrated in Figure 98 and is a liquid nitrogen cooled liner for the 5 by 10 foot system. It is electrically isolated from the remaining shroud and the thrust beam collector and can be separately biased for ion current drainage from the neutralizer plasma plume.

In the measurements discussed above, this shroud was held at V = 0 while the electrical bias of the cylinder was varied. In the measurements described here, the cylinder is maintained at V = 0 while the shroud bias

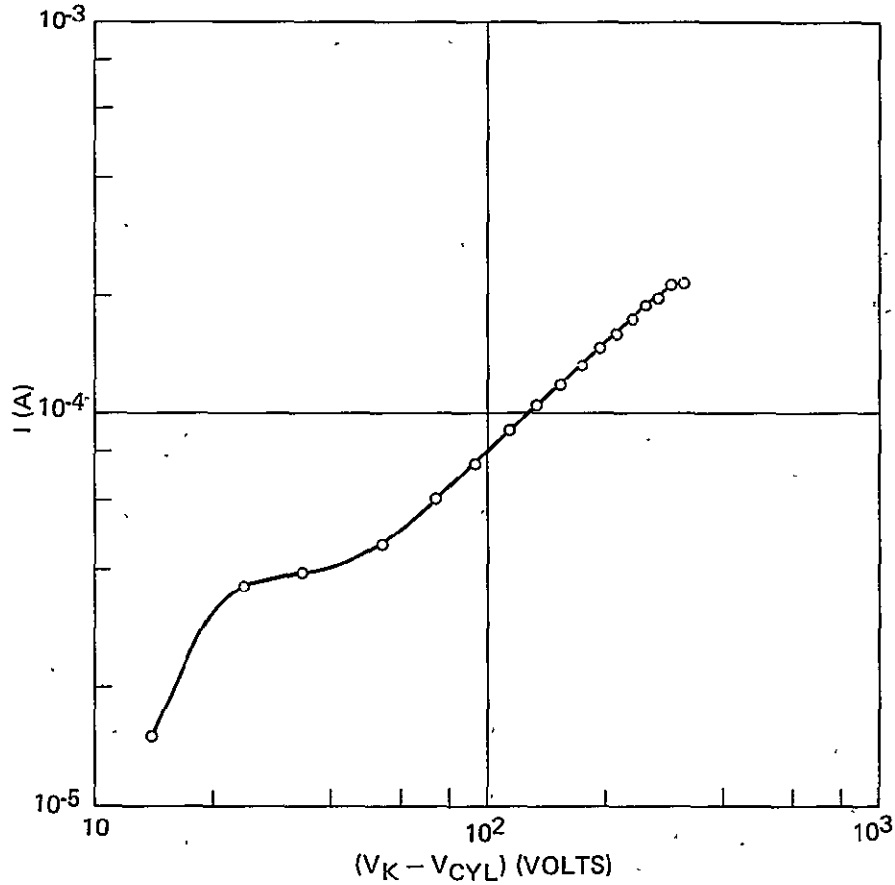

Figure 100. Ion Drainage Current to the Cylinder, Logarithmic Presentation

voltage is varied. For both this and the preceding data, the thruster sputter shield was held at V ≈ 0.

Figure 101 illustrates the ion current to the upper shroud as the shroud bias is varied. The general behavior of the drainage current to this element is similar to that observed for ion flow to the cylinder. For comparatively small voltages, the shroud ion drainage reaches levels of ~200 microamperes. Further increases in shroud voltage, beyond ~-300 volts, cause an abrupt collapse of the observed ion flow which remains small, even for subsequent relaxations of the bias voltage, until the bias approaches -100 volts at which point the ion flow is reestablished at the several hundred microampere level. The slope of the I - V curve is less than for the biased cylinder case.

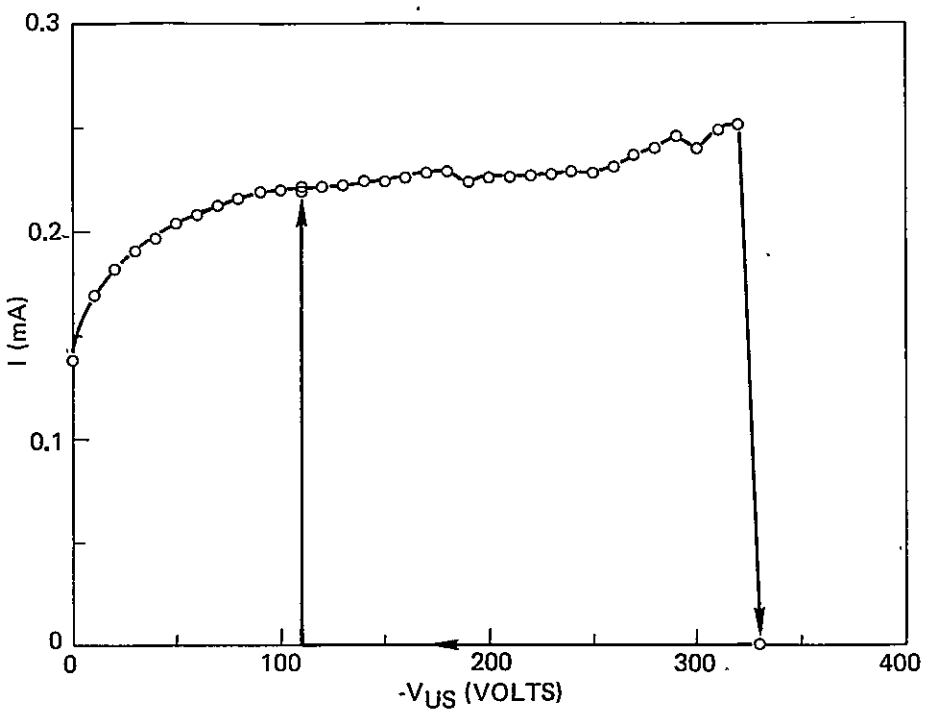

Figure 101. Ion Drainage Current to Upper Shroud

The data in Figure 101 may be considered even more surprising in some respects than for the observed ion flow to the cylinder, in view of the generally larger distances of ion transport to move from the thruster neutralizer to this downstream electrode. If the ion transport is, indeed, the result of the formation of a large and dilute plasma cloud emanating at the thruster neutralizer, then the dimensions of this cloud, from the standpoint of effective ion transport, must be of the order of 1 or more meters.

The abrupt cut-off of the ion drainage at ~240 microamperes is similar to the current level at cut-off for ion flow to the cylinder. In the above discussions of mechanisms for an implied plasma cloud collapse, it was considered that ion extraction beyond some level could exhaust the total ion production rate of the thruster neutralizer causing the plasma cloud to dissipate. If this mechanism is, indeed, present, the similarity of the cut-off levels in the two cases of ion flow would tend to be indicative of such a process.

Measurements of Drainage Current to the Thruster Sputter Shield

Figure 102 illustrates the ion current to the sputter shield as a function of sputter shield bias voltage. The behavior exhibited there is strongly similar to that behavior shown for ion flow to the cylinder and is relatively similar to the ion flow observed at the shroud. The hysteresis-loop aspects of the ion flow are present, and cut-off drainage level for hypothesized plasma cloud collapse is, again, at ~300 microamperes. As noted earlier, this similarity in ion current cutoff levels tends to support an exhaustion hypothesis for a plasma cloud collapse.

The thruster sputter shield was also biased positively to cause an extraction of electrons. Figure 103 illustrates these data. Electron current cut-off and plasma cloud collapse would not be expected for this condition and this level of current drainage and was not observed.

4.9.3 Implications of the Observed Ion Current Drainage Behavior

The principal feature of the data in Figures 99 through 102 is the comparative ease in which ion currents, at levels from tens to hundreds of microamperes, can be drawn from the thruster neutralizer plasma plume to relatively remote surface locations. If similar circumstances are present in space, then the flow of ions to negatively charged spacecraft surfaces should proceed at sufficient rates to match, essentially, the electron deposition levels on those surfaces. It is not positively determined, however, that all of the electrical equilibration features for spacecraft in energetic dilute charged particle environments in space can be simulated in laboratory facilities, and circumstances can be envisioned in which the various electric fields to and from various spacecraft surfaces could act to inhibit as well as to encourage the ion flow from the thruster neutralizer.

The observed phenomena of ion flow cut-off for extraction currents above a particular level (~300 microamperes) should not restrict possible applications of the plasma discharge neutralizer as a differential surface-charge neutralizer, at least for geosynchronous substorm conditions. As noted earlier, the electron depositions in such storms are at ~10^{-9} A/cm^2 levels, and

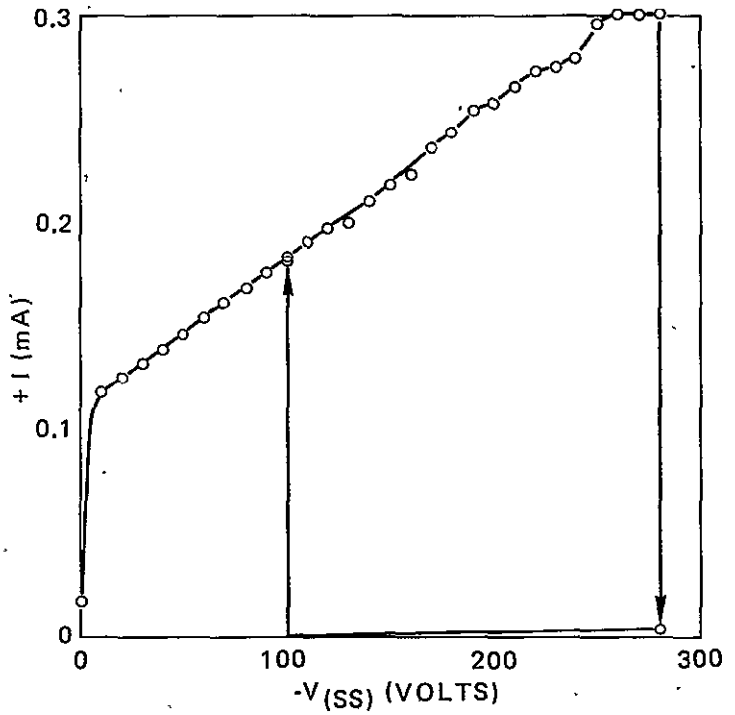

Figure 102. Ion Drainage Current to Sputter Shield

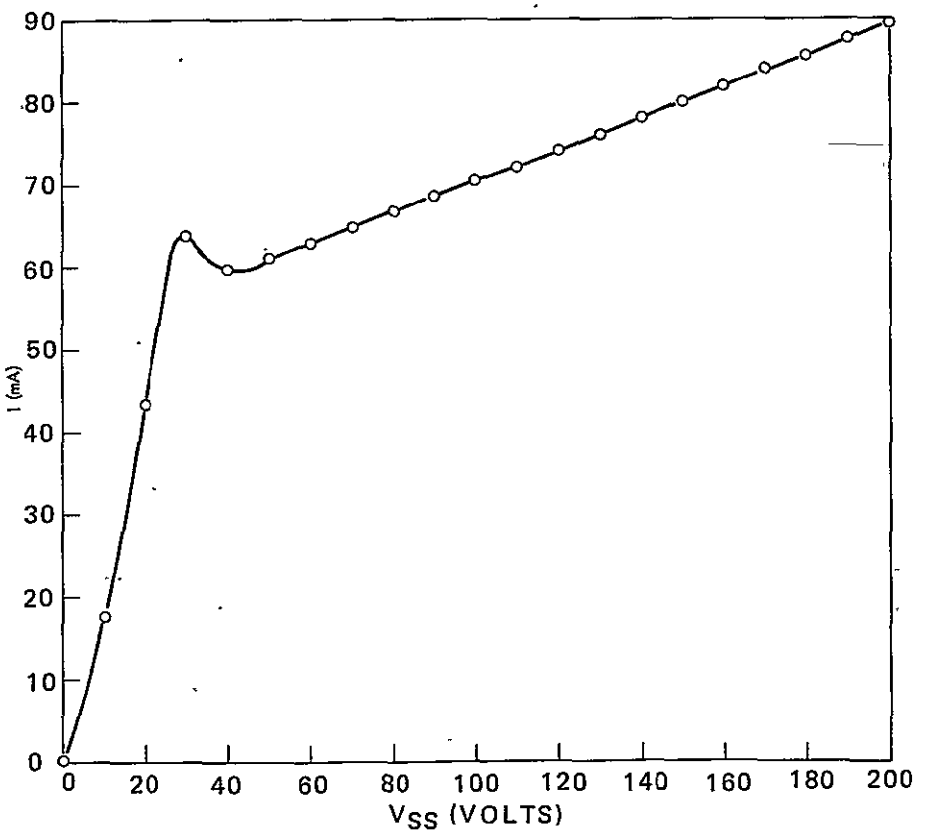

Figure 103. Electron Drainage Current to Sputter Shield

the 300 μA ion current production rate would represent a substorm electron deposition over an approximate area of 10^5 cm^2 (10 m^2). It would also appear possible to increase this ion current cut-off limit by suitable modification of the neutralizer.

5. USERS MANUAL

A Users Manual was prepared in order to describe the principal characteristics of the 8-cm mercury ion thruster system as an aid to potential spacecraft designers. The manual describes the hardware that has been developed, contains technical design data pertinent to its integration on a spacecraft, and gives examples of typical spacecraft that were designed to use the equipment. The manual outline is shown in Table 49.

The introduction to the manual presents the advantages and principal applications of ion engine auxiliary propulsion followed by an initial overview outlining and defining the scope of the various sections comprising the manual. The overview is organized in terms of how to use the information contained in the manual. The introduction also identifies the major considerations in using ion engines, namely, the time to perform a thrusting maneuver, the power for propulsion, thruster placement to assure efflux compatibility, and spacecraft electrical equilibration.

Table 49. Users Manual Outline

Section	Title
1	Introduction
2	Propulsion Subsystem Analysis and Selection
3	Subsystem Configuration
4	Interface Requirements
5	Design Constraints
6	Environmental Qualifications
7	Reliability and Redundancy
8	Future
9	References
10	Nomenclature

Section 2 of the manual identifies geosynchronous mission requirements that can be performed using ion auxiliary propulsion. The requirements are given for north-south stationkeeping, east-west stationkeeping, station changing, attitude control and momentum wheel dumping.

Once the mission requirements are identified, the method for propulsion subsystem selection is described. It consists of:

- Calculating thrust level/operating time requirements
- Calculating propellant requirements
- Selecting equipment
- Identifying power and weight allocations
- Selecting thruster locations on the spacecraft
- Trading off thrust level/system weight/reliability

The methods for comparison with alternate propulsion methods, e.g., cold gas, hydrazine, are given. A sample case is identified.

Section 3 describes the equipment that is used in an ion engine propulsion subsystem. First, it briefly explains the principle of thruster operation. Then it gives an overall subsystem description showing the function of each piece of equipment and identifying how the pieces may be tied together. It describes the thruster, gimbal assembly, propellant reservoir, power electronics unit, digital interface unit, and digital control unit. Next, integration hardware is presented. Integration hardware includes valves, fittings, electrical cabling, connectors, and relays. Finally, examples of ion propulsion subsystem applications are shown. The two examples are those studied under Task I of the program.

Section 4 contains detailed mechanical, electrical, and thermal interface data. Mechanical data include equipment dimensions, weight, mounting provisions, and alignment requirements. Electrical data include input voltage and power requirements, isolation and grounding constraints, input command and output telemetry characteristics, and identification of all electrical connections on the hardware. Thermal data identify equipment temperature limits and heat dissipation from the equipment when operating.

Section 5 discusses interactions between the thruster and spacecraft. It contains efflux characteristics data, both with and without a sputter shield

installed. Reference is given to the literature for effects on typical spacecraft surfaces. Sample calculations are included, based on Task I analyses, to show how the data are employed to locate the thruster on typical geosynchronous satellite configurations. Electromagnetic compatibility design information is presented based on the specifications for the thruster subsystem. Spacecraft neutralization is described, and spacecraft charge control implementation procedures are discussed. Thruster optical radiation data and magnetic field data are given, together with a brief discussion showing that interaction levels are extremely low so that they are insignificant for most applications.

The environmental design information contained in Section 6 derives from the specifications for the thruster subsystem. It identifies safe operating and nonoperating environments for the equipment.

Available data and test results are compiled and presented in Section 7 to permit reliability predictions to be made for various missions. Redundancy techniques are suggested that can be readily implemented with available hardware to enhance mission reliability. Other reliability improvement techniques are identified for completeness, even though implementation may be more complex.

Future plans for hardware development are presented in Section 8, together with anticipated parametric characteristics of 1/2 mlb (2.2 mN) and 2-mlb (8.9 mN) thruster subsystem options.

6. DISCUSSION OF RESULTS

The study program has shown that large weight savings are obtained when ion propulsion is used for auxiliary propulsion on geosynchronous spacecraft in place of hydrazine propulsion. This weight savings can be used for increased payload. For example, reference 20 discusses the cost benefits to be expected with ion propulsion on communications satellites, and estimates that each 9 to 11 kg (20 to 25 pounds) of additional transponder payload generates $2 million per year revenue, or $20 million over a 10-year spacecraft lifetime.

The reduced propellant volume requirements for ion propulsion can result in cost savings for Shuttle-launched payloads. The MMS example studied showed that the reduced propulsion module length could save $1.5 million per launch based on current pricing policy and launch cost.

Pointing accuracies with ion propulsion are very favorable when compared with the more conventional hydrazine. This is because of the low thrust level, vectorable nature of the thruster, and essentially steady-state operation. Pointing transients of less than 4×10^{-4} degree are predicted from computer simulation results for the MMS. This advantage could be more important than orbital correction propellant weight savings for missions requiring high pointing accuracies.

Nonsymmetric spacecraft designs are better suited for ion propulsion because the thrusters can easily compensate for the solar pressure disturbance torques resulting from an offset array. This configuration can be advantageous from a satellite design aspect since only one solar array drive is required for oriented arrays and large payload appendices can be extended on the side opposite the array without shading it.

The data base for plume analysis was greatly expanded in the experimental portions of this study. Efflux analysis has shown that the 8-cm thruster can be integrated on all types of geosynchronous spacecraft. Spin stabilized spacecraft afford an unobstructed, hemispherical field of view for the thruster exhaust. That is also the case for three-axis stabilized spacecraft with the thrusters mounted at the array tips, or for three-axis,

nonsymmetrical spacecraft with body mounted thrusters. In the case of three-axis, symmetric spacecraft with central body mounted thrusters, it was found necessary to provide a sputter shield, lateral separation of the thrusters from the solar array axis, and canting of the thrusters from this axis to achieve best efflux compatibility.

The basic strategy for supplying electric power to an ion propulsion subsystem on a communications satellite using advanced nickel-hydrogen batteries was developed in a previous study (reference 10). In the present study, it was shown that the same strategy can be used with nickel-cadmium batteries. Nickel-cadmium batteries have a long history of successful service in orbit. Thus, the 8-cm thruster could be integrated on an advanced communications satellite without adding additional solar array or battery weight.

In view of the above considerations, it is desirable to qualify the 8-cm thruster subsystem as early as possible to make it available for application. In anticipation of this activity, the Users Manual has been prepared to acquaint potential spacecraft designers with the subsystem's capabilities. Also, in order to enhance user confidence, a joint NASA/Air Force flight test of the subsystem has been scheduled for launch. Plans are similarly being made to obtain additional efflux measurements in space on Shuttle experiments, where low arrival rate efflux determinations can be made in the absence of background effects induced by the presence of ground test facilities.

It is recommended that development of a high-performance propulsion module for MMS be initiated as a result of the advantages identified during this study. Such a development program would provide meaningful inputs to the hardware specifications for an operational flight configuration of the 8-cm thruster subsystem. In order to achieve early hardware qualification, it is necessary to retain only critical functions within the subsystem, and to delete the rest that are being used only for diagnostic purposes or expanded capabilities.

Development of ground support equipment for the thruster subsystem should also be initiated. This should include a thruster unit simulator and

ground checkout console to provide for thruster electrical integration testing. The simulator substitutes for the flight thruster during integrated spacecraft system testing when it is necessary to run an end-to-end electrical check but is impractical to operate the thruster. Also, a test connector has to be added to the thruster to verify the spacecraft-to-thruster interface when the thruster replaces the simulator. A special connector cap with jumper connections completes the electrical circuitry after interface verification.

It is also recommended that a thruster switching unit, based on vacuum ceramic relays, be qualified to enable implementation of redundant thrusters as discussed in Section 3.2.7. Increased subsystem reliability at modest weight penalty is achieved in this manner.

7. CONCLUSIONS

Two specific near-term spacecraft missions were examined to assess 8-cm mercury ion thruster applicability, advantages, and interface requirements. It was found that these ion thruster subsystems could replace hydrazine propulsion for the missions examined, and be fully compatible with other existing spacecraft subsystems.

Using an ion propulsion subsystem instead of electrothermal hydrazine on an advanced 1000 kg (2200 lb) communications satellite increases the weight available for additional payload by about 82 kg (181 lb). This additional weight can be used to increase communications payload and revenue.

A high performance propulsion module was designed for NASA's Multimission Modular Spacecraft (MMS). This 112 kg (247 lb) module incorporates four ion thrusters, and can provide over 6.4×10^5 N.s total impulse. It is only 18 inches (0.46 meter) long, which results in recurring Shuttle launch cost savings compared to a hydrazine module. The ion propulsion module is compatible with a tight pointing accuracy of 10^{-2} degree, 10^{-6} deg/sec drift rate deviation, and 6×10^{-4} degree jitter without payload constraints, i.e., without payload interruption during thrusting periods. This high performance module was studied for both low earth orbit and geosynchronous missions. Its design is flexible enough to permit integration in both cases, while meeting all interface requirements of the MMS and Space Transportation System (Shuttle).

Efflux characteristics data were obtained with a NASA-furnished 8-cm thruster. These data, which were taken with and without a sputter shield installed on the thruster, are now available for integration analysis. The data were used to specify thruster locations on the two specific spacecraft studied.

The sputter shield was effective for body mounted thruster integration on the three-axis stabilized, symmetrical advanced communications satellite configuration. It was not required on the MMS missions examined. In general, the north-south stationkeeping thrusters have an unobstructed, hemispherical exhaust field of view when mounted on solar array tips,

spin-stabilized spacecraft, or three-axis, asymmetric spacecraft. These gimballed thrusters can then be used for other propulsive functions, such as attitude control, east-west stationkeeping and momentum dumping. The most difficult efflux integration task is related to the three-axis symmetrical spacecraft with body mounted thrusters. Avoiding potential efflux problems required lateral thruster separation from the solar array axis, canting of the thrusters with respect to this axis, and incorporation of the sputter shield.

Optical radiation measurements taken with the thruster showed very low power densities, thereby demonstrating compatibility with current sun sensor attitude control systems. Sensitive star tracker systems are also probably compatible with these thrusters.

The principal thruster magnetic field is that of its permanent magnets and has a dipole characteristic. This magnetic field is compatible with all but very sensitive scientific spacecraft.

The neutralizer assembly on the thruster is a sufficiently large source of low energy ions for discharging surfaces at geosynchronous altitudes that may otherwise be subjected to large negative voltage excursions. Neutralization of differentially charged spacecraft surfaces was shown to be feasible as a result of laboratory experiments with the thruster and a biasable surface placed near it.

At the conclusion of the program, a Users Manual for the 8-cm mercury ion thruster subsystem was prepared. It describes the equipment that is used in an ion propulsion subsystem, and contains detailed mechanical, electrical, and thermal interface data. It identifies geosynchronous mission requirements that can be performed using ion auxiliary propulsion. Interactions between the thruster and spacecraft are discussed, drawing heavily on the data taken with the 8-cm thruster. Equipment environmental limits and reliability information are also presented. The manual concludes with a description of other thruster options to operate at 1/2-mlb (2.2 mN) and 2-mlb (8.9 mN) thrust levels.

REFERENCES

1. W.R. Hudson and R.C. Finke, "NASA Electric Propulsion Program," AIAA Paper No. 76-1068, November 1976.

2. B.A. Banks, et. al., "8-cm Mercury Ion Thruster System Technology," NASA TM X-71611, October 1974.

3. S. Nakanishi, "A 15,000-Hour Cyclic Endurance Test of an 8-cm Diameter Mercury Bombardment Ion Thruster," AIAA Paper No. 76-1022, November 1976.

4. B.G. Herron, J. Hyman, Jr., and D.J. Hopper, "Development of an 8-cm Engineering Model Thruster System," AIAA Paper No. 76-1058, November 1976.

5. D.H. Mitchell and M.N. Huberman, "Ion Propulsion for North-South Stationkeeping of Communications Satellites," AIAA Paper No. 76-290, April 1976.

6. G.K. Komatsu and J.M. Sellen, Jr., "Beam Efflux Measurements for a 30-cm Mercury Ion Thruster," AIAA Paper No. 76-1052, November 1976.

7. "Summarized NASA Payload Descriptions — Automated Payloads, Level A Data," (Preliminary) Prepared by Program Development, NASA Marshall Space Flight Center, July 1975.

8. "Payload Descriptions, Volume 1 — Automated Payloads, Level B Data," NASA Marshall Space Flight Center, July 1975.

9. "Low Cost Modular Spacecraft Description," (now called Multimission Modular Spacecraft), NASA Document X-700-75-140, Goddard Space Flight Center, May 1975.

10. D. Rusta, "Power Source Requirements of Electric Propulsion Systems Used for North-South Stationkeeping of Communication Satellites," Eleventh IECEC Conference Proceedings, September 1976.

11. R.H. Sparks and W.R. Scott, "Application of Nickel-Cadmium Batteries in Deep Discharge Synchronous Orbit Applications," Eleventh IECEC Proceedings, September 1976.

12. P. Fono, "Spacecraft Nickel-Cadmium Battery Cycle Life Assessment," Seventh IECEC Proceedings, 1972.

13. J.H. Molitor, "Ion Propulsion Flight Experience, Life Tests, and Reliability Estimates," Journal of Spacecraft and Rockets, Vol. 11, No. 10, October 1974, pp. 677-685.

14. M.D. Thompson, "Failure Modes, Effects and Criticality Analysis," Summary Report for 8-cm Engineering Model Thruster System, Contract NAS 3-18917, July 1976.

15. R.F. Gates and K.J. McAloon, "Precision Star Tracker Utilizing Advanced Techniques and Materials," Journal of Spacecraft and Rockets, Vol. 13, No. 10, pp. 594-599, October 1976.

16. G.K. Komatsu and J.M. Sellen, Jr., "Beam Efflux Measurements," NASA CR-135038, June 1976.

17. J.M. Sellen, Jr., W. Bernstein, and R.F. Kemp, "Review of Scientific Instruments," Vol. 36, pp. 316-322, 1965.

18. Childs, "Low Pressure Mercury Arc for Ultraviolet Calibration," Applied Optics, Vol. 1, pp. 711-716, 1962.

19. H.M. Jongeruis, Thesis, Utrecht, 1961.

20. R.A. Meese, M.E. Ellion, and A. Burstein, "Application of Ion Engines to Synchronous Orbit Spacecraft," AIAA Paper No. 75-1229, September 1975.

APPENDIX A

SYMBOLS

$A(z)$	Shield area at height z, $(\text{centimeters})^2$
A_p	Probe area, $(\text{centimeters})^2$
a	Radius of single turn coil, meters
B	Magnetic field, gauss
B_e	Earth's magnetic field, gauss
B_{eh}	Horizontal component of earth's magnetic field, gauss
B_r	Radial magnetic field, gauss
B_θ	Orthogonal magnetic field component, gauss
D	Disturbance torque, newton-meters Duty cycle
D_t	Thruster diameter, centimeters
d_T	Depth-of-discharge with thrusting
d_{T_e}	Depth-of-discharge during equinox with thrusting
$d_{T_{ss}}$	Depth-of-discharge during summer solstice with thrusting
E	Energy, electron-volts
e	Electronic charge, coulombs
F	Thrust, newtons
G	Gain Gain, $(\text{seconds})^{-2}$
H	Angular momentum, newton-meter-seconds
h	Planck's constant, erg-seconds
I	Moment of inertia, kilogram-$(\text{meter})^2$ Current, amperes
I_w	Reaction wheel motor inertia, newton-meter-seconds/rpm
i	Inclination, degrees
J	Current density, milliamperes/$(\text{centimeter})^2$
$J(CK)$	Cathode keeper current, amperes
$J(E)$	Discharge emission current, amperes
$J(NK)$	Neutralizer keeper current, amperes
J_B	Beam current, milliamperes
K	Loop gain, $(\text{seconds})^{-2}$
k	Boltzmann's constant, joules/$^\circ$K

k_e	Thruster angle gain, degrees/rpm
L	Operating life, hours Distance from thruster to collector, meters
ℓ	Lever arm, meters
M	Spacecraft mass, kilograms Torque, newton-meters
N_D	Number of days firing/year
N_N	Number of nodal firings/day
N_Y	Number of years/mission
$N_{\bar{d}_T}$	Number of discharge cycles
N_e	Number of equivalent discharge cycles
P(t)	Probability
P_{sc}	Spacecraft load power, watts
R	Radial distance, polar coordinates, centimeters Probe arm length, centimeters
R(t)	Reliability
r	Radial distance, cylindrical or spherical coordinates, centimeters
T_e	Electron temperature, ^{o}K
t	Time, years Time, hours Time, seconds
V	Voltage, volts
V(CK)	Cathode keeper voltage, volts
V(NK)	Neutralizer keeper voltage, volts
V_{CYL}	Cylinder bias, volts
V_{FP}	Floating potential, volts
V_K	Neutralizer keeper potential, volts
V_P	Plasma potential, volts
V_{RP}	Retarding potential, volts
V_S	Surface charge-up, electron-volts
V_{SS}	Sputter shield bias, volts
V_{US}	Upper shroud bias, volts
V_{inj}	Injection potential, volts
x	Distance, Cartesian coordinates, centimeters
y	Distance, Cartesian coordinates, centimeters

z	Axial distance, cylindrical coordinates, centimeters Distance, Cartesian coordinates, centimeters
α	Orbital half-angle, degrees Probe rotation angle, degrees Sputtering angle of incidence, degrees
β	Reflected ion fraction
γ	Time constant, $(\text{seconds})^{-1}$ Angle of sputtered metal atom release, degrees
ΔV	Discharge voltage, volts
Δv	Velocity increment, meters/second
δ	Daily precessional angle, degrees
ϵ	Normalized efflux, $(\text{centimeters})^{-2}$
θ	Gimbal position, degrees Angular position, polar coordinates, degrees
λ	Failure rate, failures/10^9 hours
μ	Magnetic permeability
μ_o	Magnetic permeability of free space
ν	Frequency, $(\text{seconds})^{-1}$
ρ	Plasma density, particles/$(\text{centimeter})^3$
ϕ	Thruster cant angle, degrees Gimbal position, degrees Roll error, degrees Angular position, cylindrical or spherical coordinates, degrees
ψ	Yaw error, degrees
ω	Loop frequency, $(\text{seconds})^{-1}$
ω_o	Orbit rate, degrees/seconds

APPENDIX B

DESIGN OF BOOST REGULATOR BETWEEN SPACECRAFT BUS AND ION ENGINE POWER PROCESSOR

The boost regulator converts the unregulated 28 Vdc input power to a regulated 70 Vdc output voltage. The regulated output voltage is used by a power processor to generate the output voltages that are required by the ion engine.

The basic concept used is the boost type switching regulator. This type of regulator was selected because it provides the most efficient operation.

The block diagram of the regulator is shown in Figure B-1. The power section of the regulator, detailed in Figure B-2, consists of an input filter, energy storage element and power switch, and the output filter.

The control circuits consist of the low voltage inhibit, overvoltage and overload control, timer, and the ASDTIC* control signal processors which are the analog control signal processor and the digital control signal processor. The last block is the +5-volt regulator which supplies the regulated low voltage for all the control circuits.

The input filter is a two-section damped LC filter which enables the regulator to meet the conducted interference requirements by isolating the chopping action of the power switching transistor from the input line and preventing large currents from being reflected to the input. It also attenuates audio frequency and transients originating on the input line and propagating to the regulator. The filter also provides a low impedance source of energy for the pulse requirements of the power switching transistor by using a polycarbonate capacitor in the second section of the input filter.

---

*Analog Signal to Discrete Time Interval Converter (ASDTIC), Ref: Y. Yu, et al., "The Application of Standardized Control and Interface Circuits to Three DC to DC Power Converters," IEEE Power Processing and Electronics Specialists Conference, 1973.

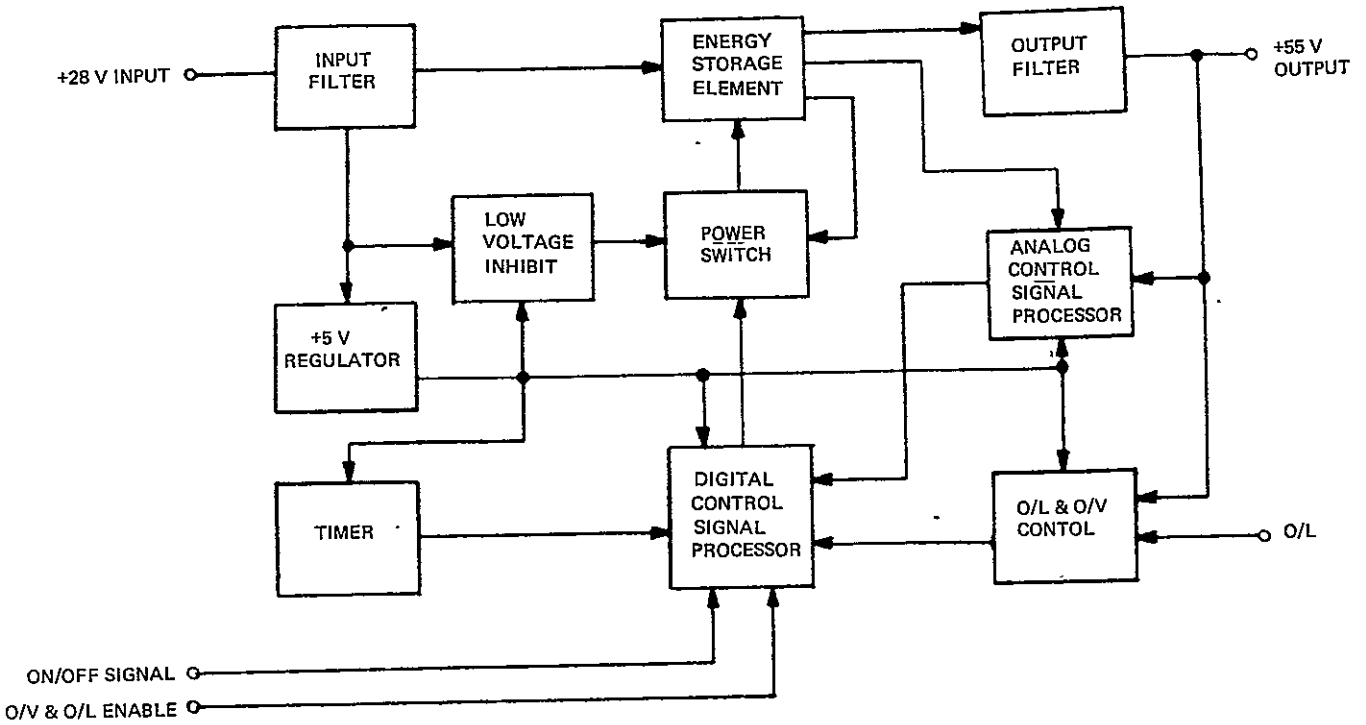

Figure B-1. Block Diagram, Boost Regulator

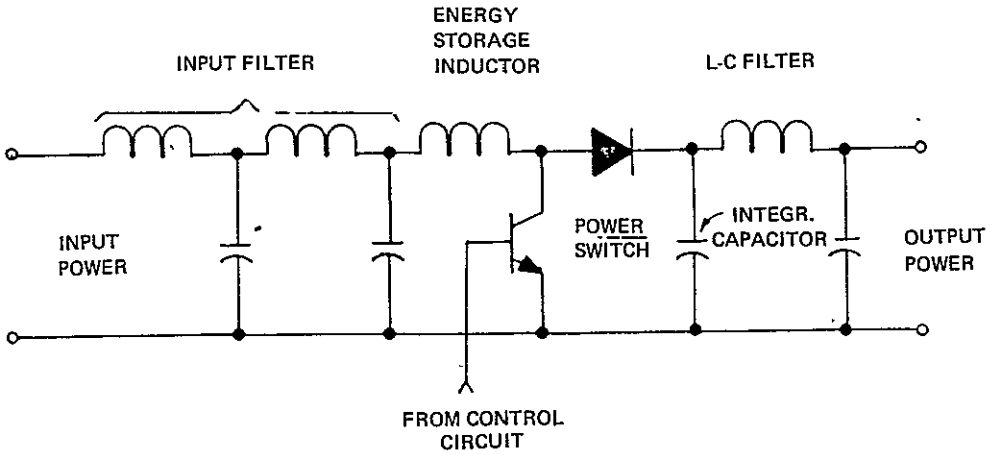

Figure B-2. Boost Regulator, Power Section

The energy storage inductor has two extra windings and performs two functions besides storing the energy. The second winding is used to supply a low impedance power source for quick turn-off of the power switch. When the power switch is "ON" and charging the inductor (storing energy), the winding supplies a voltage to the reset winding of the power switch base-drive transformer. The third winding is the ASDTIC winding which generates an AC signal for the analog control signal processor which is proportional to the input voltage.

To achieve high efficiency, a current drive is used with the power switch. The drive to the power transistor is proportional to the collector current and gives the best saturation and switching speed for all load currents because the transistor is always optimized.

The regulator uses the ASDTIC control system for regulation. The analog control signal processor senses the DC output from the output filter. The DC sense is combined in the analog control signal processor with the AC signal from the energy storage inductor to form a ramp function which is a function of both the DC output and the AC signal. The ramp function is digitized by a voltage comparator and used by the digital control signal processor to turn the power switch on and off. The digital control signal processor also receives signals from the overvoltage and overload detector, the input command signals, and the timer circuit.

When the overvoltage and overload enable circuit is enabled, the overvoltage and overload control signal can turn the regulator off when triggered by overvoltage or overload. The regulator can be turned on again by commanding the ON/OFF signal to OFF then ON. If the overvoltage and overload enable signal is disabled (OPEN), the signal from the overvoltage and overload control will be gated out so that the signal has no control over the operation of the regulator.

The timing diagram for the regulator is shown in Figure B-3. The operating frequency is set at 30 kHz by the external resistor and capacitor of the timer which establishes a very stable frequency. The output of the oscillator, shown in Figure B-3a is a very narrow negative pulse which initiates the start of each ON cycle of the switching regulator. At the same time a

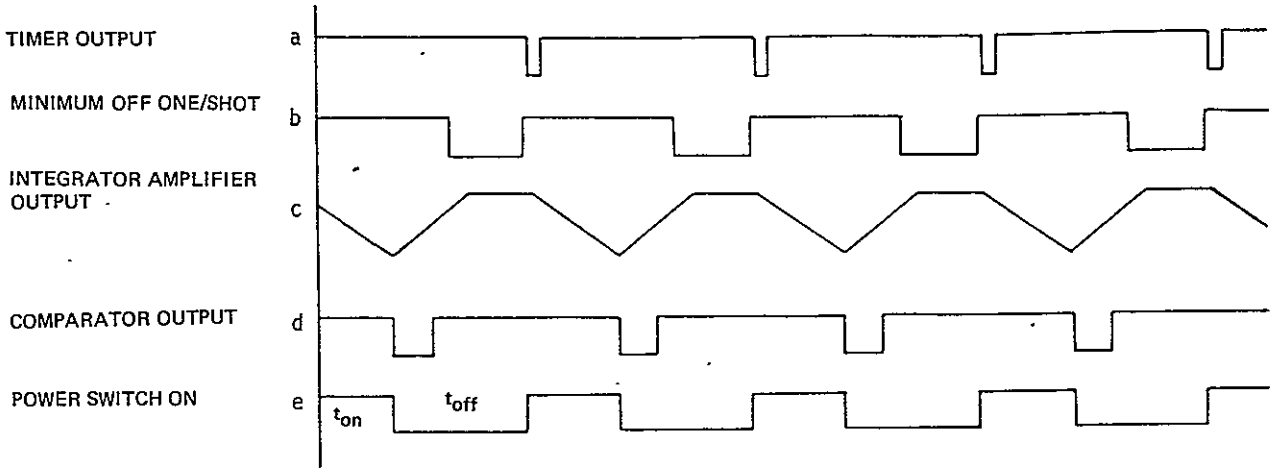

Figure B-3. Timing Diagram

one-shot is triggered which generates a pulse output that is used to control the minimum OFF time of each cycle. The minimum OFF time is required so that after each ON cycle the magnetic components can be reset. The output from the minimum OFF one-shot is shown in Figure B-3b. The output of the integrator amplifier is shown in Figure B-3c. The ramp output is generated from the ASDTIC winding. The ramp function is compared to a reference voltage by a voltage comparator. The output of the comparator is a digital signal as shown in Figure B-3d, and is used to terminate each cycle. It can be seen in Figure B-3e that the power transistor is turned ON with each timer output pulse and OFF again by the comparator output. The pulse-width modulation of the power switch is achieved by changing the comparator output which is a function of the slope of the ramp input and its DC level.

The normal operation of the regulator can be interrupted by the protective circuit such as the peak current detector or the overload and overvoltage control circuits. When the peak current detector is triggered it will terminate each cycle individually, but will not turn the regulator OFF. When an overvoltage or overload condition occurs, the regulator will be turned OFF and it will remain OFF until the ON/OFF command is cycled to OFF and then ON again. The overvoltage and overload circuits can be disabled so that they will have no effect on regulator operation by having an open circuit at the ENABLE command input. When the enable input is connected to ground all protective circuits function normally.

APPENDIX C

REACTION WHEEL ATTITUDE CONTROL SUBSYSTEM

This appendix describes the three axis stabilized attitude control subsystem assumed for the MMS geosynchronous mission. The attitude control about each body axis is achieved by means of a reaction wheel, as shown in the block diagram below. The position-plus-rate feedback is augmented by an integral compensation (accumulator). The square-law characteristics of the RW motor are linearized by a square-root operation.

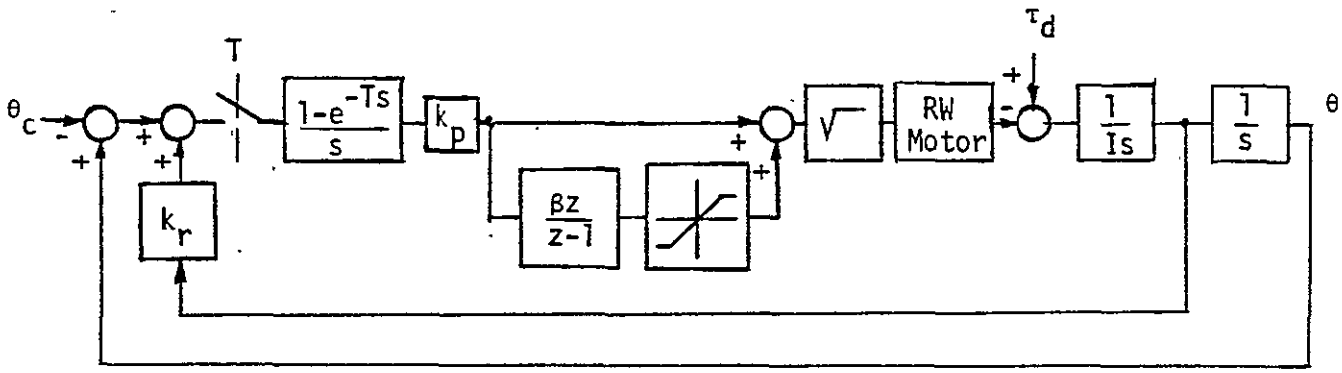

Omitting derivational steps, the major characteristics of the control loop are described below.

<u>z-Domain Characteristics</u>

Open loop equation

$$G(z) = \frac{KT^2(2+\alpha)(1+\beta)\left(z - \frac{2-\alpha}{2+\alpha}\right)\left(z - \frac{1}{1+\beta}\right)}{2\alpha(z-1)^3} \qquad (1)$$

Root Loci

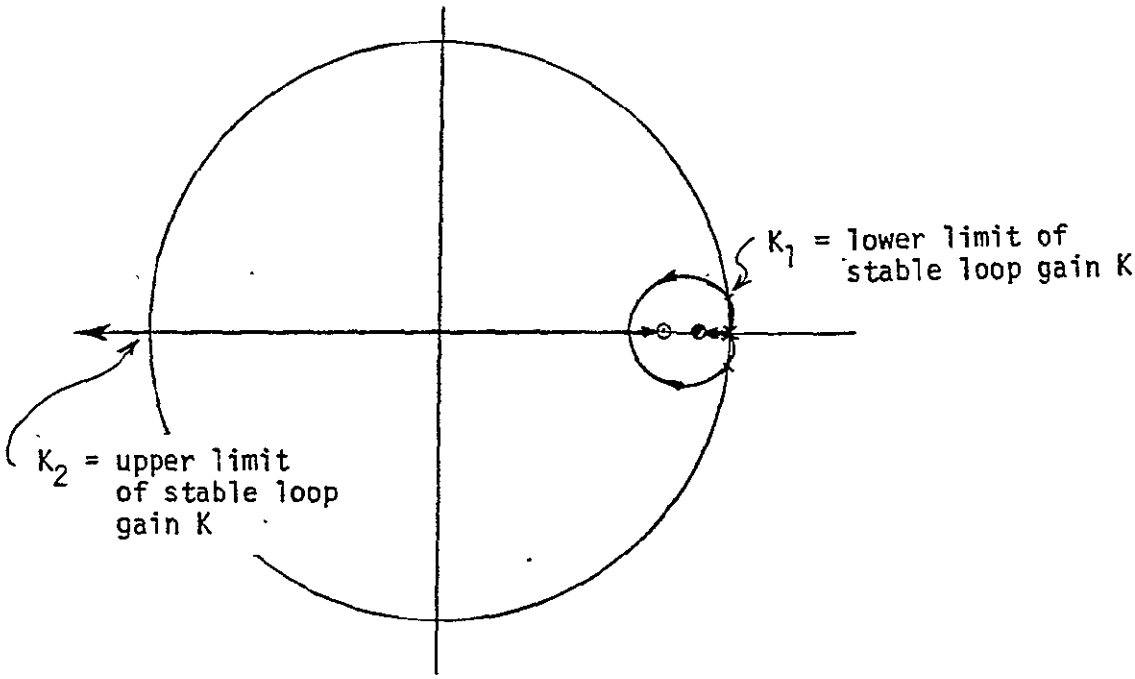

$$K = \frac{k_p k_m}{T} \ (\sec^{-2})$$

$$\alpha = \frac{T}{k_r}$$

β = accumulator gain

k_p = position gain (v^2/deg)

k_m = RW motor torque gain (newton-m/v^2)

T = sampling period (sec)

k_r = rate gain (sec)

If α, $\beta \ll 1$

$$K_1 = \frac{4\beta}{(2 - \alpha)\ (2\alpha + 2\beta + \alpha\beta)\ k_r^2} \approx \frac{\beta}{(\alpha + \beta)\ k_r^2}$$

$$K_2 = \frac{4\alpha}{(2+\beta)T^2} \approx \frac{2\alpha}{T^2}$$

s-Domain Approximation

The low frequency characteristics can be determined by using an s-domain representation, which is obtained by removing the samplers and replacing the accumulator with an integrator k_i/s, where $k_i = \beta/T$. If there is a disturbance torque τ_d

$$\frac{\theta}{\tau_d} = \frac{s/I}{s^3 + K\left[k_r s^2 + (k_i k_r + 1)\, s + k_i\right]} \tag{4}$$

If a constant disturbance such as the solar torque is exerted on an earth pointing satellite, the magnitude of the pointing error is determined by

$$\theta = \frac{\omega_o \tau_d}{kI\, k_i} \tag{5}$$

where ω_o = orbit rate

Since the integral compensation is used to minimize the steady-state error, the dynamic characteristics can be approximated by neglecting the integrator ($k_i = 0$). Then (4) can be written as:

$$\frac{\theta}{\tau_d} \approx \frac{1/I}{s^2 + K\, k_r\, s + K} = \frac{1/I}{s^2 + 2\zeta\, \omega_s + \omega^2} \tag{6}$$

By letting $\zeta = 0.7$, gains can be determined by:

$$K = \omega^2 = \frac{K_p k_m}{I} \tag{7}$$

$$k_r = \frac{1.4\omega}{K} \approx \frac{1.4}{\omega} \tag{8}$$

$$K_2 \approx \frac{2^{\alpha}}{T^2} = \frac{2}{k_r T} = \frac{1.4\omega}{T}$$

$$K_1 \approx \frac{k_i T}{\left(\frac{T}{k_r} + k_i T\right) k_r^2} = \frac{k_i}{(1 + k_i k_r)\, k_r}$$

From (5) k_i is determined from the known disturbance and accuracy requirement.

$$k_i = \frac{\omega_o T_d}{KI\ \theta} = \frac{\omega_o T_d}{\omega^2 I\ \theta} \tag{9}$$

Thus the gain margins of the controller can be determined by

$$\frac{K_2}{K} = \frac{1.4}{\omega T} \tag{10}$$

$$\frac{K}{K_1} = \frac{k_r(k_r k_i + 1) \cdot \omega^2}{k_i} = k_r^2\, \omega^2 + \frac{k_r}{k_i}\, \omega^2$$

$$= 2 + \frac{1.4\ \omega^3\ I\ \theta}{\omega_o T_d} \tag{11}$$

Parameter Selection

Using (7) through (11), two sample systems shown below were derived.

SYSTEM	A	B
ω (rad/sec)	0.2	0.5
K (sec $^{-2}$)	0.04	0.25
k_p (v^2/deg)	820	5100
k_r (sec)	7	2.8
β	0.005	0.02
accuracy (deg)	2×10^{-6}	8.4×10^{-8}
K_2/K	28 (= 28.9 db)	11.2 (= 21 db)
K/K_1	17.3 (= 24.7 db)	10.7 (= 20.6 db)

In deriving these parameters, the following constants were assumed:

$$T = 0.25 \text{ sec}$$

$$I = 410 \text{ kg-m}^2$$

$$k_m = 3.5 \times 10^{-4} \text{ N.m/v}^2$$

$$\omega_o = 7.27 \times 10^{-5} \text{ rad/sec (= 24 hr orbit)}$$

$$\tau_d = 1.5 \times 10^{-4} \text{ N.m}$$

$$\tau_f = \text{wheel friction} = 0.01 \text{ N.m}$$

The performance characteristics of these systems are demonstrated by simulating the transient response during wheel speed reversal, as shown in Figures C-1 and C-2. The peak pointing errors for systems A and B are, respectively 0.034 and 0.0032 deg. The steady-state pointing errors are on the order of 10^{-8} and 10^{-10} deg. These are much smaller than those shown in the table above since the rate of the disturbance torque variation is negligibly small at the orbit position selected for the simulation.

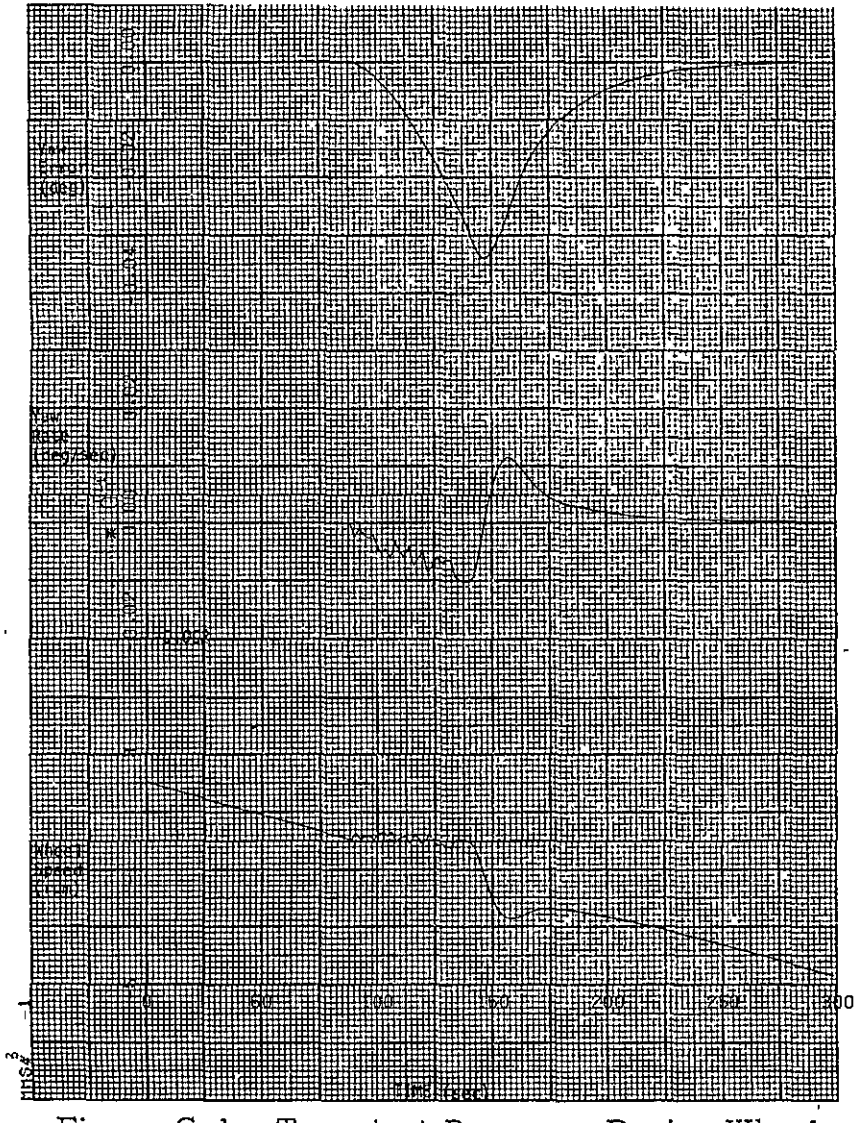

Figure C-1. Transient Response During Wheel Speed Reversal (System A)

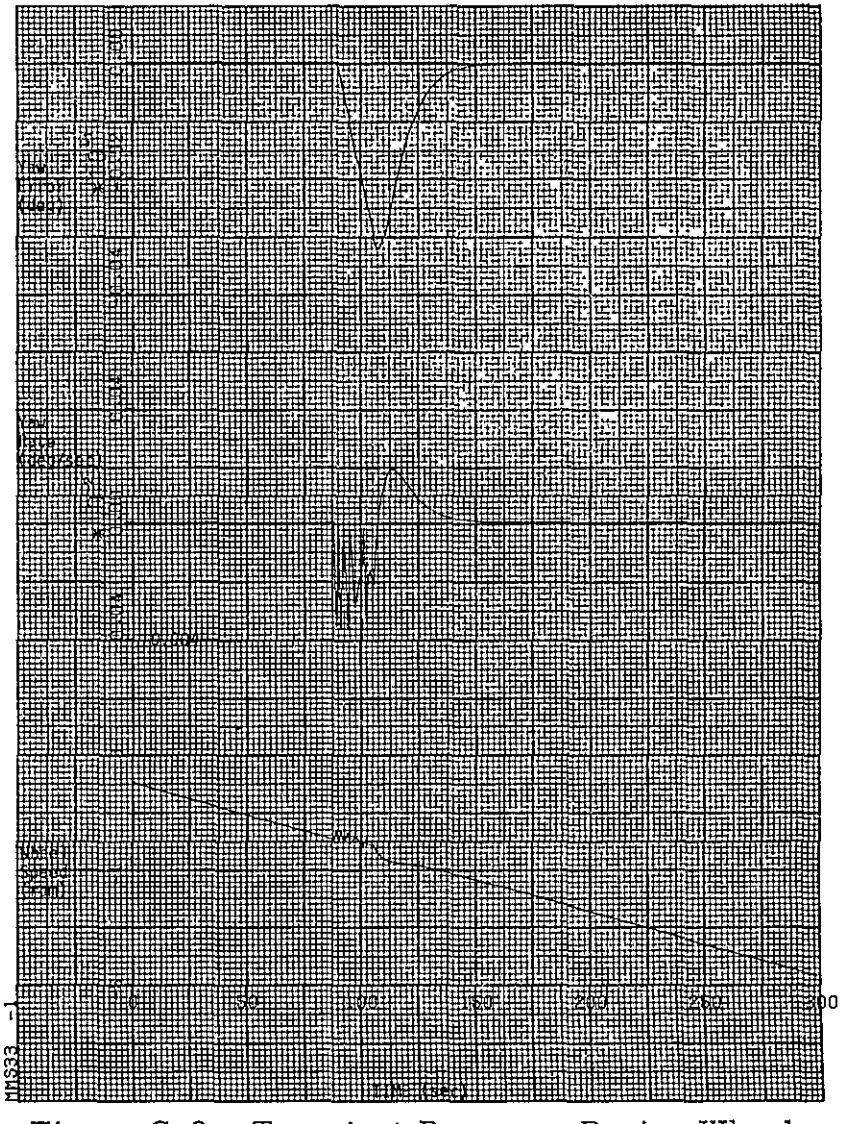

Figure C-2. Transient Response During Wheel Speed Reversal (System B)

APPENDIX D

FACTORS IN THE DESIGN OF A SPUTTER SHIELD FOR AN 8 CM MERCURY ION THRUSTER

In the sections to follow, the various design factors which influence the configuration of a sputter shield for a mercury ion thruster will be examined. This examination will specifically treat three selected sputter shield configurations. For these three sputter shields, the location of the umbra will be determined in a given axial plane (at z = 100 cm from the face of the ion thruster) as a function of source position over the face of an 8 cm mercury ion thruster for line-of-sight (thrust ion) particle trajectories. Using measured thrust ion current densities from an 8-cm thruster, the normalized efflux contours for the thrust ions will also be calculated for the specific axial plane described above. The combined normalized efflux contours and the umbra locations allow the calculation of permissible spacecraft surface exposure time over the duration of a reference mission. That reference mission requires 20,000 hours of thruster operation which results in the release of 3.24×10^{25} Hg^+ thrust ions.

In the calculations to follow some simplifying approximations will be made. For the normalized thrust ion efflux contours, the ions will be assumed to be released from a point source at the center of the accelerator grid and with that angular distribution determined experimentally through the use of the swinging J_+ probe. Because the swinging J_+ probe moves at a constant polar radius of R = 35.6 centimeters, and because the source width of the emitted ions is the 8 centimeter diameter of the accelerator grid, it follows that the point source assumption of ion emission for the calculation of normalized flux contours at large axial distance where finite source size effects are no longer important will produce an (conservative) overestimate of the ion flux at the larger polar angles, and an underestimate of the on-axis flux. A conservatively based high angle overestimate of the flux is preferable to the reverse situation. If, however, a (ultimate) spacecraft design indicates only marginal survivability for surfaces located at specific points or moving through specified paths relative to the thruster, then the normalized flux contours should be reexamined to determine the effects of finite source size inclusion in

the calculations. Finally, simplifying assumptions have been made in the calculations of sputter shield erosion. For this sputter shield, however, the experimental determination of the erosion is a planned activity, and the reliance on analysis is, therefore, lessened.

1. COORDINATE SYSTEMS

In these sputter shield design calculations it will be convenient at one point or another to employ differing coordinate systems to describe the location of boundaries or efflux contours or ion source points. Figure D-1 illustrates the three coordinate systems that will be used. The first of these is a polar coordinate system (R, θ, ϕ) in which the thrust axis of the ion beam occurs along the polar ($\theta = 0$) axis and $R = 0$ is the center point of the accelerator grid. For assumed thrust ion azimuthal symmetry, ϕ is an ignorable coordinate, and the only coordinates required become R and θ. These are the coordinates in which the swinging J_+ probe data is obtained and is the usual system for the calculation of normalized thrust ion efflux contours (noting, however, that these normalized flux contours will, where appropriate, be given in other coordinate frames).

A second coordinate system to be employed is the cylindrical system (r, z, ϕ) in which $r = z = 0$ is the center of the accelerator grid and the z axis of the system is the axis of the thrust beam. This coordinate system is useful for the parametric description of two of the three sputter shield designs. The remaining coordinate system is a Cartesian system (x, y, z) in which $x = y = z = 0$ is the center of the accelerator grid, and the z axis is the axis of the thrust beam. This coordinate system will be used for projections of various umbra region boundaries, for the description of the location of a source point on the face of the ion thruster, and for a description of the third of the three sputter shield designs. In this coordinate system the orientation of the thruster will be such that the y axis contains the center of the thruster and thrust beam neutralizer and the y-z plane will correspond to $\phi = 0$ in both the cylindrical and the polar coordinate systems.

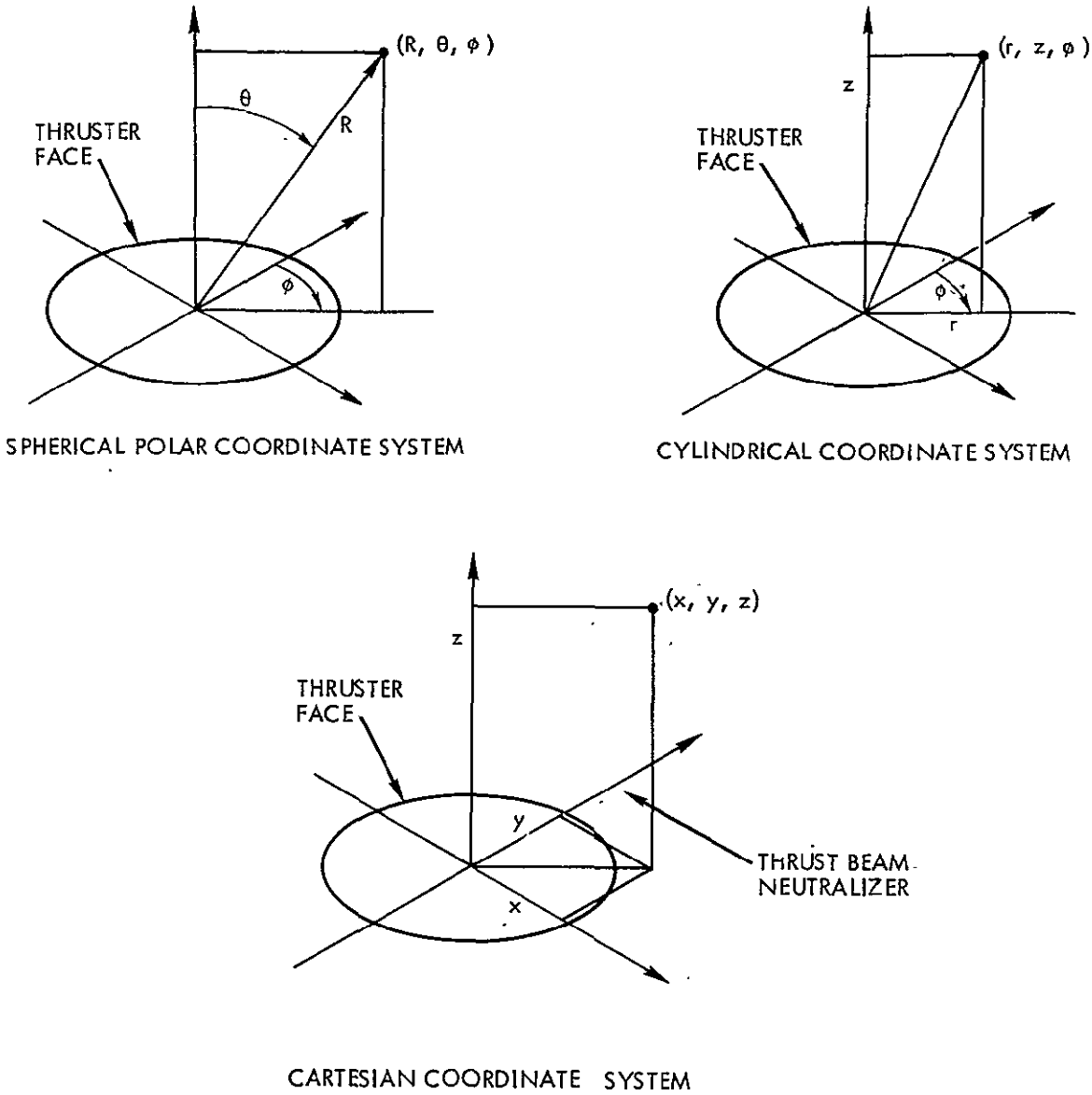

Figure D-1. Spherical Polar, Cylindrical, and Cartesian Coordinate Systems to be Used in the Sputter Shield Design Calculations

2. SPUTTER SHIELD DESIGNS

Figure D-2 illustrates the three sputter shield designs to be examined. The first design illustrated there is the "slashed" cylinder. The parametric description of the upper edge of the shield is:

$$\left.\begin{aligned} r &= 10.8 \\ z &= 14.8 \cos \phi \end{aligned}\right\} -\pi/2 \le \phi \le \pi/2$$

$$\left.\begin{aligned} r &= 10.8 \\ z &= 0 \end{aligned}\right\} \pi/2 \le \phi \le 3\pi/2$$

where dimensions are in centimeters and the coordinate system used is the cylindrical (r, z, ϕ) system.

The second shield design is the "truncated slashed cylinder." For this shield the parametric description of the upper edge of the shield is:

$$\left.\begin{aligned} r &= 10.8 \\ z &= 14.8 \end{aligned}\right\} -\pi/4 \le \phi \le \pi/4$$

$$\left.\begin{aligned} r &= 10.8 \\ z &= 20.9 \cos \phi \end{aligned}\right\} \pi/4 \le \phi \le \pi/2 \text{ and } -\pi/2 \le \phi \le -\pi/4$$

$$\left.\begin{aligned} r &= 10.8 \\ z &= 0 \end{aligned}\right\} \pi/2 \le \phi \le 3\pi/2$$

where, again, dimensions are in centimeters and the coordinate system is the (r, z, ϕ) cylindrical system.

The third shield design is the rectangle. A parameter description of the upper and outer edges of this shield is:

$$\left.\begin{aligned} y &= 10.8 \\ z &= 14.8 \end{aligned}\right\} -10.8 \le x \le 10.8$$

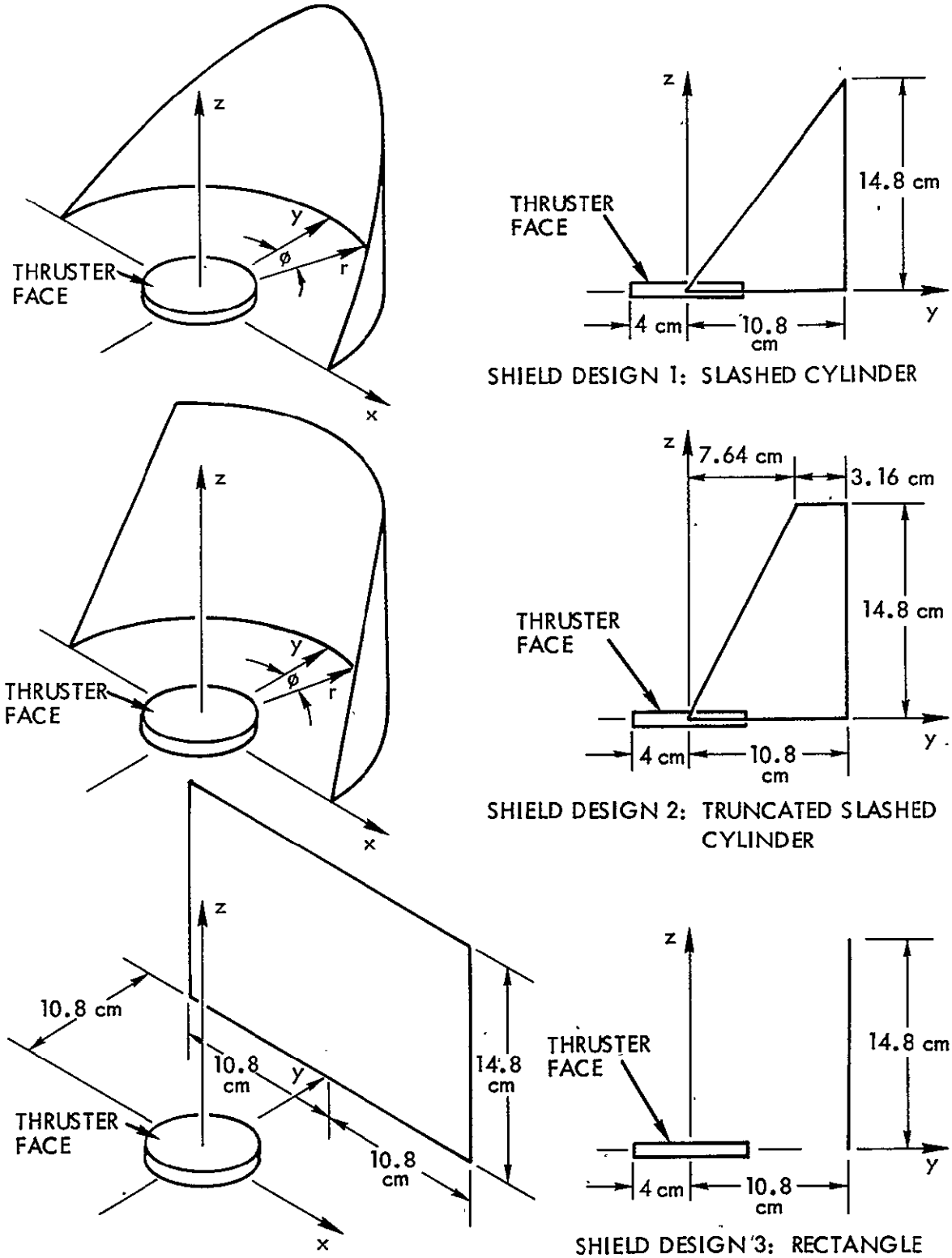

Figure D-2. Dimensions and Configuration of the Three Shield Designs

$$\left.\begin{array}{l} x = \pm 10.8 \\ y = 10.8 \end{array}\right\} 0 \le z \le 14.8$$

where all dimensions are in centimeters and the Cartesian coordinate system (x, y, z) is used.

3. LOCATION OF THE UMBRA REGION AS A FUNCTION OF SOURCE POINT PLACEMENT

For line-of-sight particle trajectories from a given source point, the umbra is defined as that region in space in which particle trajectories are absent because of the presence of the shield. In the calculations of the boundary of the umbra for the three shield designs and for various positions over the face of the thruster of the source point of the ion trajectories, the plane at z = 100 cm will be used (x, y, z system). In this Cartesian system the center of the ion accelerator grid is x = y = z = 0. The motion of the source point over the face of the thruster permits

$$-4 \le y_s \le 4 \qquad x_s = 0$$

and

$$-4 \le x_s \le 4 \qquad y_s = 0$$

where (x_s, y_s) denotes the source point and dimensions are in centimeters. It should also be noted that the y axis of the thruster corresponds to $\phi = 0$ in the cylindrical system used to describe shield designs 1 and 2.

Figure D-3 illustrates the umbra intersection with the plane $z_p = 100$ cm for the source points (x_s, y_s) at (0, -4), (0, -2), (0, 0), (0, 2), and (0, 4). The umbra intersection at $z_p = 100$ cm for $-4 \le x_s \le 4$ at $y_s = 0$ is also, because of the properties of the slashed cylinder design, the umbra intersection for $x_s = 0$, $y_s = 0$ in Figure D-3. Thus, the figure provides a comparatively complete description of the intersection of the umbra for the various source points over the face of the thruster even though all (x_s, y_s) combinations have not been described in the plotted curves.

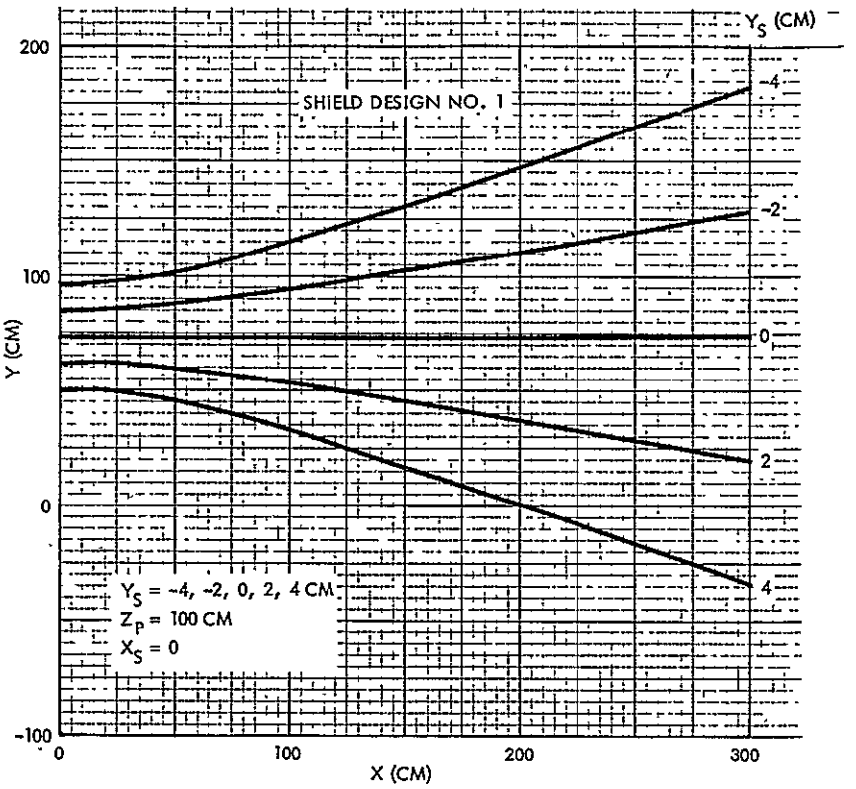

Figure D-3. Intersection of the Umbra Region of a Point Source with the Plane z_p = 100 cm as a Function of Source Position for Shield Design 1

For an actual ion source emitting over all x_s and y_s (subject to $(x_s^2 + y_s^2)^{1/2} \leq 4$) the region between the curves for $y_s = -4$ and $y_s = +4$ will be a penumbra region, partially illuminated by the ion trajectories, points at (x, y) "above" the $y_s = -4$ curve will be totally nonilluminated (an umbra for the total ion source) and points at (x, y) below the $y_s = +4$ curve would be in view of all ion source points. To determine the actual amount of ion interception for an (x, y) point in this plane at z = 100 cm will require additional information, which will be provided in the normalized thrust ion efflux calculations of Section 4.

Figures D-4 and D-5 illustrate the intersections of the umbra regions with the z_p = 100 cm plane for the "truncated slashed cylinder," Design 2, for y_s = -4, -2, 0, +2, and +4 cm at $x_s = 0$, and for x_s = -4, -2, 0, +2, and +4 cm at $y_s = 0$. When these curves are compared to those in Figure D-3, it may be

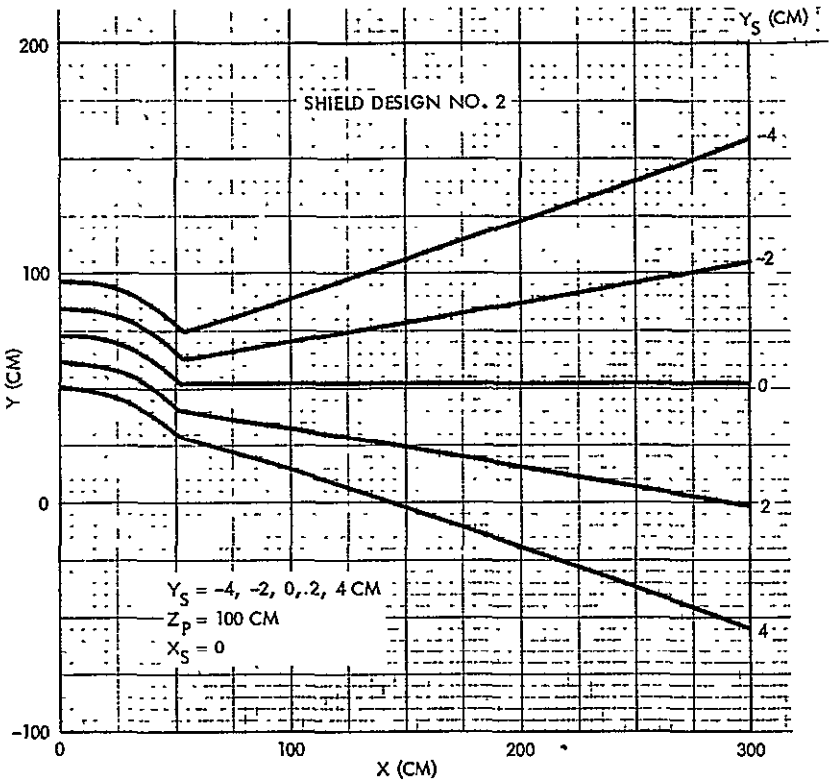

Figure D-4. Intersection of the Umbra Region of a Point Source with the Plane z_p = 100 cm as a Function of Source Position for Shield Design 2

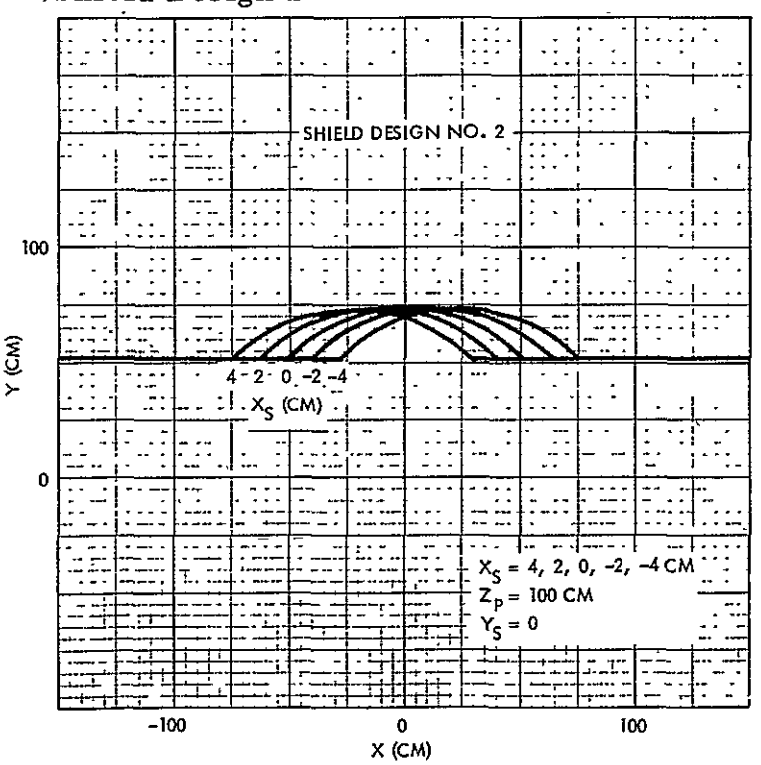

Figure D-5. Intersection of the Umbra Region of a Point Source with the Plane z_p = 100 cm as a Function of Source Position for Shield Design 2

seen that the "additional continuation" of the cylinder in Design 2, compared to Design 1, does provide a movement of the umbra boundary intersection in the negative y direction thus providing additional protection for spacecraft surfaces in the +y direction (which is the assumed placement region, in general, for the spacecraft, with open space being encountered in the negative y directions). The additional protection of spacecraft surfaces by Shield Design 2 must, however, be considered together with the additional amounts of sputtered material released from the sputter shield in this more "enveloping" structure. Section 7 will evaluate the magnitude of these secondary material transports.

A final series of umbra boundary intersections with the z_p = 100 cm plane is given in Figure D-6 for Shield Design 3, the rectangle. In Figure D-6, the ion source points utilized are y_s = -4, -2, 0, 2, and 4 cm and x_s = 0. As may be noted by comparison of these results with Figures D-3, D-4 and D-5, this rectangular shield provides the least protection to spacecraft surfaces of all three shield designs. The rectangle shield, however, has somewhat reduced ion interception on its upper and outer edges and would, thus, provide some measure of relief if there should be excessive secondary material transport from the sputter shield back to the face of the ion thruster.

4. NORMALIZED THRUST ION EFFLUX CONTOURS

The calculations of Figures D-3 through D-6 are helpful in determining those regions either partially or totally visible to the ion source and those regions for which there is no direct visibility of the source. The curves given there do not, however, permit an evaluation of the degree of ion flux interception for surfaces located outside of the "total source" umbra. To evaluate this ion interception, it is necessary to measure the angular distribution of ion flux from the thruster. For convenience, this ion flux will be given in terms of the "normalized" efflux. For thrust ions, this normalized efflux is

$$\epsilon_{+,t}(x, y, z) = \frac{J_{+,t}(x, y, z)}{J_B} \tag{1}$$

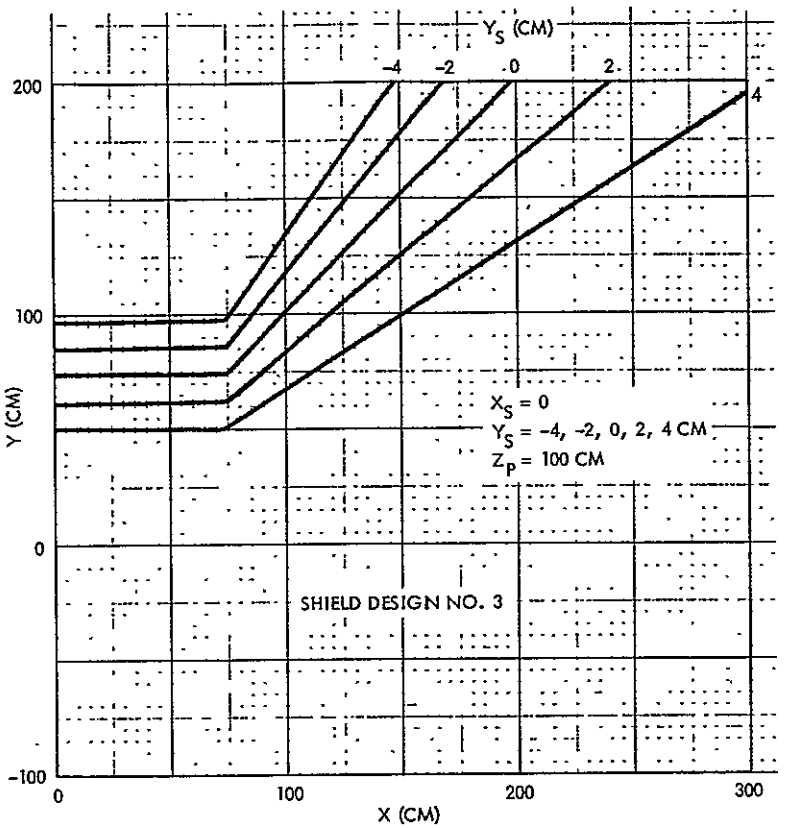

Figure D-6. Intersection of the Umbra Region of a Point Source with the Plane z_p = 100 cm as a Function of Source Position for Shield Design 3

where (x, y, z) is the point at which the flux is to be described, $J_{+,t}$ (x, y, z) is the measured thrust ion current density at this point, and J_B is the total thrust ion current released by the thruster (~72 milliamperes for the 8 cm ion engine). From Equation (1), the dimensions of $\epsilon_{+,t}$ are in cm^{-2}. To determine total intercepted ion flux over a reference mission, the $\epsilon_{+,t}$ term is multiplied by the total thrust ion release (3.24×10^{25} thrust ions for the reference mission of 20,000 hours of 8 cm thruster operation at 72 milliamperes). A surface located at $\epsilon_{+,t} = 10^{-8}$ cm^{-2}, for example, would intercept 10^{-8} (3.24×10^{25}) = 3.24×10^{17} thrust ions/cm^2 over the duration of the mission.

To determine the $\epsilon_{+,t}$ contours at z_p = 100 cm, the swinging J_+ thrust ion measurements were used. The previously discussed approximation of all ion emission from x = y = 0 was made and $\epsilon_{+,t}$ was calculated using

$$\epsilon_{+,t}(y_p) \Big/ \Big|_{x_p = 0,\ z_p = 100\ \text{cm}} = \frac{[I_{+,t}(SJ_+)]\ R_{SJ_+}^{\ 2}}{A_{SJ_+}\left(y_p^2 + z_p^2\right) J_B} \qquad (2)$$

Using swinging J_+ data, A_{SJ_+} (the swinging J_+ cup area) of 6.12 cm^2, the R_{SJ+} (the polar radius of the J_+ probe arm) of 35.6 cm, J_B (thrust ion current) of 72 milliamperes, and z_p = 100 cm, leads to the $\epsilon_{+,t}$ calculations given in Figure D-7. At the center of the beam, $\epsilon_{+,t} = 3.5 \times 10^{-4}\ cm^{-2}$ and a surface location at this point would result in an interception over the duration of the 20,000 hours of thruster operation of 1.134×10^{22} thrust ions/cm^2. For ion sputtering at unity, this would cause removal of 1.1×10^{22} atoms/cm^2 which, for conventional material densities of $\sim 6 \times 10^{22}$ atoms/cm^3, would lead to an erosion depth of ~1.9 millimeters. It is obvious that such a spacecraft surface configuration and surface placement is not permissible.

To determine the actual $\epsilon_{+,t}$ contours for ions emitted from all source points and for a given shield design, the calculations would require a measured ion emission over the face of the thruster and, in addition, would require a measured angular distribution of the release at each source point. This last quantity is not, in point of fact, available. The swinging J_+ probe determines the angular distribution of ion emission for all source points. For the present simplified analysis, the emission of all ions from $x_s = y_s = 0$ would result in an $\epsilon_{+,t}$ of $\sim 10^{-5}\ cm^{-2}$ near the point ($x_p = 0$, $y_p = +75$, $z_p = 100$ cm) for shield Design 1 where the umbra is encountered for ions emitted from the thruster center. From the above calculations of ion erosion at $\epsilon_{+,t} = 3.5 \times 10^{-4}\ cm^{-2}$, it follows that erosion of a surface near the (0, 75, 100 cm) point would be $\sim 5 \times 10^{-3}$ cm (2×10^{-3} inches) over the mission duration. While this erosion depth is not significant in terms of structural materials, other spacecraft materials (such as thermal control blankets) would have their upper layers totally eroded. A specific upper boundary to the tolerable erosion depth cannot be given without a direct element-by-element examination of all of the pieces of a prospective spacecraft design. For certain highly sensitive surfaces, the permissible erosion depth may be in the range of 10^{-7} to 10^{-6} cm. For these surfaces, the time averaged $\epsilon_{+,t}$ over the mission life must be in the range from $2 \times 10^{-10}\ cm^{-2}$ to $2 \times 10^{-9}\ cm^{-2}$, and, obviously,

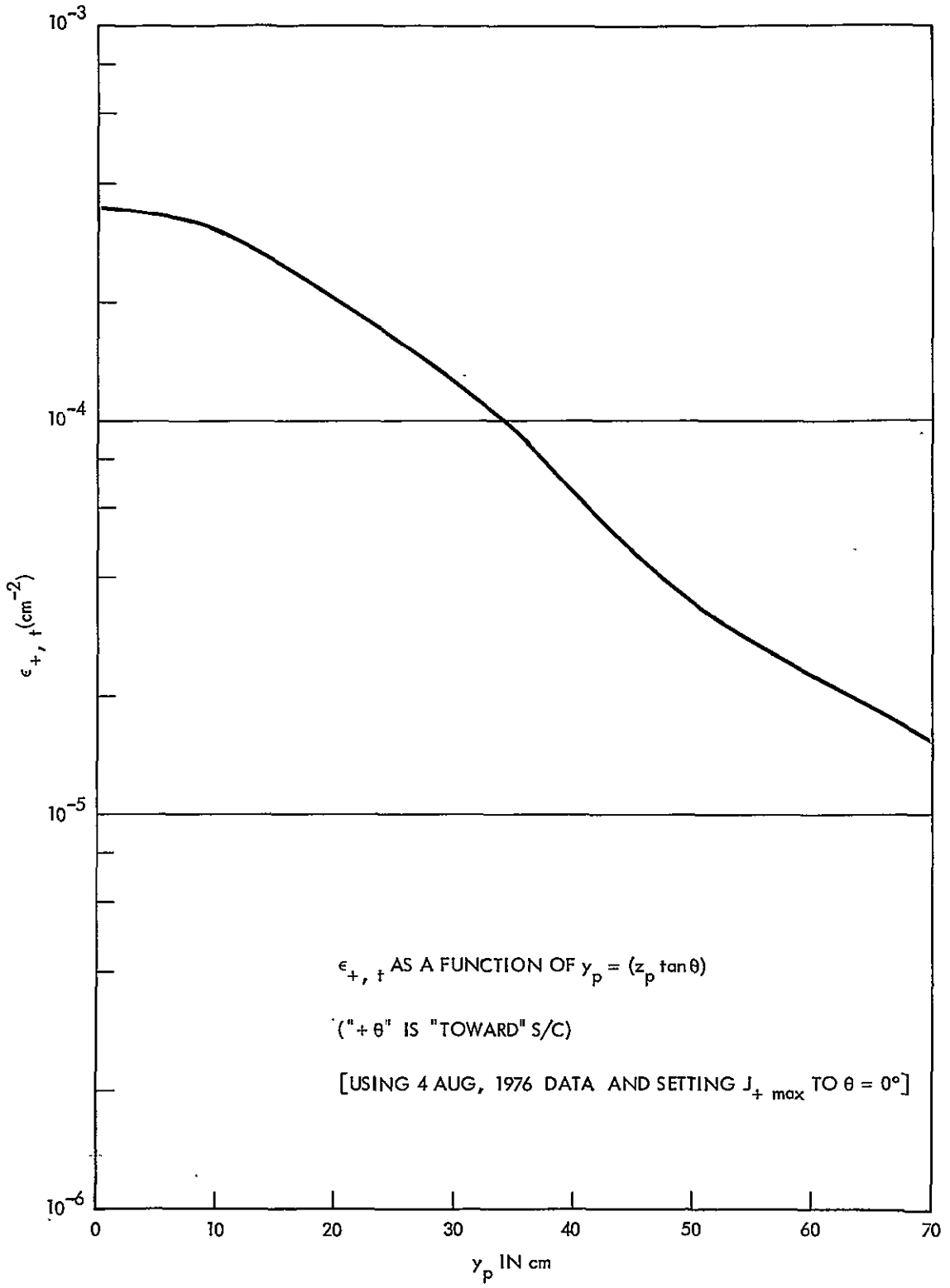

Figure D-7. Normalized Thrust Ion Efflux, $\epsilon_{+,t}$, as a Function of y_p in the Plane z_p = 100 cm

must use the protection afforded by the shield and may, in point of fact, require surface placement in the total umbra region.

To examine the $\epsilon_{+,t}$ contours in somewhat greater detail and under conditions for which the shield is either present or absent, the values of $\epsilon_{+,t}$ were calculated as functions of y_p for z_p = 100, 200, and 400 cm and for $x_p = 0$. These calculations are illustrated in Figure D-8 where the solid curves are $\epsilon_{+,t}$ for the shield absent condition and the dashed curves illustrate the effective reduction of $\epsilon_{+,t}$ for the shield present condition. For these calculations, it has been assumed that ion emission is uniform over the face of the thruster and that every emissive point has the same angular distribution function for thrust ion emission.

5. ION SPUTTERING COEFFICIENTS AND SHIELD EROSION CALCULATION ESTIMATES

Knowledge of the ion sputtering coefficients is necessary to calculate erosion from exposed spacecraft surfaces and is also necessary to evaluate the erosion of the sputter shield and the extent of the secondary material transport from this shield back to the face of the thruster. The discussion in this section will be specifically concerned with the erosion of the sputter shield and the resultant secondary material transport.

A review of the literature on the sputtering of surfaces by Hg^+ ion bombardment leads to the indicated use of titanium for the sputter shield. For normal incidence, the measured sputtering coefficient at 250 eV of Hg^+ energy is ~0.2 (ref. 1) and is ~2 at 4 keV (ref. 2). These values are amongst the lowest observed for Hg^+ on metal surfaces and may result from the large mass "mismatch" between the mass of the incident ion, Hg^+ (M ~ 200) and the mass of the surface atom, Ti (M ~ 48). An additional benefit of titanium is the comparatively low density, thus permitting a reasonable material thickness (~1 mm) over the surface area (~300 cm^2) of the shield designs described earlier, without exceeding the allowed 150 gram sputter shield mass limit set by NASA-LeRC. For these reasons the material for the submitted sputter shield designs was titanium and this analysis of shield erosion will utilize sputtering ratios of Hg^+ on titanium. From the data in both references 1 and 2, a value of sputtering ratio, S, of unity will be used for the

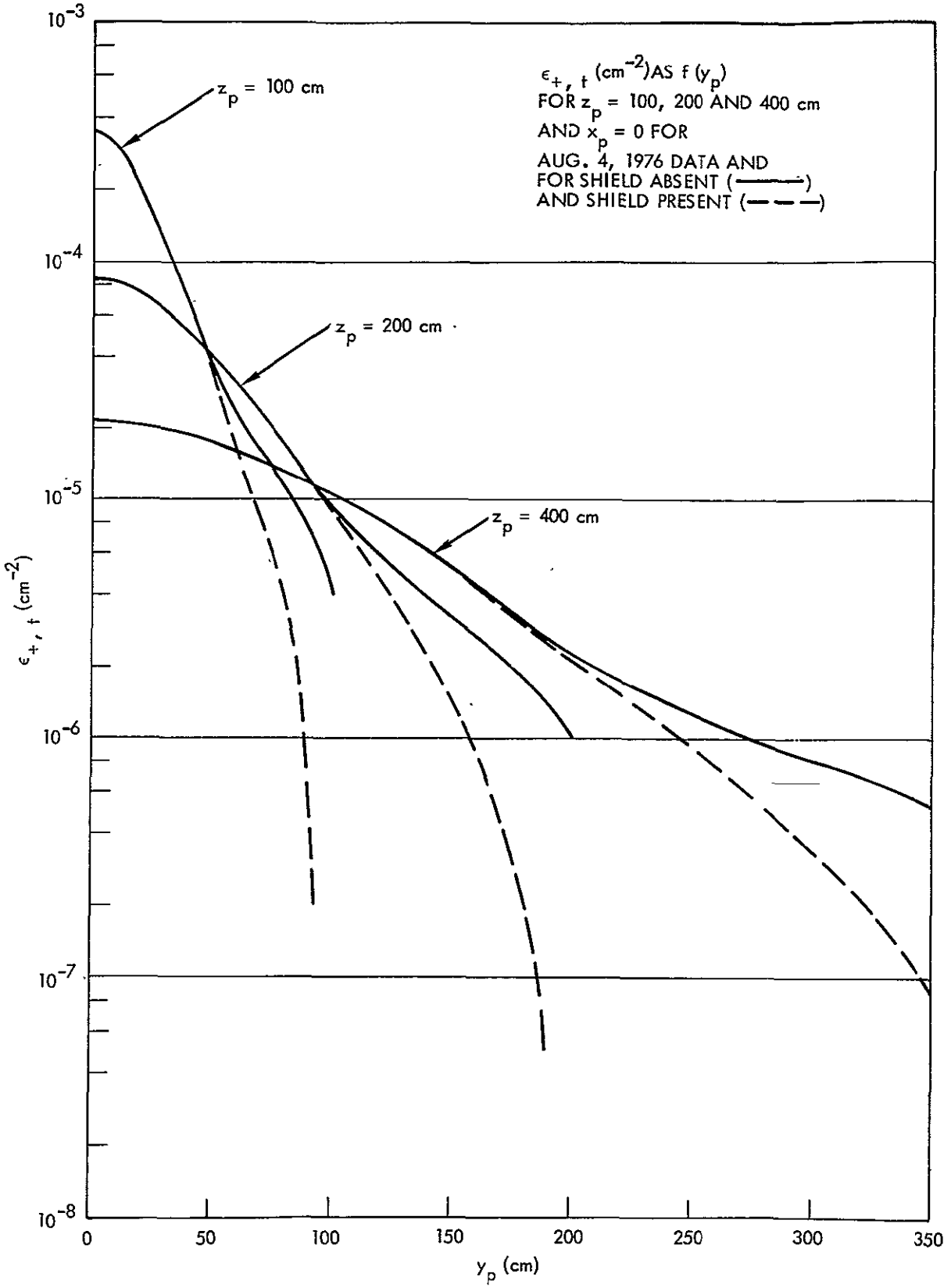

Figure D-8. Normalized Thrust Ion Efflux Contours as $f(y_p)$ for z_p = 100, 200, and 400 cm for Shield Absent and Shield Present Conditions

Hg^+ thrust ions of the 8-cm ion thruster for normal incidence on titanium surfaces.

To determine total erosion at the point x = 0, y = 10.8, z = 14.8 cm on the shield (which is an important location because this is probably the point of highest erosion), Equation (2) will be modified to

$$\epsilon_{+,t}(0,\ 10.8,\ 14.8) = \frac{I_{+,t}\ (SJ_+ \text{ at } R,\ \theta = 36.12^\circ)\ R_{SJ_+}^{\ 2}}{A_{SJ_+}\left[(10.8)^2 + (14.8)^2\right] J_B} \qquad (3)$$

where R = 35.6 cm, A_{SJ+} = 6.12 cm^2, J_B = 72 mA, and $J_{+,t}$ for the swinging J_+ is evaluated at $\theta = 36.12^\circ$ since this is the polar angle from x = y = z = 0 to the point (0, 10.8, 14.8) on the sputter shield. Inserting values of swinging J_+ signal leads to values of $\epsilon_{+,t}$ (0, 10.8, 14.8) of $\sim 6.42 \times 10^{-4}$. Over the 20,000-hour operation period, a surface area arranged for normal incidence would receive $\sim 2 \times 10^{22}$ thrust ions/cm^2. It should be noted that the surface of the upper tip of the sputter shield has a projection angle, α, of $(90^\circ - 36.12^\circ) \simeq 54^\circ$ and, thus, the actual thrust ion arrival density is $2 \times 10^{22} \cos 54^\circ$ which is $\sim 10^{22}$ ions/cm^2. It should also be noted, however, that sputtering at more grazing impact angles of the incident ion is more severe (ref. 3) than for normal incidence and may, in point of fact, be increased by factors larger than the ratios of actual surface area to projected surface ($1/\cos 54^\circ$ in the specific case at hand). An approximation to be made here will be that $S \cos \alpha$ = constant, i.e., that the product of the sputtering coefficient and the angle of incidence remains at the value of S ($\alpha = 0^\circ$, normal incidence). This approximation could be the subject of later review if particularly high values of shield removal are calculated, thus making all of the assumptions in this shield erosion evaluations more critical.

For assumed $S \cos \alpha = 1$ and 2×10^{22} ions/cm^2 over the mission duration, and for a material density of titanium of 5.7×10^{22} atoms/cm^3, the calculated erosion depth at x = 0, y = 10.8, z = 14.8 on the various shield designs would be $\sim (2/5.7)$ cm = 3.5 mm. From the allowable shield weight of 150 grams and for an even distribution of this material over the area

(~300 cm^2) of the sputtering shield, it follows that the shield thickness is ~1 mm and that complete erosion of the upper end point of the shield would occur at approximately the 6000-hour point in thruster operation.

There are several possible directions of action for the system design at this point. One of these directions would be to transfer some of the shield material into the upper edge of shield to prevent a complete cut-through. This direction would also be in line with a possible rolled upper edge to the shield to provide additional stiffness in the member. A second direction in design would be to move the shield to either higher angles or, retaining the angle of total umbra formation, to move the shield backward. A third direction is to leave the designs as they presently stand and to determine the erosion rates experimentally before making any further configurational decisions. It is this last course of action which will be recommended.

The principal reasons for a recommended reliance on measurements at this point are the present levels of uncertainty in the analysis and in the data base from which the ion current arrival rates are to be calculated. As noted earlier, the measurements of the angular distribution function of thrust ion release is made by the swinging J_+ probe which, because of finite source size effects (a thruster diameter of 8 cm and a probe separation radius of 35.6 cm), has an apparent "θ broadening" of the emerging ion flow. This extra angular width in the thrust beam (total $\Delta\theta \sim D_i/R_{SJ_+} \sim 8/35.6 \sim$ 0.225 radian ~ 12.9 degrees) will have the result of overestimating the flux at a given polar angle θ. In addition, the mounting arm of the swinging J_+ probe has a backlash (estimated to be of the order of a few degrees) which reverses in direction as the probe swings from one side of the beam to the other, but has the overall result of adding a total $\Delta\theta$ in the thrust ion divergence of approximately twice the backlash angle. There are, finally, indications of side-to-side asymmetries in the thrust ion angular distribution with an extra angular broadening on that side containing the neutralizer compared to the reverse (neutralizer absent) edge of the beam. These several factors tend to argue for a shift in emphasis to direct measurement of erosion, followed, if necessary, by design alteration.

6. SECONDARY MATERIAL TRANSPORT CALCULATIONS

To determine the total secondary material transport and the effect of that material transport, two quantities must be known. The first of these is the total sputtering erosion of each surface element of the sputter shield and the second is the deposition pattern, over all possible emergence directions of the material released from a given surface element. Neither of these quantities is known accurately and the discussion in this section is necessarily qualitative in nature. There are, however, some quantities which may be calculated and which may be of assistance in the selection of a shield design.

A first calculation of interest is the value and range in divergence angle from various surface elements on the shield to various source points on the face of the thruster. Table D-1 provides calculated minimum and maximum θ values from source points on the thruster face to surface elements along the upper edge of the sputter shield. Also given there is the θ value from $x_s = y_s = 0$ (the center of the accelerator grid) to these same surface elements. The means for identifying the location of a surface element along the upper edge of the sputter shield is in terms of the ϕ value in the (r, z, ϕ) cylindrical system (see Section 1 for these coordinate systems and Section 2 for a parametric representation of the upper edges of the three designs of sputter shields).

A somewhat troublesome aspect of Design 2 compared to Design 1, is the extent of the number of surface elements along the upper edge of the shield which have θ values in the range below 40° (where significant levels of ion flux can still be encountered). Design 3, the rectangular sputter shield, appears to be somewhat better than Design 1, but, it should be kept in mind, does offer less protection to spacecraft surfaces.

A second quantity of interest which can be calculated is the total area of exposed sputter shield in the height element dz at height z along the sputter shield. Table D-2 provides these values. As may be seen from the numbers given there, Design 2 has a comparatively large area of exposed material, compared to Design 1, in the height range above, for example, 11 cm (chosen here because $z = 11$ leads to a $\theta \sim 45^{\circ}$ from the thruster for ion interception,

Table D-1. Values of Minimum and Maximum Divergence Angle, θ_{min} and θ_{max} From Source Points on Ion Thruster Surface to Surface Elements at Upper Edge of Sputter Shield for Designs 1, 2, 3. (Also given is divergence angle from $x_s = y_s = 0$ to the upper edge of the sputter shield for the various shield designs. Specification of sputter shield edge point location is via the angle ϕ of the cylindrical system (r, z, ϕ)).

	θ_{min} (degrees)			$\theta_{\mathfrak{C}}$ (degrees)			θ_{max} (degrees)		
ϕ(°)	Design 1	Design 2	Design 3	Design 1	Design 2	Design 3	Design 1	Design 2	Design 3
0	24.7	24.7	24.7	36.1	36.1	36.1	45.0	45.0	45.0
10	25.0	24.7	25.2	36.5	36.1	36.5	45.4	45.0	45.3
20	26.1	24.7	26.9	37.8	36.1	37.8	46.8	45.0	46.3
30	28.0	24.7	29.8	40.1	36.1	40.1	49.1	45.0	48.1
40	30.1	24.7	34.3	43.6	36.1	43.6	52.6	45.0	50.7
45	33.0	24.7	37.3	45.9	36.1	45.9	54.7	45.0	52.5
50	35.6	26.8	90.0	48.6	38.8	90.0	57.3	47.7	90.0
60	42.6	33.0	90.0	55.6	45.9	90.0	63.4	54.7	90.0
70	53.3	43.5	90.0	64.9	56.5	90.0	71.1	64.2	90.0
80	69.3	61.9	90.0	76.6	71.4	90.0	80.2	76.2	90.0
90	90.0	90.0	90.0	90.0	90.0	90.0	90.0	90.0	90.0

Table D-2. Total Sputter Shield Area Exposed to Thrust Ion Sputtering in Height Element, dz, at Height, z, for Designs 1, 2, and 3

z (cm)	$\left[\frac{dA(z)}{dz} \text{IN } \frac{CM^2}{CM} \text{AS A } F(z)\right]$ Design 1	Design 2	Design 3
14.8	0.0	17.0	21.6
14.0	7.1	18.1	21.6
13.0	10.8	19.5	21.6
12.0	13.5	20.7	21.6
11.0	15.8	22.0	21.6
10.0	17.9	23.2	21.6
9.0	19.8	24.3	21.6
8.0	21.6	25.5	21.6
7.0	23.3	26.6	21.6
6.0	24.9	27.6	21.6
5.0	26.5	28.7	21.6
4.0	28.0	29.8	21.6
3.0	29.5	30.8	21.6
2.0	31.0	31.9	21.6
1.0	32.5	32.9	21.6
0	33.9	33.9	21.6

and there is still a significant level of ion flux at $\theta = 45^{o}$). On the basis of the area of material exposed for $z > 11$ cm, Design 3 does not look particularly appealing, relative to Design 1.

In addition to calculations of θ values to points along the sputter shield edges and total exposed shield area as f(z), the extent of the deposition back at the thruster can be made for a specified metal atom release from the shield. The directions of emergence of sputtered metal atoms from a bombarded surface are given in reference 4. In the results there the angular distribution function is approximately $\cos \gamma$ where γ is the angle from the surface normal to the ray along which the deposition is to be estimated. In the discussion here, this release form will be further simplified to state simply that emission will be uniform over the 2π steradians of available solid angle for metal atom release. This simplifying approximation will tend to overestimate the secondary material transport back to the face of the ion thruster, but it is probably the better course of action to provide a conservatively based estimate of material transport here than to underestimate this transport.

For uniform metal atom emission over 2π steradians and for metal atom emission from $z = 14.8$ and $y = 10.8$ cm (a source point at the middle of the top edge of the shield), the secondary material transport per unit area at $x = y = z = 0$ (the center of the thruster face) is $\sim 5 \times 10^{-4}$ cm^{-2} for each atom of released material. To estimate total metal atom deposition per square centimeter on the thruster accelerator face the total effective area of exposed sputter shield must be estimated and an estimate must be made of the metal atom release per square centimeter on this exposed surface. If 1 cm^2 of sputter shield surface is to be considered, as an example, and if the shield erosion at that point proceeds to cut-through (1 mm erosion for a 1 mm thick shield), then $\sim 6 \times 10^{22}$ metal atoms/cm^2 are released and would be redeposited on the thruster face at an approximate efflux of 3×10^{19} atoms/cm^2 for an effective material depth of $\sim 5 \times 10^{-5}$ cm. If the total sputter shield area participating in material loss at this cut-through level is 100 cm^2, then a layer of $\sim 100 \times 5 \times 10^{-5}$ cm = $\sim 5 \times 10^{-3}$ cm would result over the face of the ion thruster. This depth does not seem to be particularly large (2×10^{-3} inches over the total duration of the mission) and there will be some cleanup of this deposited material by charge exchange ion back bombardment

of the accelerator grid. For 3×10^{21} atoms/cm^2 deposited over the accelerator grid surface (from 100 cm^2 of sputter shield eroded to the cut-through point), total deposited metal atoms are $\sim 1.5 \times 10^{23}$ atoms. The total thrust ion release from the thruster of 3×10^{25} ions may cause from $\sim 3 \times 10^{22}$ to $\sim 10^{23}$ thrust ions to back bombard this accelerator grid. These charge exchange ions are of lower energy (~300 eV for present settings of accelerator grid potential) and may have sputtering ratios of ~ 0.5. The total material removal by backbombardment, thus, is from $\sim 1.5 \times 10^{22}$ atoms to $\sim 5 \times 10^{22}$ atoms over the face of the thruster and ranges from ~10% to ~30% of the calculated deposition for the specific example (assumed area of 100 cm^2 of shield totally eroded). There would appear to be, thus, some relief from metal atom accumulation as a result of charge exchange ion back bombardment and the deposition (even in the absence of back bombardment) is not particularly severe.

7. SUMMARY

The design calculations have examined three shield designs which may be termed a slashed cylinder (Design 1), a truncated slashed cylinder (Design 2), and a rectangle (Design 3). The intersections of the umbra for source points over the face of the thruster have been calculated for the various shield designs for a specific axial plane (z = 100 cm). The greatest spacecraft surface protection is given by Design 2, and the least protection is given by Design 3. The slashed cylinder (Design 1) affords almost as much protection as Design 2, however.

The sputtering erosion for spacecraft surfaces in the specified axial plane of z = 100 cm has been examined and, in general, will require that placement occur at least in the penumbra region and, possibly, in the total umbra region (i.e., that region total excluding all ion source points).

Erosion from the surfaces of the sputter shields has been examined and may constitute a problem for the reference mission (20,000 hours of thruster operation). For a favorable resolution of the present uncertainties in this analysis, erosion would not lead to cut-through, while for an unfavorable resolution of these uncertainties, cut-through could take place for sputter shield material thicknesses at the design point of 1 mm.

Total material release from the various shields has been examined qualitatively. Shield Design 2 has a troubling amount of exposed surface area in regions which may suffer extensive erosion. Shield Design 1 appears to have fewer problem areas here than Design 2. The deposition of material from this sputter shield has also been examined qualitatively. On the basis of that examination, the truncated slashed cylinder (Design 2) will deposit the largest amount of material on the thruster face, while the slashed cylinder (Design 1) will deposit the least material. For the assumed conditions used in the example calculations, this secondary material transport does not appear to present operational problems for the ion thruster.

8. REFERENCES

1. Sh. G. Askerov and L.A. Sena, "Cathode Sputtering of Metals by Slow Mercury Ions," Sov. Phys - Solid State, 11, 1288-1293 (1969).

2. G.K. Wehner and D. Rosenburg, "Mercury Ion Beam Sputtering of Metals at Energies 4-15 keV," JAP, 32, 887-890 (1961).

3. G. Wehner, "Influence of the Angle of Incidence on Sputtering Yields," JAP, 30, 1762-1765 (1959).

4. G.K. Wehner and D. Rosenburg, "Angular Distribution of Sputtered Material," JAP, 31, 177-179 (1960).